Detection of extracellular vesicles: size does matter

Edwin van der Pol

Detection of extracellular vesicles: size does matter

The work described in this thesis was carried out in the groups *Biomedical Engineering & Physics* and *Laboratory Experimental Clinical Chemistry* at the *Academic Medical Center* of the *University of Amsterdam*, Amsterdam, The Netherlands. Part of this work was funded by the *European Metrology Research Programme* (EMRP) under the Joint Research Project HLT02 (`www.metves.eu`). The EMRP is jointly funded by the EMRP participating countries within the *European Association of National Metrology Institutes* and the European Union.

Cover: The front cover shows an artist impression of a swarm of extracellular vesicles. The back cover shows extracellular vesicles in human urine drawn to scale. A realistic size distribution and concentration of vesicles are selected based on the contents of this thesis. The size distribution is based on a power-law distribution ($m = 4 \cdot 10^{16}$, $k = 4$). The total concentration of vesicles is $10^{11}\,\mathrm{mL}^{-1}$. The field-of-view is $10.0 \times 7.1 \times 14.1\ \mu\mathrm{m}^3$, resulting in a total volume of 1,000 fL. The most sensitive implementation of a widely applied technique to study vesicles can only detect the largest (300 nm) vesicle on the back cover.

Printed: ProefschriftMaken - `www.proefschriftmaken.nl`
Vianen, The Netherlands
ISBN: 978-9-46-295069-6
URL: `www.edwinvanderpol.com`

2nd edition

Detection of extracellular vesicles: size does matter

ACADEMISCH PROEFSCHRIFT

ter verkrijging van de graad van doctor
aan de Universiteit van Amsterdam
op gezag van de Rector Magnificus
prof. dr. D.C. van den Boom
ten overstaan van een door het College van Promoties ingestelde
commissie, in het openbaar te verdedigen in de Agnietenkapel
op donderdag 29 januari 2015 te 14:00 uur

door

Edwin van der Pol

geboren te Sneek

Promotiecommissie

Promotores:
Prof. Dr. A.G.J.M. van Leeuwen
Prof. Dr. A. Sturk

Co-promotor:
Dr. R. Nieuwland

Overige leden:
Dr. P. Harrison
Prof. Dr. Ir. A.G. Hoekstra
Prof. Dr. J.C.M. Meijers
Prof. Dr. L.W.M.M. Terstappen
Prof. Dr. M.H.M. Wauben

Faculteit der Geneeskunde

Table of contents

Chapters

CHAPTER 1

Introduction

1.1 Thesis motivation

Cells release small biological sacks filled with fluid, which are called "extracellular vesicles". The diameter of extracellular vesicles typically ranges from 30 nm to 1 µm [69, 19], the smallest being some 100-fold smaller than the smallest cells in the human body. Fig. 1.1A shows a scanning electron microscopy image of vesicles that are released by an endothelial cell. Because cells release vesicles into their environment, body fluids, such as blood, saliva, and urine, contain numerous cell-derived vesicles. Cells employ vesicles to remove waste and transport and deliver cargo, such as receptors and genetic information, to other cells. Since the cargo allows vesicles to target messages to specific cells, vesicles most likely play a key role in intercellular communication. In addition, the size, concentration, cellular origin, and composition of vesicles in body fluids is changed during diseases. For example, increased levels of vesicles in plasma are associated with thrombosis and metastatic carcinomas [37, 73]. The functions of vesicles and their change of properties during disease imply that vesicles have many clinical applications. For example, an abundant concentration of a particular vesicle type could be indicative for the presence of a disease. Such information would enable early recognition of a disease and monitoring the efficacy of therapy. Furthermore, vesicles can be used to deliver drugs specifically to the diseased organ without being cleared by the immune system [284]. For these applications to become reality, we need to gain a profound understanding of extracellular vesicles.

Rose Johnstone appointed her discovery of vesicle formation in 1987 as "Alice in Blunderland" [74]. Although the field of vesicle research is growing exponentially ever since (Fig. 1.1B) and much progress has been made, Johnstone's statement still applies to the current state of the field. Physical properties of vesicles, such as their size distribution, morphology, refractive index, and concentration are still unknown. For example, the reported concentrations of vesicles in human plasma from healthy individuals differ 100,000,000-fold [37, 316, 90, 335]. However, since normal cell counts differ less than 10-fold between healthy individuals, the true range in vesicle concentrations is probably orders of magnitude smaller.

The main reasons for the differences in the reported concentrations are the small size of extracellular vesicles and the limited sensitivity of detection techniques. Flow cytometry, which is the most widely applied technique to study single vesicles, detects only 1 % of all vesicles present. Other techniques measure millions

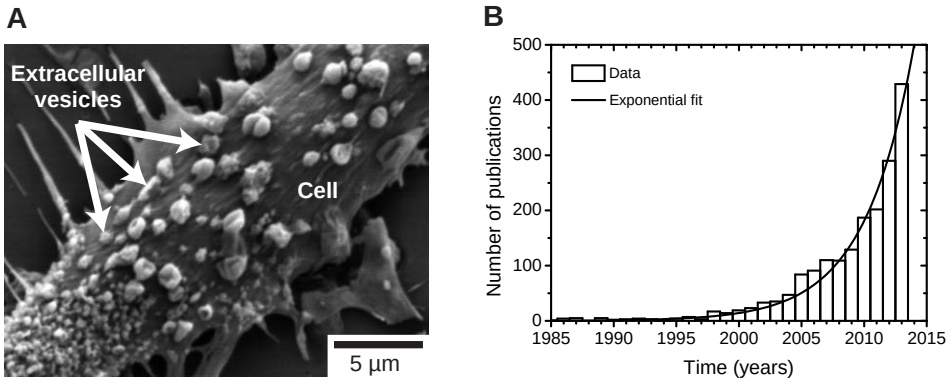

Figure 1.1: (A) Scanning electron microscopy image of extracellular vesicles (arrows) that are secreted by an endothelial cell. Image courtesy of Anita Böing. (B) Number of publications per year about extracellular vesicles (bars) fitted by an exponential function (line, $R^2 = 0.98$) [3].

of vesicles simultaneously and are therefore unable to identify sub-populations of vesicles. Over the last decade, novel techniques found their way to the vesicle labs, but their suitability for vesicle detection is not sufficiently tested and understood.

The aim of this thesis is to improve the detection of extracellular vesicles by (1) obtaining insights into fundamental physical properties of vesicles, and (2) gaining a profound understanding of the currently used and novel detection techniques. Since this knowledge is a prerequisite to understand the biological relevance of vesicles in health and disease and increase the clinical usefulness of vesicles, this thesis paves the way to Vesicles' Wonderland.

1.2 Thesis contents

Chapter 2 contains an introduction to extracellular vesicles. The history, nomenclature, classification, types, properties, functions, and clinical relevance of extracellular vesicles are discussed. In *Chapter 3*, an overview is provided of 14 currently available and potentially applicable methods for optical and non-optical determination of the size, concentration, morphology, biochemical composition and cellular origin of vesicles. The working principle of all techniques is briefly discussed, as well as their capabilities and limitations based on the underlying physical parameters of the technique. To compare the precision in determining the size of vesicles between the discussed techniques, a mathematical model is developed to calculate the expected size distribution for a reference vesicles population. In *Chapter 4*, an experimental evaluation is performed of 5 of the 14 methods. The most widely used methods capable of detecting single vesicles are selected, which are transmission electron microscopy, a conventional flow cytometer, a flow cytometer dedicated to detecting sub-micrometer particles, nanoparticle tracking analysis

and tunable resistive pulse sensing. The accuracy, precision and detection range of these methods are determined. Insight into the capabilities of the applied methods to measure the size distribution of vesicles enabled to explain why the reported concentrations of vesicles in human blood plasma differ 100,000,000-fold.

Chapter 5 further addresses vesicle detection by flow cytometry, which is the most widely used technique to study single vesicles. It is shown that vesicle detection by flow cytometry is partly attributed to swarm detection of smaller vesicles, that is, multiple vesicles are simultaneously illuminated by the laser beam and counted as a single event signal. In addition, the relationship between light scattering and the diameter of vesicles is modeled to demonstrate that the current vesicle gating strategy selects vesicles and cells with a diameter between 800 nm and 2,400 nm.

For optical detection and characterization of vesicles, the refractive index of vesicles is an important but unknown property. The refractive index is important because it relates light scattering to the size and composition of a vesicle. In *Chapter 6*, a novel method is described to determine both the refractive index and the diameter of single vesicles in suspension.

In chapter 4 it is shown that tunable resistive pulse sensing is the most accurate technique to determine the size and concentration of vesicles in suspension. However, the reproducibility of tunable resistive pulse sensing is not investigated. In *Chapter 7*, the reproducibility is quantified. Furthermore, a protocol is developed to improve both the reproducibility and sensitivity of tunable resistive pulse sensing.

Because body fluids contain many particles other than vesicles, vesicles require isolation prior to detection. However, isolation of vesicles from particularly plasma is challenging due to the high complexity of this body fluid. In *Chapter 8* it is demonstrated that a single step isolation procedure of vesicles from plasma by size-exclusion chromatography can be used. The acquired knowledge on vesicle detection is used to demonstrate that size-exclusion chromatography has excellent recovery and enrichment.

In *Chapter 9*, the reader is taken beyond the state of the art. The applicability of vesicle detection by specialized techniques, such as Raman microspectroscopy, micro nuclear magnetic resonance, small-angle X-ray scattering and anomalous small-angle X-ray scattering is discussed.

Chapter 10 contains the general discussion, where the major findings of this thesis are placed into the context of the current state of the field. To finish off, the future of extracellular vesicles detection is enlightened.

CHAPTER 2

Classification, functions, and clinical relevance of extracellular vesicles

Abstract

Both eukaryotic and prokaryotic cells release small, phospholipid-enclosed vesicles into their environment. Why do cells release vesicles? Initial studies showed that eukaryotic vesicles are used to remove obsolete cellular molecules. Although this release of vesicles is beneficial to the cell, the vesicles can also be a danger to their environment, for instance in blood, where vesicles can provide a surface supporting coagulation. Evidence is accumulating that vesicles are cargo containers used by eukaryotic cells to exchange biomolecules as transmembrane receptors and genetic information. Because also bacteria communicate to each other via extracellular vesicles, the intercellular communication via extracellular cargo carriers seems to be conserved throughout evolution, and therefore vesicles are likely to be a highly efficient, robust, and economic manner of exchanging information between cells. Furthermore, vesicles protect cells from accumulation of waste or drugs, they contribute to physiology and pathology, and they have a myriad of potential clinical applications, ranging from biomarkers to anticancer therapy. Because vesicles may pass the blood-brain barrier, they can perhaps even be considered naturally occurring liposomes. Unfortunately, pathways of vesicle release and vesicles themselves are also being used by tumors and infectious diseases to facilitate spreading, and to escape from immune surveillance. In this chapter, the different types, nomenclature, functions, and clinical relevance of vesicles will be discussed.

Parts of this chapter have been published as:

- E. van der Pol, A.N. Böing, P. Harrison, A. Sturk, and R. Nieuwland. Classification, functions, and clinical relevance of extracellular vesicles. *Pharmacol. Rev.* **64**(3), 676−705 (2012)
- E. van der Pol, T.G. van Leeuwen, and R. Nieuwland. *An overview of novel and conventional methods to detect extracelllular vesicles.* In: P. Harrison, C. Gardiner, and I.L. Sargent, ed. Extracellular vesicles in health and disease, 1st edn., Singapore, Pan Stanford Publishing (2014)
- R. Nieuwland, E. van der Pol, and A. Sturk. *Overview of microvesicles and exosomes in health and disease.* In: P. Harrison, C. Gardiner, and I.L. Sargent, ed. Extracellular vesicles in health and disease, 1st edn., Singapore, Pan Stanford Publishing (2014)

2.1 Introduction

2.1.1 Cell-derived vesicles

Both eukaryotic and prokaryotic cells release vesicles, which are spherical particles enclosed by a phospholipid bilayer. The diameter of vesicles typically ranges from 30 nm to 1 µm [69], the smallest being some 100-fold smaller than the smallest cells. Because cells release vesicles in their environment, body fluids such as blood and urine, but also conditioned culture media, contain numerous cell-derived vesicles, usually more than 10^{10} per mL [335, 90]. It is becoming increasingly clear that most vesicles have specialized functions and play a key role in, for example, intercellular signaling, waste management, and coagulation. Consequently, there is a growing interest in the clinical applications of vesicles. Vesicles can potentially be used for therapy, prognosis, and biomarkers for health and disease. Nevertheless, because of the small size and heterogeneity of vesicles, their detection and classification is challenging [235]. Although different types of vesicles have been identified, widely used terms, such as "exosomes" and "microparticles," are often inconsistent, especially in the older literature. Even if "purified exosomes" are claimed to be measured, it is prudent to remain cautious. Moreover, it should be emphasized that the extent to which vesicles really contribute to processes underlying physiology and pathology is virtually unexplored, and therefore one should also remain cautious to extrapolate results from in vitro studies on vesicles and their functions to the in vivo situation.

In this chapter, the focus will be on exosome-mediated signaling, although we will also outline recent developments on other vesicles within the relatively novel and rapidly expanding research field. A screening of the literature on cell-derived vesicles provided more than 6,000 publications, from which approximately 500 were selected for review, with emphasis on recent publications from high-impact journals.

2.1.2 History

The discovery of cell-derived vesicles dates back to 1940, when preliminary studies were performed, addressing the "biological significance of the thromboplastic protein of blood" [61]. Clotting times of plasma were determined after centrifugation at different speeds, and prolonged high-speed centrifugation (150 min at 31,000 g was shown to significantly extend the clotting time of the supernatant. Furthermore, when the pellet containing "the clotting factor of which the plasma is deprived" was added to plasma, the clotting times shortened, indicating that cell-free plasma contains a subcellular factor that promotes clotting of blood [61]. More than 20 years later, in 1967, this subcellular fraction was identified by electron microscopy and was shown to consist of small vesicles, originating from platelets and termed "platelet dust" [329]. These vesicles were reported to have a diameter between 20 and 50 nm and had a density of 1.020 to 1.025 g mL^{-1} [329]. One decade

later, fetal calf serum was also shown to contain "numerous microvesicles" ranging in diameter from 30 to 60 nm [78].

Meanwhile, within a completely different line of research, the term "exosomes" was introduced when vesicles were isolated from conditioned culture medium of sheep reticulocytes. These vesicles had several characteristic activities in common with the reticulocyte plasma membrane, including the presence of the transferrin receptor, whereas cytosolic enzyme activities were not detected. Therefore, it was concluded that "vesicle externalization could be a mechanism for shedding of specific membrane functions, which are known to diminish during maturation of reticulocytes to erythrocytes" [152]. Because these exosomes contained the transferrin receptor but expressed no lysosomal activities, it was also suggested that there may be a common mechanism to segregate and externalize specific plasma membrane proteins [153]. The formation of the transferrin receptor-containing exosomes proved to be a major route for removal of plasma membrane proteins. Because not only mammalian but also embryonic chicken reticulocytes were shown to produce transferrin receptor-containing exosomes, this may be a conserved and common pathway [154, 116]. It was then discovered that exosomes are formed within multivesicular endosomes (MVEs), also known as multivesicular bodies, and are being released when membranes of MVEs fuse with the plasma membrane. This pathway of protein sorting turned out to be highly selective, because other major transmembrane proteins, such as the anion transporter, are fully retained within the mature red cell and are absent within exosomes [151]. Taken together, these early studies revealed that exosomes might be essential in a sophisticated and specific mechanism to remove obsolete transmembrane proteins.

2.1.3 Nomenclature

Because of the detection difficulties, the multidisciplinary research field, and different ways of classification, there is currently no consensus about the nomenclature of cell-derived vesicles. For example, cell-derived vesicles have often been called after the cells or tissues from which they originate [e.g., dexosomes (dendritic cell-derived exosomes) [186], prostasomes (prostate-derived vesicles) [279], matrix vesicles (vesicles in bone, cartilage and atherosclerotic plaques) [286], and synaptic vesicles (vesicles from neurons) [315]]. However, such names do not provide a clue for classification with regard to the type of vesicles involved.

Types of vesicles in recent literature

In four recent reviews, vesicles were classified into between two and six major different types [66, 296, 32, 197]. Two common types were distinguished unanimously [i.e., exosomes and microvesicles (also called shedding vesicles, shedding microvesicles, or microparticles)], and in three of these reviews, apoptotic vesicles (also called apoptotic blebs, or apoptotic bodies) became a separate class [296, 32, 197]. In addition, "ectosomes," "membrane particles," and "exosome-like vesicles" were distinguished on the basis of the physicochemical characteristics of vesicles, in-

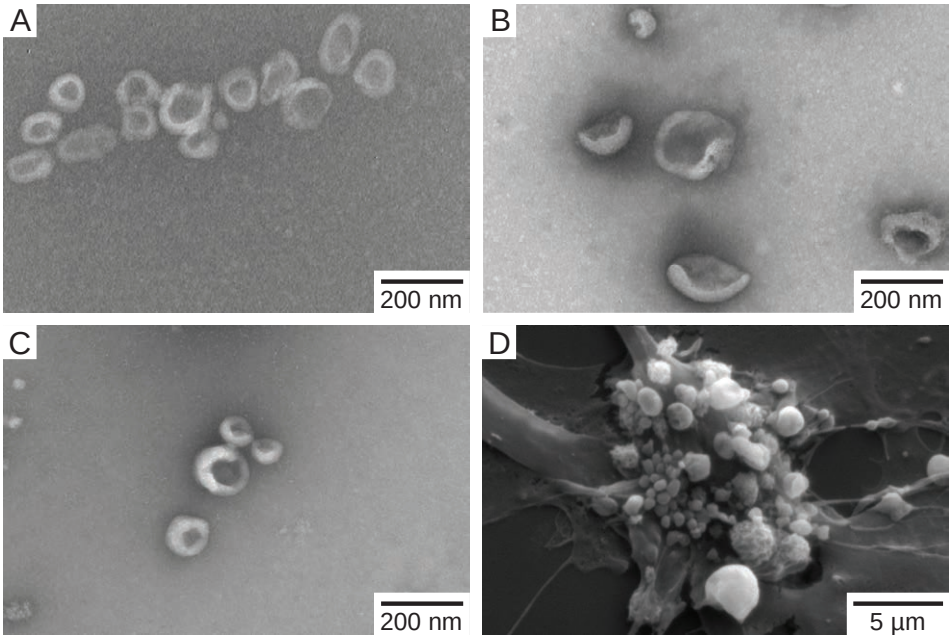

Figure 2.1: Different types of eukaryotic cell-derived vesicles. Transmission electron micrographs of cell-derived vesicles isolated by differential centrifugation from plasma (A; exosomes, diameter < 100 nm, urine (B; microvesicles, diameter > 100 nm), or saliva (C; either exosomes or membrane particles, diameter < 100 nm) of a healthy human subject. A scanning electron micrograph (D) showing a human umbilical vein endothelial cell releasing apoptotic vesicles. Please notice the much larger size of apoptotic vesicles compared with the other types of vesicles, and the typical cup shape of vesicles.

cluding size, density, appearance in microscopy, sedimentation, lipid composition, main protein markers, and subcellular origin [i.e., originating from intracellular compartments (exosomes) or plasma membranes] [296]. Although this classification is the best and most extensive so far, it is difficult to use in daily practice. For instance, a vesicle with a diameter of 50 nm can be classified either as an exosome, ectosome, membrane particle, exosome-like vesicle, or apoptotic vesicle according to this scheme, and, as correctly mentioned by the authors "in practice, all vesicles preparations are heterogeneous, with different protocols allowing the enrichment of one type over another."

Types of vesicles in this chapter

In this chapter, we propose to distinguish four different types of eukaryotic cell-derived vesicles: (1) exosomes, (2) microvesicles (microparticles), (3) membrane particles, and (4) apoptotic vesicles, thereby omitting "ectosomes" and "exosome-like vesicles," because there is insufficient evidence to support the existence of

Table 2.1: Overview of the main characteristics of different types of eukaryotic cell-derived vesicles

Vesicle type	Diameter (nm)	Density (g mL^{-1})	Morphology	Cellular origin	Subcellular origin	Composition
Exosomes	50−100 [93, 129, 245, 300]	1.13−1.19 [93, 245]	Cup-shaped [93, 129, 245, 18]	Most cell types	Plasma membrane endosomes [43, 96, 123, 187, 224]	Biochemical composition known, but most proteins and lipids not unique for exosomes [93, 129, 18, 32, 290, 296, 302]
Microvesicles	20−1,000 [129, 302, 90, 120, 329]	Unknown	Cup-shaped	Most cell types	Plasma membrane [329, 14, 75, 110, 111]	Insufficiently known
Membrane particles	50−80, 600 [138]	1.032−1.068 [138]	Cup-shaped [196]	Epithelial cells only [138]	Plasma membrane [138]	CD133 [138]
Apoptotic vesicles	1,000−5,000 [296, 302, 138, 164]	1.16−1.28 [302]	Heterogeneous [164]	All cell types	Plasma membrane endoplasmic reticulum [35]	Histones, DNA [302, 138, 164, 35, 136]

Morphology is obtained by transmission electron microscopy.

these types of vesicles [296]. The main characteristics of these types of vesicles are summarized in Table 2.1 and Fig. 2.1 illustrates the various types of vesicles.

"Ectosomes" have been omitted because (1) the reported size of these neutrophil-derived vesicles (50−200 nm) was based partially on flow cytometry using 200 nm beads, a procedure now known to lead to underestimation of the diameter and concentration of the vesicles as a result of differences in refractive indexes between the beads and the vesicles [235, 58, 234], (2) these vesicles were observed in vitro only, and (3) neutrophils also release microvesicles, which was not known when the term "ectosomes" was introduced [77].

The "exosome-like vesicles" were omitted because (1) these vesicles, which were shown to contain the 55 kDa full length from the tumor necrosis factor (TNF)-α receptor, were erroneously reported to be mainly present in the 175,000 g fraction of conditioned medium of human umbilical vein endothelial cells and bronchoalveolar lavage (BAL) fluid, whereas they are present predominantly in the 100,000 g fractions (i.e., the fraction in which also exosomes are usually isolated) [296], (2) the transmission electron microscopy (TEM) micrographs show damaged and disrupted vesicles, which makes estimation of the real vesicle size difficult, and (3) endothelial-conditioned medium and BAL also contain exosomes [11, 238, 165, 318].

2.1.4 Current limitations of classification

Important criteria for classification with regard to the type of cell-derived vesicles are size, density, morphology, lipid composition, protein composition, and subcellular origin [296, 235], which are summarized in Table 2.1. In the near future, it is expected that also the refractive index, ζ-potential, and chemical composition will be accessible from individual vesicles to become novel relevant characteristics. It is important to point out the limitations and problems with the current criteria, which is necessary to fully understand and appreciate the literature about exosomes and other types of cell-derived vesicles.

Isolation

Because of the biological complexity of body fluids, isolation of vesicles has proven to be extremely difficult. For instance, isolation of vesicles from blood is affected by venipuncture, time between blood collection and handling, the anticoagulant, the applied separation process, the high viscosity of blood, and the presence of sticky proteins, including fibrinogen and albumin [333]. Because of their small size, vesicles are below the detection range of conventional detection methods. Consequently, recovery and contamination of the separation process cannot be reliably quantified, and isolation protocols have not been standardized. The interrelated difficulties of the detection and isolation of vesicles partly explains the differences in classification criteria and clearly exposes one of the main issues to be solved by the research field.

In most studies, vesicles are isolated by differential centrifugation. With cen-

trifugation, the centrifugal force is used for the sedimentation of particulate matter, such as vesicles in solution. Separation of the various sorts of vesicles present in a sample is based on size and density, larger and denser components migrating away from the axis of the centrifuge and smaller and less-dense components migrating toward the axis. Differential centrifugation involves multiple sequential centrifugation steps, each time removing the pellet and increasing the centrifugal force to separate smaller and less dense components than the previous step. Typically, applied centrifugal accelerations are approximately 200 to 1,500 g to remove cells and cellular debris, 10,000 to 20,000 g to pellet vesicles larger than 100 nm, and 100,000 to 200,000 g to pellet vesicles smaller than 100 nm.

Besides the size and density of vesicles, the efficiency to isolate vesicles will depend on the shape and volume fraction of the vesicles, the volume, viscosity, and temperature of the fluid in which the vesicles are present, the centrifugation time, and the type of rotor used (fixed angle or swing-out). Because vesicles are heterogeneous in all aspects involved in differential centrifugation, complete separation of vesicles with a certain diameter or density is still utopian. For example, we recently applied differential centrifugation to the best of our ability to separate vesicles smaller than 100 nm from larger vesicles, all present in human saliva, and observed substantial cross contamination (∼10 %) in both fractions [30].

Centrifugation also raises other problems that have to be taken into account. The removal of all cells from biological fluids can be challenging, for instance in the case of blood, where small platelets and apoptotic bodies overlap in size with large vesicles. When the centrifugal force applied to remove cells is too high, cells may fragment or become activated. Washing of vesicle pellets will often result in the loss of vesicles, resulting in variable yields. For instance, approximately 40 to 60 % of platelet-derived vesicles are lost at every washing step, whereas vesicles from erythrocytes are unaffected (M.C.L. Schaap and R.J. Berckmans, personal communication). In addition, a high centrifugal acceleration of 100,000 to 200,000 g may result in vesicle fusion and contamination of the pellets with proteins, thus hampering TEM and proteomic studies [21, 256, 121]. Moreover, the functional properties of vesicles may change during isolation. For example, centrifugation of vesicles may increase thier exposure of phosphatidylserine (PS), thereby enhancing the ability of vesicles to promote coagulation (R.J. Berckmans, personal communication).

Besides differential centrifugation, filtration can be applied to isolate vesicles. With filtration, the isolation of vesicles is based on differences in size, shape, and deformability between types of vesicles and other particles. Although most filters have a well-defined pore size, the filtrate may contain larger vesicles than the pore size due to the deformation of vesicles. In addition, filters may bind subpopulations of vesicles, and increasing forces have to be applied with decreasing pore size. One recent advance is the availability of nanofabricated filtration sieves, which have pores with well-defined diameters as small as 100 nm [72, 251, 301]. Fig. 2.2A shows a scanning electron micrograph of a filtration sieve containing pores with a diameter of 900 nm. Nanofabricated filters have the capability to separate plasma

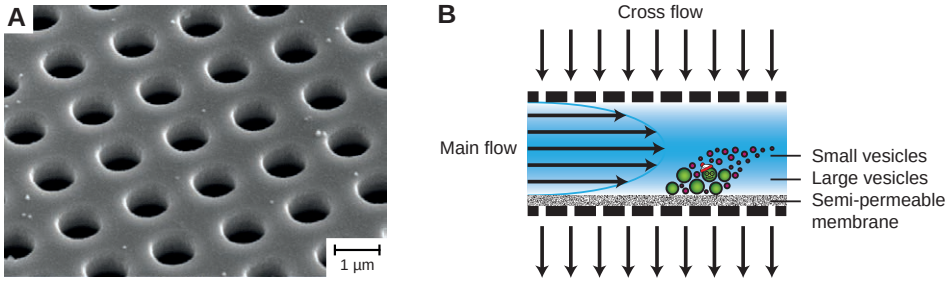

Figure 2.2: Advanced methods to isolate vesicles. (A) Scanning electron micrograph of a filtration sieve containing pores with a diameter of 900 nm. Image courtesy of C.J.M. van Rijn. (B) Schematic of the underlying principle of FFFF. Since relatively small vesicles (purple) have a large diffusion coefficient compared to relatively large vesicles (green), small vesicles are on average located more centrally in the flow channel than larger vesicles. Consequently, due to the parabolic flow profile of the channel flow, small vesicles elute faster than larger vesicles.

from whole blood by capillary forces only, as was demonstrated using a planar filter with a thickness of 500 nm [76]. However, the total obtained volume of plasma from 5 µL blood was merely 45 nL. Further investigation is necessary to employ nanofabricated filters for the isolation of EVs.

Alternatively, vesicles can be isolated and fractionated by size using flow-field flow fractionation (FFFF). Fig. 2.2B shows a schematic of the underlying principle of FFFF. In an open flow channel a laminar flow with a parabolic stream profile is formed. This main flow transports the sample through the channel to which a cross flow is applied perpendicularly. The cross flow is directed through a semipermeable membrane that is located at the bottom wall. The membrane allows the fluid to exit the channel but prevents the vesicles to pass through. Under the influence of the Brownian motion of vesicles and the counteracting cross flow, different equilibrium layer heights are formed by different vesicle size fractions. Small vesicles with high diffusion coefficients are on average located more centrally in the flow channel in fast stream lines and elute first. Larger vesicles with lower diffusion coefficients are on average located in slow stream lines and elute later. This results in size-based fractionation with a resolution of up to 10 nm without exposing the vesicles to high shear stress [170]. Although FFFF is successfully applied to isolate exosomes from human neural stem cells [159], FFFF is not widely applied because it requires extensive optimization of the settings and is expensive relative to differential centrifugation.

Size

Because vesicles are assumed to be spherical in their natural state, the size of vesicles given is usually the diameter. The relation between the range of the diameter of vesicles and their concentration is the size distribution, preferably expressed

as number of vesicles per unit particle size and suspension volume. However, because most size determinations of vesicles are based on TEM, the original volume of the suspension from which the vesicles originate cannot be assessed, and a differential size distribution is used, indicating the number of vesicles per unit particle size only. Because TEM is performed in a vacuum, fixation and dehydration are essential preparation steps likely to affect the size and morphology of vesicles [235]. Novel methods have been explored to determine the size and concentration of vesicles directly in suspension, including atomic force microscopy [269, 335], nanoparticle tracking analysis [90], and resistive pulse sensing. Typically, size distributions obtained from vesicles have the shape of a Gaussian or log normal distribution, but to what extent this reflects the natural population of vesicles is unknown, because the results are strongly influenced by (pre)analytical variables such as the isolation procedure and the detection limit of the applied detection technique. The (pre)analytical variables together with the choice of statistical parameters used to describe the size distribution (e.g., minimum, maximum, full width at half-maximum, mean, median, and mode diameter) all give rise to a marked range in the reported size for the different types of vesicles.

Density

The determination of the density of vesicles is usually based on sucrose gradient centrifugation. Because vesicles are very heterogeneous in all aspects involved in centrifugation, and because observed differences in the densities between types of vesicles are very small, discriminating types of vesicles by density is difficult.

Morphology

The morphology of cell-derived vesicles can be assessed with detection methods having subnanometer resolution, such as TEM and atomic force microscopy. For example, the morphology of exosomes has been traditionally described as "typical cup-shaped" after fixation, adhesion, negative staining, and visualization by TEM. However, to what extent this feature is either an artifact due to extensive sample preparation or actually unique for exosomes and does not apply to other vesicles is unknown [196]. The cupshaped morphology may still be a useful feature to distinguish cell-derived vesicles from similar-sized particles. With atomic force microscopy, the morphology of vesicles adhered to a surface can be studied directly in solution [269, 335]. However, because of the adhesion of vesicles to the surface, their structure changes from spherical to hemispherical or flat, depending on the composition of the membrane [160], which may cause artifacts in the interpretation of both size and morphology.

Lipid composition, protein composition, and cellular origin

Studies on the cellular origin and intracellular versus plasma membrane origin of vesicles are often based on the measurement of the lipid and protein composition of the total population of vesicles that has been isolated (e.g., by Western blotting and

mass spectroscopy). Obviously, this approach does not provide information on the presence of contaminants, such as other types of vesicles or copurified proteins. For example, exosomes from malignant pleural effusions isolated by sucrose gradient centrifugation contain immunoglobulins [21]. By far the most widely used method to establish the cellular origin and phenotype of single vesicles is flow cytometry, which is based on the detection of light scattering and fluorescence from labeled vesicles. Nevertheless, the smallest detectable single vesicle by flow cytometry varies between 300 and 700 nm on older generation flow cytometers [234]. Modern flow cytometers using high collection angle optics are capable of detecting single polystyrene beads with a diameter as small as 100 nm [252], corresponding to vesicles with a diameter larger than 150 nm owing to refractive index differences [58]. Because most vesicles have a diameter smaller than 100 nm, it is not surprising that according to recent estimates only 1 to 2 % of all vesicles present in biological fluids (e.g., plasma and urine) are actually detected [235, 335, 58]. One popular solution to this problem has been to use specific capture beads that are sufficiently large to be measurable. The capture beads bind multiple smaller vesicles, thus facilitating their phenotyping by flow cytometry.

In sum, although there is no doubt that different types of cell-derived vesicles do exist, the interrelated difficulties of the detection and isolation of vesicles hamper the development of criteria to distinguish them. Consequently, the classification of vesicles is clearly work in progress. Nonetheless, recent studies have shown that the detection of single vesicles smaller than 100 nm is becoming feasible. Therefore, new developments on the detection of vesicles are likely to improve the criteria for classification [235, 335, 90].

2.2 Types of cell-derived vesicles

2.2.1 Exosomes

Exosomes are cell-derived vesicles that are present in many and perhaps all biological fluids, including urine, blood, ascites, and cerebrospinal fluid [229, 53, 163, 311], fractions of body fluids such as serum and plasma, and cultured medium of cell cultures. The reported diameter of exosomes is between 30 and 100 nm and the density ranges between 1.13 and 1.19 $\mathrm{g\,mL^{-1}}$. Exosomes are usually isolated by ultracentrifugation (100,000 to 200,000 g). The morphology of exosomes has been described as cup-shaped after fixation, adhesion, negative staining, and visualization by TEM. Regarding their biochemical composition, exosomes are surrounded by a phospholipid membrane containing relatively high levels of cholesterol, sphingomyelin, and ceramide and containing detergent-resistant membrane domains (lipid rafts) [331, 270, 296, 197]. The membrane proteins have the same orientation as the cell. Exosomes are characterized by the presence of proteins involved in membrane transport and fusion, such as Rab, GTPases, annexins, and flotillin, components of the endosomal sorting complex required for transport (ESCRT) complex such as Alix, tumor susceptibility gene 101 (TSG101), heat shock

proteins (HSPs), integrins, and tetraspanins, including CD63, CD81, and CD82 [66, 270, 296, 32, 197, 39, 60, 248].

Although all of the aforementioned properties of exosomes are frequently reported and accepted, none of these properties is unique and identifies exosomes. There is increasing evidence that there is overlap between properties previously thought to be unique for exosomes and properties of other types of cell-derived vesicles, suggesting that there is a continuum of vesicle types with overlapping properties present in body fluids.

For example, the typically reported diameter of exosomes may be biased toward smaller particles for two reasons. First, exosomes are often isolated by differential centrifugation, which involves a loss of relatively large vesicles during removal of cells by centrifugation. Second, because in most studies only a limited number of exosomes are visualized by TEM, and because the size distribution of vesicles typically has the shape of a Gaussian or log normal distribution with a peak below 100 nm, as also confirmed by novel detection methods, such an analysis will easily overlook the presence of vesicles larger than 100 nm. Although these larger vesicles represent only a relatively small fraction of the total population, their total surface area or volume and thus their functional contribution may be relatively large.

Identification of exosomes based on their cup-shaped morphology after negative staining and visualization by TEM seems questionable. For example, exosomes and similar-sized vesicles, called membrane particles or prominosomes, both appear with a cup-shaped morphology on the same electron micrographs [196]. Fig. 2.1 shows that not only exosomes but also vesicles larger than 100 nm may appear cup-shaped by TEM. Finally, recent evidence indicates that not all exosomes originate from intracellular MVEs, the "classic pathway" of exosome formation, thereby making identification of exosomes even more complex.

Classic pathway of exosome formation

The "classic pathway" of exosome formation is by far the best studied and involves the formation of intraluminal vesicles within MVEs (Fig. 2.3). In turn, MVEs can fuse with either lysosomes for cargo degradation or with the plasma membrane to secrete the intraluminal vesicles, which are then released as exosomes.

Different intracellular sorting pathways exist in directing proteins toward intraluminal vesicles predestined for either degradation or secretion, thus implicating the existence of different types of MVEs. Redundant transmembrane receptors are sorted to intraluminal vesicles predestined for lysosomal degradation after ubiquitination, a post-translational modification that is executed by ESCRT [20, 204]. On the other hand, there is no compelling evidence that the ESCRT is involved in the sorting of transmembrane receptors to intraluminal vesicles that are predestined to become secreted as exosomes [295, 51, 52, 299, 270, 285, 39]. Although several ESCRT proteins [295] and ubiquitinated proteins [51] are present in exosomes, the ubiquitinated proteins are soluble proteins and not transmembrane proteins, suggesting that ubiquitination may have occurred in the cytosol rather than by the ESCRT. Likewise, the sorting of the proteolipid protein to intralu-

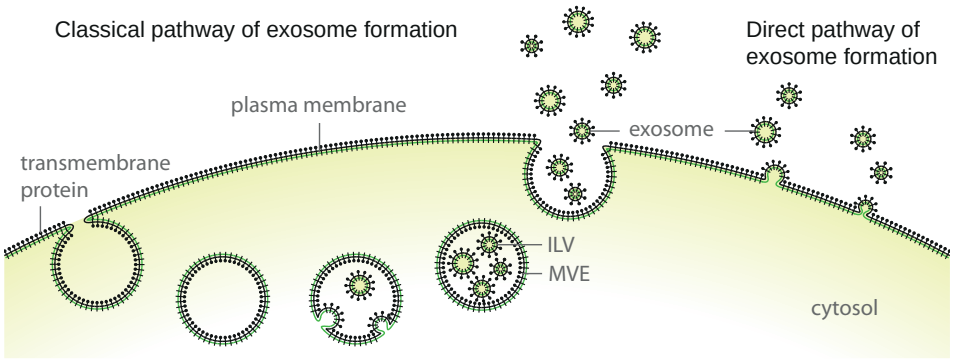

Figure 2.3: Pathways of exosome formation. Cells release exosomes via two mechanisms. The classic pathway (left) involves the formation of intraluminal vesicles (ILVs) within multivesicular endosomes (MVEs). In turn, the membrane of MVE fuses with the plasma membrane, resulting in the release of ILVs. When secreted, ILVs are called exosomes. Alternatively, the direct pathway (right) involves the release of vesicles, indistinguishable from exosomes, directly from the plasma membrane.

minal vesicles predestined to become secreted as exosomes is independent from the ESCRT but depends on the sphingolipid ceramide [194, 299]. Further evidence for two pathways comes from studies showing that lysobisphosphatidic acid induces the formation of intraluminal vesicles predestined for lysosomal degradation but does not affect the formation of exosomes [198]. This is confirmed by studies in which cholesterol is labeled with perfringolysin O, which reveals perfringolysin O-positive and -negative MVEs in B cells, of which only the cholesterolcontaining MVEs fuse with the plasma membrane resulting in the release of exosomes [207]. In addition, both epidermal growth factor and the epidermal growth factor receptor (EGFR) travel to exosomes via MVEs not containing the lipids bis(monoacylglycero)phosphate/lysobisphosphatidic acid, whereas the bis(monoacylglycero) phosphate/lysobisphosphatidic acid-containing vesicles are degraded by lysosomes [324]. Thus, clearly two intracellular pathways of MVE sorting exist.

Cytosolic domains of proteins [293] or lipid domains enriched in the tetraspanins CD9 or CD63 are thought to play a role in the sorting of transmembrane proteins toward intraluminal vesicles [52, 39]. Several different types of small GTPases from the Rab family play a role in the intracellular trafficking of MVEs toward either the plasma membrane [260, 139, 222] or to lysosomes for degradation [280], as well as cytosolic calcium levels [261, 98, 172], citron kinase, [189], and a still unidentified combination of soluble N-ethylmaleimidesensitive factor attachment protein receptors, which is involved in the final fusion of the MVE membrane with the plasma membrane [244].

Direct pathway of exosome formation

Next to the "classic pathway" of exosome biogenesis, there is a second and much more immediate route of exosome formation (Fig. 2.3). T cells and erythroleukemia cell lines release exosomes directly from their plasma membrane, both spontaneously as well as upon expression of HIV Gag or Nef, or after cross-linking of surface receptors [43, 96, 187]. These vesicles are indistinguishable from exosomes formed by the classic endosomal pathway because they are enriched in classic exosome markers such as CD63 and CD81 and have a similar diameter and density. The extent to which such exosomes are also released from other cells or in vivo (e.g., in biological fluids) is unknown.

2.2.2 Microvesicles

Microvesicles, often called microparticles, is a term used for vesicles that are released from the plasma membrane during cell stress. This term is also often used to describe total populations of vesicles isolated from biological fluids [215, 129, 32]. In addition, microvesicles are present in most if not all biological fluids, atherosclerotic plaques and conditioned culture medium [192, 29, 30, 55, 210]. Although microvesicles are believed to be larger than exosomes and are usually reported to range in size between 100 nm and 1.0 µm in diameter [296], there is much confusion on this matter. For instance, with regard to the diameter of vesicles in plasma from healthy human individuals, the following size ranges have been reported: 20 to 50 nm by TEM [329], 200 to 800 nm by TEM [302], 180 nm (mean) by TEM and atomic force microscopy [120], and 80 nm (mean) by nanoparticle tracking analysis [90]. Consequently, the size ranges of microvesicles and exosomes may overlap, especially when body fluids are used as a source for isolation of vesicles. In vitro, activated platelets release two clearly distinct populations of vesicles, small (< 100 nm) vesicles exposing CD63, exosomes, and large ($100-1{,}000$ nm) microvesicles exposing typical platelet receptors such as glycoprotein Ib [129]. Therefore, when only a single cell type is studied in vitro, both types of vesicles may be distinguishable. The density of microvesicles is unknown, and microvesicles are usually isolated by centrifugation at 10,000 to 20,000 g [296]. The term "microparticles", however, has also been used for total populations of vesicles isolated from human plasma at 100,000 g [267] and such populations will contain exosomes [129]. Exosomes have a typical cup shape when studied by TEM (Fig. 2.1A), but larger vesicles (Fig. 2.1B) also show this morphological feature. Although exposure of PS is often mentioned as a typical marker for microvesicles [296, 32], this seems questionable at best, because a substantial number of microvesicles do not expose PS [156, 70], and because exposure of PS is markedly increased by centrifugation and freeze-thaw procedures [70]. The mechanisms underlying the formation of microparticles have been recently summarized elsewhere [210]. Taken together, although exosomes and microvesicles are distinct types of vesicles, neither size, morphology, nor exposure of PS is a sufficient criterion to distinguish both types of vesicles from each other.

2.2.3 Membrane particles

The lumen of the neural tube of embryonic mouse brain contains ventricular fluid, in which two types of prominin-1 (CD133)-exposing vesicles are present [196], called prominosomes or membrane particles [196, 296]. One type of membrane particle has a diameter of approximately 600 nm, whereas the other type has a diameter between 50 and 80 nm as determined by TEM. Although the small type of membrane particles is precisely in the size range of exosomes, they showed a slightly lower density ($1.032-1.068\,\mathrm{g\,mL^{-1}}$) than exosomes on sucrose gradients, and they do not expose CD63. Because these $CD133^+$ vesicles (1) originate from the plasma membrane of epithelial cells, (2) occur in human body fluids that contact the epithelium, such as saliva, urine, and seminal fluid, and (3) coexist with exosomes in saliva [196, 30], we assume these $CD133^+/CD63^-$ vesicles to be different from exosomes. The extent to which the larger type of membrane particle is different from microvesicles, however, will need additional studies.

2.2.4 Apoptotic vesicles

When cells are undergoing apoptosis, they release PS-exposing vesicles, often called apoptotic bodies or vesicles. The major difference between apoptotic vesicles and other cell-derived vesicles is their size. In all studies so far, the diameter of apoptotic vesicles is reported to range between 1 and 5 μm [164, 295, 138, 302]. This is in the precise size range of platelets in the human blood. Because activated platelets or platelets undergoing a process resembling apoptosis also express PS, it may be impossible to resolve apoptotic bodies from platelets based upon size and a PS-positive phenotype. The density of apoptotic vesicles is 1.16 to $1.28\,\mathrm{g\,mL^{-1}}$, which is partly overlapping with the density of exosomes, and their morphology is typically more heterogeneous than other cell-derived vesicles when visualized by TEM.

The inappropriate clearance of apoptotic vesicles is considered to be the primary cause of developing systemic autoimmune disease. Apoptotic cells release at least two immunologically distinct types of apoptotic vesicles. Apoptotic vesicles originating from the plasma membrane contain DNA and histones, whereas apoptotic vesicles originating from the endoplasmic reticulum do not contain DNA and histones but expose immature glycoepitopes [35].

In general, the process of "membrane blebbing" is thought to precede the release of apoptotic vesicles and microvesicles. The extent to which this assumption is true, however, is unclear. Membrane blebbing requires phosphorylation of myosin light chain and Rho-associated coiled coil kinase I activity, which becomes constitutively active upon cleavage by caspase 3, induces a net increase in myosin light chain phosphorylation and subsequent membrane blebbing [262]. The key role of caspase 3, one of the executioner enzymes of apoptosis, in membrane blebbing is confirmed by the observation that a human breast cancer cell line, MCF7, which is deficient of functional caspase 3, lacks membrane blebbing [146]. Alternatively, granzyme B cleaves Rho-associated coiled coil kinase II, which produces

a constitutively active enzyme, and increases myosin light chain phosphorylation as well as membrane blebbing [275].

2.3 Functions and clinical applications of cell-derived vesicles

An extensive description of the functions and clinical applications of cell-derived vesicles is beyond the scope of this thesis and can be found elsewhere [231]. In short, vesicles play a role in intercellular signaling (e.g. immune suppression, antigen presentation, inflammation), cell adhesion, waste management, coagulation, and protection against extracellular and intracellular stress. Vesicles have potential clinical applications spanning therapy, prognosis and biomarkers for disease.

2.4 Conclusions and future directions

The research on cell-derived vesicles from eukaryotic cells is a fast-growing and exciting new field. Although major progress has been made during the last decade, our understanding of the molecular mechanisms underlying the release of vesicles and the sorting of compounds into these vesicles are still incompletely understood, the criteria to identify different types of vesicle have only been partially elucidated so far, and, most importantly, the biological relevance of vesicles in health and disease is poorly understood, especially in vivo.

The finding that vesicles enable the intercellular exchange of biomolecules suggests a new level of communication that may increase our understanding of disease development and progression. Moreover, vesicles may be useful as clinical instruments for prognosis and biomarkers, and they are promising as autologous drug vehicles capable of passing pharmacological barriers. To increase their clinical usefulness, however, novel and dedicated instruments will have to be developed to detect vesicles and to standardize vesicle measurements between laboratories.

CHAPTER 3

Methods for detection and characterization of extracellular vesicles

Abstract

Microparticles and exosomes are cell-derived vesicles present in body fluids that play a role in coagulation, inflammation, cellular homeostasis and survival, intercellular communication, and transport. Despite increasing scientific and clinical interest, no standard procedures are available for the isolation, detection and characterization of microvesicles and exosomes, because their size is below the reach of conventional detection methods. Our objective is to give an overview of currently available and potentially applicable methods for optical and non-optical determination of the size, concentration, morphology, biochemical composition and cellular origin of microvesicles and exosomes. The working principle of all methods is briefly discussed, as well as their applications and limitations based on the underlying physical parameters of the technique. For most methods, the expected size distribution for a given vesicle population is determined. The explanations of the physical background and the outcomes of our calculations provide insights into the capabilities of each method and make a comparison possible between the discussed methods. In conclusion, several (combinations of) methods can detect clinically relevant properties of microvesicles and exosomes. These methods should be further explored and validated by comparing measurement results so that accurate, reliable and fast solutions come within reach.

This chapter has been published as:

- E. van der Pol, A.G. Hoekstra, A. Sturk, C. Otto, T.G. van Leeuwen, and R. Nieuwland. Optical and non-optical methods for detection and characterization of microparticles and exosomes. *J. Thromb. Haemost.* **8**(12), 2596-2607 (2010)

3.1 Introduction

Cells release vesicles that function as vehicles for the transport and delivery of cargo between cells [270, 217]. In addition, vesicles promote coagulation and inflammation. Throughout this chapter, we will use "vesicles" as a generic term for all types of cell-derived extracellular vesicle, unless stated otherwise. Although the clinical interest and relevance of vesicles is increasingly recognized [246], their isolation and detection is still cumbersome [157]. At present, novel detection methods are being explored [335, 185, 159, 227, 340]. This chapter is an assessment of the accuracy and practicability of methods for the detection of vesicles.

3.1.1 Microparticles and exosomes

The best studied types of vesicle are exosomes and microvesicles. Although a generally accepted definition is lacking [74, 50], there are several features characterizing exosomes and microvesicles. Exosomes are released from cells containing multivesicular bodies when the membranes of multivesicular bodies fuse with the plasma membrane. By transmission electron microscopy (TEM), exosomes appear with characteristic doughnut morphology, and their diameter ranges between 30 and 100 nm [69]. Their density ranges from 1.13 to 1.19 $\mathrm{g\,mL^{-1}}$ [294], and proteomes contain characteristic but not unique protein families, including heat shock proteins and tetraspannins [297]. The main function of exosomes is to modulate the immune response [296].

Microparticles are released from the plasma membrane during "budding" or "shedding". Most, if not all, eukaryotic cells release microvesicles, especially during conditions related to stress, such as activation and apoptosis [106]. Microparticles are larger and more heterogeneous in morphology than exosomes, with reported diameters ranging between 100 nm and 1 µm [66]. Microparticles are best known for binding coagulation factors and exposing tissue factor [271, 215, 112]. Their absence is associated with a bleeding tendency [272], and their (increased) presence is associated with disseminated intravascular coagulation and thrombosis [214, 37]. There is increasing evidence that exosomes and microvesicles are "multipurpose carriers" facilitating the intercellular exchange of transmembrane receptors, mRNA, microRNA, and signaling molecules [306, 83, 13]. Furthermore, they promote cellular survival by removing dangerous or redundant intracellular compounds [109, 7, 258].

3.1.2 Vesicle isolation, detection, and characterization

Currently, progress in vesicle research is hampered by several factors. Because of the biological complexity of body fluids, isolation of vesicles has proven to be extremely difficult. For instance, isolation of vesicles from blood is affected by venepuncture, time between blood collection and handling, the anticoagulant, centrifugation and washing procedures, the presence of lipoprotein particles and small platelets within the size range of vesicles, the high viscosity of blood, and the pres-

ence of sticky proteins, including fibrinogen and albumin. Because of their small size, vesicles are below the detection range of conventional detection methods. As a consequence, recovery and contamination cannot be reliably quantified, and isolation protocols have not been standardized. For example, conflicting results were reported on the procoagulant properties of vesicles from sickle cell disease patients [27, 267]. Both studies attributed the procoagulant features to "microvesicles", but they used markedly different isolation protocols, involving centrifugation at 18,890 g [27] or 100,000 g [267], presumed to result in isolation of microvesicles or microvesicles and exosomes, respectively.

3.1.3 Clinically relevant properties of vesicles

In this chapter, currently available and potentially applicable methods for the detection and characterization of vesicles are presented. Clinically relevant properties of vesicles are size, concentration, morphology, biochemical composition, and cellular origin. From the size information of individual vesicles, a relative size distribution can be obtained, providing insights into the number of vesicles of one particular size relative to those of another size. We define concentration as the number of vesicles per unit volume. If both the relative size distribution and concentration are known, an absolute size distribution can be obtained, which gives the number of vesicles of one particular size per unit volume. By morphology, we mean shape and ultrastructure. Ultrastructure is illustrated in Fig. 3.1A, where vesicles differ not only in shape but also in contrast and surface pattern. The biochemical composition refers to the biological and chemical components of which vesicles are composed. The cellular origin refers to the cell type from which the vesicles originate.

3.1.4 Standard population and outline

For each detection method, the working principle is briefly explained and the measurement time is estimated, assuming the detection of 10,000 particles, a number that is common in flow cytometry. In addition, we give a prediction of the performance of each method in detecting size, concentration, morphology, biochemical composition, and cellular origin, by considering the underlying physical parameters of the methods. To compare the performance of the methods for size detection, we made a model predicting the size distribution for a given population of vesicles (see Appendix A). As outlined previously, isolation of vesicles from blood is a challenge. Therefore, we arbitrarily chose vesicles from urine to create a standard population as a realistic input for our model. Urine can be used to prepare a relatively high concentration of vesicles without excessive contamination with, for example, platelets or proteins.

To create the standard population, we isolated vesicles from fresh cell-free urine of a healthy male individual by highspeed centrifugation (Fig. 3.1A; 30 min at 18,900 g), followed by ultracentrifugation of the supernatant (Fig. 3.1B; 1 h at 154,000 g). We imaged vesicles by TEM and measured the diameter of 500

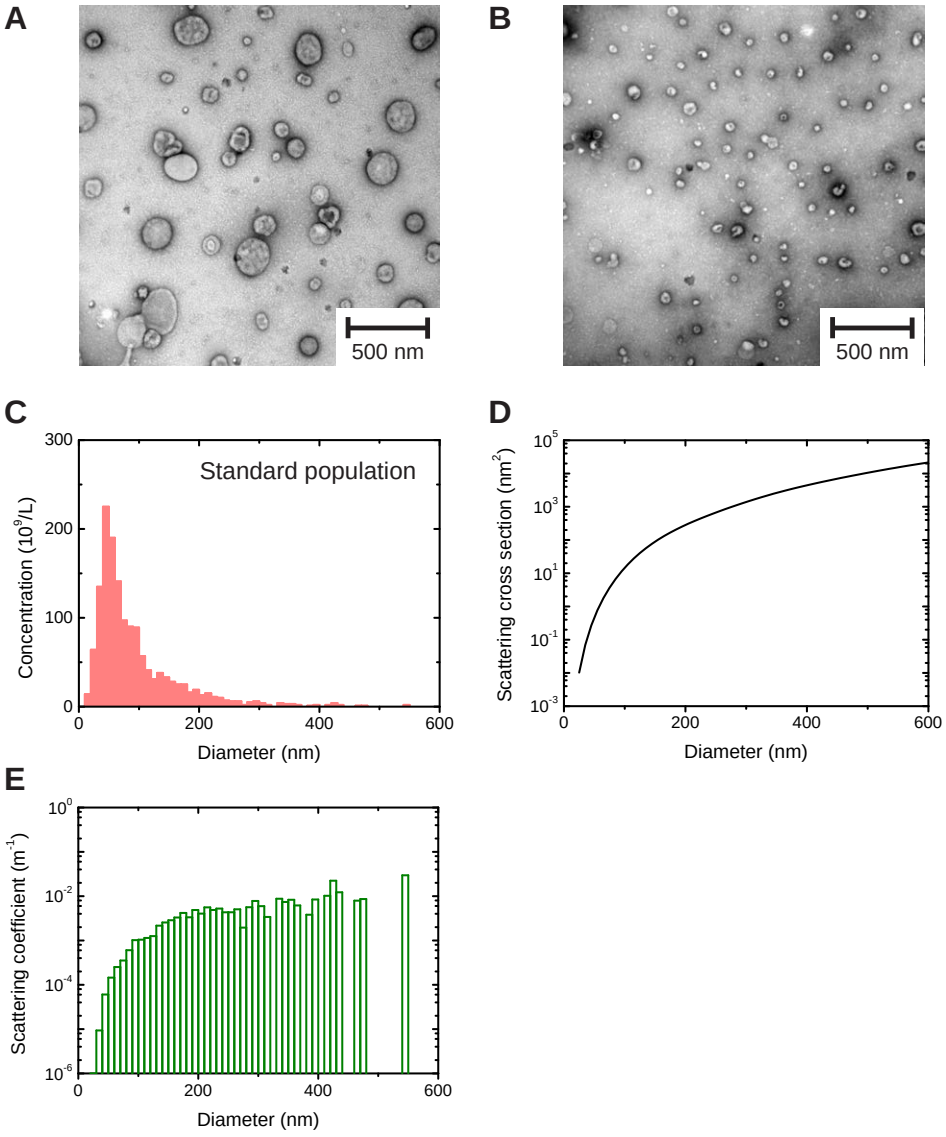

Figure 3.1: Transmission electron microscopy (TEM) of vesicles from fresh cell-free human urine. (A) vesicles isolated from cell-free human urine by centrifugation (30 min at 18,900 g). (B) vesicles isolated from microparticle-depleted urine by ultracentrifugation (1 h at 154,000 g). (C) Concentration vs. diameter for vesicles as measured by TEM, and referred to as the standard population. The plot shows a broad distribution between 20 and 440 nm, with a single peak at 45 nm. (D) Scattering cross-section vs. diameter (logarithmic scale) for vesicles, calculated using Mie theory of a sphere ($n_p = 1.38$) surrounded by a membrane (10 nm; $n_s = 1.48$). The medium is water ($n_m = 1.33$) and the wavelength of the laser is 532 nm. The scattering cross-section, and thus the quantity of light scattered by a vesicle, strongly decreases with decreasing diameter. (continued)

Figure 3.1: (E) Scattering coefficient vs. diameter (logarithmic scale) for the standard population. The scattering coefficient, which is the average number of scattering events that light encounters per unit length, is given by the product of the concentration of the standard population and the scattering cross-section. The scattering coefficient strongly increases with increasing diameter, indicating that the contribution of light scattered by vesicles smaller than 100 nm is relatively small.

vesicles in each fraction. The combined size distributions are shown in Fig. 3.1C. As different size distributions of vesicles in blood have been reported [335, 185, 269, 253], it is difficult to compare our standard population with its plasma counterpart. Nevertheless, our standard population corresponds well with recent data on the size distribution of plasma vesicles [335]. One has to bear in mind that the reported absolute size distributions are affected by isolation procedures. In the literature, vesicle concentrations in plasma range from 10^7 to 10^{12} L^{-1} [335, 340, 253, 263, 213, 124]. As our simulations demand an absolute size distribution as input, we arbitrarily multiplied our relative vesicle size distribution by 10^9 L^{-1}, as this concentration is usually reported in plasma.

The outline of this chapter is as follows. The first part describes optical detection, and is subdivided into methods based on light scattering or fluorescence. The second part describes non-optical detection methods. Table 3.1 provides an overview of all detection methods.

3.2 Optical methods

Optical methods have the potential to accurately obtain all clinically relevant properties of single vesicles at a high speed. Two important parameters in optics are the wavelength of light and the refractive index of particles relative to the suspending medium. Optical phenomena, including reflection and refraction, depend on the refractive index n of the material. The refractive index depends on the wavelength λ, and is defined as the ratio of the speed of light in vacuum to that in the material. In practice, the higher the difference between the refractive index of a vesicle and its surroundings, the more light will be scattered.

3.2.1 Light scattering

Light that illuminates a vesicle is partly absorbed and partly scattered. As many optical setups are based on the detection of scattered light, it is important to know how much light is scattered by a single vesicle. The quantity of light scattered by a single vesicle is proportional to the scattering cross-section σ. When the diameter

Table 3.1: Assessed capabilities of (potential) methods for the detection of microvesicles, based on the underlying physical parameters of the method

Method	Resolution (nm)	Detection limit	Size distribution	Requirements and/or assumptions	Concentration	Requirements and/or assumptions	Biochemical information	Measurement time
Optical methods								
Scattering								
Optical microscopy	200	>10 nm	−		+/−	V_d	−	H
Scattering flow cytometry		≥300 nm	−	Calibration with beads	+/−	Q	+/−	S
DLS		1 nm to 6 µm	+/−	T, η, n_v, n_m, model	−		−	M
NTA	1,000	50 nm to 1 µm	+/−	T, η	+/−	Calibration with beads	−	M
Raman spectroscopy	350	To be investigated	?	Raman signal $\propto d$	+/−		+	H
Fluorescence								
Fluorescence microscopy	200	Single molecule/QD	−	Fluorescence signal $\propto d$	+/−	V_d	+	H
STED microscopy	30	Single molecule/QD	+	Surface labeling	+/−	V_d	+	H
Fluorescence flow cytometry		Single QD	−	Fluorescence signal $\propto d$	+/−	Q	+	S
F-CS		Single molecule/QD	+/−	T, η, V_d, model	+	V_d	+	M
F-NTA	600	Single QD	+	T, η	+	Calibration with beads	+	M
Non-optical methods								
X-ray microscopy	12		+		+/−			
TEM	∼ 1		+	No shrinkage	−		+/−	H
AFM	< 1	<1 nm	+	Isovolumetric deformation	+/−	100 % surface binding	+	H
Impedance-based flow cytometry		≥300 nm	−	d_c, l_c	+/−	d_c, $\nu_{s,\mathrm{av}}$	−	S

Abbreviations and symbols are clarified on page 35.

AFM, atomic force microscopy; DLS, dynamic light scattering; F-CS, fluorescence correlation spectroscopy; F-NTA, fluorescence nanoparticle tracking analysis; NTA, nanoparticle tracking analysis; QD, quantum dot; STED, stimulated emission depletion; TEM, transmission electron microscopy. For each method, the resolution, detection limit, ability to measure the size distribution and concentration, ability to provide biochemical information, and the measurement time are estimated. Requirements of the method and/or assumptions that have to be made to determine the size distribution and concentration are also listed. d is the microvesicle diameter, d_c is the channel diameter, l_c is the channel length, η is the viscosity of the solvent, n_v is the refractive index of the vesicle, n_m is the refractive index of the medium, Q is the flow rate, T is the temperature of the solvent, V_d is the detection volume, and $\nu_{s,av}$ is the average particle transport velocity. A method that is incapable, capable but with limitations, or capable of providing information on the size distribution, particle concentration or biochemical composition is indicated by −, +/−, and +, respectively. The measurement time is indicated by S, M, and H, which mean shorter than 1 min, between 1 min and 1 h, and longer than 1 h, respectively. Assumptions which are not explained in this chapter are provided in Appendix A.

is at least 10 times smaller than the wavelength, the Rayleigh approximation can be applied to calculate the scattering cross-section,

$$\sigma \propto \frac{d^6}{\lambda^4} \left(\frac{m^2 - 1}{m^2 + 2} \right)^2 \tag{3.1}$$

where $\propto$ denotes "proportional to", d is the particle diameter, and $m = n_v/n_m$ is the refractive index ratio of the vesicle and the medium [140]. At a wavelength of 532 nm, which is commonly used in optical devices, the Rayleigh approximation can be applied to particles of $532/10 \approx 50$ nm and smaller, which is typically the size of the smallest exosomes. From Eqn 1, it follows that if a vesicle is only 10-fold smaller than another vesicle, the scattering cross-section and thus the scattered amount of light decreases 10^6-fold.

Mie theory provides exact predictions of the absorption and scattering of light from spheres with arbitrary diameter and refractive index [40]. The solid line in Fig. 3.1D shows the scattering cross-section vs. the diameter for a sphere that contains a high refractive index shell, for example a phospholipid membrane, as calculated with Mie theory. The calculation parameters are chosen to be as realistic as possible for the case of vesicles. Fig. 3.1D, in a semi-logarithmic representation, shows that the scattering cross-section drops rapidly for smaller vesicles. To illustrate how this decrease affects light scattered from all vesicles of the standard population, the concentration (Fig. 3.1C) is multiplied by the scattering cross-section (Fig. 3.1D) to obtain the scattering coefficient per diameter (Fig. 3.1E). The scattering coefficient, depicting the mean number of scattering events of the light per unit length, is a measure of the amount of light scattered by all vesicles per diameter. Please note that the contribution of light scattered by vesicles smaller than 100 nm is surprisingly small (Fig. 3.1E), given their high concentration (Fig. 3.1C). Consequently, smaller vesicles require more sensitive

optical detection than larger vesicles, and scattering of small particles can easily be overwhelmed by scattering of large particles.

Optical microscopy

In a bright-field optical microscope, the sample is illuminated by visible light. Scattered light from the sample is collected by a microscope objective and focused on a charge-coupled device (CCD) camera. The resolution is the shortest distance between two adjacent points that can be distinguished by an optical microscope. The best achievable resolution R is given by the Rayleigh criterion,

$$R = \frac{1.22\lambda}{2\mathrm{NA}} \tag{3.2}$$

where NA is the numerical aperture of the microscope objective. NA characterizes the range of angles over which the microscope objective accepts light. Oil-immersion microscope objectives have an NA up to 1.4. Assuming a wavelength of 532 nm, the best resolution of a standard optical microscope is approximately 200 nm. So, it is impossible to measure the size and morphology of vesicles smaller than 200 nm by optical imaging. Despite this limitation, gold particles down to 10 nm in diameter have been detected, because gold particles scatter light very efficiently [87]. They appear as bright spots, but their true particle size is hard to determine by optical microscopy. For vesicles with light scattering higher than the detection limit, an estimation of the concentration can be made from the count of the number of scatter events if the detection volume V_d is known. The time needed to measure 10,000 vesicles with a standard optical microscope is in the order of hours, and no information on the biochemical composition or cellular origin is provided.

Scattering flow cytometry

Flow cytometry is well known for counting and separating single cells (diameter $> 1\,\mu\mathrm{m}$) in fluids at a rate of thousands per second. Most flow cytometers can detect scattered light and fluorescence. In this section, we consider only light scattering.

A flow cytometer guides cells and vesicles through a laser beam in a hydrodynamically focused fluid stream. One detector is placed in line with the laser beam and measures the forward scattered light (FSC). A second detector measures the side scattered light (SSC) perpendicular to the beam. From light-scattering theory, the following approximate results can be expected. Particles larger than the wavelength of light, such as cells, predominantly scatter light in a forward direction. Hence, FSC is associated with particle size. Particles smaller than the wavelength, such as organelles, scatter relatively more light in a perpendicular direction, so SSC is associated with the complex anatomy of cells. In reality, however, light scattering is a complex process. Therefore, light scattering of biological particles is an active research field [134, 135].

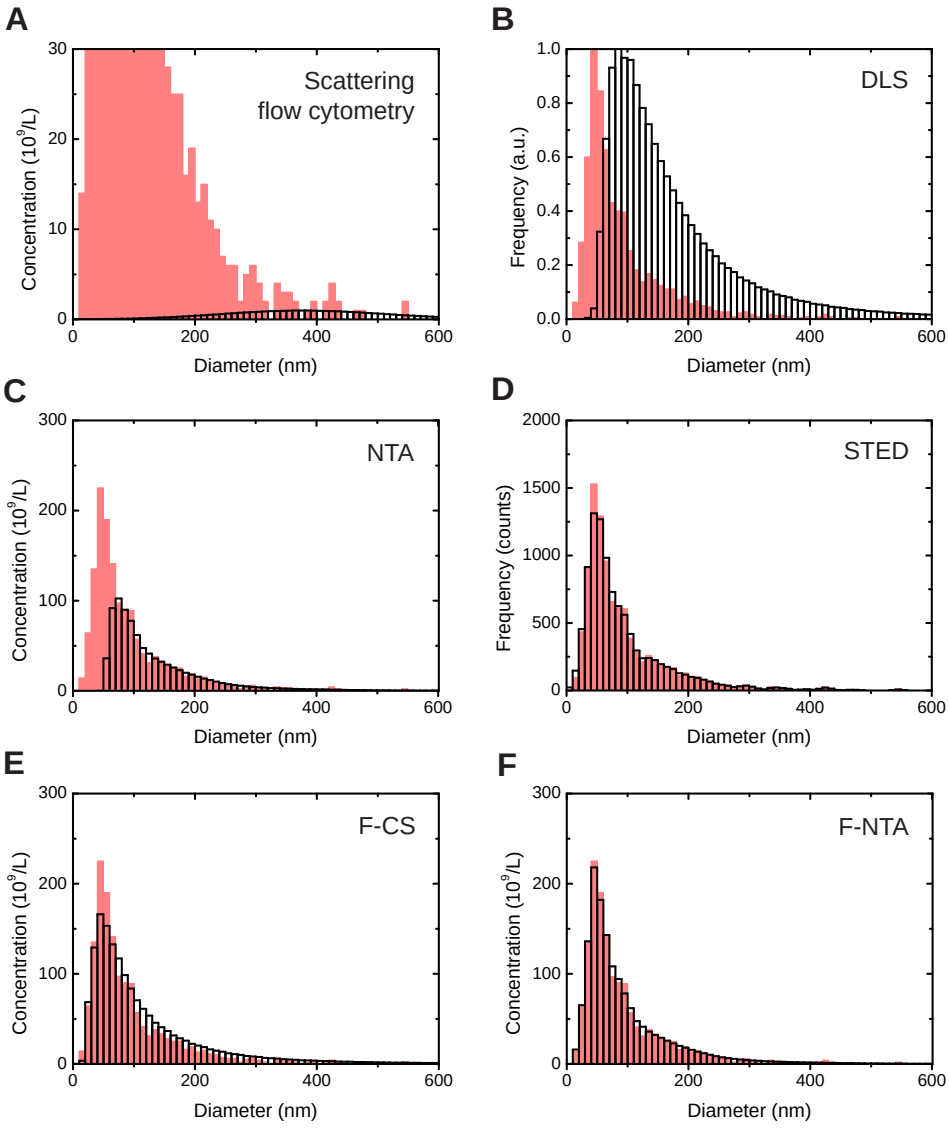

Figure 3.2: Calculated size distribution for optical detection methods (open black) relative to the standard population (transparent red), based on the underlying physical parameters of each method. (A) Scattering flow cytometry determines concentration vs. diameter. Vesicles larger than 300 nm in diameter are detected, but vesicles smaller than 300 nm are detected with low efficiency. (B) Dynamic light scattering (DLS) determines the relative size distribution. The distribution is normalized to 1, and shows a shift to larger diameters. (C) Nanoparticle tracking analysis (NTA) determines the absolute size distribution with high precision for vesicles larger than 100 nm, but is currently not sensitive enough to detect vesicles smaller than 50 nm. (continued)

Figure 3.2: (D) Stimulated emission depletion (STED) microscopy determines counts vs. diameter. The distribution is normalized to a total count of 10,000 vesicles, and shows a high correlation with the standard population. (E, F) Both fluorescence correlation spectroscopy (F-CS) and fluorescence NTA (F-NTA) determine the absolute size distribution, which shows a high correlation with the standard population. The Pearson correlation coefficients between the calculated distribution and the standard population are 0.61 (scattering flow cytometry), 0.40 (DLS), 0.53 (NTA), 1.00 (STED), 0.98 (F-CS), and 1.00 (F-NTA).

A flow cytometer performs well in the distinction of cell types, but has major drawbacks in determining the size of vesicles. First, the lower detection limit of commercial flow cytometers for polystyrene beads is 300−500 nm [227, 269, 278]. Consequently, only a small fraction of vesicles can be detected. Second, only particles that differ by approximately 280 nm or more in size can be resolved with flow cytometers [227, 253]. Third, quantitative size information is obtained by comparing the scattering intensity of vesicles with that of beads of known size. The scattering intensity, however, depends not only on size but also on shape, refractive index, and absorption. The refractive index and absorption are even interconnected via Kramers-Kronig relationships [94]. For example, according to Mie calculations, a spherical gold particle 200 nm in diameter scatters 27 times more light than a polystyrene sphere of a similar size, which, in turn, scatters 15 times more light than a vesicle, owing to refractive index differences (see Appendix D.1). Furthermore, for non-spherical geometries, complex computer simulations are required [304].

Fig. 3.2A shows an impression of the size distribution as calculated for a flow cytometer in scattering mode, using the standard population as input. As the detection limit is approximately 300 nm, smaller vesicles are detected with low efficiency [227, 253]. Consequently, the measurements do not reflect the standard population. The poor capability to resolve size differences results in a smooth curve. The concentration of vesicles can be estimated when the flow rate Q is known. No specific information on morphology is obtained from the light-scattering intensity.

Biochemical information is obtained by correlating the FSC with the SSC signal. As vesicles have a size in the order of the wavelength of visible light or smaller, they scatter light substantially in a perpendicular direction. Side scatter from a large vesicle therefore overwhelms side scatter from smaller structures inside. As a consequence, distinguishing vesicles with different cellular origins by correlating FSC and SSC signals is difficult, but it can be improved by analyzing the polarization of sideward scattered light [117].

Dynamic light scattering (DLS)

DLS, also known as photon correlation spectroscopy or quasi-elastic light scattering, determines the relative size distribution in a fluid of particles ranging in size between 1 nm and 6 µm [65, 85]. Particles in a fluid continuously move in random

directions, owing to continuous collisions with solvent molecules. This causes a random motion of particles called Brownian motion. The velocity distribution of particles depends on the temperature T, viscosity η, and (hydrodynamic) particle diameter d. The smaller the particle, the faster the Brownian motion. Particles undergoing Brownian motion cause intensity fluctuations of scattered light, which is measured typically in 30 s. The relative size distribution is obtained from the intensity fluctuations by applying a mathematical algorithm following from light-scattering theory. Light scattering theory requires the refractive index ratio $m = n_v/n_m$ of the vesicles and the medium, which is currently unknown. DLS performs well in the size determination of monodisperse samples, i.e. samples containing particles of one particular size, and monitoring a change in a sample such as aggregation [48, 101, 137]. Detection of the size distribution of polydisperse samples, i.e. samples containing different-sized particles, is less accurate, as the measured size distribution is influenced by the presence of small numbers of larger particles, such as platelets or other contaminants, which scatter more light than small vesicles, as shown in Fig. 3.1D [101, 137]. Furthermore, the result depends on the applied mathematical algorithm [48, 101], and two populations can only be resolved if the particle diameter differs at least two-fold [48, 101, 137, 170].

Fig. 3.2B shows the calculated relative size distribution for DLS relative to the standard population. The maximum value of the distribution is arbitrarily set to 1, as the concentration is unknown. Because larger vesicles scatter light more efficiently than smaller ones, the smallest vesicles become undetectable, and the distribution shifts to larger diameters. Our calculations closely fit the size distribution measurement of vesicles from fresh frozen plasma obtained with the N5 Submicron Particle Size Analyzer [185]. DLS does not provide information on the biochemical composition or cellular origin.

Nanoparticle tracking analysis (NTA)

NTA measures the absolute size distribution of particles ranging in size from 50 nm for biological particles to 1 µm. Particles in a fluid are illuminated by a laser beam and therefore scatter light, which is collected by a conventional optical microscope. NTA visualizes the scattered light from single particles in the field of view of the microscope. The scattered light shows up as small bright spots moving because of Brownian motion. The movements of individual particles are followed through a video sequence acquired over one to several minutes, and the mean velocity of each particle is calculated with image analysis software [124]. Because the velocity of Brownian motion depends on the temperature T, viscosity η, and (hydrodynamic) particle diameter d, it is possible to obtain an absolute size distribution after system calibration with beads of known size and concentration.

Fig. 3.2C shows the calculated absolute size distribution for NTA. On the basis of our assessment, NTA performs well for vesicles larger than 50 nm, but detection of vesicles smaller than 50 nm is not possible, owing to the detection limit of the microscope. NTA does not detect biochemical composition or cellular origin.

Raman spectroscopy

Raman spectroscopy is an inelastic light-scattering technique used to reveal the structure and biochemical composition of macromolecules inside single living cells [242, 305]. The sample is illuminated by monochromatic laser light. Molecular vibrations in the sample cause an energy loss or gain during a scattering event, resulting in a change in wavelength of the scattered light, which can be detected by specialized, sensitive spectrometers. The pattern of molecular vibrations is molecule-specific. As vesicles are composed of many different biomolecules, which all have unique Raman spectra, the chemical composition can be investigated without labeling. A confocal Raman microspectrometer can detect the Raman spectrum of volume elements of approximately $0.3\,\mu m^3$ [241, 240], which overlaps with the dimension of vesicles, such that the chemical composition of single vesicles can potentially be detected without labeling. Furthermore, Raman microspectroscopy is a quantitative technique. The signal strength is linearly proportional to the number of molecules. For a vesicle that fits within the probe volume, the magnitude of the Raman signal strength is proportional to the volume of a single vesicle, and therefore estimates the relative size; this is a method that warrants further investigation before a reliable comparison with the standard population can be made. The concentration can be determined if the detection volume V_d is known. The estimated measurement time is 3 h.

3.2.2 Fluorescence

Fluorescence is the property of a material whereby the material absorbs light of a particular wavelength and re-emits it at a usually longer wavelength. Most cells and vesicles exhibit no intrinsic fluorescence by which they can be distinguished. Therefore, vesicles are labeled with conjugates of antibodies or proteins with fluorophores [200]. Commonly used fluorophores are organic dye molecules and quantum dots. Quantum dots have a typical diameter of $2-20\,nm$, and have been used as an artificial light source with which a vesicle can be labeled [337]. In general, quantum dots are brighter and more stable than organic dye molecules or fluorescent proteins. As vesicles usually expose antigens from the parental cells, all methods based on fluorescence detection potentially provide information on the biochemical composition and cellular origin of vesicles. Fluorescence also offers opportunities to acquire additional chemical information, as the fluorescence intensity, wavelength and average time for which light is absorbed (fluorescence lifetime) depend on the molecular environment [309, 211].

Fluorescent multilabeling analysis is not easy to perform, and there are several practical problems. For example, antibodies usually bind not only to the antigen of interest but also to Fc receptors. Furthermore, antibodies adhere nonspecifically or form aggregates, interfering with quantitative optical methods [243]. In addition, other optical difficulties limit the feasibility of fluorescence detection. For example, it may be difficult to distinguish the fluorescence signal of interest from background radiation caused by autofluorescence, or irreversible photobleaching of fluorophores

may occur [128]. In the case of multilabeling, fluorophores can spectrally overlap, such that fluorescence associated with one fluorophore is detected by more than one detector [25].

Fluorescence microscopy

A fluorescence microscope is an optical microscope optimized for fluorescence detection. Usually, the fluorescence emission is separated from the excitation light with a spectral filter, before detection by a CCD camera. Modern fluorescence microscopes are able to detect fluorescence from a single fluorophore. For example, Zhang et al. [337] loaded a synaptic vesicle with a single quantum dot (approximately 15 nm) to monitor membrane fusion and retrieval by high-speed imaging fluorescence microscopy.

In the case of autofluorescence, the size of vesicles can conceptually be determined, as the fluorescence signal may be proportional to the vesicle volume. However, in the case of fluorescent labeling, it is highly unlikely that the fluorescent amplitude will be proportional to the volume, so no size information can be obtained. Fluorescence microscopy allows an assessment of the concentration of vesicles with a certain property under the assumption that all vesicles with that property are indeed labeled and that the detection volume V_d is known. A typical measurement time is approximately 1 h.

Stimulated emission depletion (STED) microscopy

In practice, STED microscopy is high-resolution fluorescence microscopy with better spatial resolution than described by Eqn. 3.2 for diffraction-limited optics. A resolution of 16 nm in diameter was successfully demonstrated, and this is sufficiently small to size vesicles [322, 325]. Sizing vesicles by STED, however, requires labeling of the entire surface of vesicles. Under the assumption that such labeling can be performed, Fig. 3.2D shows the calculated size distribution. The predicted distribution correlates well with the standard population. Not only is STED microscopy promising for determining the size of and locating fluorescently labeled vesicles, but the high resolution can potentially be used to gain information on morphology and to determine the distribution of labeled receptors at the surface of larger vesicles, just as is presently done for organelles inside living cells [130]. The concentration can be determined if the detection volume V_d is known, and the measurement time for probing 10,000 particles is in the order of hours.

Fluorescence flow cytometry

In a fluorescence flow cytometer, the fluorescence from single particles present in a hydrodynamically focused fluid stream is measured at a rate of thousands of particles per second. With fluorescence flow cytometry, it is possible to distinguish vesicles on the basis of the spectral properties of the fluorescence signal [227]. For detection of nanometer-sized particles by flow cytometry, the signal-to-noise ratio for fluorescence is higher than the signal-to-noise ratio for scattering, so

fluorescence flow cytometry is likley to be more sensitive than scattering flow cytometry. Flow cytometers with confocal optics can detect single fluorophores with an efficiency of approximately 10 % by minimizing background fluorescence [100]. As in fluorescence microscopy, the size distribution can, in principle, be determined when the amplitude of the fluorescence signal is proportional to the vesicle volume, a method that warrants further investigation. Fluorescence flow cytometry can estimate the concentration if the flow rate Q is known, again under the assumptions that all vesicles are labeled and have a fluorescence intensity above the detection limit and threshold of the flow cytometer.

Fluorescence correlation spectroscopy (F-CS)

F-CS was originally introduced to measure parameters of molecular diffusion [319]. It can determine the absolute size distribution and fluorescence signal of particles in a fluid [276]. The size distribution is obtained from fluorescence intensity fluctuations caused by particles moving by Brownian motion through a well-characterized illuminated volume. Unlike DLS, F-CS detects single fluorescent molecules, and is therefore more sensitive for vesicles smaller than 50 nm; the size distribution can be more accurately determined in the presence of larger vesicles, and the concentration can be measured if the detection volume V_d is known [276]. Fig. 3.2E shows the calculated absolute size distribution, under the assumption that all vesicles are labeled. Although good correlation with the standard population can be simulated, we should be aware that small numbers of larger particles may influence the size distribution substantially. The measurement time is in the order of minutes.

Fluorescence NTA (F-NTA)

F-NTA determines the absolute size distribution and fluorescence signal of particles in a fluid. The method is similar to NTA, but is based on tracking of fluorescent particles. F-NTA is an extremely sensitive method for vesicles in the size range of exosomes, because the signal-to-noise ratio for fluorescence is expected to be considerably higher than signal-to-noise ratio for light scattering. With F-NTA, individual quantum dots can be detected. However, bleaching of the fluorescent marker may limit the tracklength. The good size and concentration detection properties are illustrated in Fig. 3.2F. Here, the simulations of the absolute size distribution of vesicles by F-NTA show an excellent correlation with the standard population.

3.3 Non-optical methods

X-ray microscopy

X-ray microscopy is a relatively new method in biomedical science for imaging the intact structure of a biological sample at a resolution of 12 nm [59]. For example,

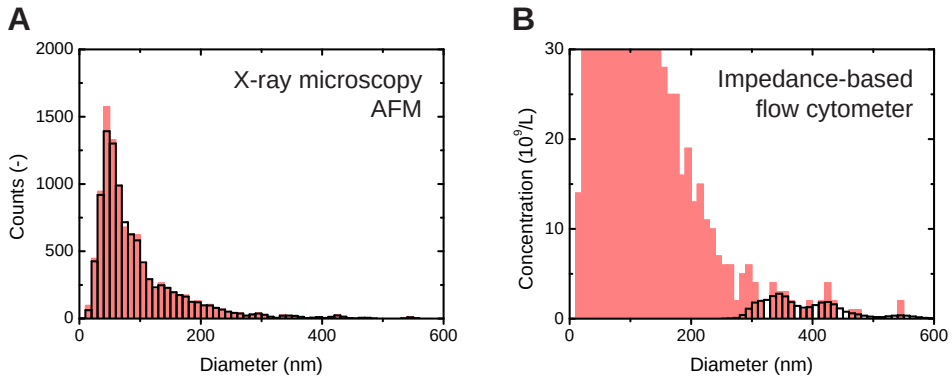

Figure 3.3: Calculated size distribution for non-optical detection methods (open black) relative to the standard population (transparent red), based on the underlying physical parameters of each method. (A) X-ray microscopy and atomic force microscopy (AFM) determine counts vs. diameter. The methods can resolve size differences in the order of a few nanometers, and the results show a high correlation with the standard population. (B) Absolute size distribution of a commercial impedance-based flow cytometer with a channel diameter of 25 µm. Vesicles smaller than 300 nm are detected with low efficiency. The Pearson correlation coefficients between the calculated distribution and the standard population are 1.00 (X-ray microscopy, AFM) and 0.27 (impedance-based flow cytometer).

the surface of macrophages was analyzed in their natural state [332] and cryo-fixed eukaryotic cells were imaged in three dimensions by X-ray tomography [225]. The high resolution of X-ray microscopy is achieved by reducing the wavelength to a few nm. According to Eqn. 3.2, a shorter wavelength lowers the diffraction limit. Considering the high resolution, X-ray microscopy is a promising method for detecting the size and possibly the morphology of vesicles in their physiological state. Fig. 3.3A shows the calculated size distribution of vesicles using an X-ray microscope with 12 nm resolution. Due to the high resolution there is a high correlation with the standard population.

An interesting feature of X-ray microscopy is the potential to detect the biochemical composition without labeling, since X-rays induces fluorescence of most substances. Furthermore, with X-ray microscopy the localization of chemical elements within cells can be visualized when using X-ray absorption near-edge structure spectra [10].

Presently, a major drawback of X-ray microscopy is that X-ray sources are scarce (synchrotron radiation) or impractical for clinical use (laser plasma x-ray contact microscopy). However, the field is rapidly evolving, which is exemplified by the increased availability of the required instrumentation [9].

Transmission electron microscopy (TEM)

TEM uses electrons instead of photons to create an image. The best achievable imaging resolution of TEM is given by Eqn. 3.2, and depends largely on the spatial stability of the electron beam in combination with the chemical stability of the sample. As the wavelength of electrons is more than three orders of magnitude shorter than the wavelength of visible light, the resolution of TEM can be lower than 1 nm. Because of this high resolution, it is possible to determine the size and morphology of vesicles [229].

As TEM is performed in a vacuum, biomaterials require fixation and dehydration, which affect size and morphology. Furthermore, the concentration of vesicles has to be increased by (ultra)centrifugation. As a consequence, the size distribution depends upon preanalytical conditions, and the concentration of vesicles cannot be determined. With immuno-gold labeling, it is possible to provide biochemical information [229]. The measurement time is in the order of hours.

Atomic force microscopy (AFM)

AFM was developed in 1986 by Binnig et al. [36], and provides subnanometer resolution topography imaging. An atomic force microscope consists of a cantilever with a sharp tip at its end that scans a sample surface without physical contact. Movements of the tip are measured, and a three-dimensional image is created by software.

Owing to a lateral resolution of 3 nm and a vertical resolution < 0.1 nm [36], AFM is suitable for size detection and performs better than DLS on polydisperse samples [137]. Siedlecki et al. and Yuana et al. showed that AFM can be used to measure the relative size distribution of vesicles in their physiologic state [335, 269]. Because of the high resolution of AFM, vesicles must be bound to an extremely flat surface, such as mica. Antibodies can be used to bind vesicles to the surface, so that biochemical information can also be obtained [335]. Because the efficiency of vesicle binding to a surface using antibodies is unknown, the concentration of vesicles cannot be determined with certainty. Furthermore, the surface binding may affect the morphology of vesicles, and this may hamper the determination of the real diameter.

Fig. 3.3A shows the calculated relative size distribution for 10,000 counts as measured with AFM, assuming isovolumetric particle deformation and equal surface binding. Under these assumptions, there is excellent correlation with the standard population, owing to the high resolution. The measurement time is in the order of hours.

Impedance-based flow cytometry

The Coulter principle is employed in an impedance-based flow cytometer to count and measure the size of single particles in a fluid within seconds. An impedance-based flow cytometer consists of two chambers divided by an insulatingmembrane containing a single channel. In each chamber, an electrode is immersed in an

electrolyte to drive an ionic current through the channel. Particles driven into the channel cause a reduction in current. A relative size distribution can be calculated from the change in current when the channel length l_c and diameter d_c are known. The concentration can also be determined if the average particle transport velocity $\nu_{s,\mathrm{av}}$ is known.

The sensitivity of impedance-based flow cytometry depends on the channel size with respect to the vesicle size. The vesicle diameter must be between approximately 0.1 and 0.7 times the channel diameter [144]. In practice, at least two impedance-based flow cytometers, each with a different channel diameter, are required to cover the whole size range of vesicles. The lower detection limit of commercial impedance-based flow cytometers is currently 300 nm [340]. Consequently, only a small fraction of vesicles can be detected.

Fig. 3.3B shows the calculated absolute size distribution for a commercial impedance-based flow cytometer with a channel diameter of 25 µm [340]. As the detection limit is approximately 300 nm, smaller vesicles are detected with low efficiency. An impedance-based flow cytometer does not provide information on the morphology, biochemical composition, or cellular origin, but the method can be combined with light scattering and fluorescence flow cytometry.

3.4 Discussion and conclusion

This chapter gives an overview of (potential) methods for the detection and characterization of vesicles. Table 3.1 lists the assessed possibilities and limitations of each method, based on the underlying physical parameters of each technique.

Considering the optical methods based on light scattering, DLS and NTA are potentially capable of measuring relative and absolute size distributions, respectively, of vesicles within minutes. Except for Raman spectroscopy, methods based on light scattering cannot distinguish vesicles from similar-sized lipoprotein particles or small platelets, as no biochemical information is obtained. Raman spectroscopy could potentially detect the size, concentration, and biochemical composition of single vesicles without labeling, but the measurement time is in the order of hours.

Of the optical methods based on fluorescence, STED microscopy, F-NTA, and F-CS are potentially capable of measuring the absolute size distribution and obtaining biochemical information by the application of fluorescent antibody labeling. Fluorescent antibody labeling which is not easy to perform, and involves several practical and optical problems. Real size distribution measurements may be less accurate, as optical detection can be influenced by many factors, such as age of the light source, cleanliness of the cuvette or flow channel, stability of the building and supporting table, and preanalytical conditions.

Among the non-optical methods, X-ray microscopy, TEM and AFM have high (≤ 12 nm) imaging resolution as compared with optical methods. Size and morphology information can be obtained by imaging, and biochemical information can also be obtained. However, measurements are based on many assumptions, and

the measurement time is more than 1 h per sample. A fast non-optical method is impedance-based flow cytometry, which can resolve small size differences but only within a limited size range. This technique provides no biochemical information unless combined with fluorescence flow cytometry.

From Table 3.1, F-NTA seems to be the most suitable method for the detection of size, concentration, biochemical composition, and cellular origin of vesicles at high speed, especially as the method can determine the relevant characteristics of vesicles directly in body fluids. Nevertheless, the other methods mentioned in this chapter are being rapidly developed, and this might lead to new possibilities and shorter measurement times.

3.4.1 Combining methods

Methods that have been successfully combined for vesicle detection are flow field-flow fractionation (F-FFF) with multiangle light scattering (MALS) or DLS [159]. F-FFF can fractionate 27 nm diameter vesicles from 36 nm diameter vesicles [170]. Subsequently, DLS or MALS can accurately determine the size, as the fractionated sample is monodisperse. MALS is based on angle resolved light scattering, and is used for molar mass and mean particle size determination. We did not discuss MALS earlier, because the technique does not provide a size distribution for polydisperse samples. Another method that is practically extendable is Raman spectroscopy, which was recently successfully combined with both Rayleigh scattering and fluorescence microscopy for intracellular chemical analysis [239]. Raman spectroscopy can also be extended with electron microscopy to correlate detailed biochemical information with the relative size distribution and morphology [307]. Finally, Raman spectroscopy can be integrated with optical coherence tomography to obtain quantitative information on the concentration-dependent scattering coefficient [95, 226].

3.4.2 Improving methods

A conventional method that can be optimized for the detection of vesicles is flow cytometry. By reducing flow chamber dimensions, optimizing the flow chamber shape, reducing the flow velocity, and using large-aperture optics, the sensitivity can be increased tremendously. Steen extended a commercial flow cytometer with dark-field illumination and detection to improve the detection limit to 70 nm for polystyrene spheres [278]. Single quantum dots can be detected with 99 % accuracy by flow cytometry when a submicrometer fluidic flow channel combined with a confocal microscope is used [277]. NTA is a relatively new method, and is currently showing a high degree of development. Increasing the detector sensitivity and decreasing the wavelength may lower the detection limit to 30 nm for biological particles, so that even the smallest vesicles come within reach without the need for fluorescent labeling. In specialized laboratories, two impedance-based flow cytometers have been optimized for the detection of submicrometer particles by reducing the channel diameters to 500 and 132 nm [144, 259]. In combination with

a commercial impedance-based flow cytometer, this covers the whole size range of vesicles, but centrifugation or filtration of the sample is required to prevent frequent problems with blocking of the flow channel.

3.4.3 Recently obtained results

Recently, some of the methods discussed have been applied to vesicles [107]. Here, we give an interpretation of these results based on our analysis. The concentration of vesicles in platelet-free plasma was reported to be $200-260 \cdot 10^9$ L^{-1} by NTA [124] and $3-702 \cdot 10^9$ L^{-1} by AFM [335]. It is possible that the real concentration is higher, as the detection efficiency of both methods is $< 100\,\%$. However, if we consider false positives such as lipoprotein particles, the real concentration may also be lower. With flow cytometry, Yuana obtained a 1,000-fold lower $CD41^+$-vesicle concentration, of $11-291 \cdot 10^6$ L^{-1}, than was obtained with NTA and AFM. The discrepancy in results between flow cytometry and NTA and AFM can be explained by considering the detection limit of commercial flow cytometers, which is insufficient to detect vesicles smaller than 300 nm. As most vesicles are smaller than 300 nm and are therefore not detected (Fig. 3.3A), the detection efficiency is $< 2\,\%$. In addition, different results have also been obtained with the same method. Lawrie et al. used DLS equipment from two companies, and obtained different size distributions for the same vesicles in fresh frozen plasma [185]. Sources of these differences could be the detection angle and the applied mathematical algorithm. In conclusion, several (combinations of) methods can correctly detect clinically relevant properties of vesicles. These methods should be further explored and validated by comparing measurement results, so that accurate, reliable and fast analyses of extracellular vesicles come within reach.

CHAPTER 4

Particle size distribution of extracellular vesicles determined by transmission electron microscopy, flow cytometry, nanoparticle tracking analysis, and tunable resistive pulse sensing

Abstract

Background: Enumeration of extracellular vesicles has clinical potential as a biomarker for disease. In biological samples, the smallest and largest vesicles typically differ 25-fold in size, 300,000-fold in concentration, 20,000-fold in volume, and 10,000,000-fold in scattered light. Because of this heterogeneity, the currently employed techniques detect concentrations ranging from 10^4 to 10^{12} vesicles mL^{-1}. *Objectives*: To investigate whether the large variation in the detected concentration of vesicles is caused by the minimum detectable vesicle size of five widely used techniques. *Methods*: The size and concentration of vesicles and reference beads were measured with transmission electron microscopy (TEM), a conventional flow cytometer, a flow cytometer dedicated to detecting submicrometer particles, nanoparticle tracking analysis (NTA), and tunable resistive pulse sensing (TRPS). *Results*: Each technique gave a different size distribution and concentration for the same vesicle sample. *Conclusion*: Differences between the detected vesicle concentrations are primarily caused by differences between the minimum detectable vesicle sizes. The minimum detectable vesicle sizes were 70−90 nm for NTA, 70−100 nm for TRPS, 150−190 nm for dedicated flow cytometry, and 270−600 nm for conventional flow cytometry. TEM could detect the smallest vesicles present, albeit after adhesion on a surface. Dedicated flow cytometry was most accurate in determining the size of reference beads, but is expected to be less accurate on vesicles, owing to heterogeneity of the refractive index of vesicles. Nevertheless, dedicated flow cytometry is relatively fast and allows multiplex fluorescence detection, making it most applicable to clinical research.

This chapter has been published as:

- E. van der Pol, F.A.W. Coumans, A.E. Grootemaat, C. Gardiner, I.L. Sargent, P. Harrison, A. Sturk, T.G. van Leeuwen, and R. Nieuwland. Particle size distribution of exosomes and microvesicles by transmission electron microscopy, flow cytometry, nanoparticle tracking analysis, and resistive pulse sensing. *J. Thromb. Haemost.* **12**(7), 1182−1192 (2014)

4.1 Introduction

Extracellular vesicles, such as exosomes and microvesicles, are released by cells into their environment as submicrometer particles enclosed by a phospholipid bilayer [69]. These vesicles contribute to many homeostatic processes, e.g. coagulation and inflammation [246, 270, 231], and therefore have potential clinical applications [30, 193, 247, 17]. Unfortunately, most single vesicles are below the detection range of many techniques, owing to their small size and low refractive index [235, 233], leading to misinterpretation of data and reported concentrations ranging from 10^4 to 10^{12} vesicles mL^{-1} in plasma [235, 233, 316, 90, 335, 169, 234].

In Chapter 3, we reviewed the theoretical performance of 14 methods to determine the particle size distribution (PSD) of vesicles [235]. The PSD describes the concentration as a function of size, and defines which vesicle types are measured [231]. Unexpectedly, our simulations predicted that each method would obtain a different PSD, thereby hampering data interpretation, data comparison, and standardization.

In this chapter, we performed an experimental evaluation of five of the 14 methods. We selected the most widely used methods capable of detecting single vesicles: transmission electron microscopy (TEM), a conventional flow cytometer, a flow cytometer dedicated to detecting submicrometer particles, nanoparticle tracking analysis (NTA), and tunable resistive pulse sensing (TRPS). The PSDs of a standard population of reference beads and a standard population of vesicles were measured with all methods.

4.2 Methods

4.2.1 PSD

Throughout this chapter, we define "size" as the diameter of a particle, and the PSD as the histogram of particle sizes, providing the mean number of particles per milliliter per 10 nm bin [155]. Data processing and representation were performed with OriginPro (v8.0724; OriginLab Corporation, Northampton, MA, USA).

4.2.2 Reference beads

To create a reference sample with a known PSD, a mixture of traceable polystyrene beads (Nanosphere; Thermo Fisher, Waltham, MA, USA) was prepared in deionized water. TRPS measurements require a conductive medium; therefore, the beads were suspended in electrolyte buffer (Izon, Christchurch, New Zealand). The size and concentration of the reference beads were selected to resemble those of previously reported vesicle PSDs [235, 316, 90, 335, 234, 216]. Table 4.1 shows the size of the reference beads according to TEM data of the manufacturer. The concentration (beads mL^{-1}) was derived from the specifications. Fig. 4.1A shows the PSD of the reference beads under the assumption that each subpopulation

Table 4.1: Catalog numbers, diameters, and concentrations of the subpopulations of polystyrene reference beads as determined by five methods

Catalog number	3050A	3100A	3200A	3400A	3600A
Diameter (nm)					
TEM	46 ± 7	102 ± 5	203 ± 5	400 ± 7	596 ± 8
Conventional flow cytometer			209 ± 8	427 ± 33	592 ± 20
Dedicated flow cytometer		105 ± 4	193 ± 4	399 ± 6	589 ± 7
NTA	49 ± 11	93 ± 21	189 ± 23	380 ± 64	607 ± 27
TRPS		104 ± 10	200 ± 10	418 ± 31	623 ± 36
Concentration (beads mL^{-1})					
Prepared	$2.0 \cdot 10^9$	$1.0 \cdot 10^9$	$1.0 \cdot 10^8$	$1.0 \cdot 10^7$	$1.0 \cdot 10^6$
Conventional flow cytometer			$1.0 \cdot 10^8$	$1.0 \cdot 10^7$	$0.7 \cdot 10^6$
Dedicated flow cytometer		$0.5 \cdot 10^9$	$0.8 \cdot 10^8$	$0.8 \cdot 10^7$	$0.9 \cdot 10^6$
NTA	$0.1 \cdot 10^9$	$1.0 \cdot 10^9$	$1.2 \cdot 10^8$	$2.5 \cdot 10^7$	$1.0 \cdot 10^6$
TRPS		$1.1 \cdot 10^9$	$1.2 \cdot 10^8$	$1.0 \cdot 10^7$	$1.0 \cdot 10^6$

NTA, nanoparticle tracking analysis; TRPS, tunable resistive pulse sensing; TEM, transmission electron microscopy. Diameter is expressed as mean ± standard deviation.

Table 4.2: Manufacturers, catalog numbers, and diameters of silica beads obtained by imaging at least 500 beads with transmission electron microscopy

Manufacturer	Catalog number	Diameter (nm)
Corpuscular	147020-10	105 ± 21
Kisker	Psi-0.2	206 ± 18
	Psi-0.4	391 ± 18
	Psi-0.6	577 ± 20
	Psi-0.8	772 ± 21
	Psi-1.0	918 ± 14

Diameter is expressed as mean ± standard deviation.

has a Gaussian distribution. The reference sample contained five subpopulations, among which larger beads have lower concentrations

The total concentration was $3.1 \cdot 10^9$ beads mL^{-1}. Prior to analysis, the reference sample was sonicated for 10 s and vortexed for 10 s. Table 4.2 lists the diameters of silica beads (Silica oxide size standards, Corpuscular, Cold Spring, NY, USA; Plain silica, Kisker, Steinfurt, Germany) used to calibrate the flow cytometers and NTA instrument.

4.2.3 Vesicle standard

As isolation of vesicles from blood is challenging [333], we selected urinary vesicles for our biological standard sample. Urine contains a relatively high concentration of vesicles with low contamination [235]. Urine from five healthy male individuals was collected, pooled, and centrifuged twice (8·50 mL, 10 min, 180 g, 4 °C; and 20 min, 1,550 g) to remove cells. Cell-free urine aliquots (12 mL) were frozen in liquid nitrogen and stored at −80 °C. Prior to analysis, samples were thawed on

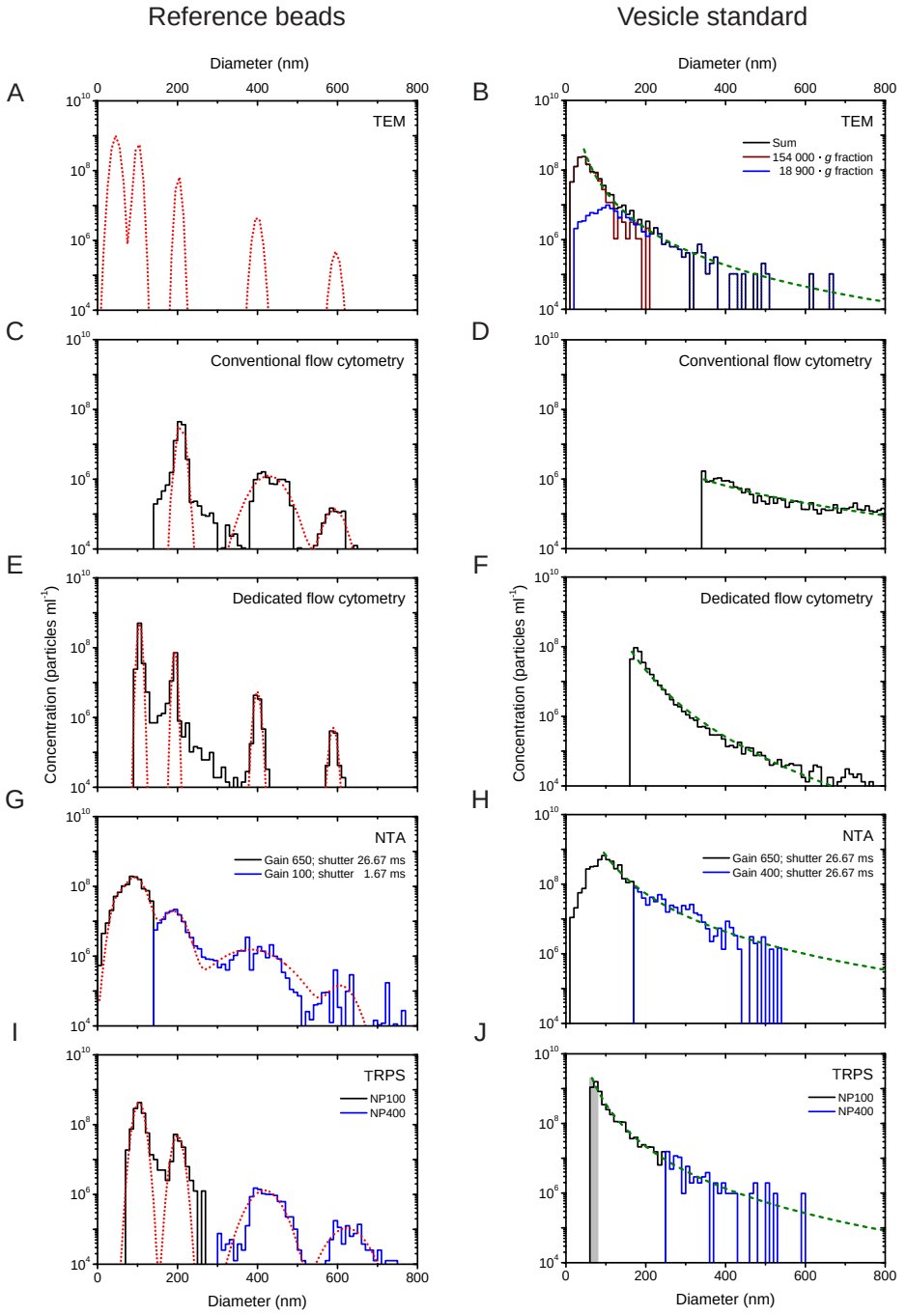

Figure 4.1: Particle size distributions (PSDs) of reference beads and the vesicle standard. (continued)

Figure 4.1: Concentrations (on a logarithmic scale) of the reference beads (left) and the vesicle standard (right) detected by (A, B) transmission electron microscopy (TEM), (C, D) conventional flow cytometry, (E, F) dedicated flow cytometry, (G, H) nanoparticle tracking analysis (NTA) and (I, J) tunable resistive pulse sensing (TRPS) are shown. The bin width is 10 nm. PSDs of the reference beads (black line) were fitted by a sum of Gaussian functions (dotted red line). PSDs of the vesicle standard (black line) were fitted by a power-law function (dashed green line). The PSD of the reference beads determined by TEM is based on data from the manufacturer. PSDs given by NTA and TRPS originate from two measurements with relatively high-sensitivity (black) and low-sensitivity (blue) settings.

melting ice for 1 h, centrifuged (10 min, 1,550 g, 4 °C) to remove precipitated salts, and diluted in 0.2 µm-filtered (MilliPore, Billerica, MA, USA) phosphate-buffered saline.

4.2.4 TEM

Data from the manufacturer were used to create the PSD of reference beads by TEM. To analyze the vesicle standard by TEM, vesicles were isolated by centrifugation (12·1,000 µL, 60 min, 18,900 g, 4 °C). From each aliquot, 900 µL was collected for ultra-centrifugation, the next 75 µL was discarded, and the remaining 25 µL contained the relatively large vesicles. The 900 µL aliquots were ultra-centrifuged (60 min, 154,000 g, 4 °C) to collect smaller vesicles from the pellet. All pellets present in the remaining 25 µL from both centrifugation speeds were resuspended in 975 µL PBS citrate and centrifuged as before. For both centrifugation speeds, the washed pellets were pooled to a final volume of 300 µL. Each pool was prepared as follows: 145 µL was diluted with 145 µL PBS containing 0.2 % paraformaldehyde (w/v). After fixation for 24 h, 10 µL was applied to a formfar-carbon coated 300 mesh grid (Electron Microscopy Sciences, Hatfield, USA) for 7 min, followed by staining with 1.75 % uranyl acetate (w/v). Samples were allowed to dry at room temperature for 2 h and imaged with TEM (CM-10, Philips, Eindhoven, The Netherlands) at 100 kV.

Next, 1,000 vesicles were segmented manually using the Quick selection tool of Photoshop v11.0.2 (Adobe Systems, San Jose, CA). Overlapping vesicles were included in the analysis as their boundaries could be clearly observed. A custom-made Javascript saved the surface area of the segmented vesicles to a .csv file. The vesicle size d was calculated from the surface area A using $d = \sqrt{4A/\pi}$, thereby assuming that vesicles are spherical. The overall PSD was obtained by summation of the PSDs obtained by both centrifugation speeds.

To obtain the vesicle concentration, we multiplied the mean number of vesicles per surface area by the grid area, divided by the sample volume. Here, we assumed that all vesicles adhered to the grid and were distributed uniformly.

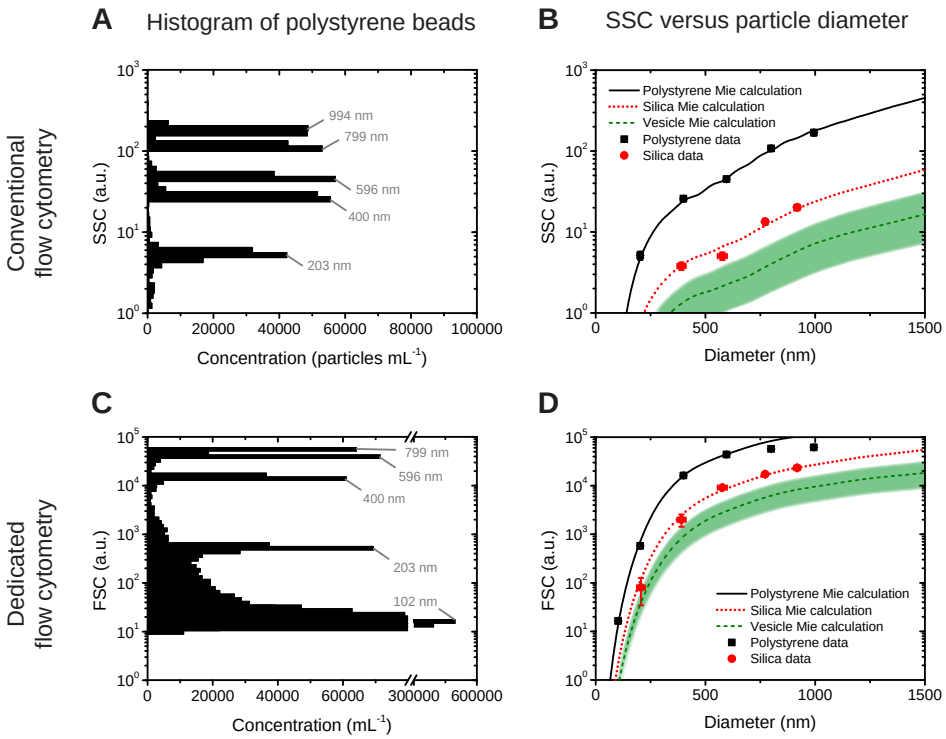

Figure 4.2: Relationship between scattering and the diameter of vesicles. (A) Side-scattered light (SSC; logarithmic scale) vs. concentration for polystyrene beads measured by conventional flow cytometry. (B) Measured (symbols) and calculated (lines) SSC (logarithmic scale) vs. diameter for polystyrene beads (black), silica beads (red), and vesicles (green). The SSC increases with increasing particle diameter, and is lower for vesicles than for beads. (C) Forward-scattered light (FSC; logarithmic scale) vs. concentration for polystyrene beads measured by dedicated flow cytometry. The concentration of 102 nm beads was 100-fold higher than that of the other sizes to discriminate between signal and background counts. (D) Measured (symbols) and calculated (lines) FSC (logarithmic scale) vs. diameter for polystyrene beads (black), silica beads (red), and vesicles (green). Mie calculations are in excellent agreement with the data, except for the 799 nm and 994 nm polystyrene beads, owing to detector saturation. a.u., arbitrary units.

4.2.5 Conventional flow cytometry

A flow cytometer (FACSCalibur; BD, Franklin Lakes, NJ, USA) with a 15 mW 488 nm laser was used to detect side-scattered light (SSC) for 10 min at a flow rate of $\sim 60\,\mu L\,min^{-1}$. The trigger was set on SSC, with a photomultiplier tube voltage of 400 V, a gain of 1, and a trigger threshold of 0 [234]. To account for the noise background, the intensity histogram of a background measurement with de-ionized water was subtracted from the intensity histogram of each dataset. To calculate the particle concentration, the flow rate was determined by weighting the sample volume aspirated during 10 min. To prevent swarm detection [234], the reference beads and vesicle standard were diluted 1,000-fold ($1.7 \cdot 10^5$ counts vs. $1.0 \cdot 10^5$ background counts) and 100-fold ($2.6 \cdot 10^5$ counts vs. $1.5 \cdot 10^5$ background counts), respectively. The absence of swarm detection was confirmed by serial dilutions.

To relate SSC to a particle size, we calibrated the flow cytometer with beads of known size and refractive index. Fig. 4.2A shows the SSC histogram of polystyrene beads. Fig. 4.2B shows the SSC of polystyrene and silica beads vs. their size. The data were fitted by Mie theory, incorporating the size and refractive index of the beads and the optical configuration of the instrument [40]. Mie calculations were performed with the scripts of Mätzler [199] in MATLAB (v7.9.0.529, MathWorks, Natick, MA, USA). More details on the light scattering calculations are provided in Appendix D. The solid curve in Fig. 4.2B was used to relate SSC to the size of the polystyrene reference beads with a refractive index of 1.61 [234]. The dashed curve in Fig. 4.2B was used to relate SSC to vesicle size, with the assumption that vesicles are spheres with a refractive index of 1.40, which was previously estimated [169] and corresponds to the refractive index of cells [309, 31].

4.2.6 Dedicated flow cytometry

Throughout this chapter, we use "dedicated flow cytometry" as a generic term for flow cytometers dedicated to detecting submicrometer particles. A flow cytometer (A50-Micro; Apogee, Hemel Hempstead, UK) with a 20 mW 488 nm laser was used to detect forward-scattered light (FSC) and SSC. The trigger was set on both the FSC and SSC detector. The gains were 1, the applied voltages were 290 V and 415 V, and the thresholds were 5 and 32 for the FSC and SSC detectors, respectively. Based on the counts from de-ionized water, a gate was set to reduce the noise background. This approach is preferable, but was not possible on the FACSCalibur due to high noise on especially the FSC detector. The sample volume injected by the internal microsyringe was used to calculate the concentration of particles. In total, $1.4 \cdot 10^5$ reference beads and $0.8 \cdot 10^5$ vesicles were analyzed. Analogously to our approach for conventional flow cytometry, we related FSC to the vesicle size by using beads and Mie theory, as illustrated for dedicated flow cytometry in Fig. 4.2C,D.

4.2.7 NTA

A dark-field microscope (NS500; Nanosight, Amesbury, UK) with a 45 mW 405 nm laser and an electron multiplying charge-coupled device (EMCCD) was used to determine the PSD by tracking the Brownian motion of single particles [90, 108]. Measurements were performed with two dilutions and two detection settings to increase the effective size range, which is needed because light scattered from the smallest and the largest beads differs by five orders of magnitude, whereas the dynamic range of the EMCCD is only approximately three orders of magnitude. Consequently, settings suitable for detecting 46 nm beads would result in extreme saturation for 596 nm beads. Two dilutions are needed, because a 50-fold dilution is required to detect the smallest beads [108], but at this dilution the probability of detecting a 596 nm bead is $< 0.5\,\%$.

Reference beads were analyzed with high-sensitivity settings (diluted 1:50; shutter, 26.67 ms; gain, 650; threshold, 22; $1.8 \cdot 10^3$ beads tracked) and low-sensitivity settings (undiluted; shutter, 1.67 ms; gain, 100; threshold, 10; $1.1 \cdot 10^4$ beads tracked). We multiplied the concentration as provided by the NTA software by the ratio between the expected and measured concentrations of calibration beads [108]. This concentration calibration was performed with 102 nm and 203 nm polystyrene beads with concentrations of $2 \cdot 10^7$ and $1 \cdot 10^8$ beads mL^{-1} for the high-sensitivity and low-sensitivity settings, respectively. The vesicle standard was analyzed with high-sensitivity settings (diluted 1:500; shutter, 26.67 ms; gain, 650; threshold, 19; $1.0 \cdot 10^3$ vesicles tracked) and low-sensitivity settings (diluted 1:100; shutter, 26.67 ms; gain, 400; threshold, 10; $1.1 \cdot 10^3$ vesicles tracked). Concentration calibration was performed with 105 nm and 206 nm silica beads with a concentration of $1 \cdot 10^8$ beads mL^{-1} for both the high-sensitivity and low-sensitivity settings [108], as the refractive indices of silica and vesicles are close.

Per sample, 20 videos of 30 s were captured at 22.0 °C and analyzed by NTA v2.3.0.17 (Nanosight), assuming a medium viscosity of 0.95 cP. To obtain the overall PSD $O(d)$, the PSDs obtained with high-sensitivity settings, $H(d)$, and low-sensitivity settings, $L(d)$, were combined at the size d_0, where the concentrations were similar [$H(d_0) \approx L(d_0)$, $O(d) = H(d)$ for all $d \leq d_0$; $O(d) = L(d)$ for all $d > d_0$].

4.2.8 TRPS

TRPS (qNano; Izon) determines the PSD from resistance pulses caused by particles moving through a pore. Measurements were performed with two pore sizes, for two reasons. First, for a single pore, the detectable size range is at best five-fold, whereas our smallest and largest reference beads differ 12-fold in size. Second, the analyzed sample volume depends on the pore size. With the NP100 pore, only 0.9 nL of sample was analyzed, containing < 1 bead of 596 nm on average. With the NP400 pore, 80 nL was analyzed, containing 77 beads of 596 nm.

The reference beads were analyzed by TRPS with high-sensitivity settings (NP100; voltage, 0.70 V; stretch, 47.0 mm) and low-sensitivity settings (NP400;

voltage, 0.26 V; stretch, 46.5 mm). The vesicle standard was diluted 1:1, and analyzed with high-sensitivity settings (NP100; voltage, 0.60 V; stretch, 46.0 mm) and low-sensitivity settings (NP400; voltage, 0.40 V; stretch, 43.5 mm). The pressure was set at 7.0 mbar. Calibration was performed with beads supplied by the manufacturer. At least 1,000 particles per sample were analyzed. A custom-made application (Microsoft Visual Basic 2008, Microsoft Corporation, Redmond, WA, USA) interrupted the measurement when the root-mean-square noise exceeded 10 pA. We required the R^2-correlation of cumulative counts with time to exceed 0.999, and the baseline current drift not to exceed 5 %. The two PSDs are combined in a similar way as for NTA.

4.3 Results

4.3.1 TEM

Fig. 4.1 shows all PSDs of the reference beads and vesicle standard. Fig. 4.1A shows the reference bead PSD based on the prepared concentrations and manufacturer-supplied data. Fig. 4.1B shows the vesicle standard PSD measured by TEM. The combined PSD has a peak at 45 nm, and for larger vesicles the concentration decreases with increasing size. The spikes on the right-hand side correspond to single vesicles. TEM can detect the smallest vesicles present, owing to an imaging resolution of ∼1 nm. However, sample preparation may cause a reduction in vesicle size [333, 294, 148]. In addition, limited and non-uniform adhesion of vesicles on the surface may affect the PSD.

4.3.2 Conventional flow cytometry

Fig 4.1C shows that the smallest polystyrene bead detected by conventional flow cytometry was 203 nm, and that the peaks were broadened as compared with the reference bead PSD. Fig. 4.1D shows that the first bin of the vesicle standard PSD corresponds to 340 nm, which is 140 nm larger than the smallest detected polystyrene bead, owing to refractive index differences. The detected concentration was $1.8 \cdot 10^7$ vesicles mL^{-1}.

4.3.3 Dedicated flow cytometry

Dedicated flow cytometry is capable of detecting single 102 nm polystyrene beads, as shown in Fig. 4.1E. The width of the peaks is comparable to the reference bead PSD. Fig. 4.1F shows that the first bin of the vesicle standard PSD corresponds to 160 nm. Consequently, dedicated flow cytometry detected approximately twice as small and thereby 18-fold more vesicles than conventional flow cytometry. The detected concentration was $3.3 \cdot 10^8$ vesicles mL^{-1}. Fig. 4.1D,F was produced on the assumption of a vesicle refractive index of 1.40 [169, 309, 31].

4.3.4 NTA

Fig. 4.1G shows the reference bead PSD as detected by NTA. By combining two measurements with different settings, NTA detected all reference bead sizes, although only 5 % of the 46 nm beads were detected. Tracking of 46 nm beads was hindered by the presence of larger beads that saturated the camera. Fig. 4.1G also shows that the peaks overlap because of broadening, which we attribute to the uncertainty in the measured diffusion coefficient, resulting from a limited track length and the uncertainty in the particle position. Fig. H shows the vesicle standard PSD obtained by combining two different settings. The peak at 95 nm is broad as compared with other vesicle PSDs. The smallest detectable vesicles appear to be 10 nm, which we attribute to broadening of the PSD. Using identical settings, we could detect only 5 % of the 46 nm polystyrene beads, which have comparable light scattering to a 70−90 nm vesicle.

4.3.5 TRPS

Fig. 4.1I shows the reference bead PSD as detected by TRPS. Through combination of measurements with an NP100 and NP400 pore, beads of 102 nm and larger were detected. The peaks are broadened as compared with the reference bead PSD, which may be caused by particle aggregation, electronic noise, and a varying pore dimension during the measurement. Fig. 4.1J shows the vesicle standard PSD with a peak at 75 nm.

4.3.6 Power-law function to describe the PSD of vesicles

The PSDs of vesicles are fitted by a mathematical function to enable quantitative comparison. To select the most appropriate function, we fitted the vesicle standard PSD with six empirical functions that are frequently used to describe PSDs of particles in suspension [155], and performed goodness-of-fit tests (Appendix B). The Gamma function, Weibull distribution and power-law function resulted in the best fits. Of these functions, we selected the power-law function, as it is least susceptible to minimum detectable vesicle size. The right panels of Fig. 4.1 show PSDs of the vesicle standards fitted by the power-law function (dashed lines).

4.3.7 Measurement error and coefficient of variation (CV) of the reference beads

The measured reference bead PSDs in Fig. 4.1 were fitted by a sum of Gaussian functions (dotted lines) to derive the mean and standard deviation of the size and the concentration for each subpopulation of beads (Table 4.1). The symbols in Fig. 4.3A indicate the relative measurement error of the size as the percentage difference between the measurement and the manufacturer specification. Because TEM data were used as reference, its relative size error is set at 0 %. The relative size error of the other methods was < 9 %. Dedicated flow cytometry had the lowest error in sizing beads, followed by TRPS, conventional flow cytometry, and NTA.

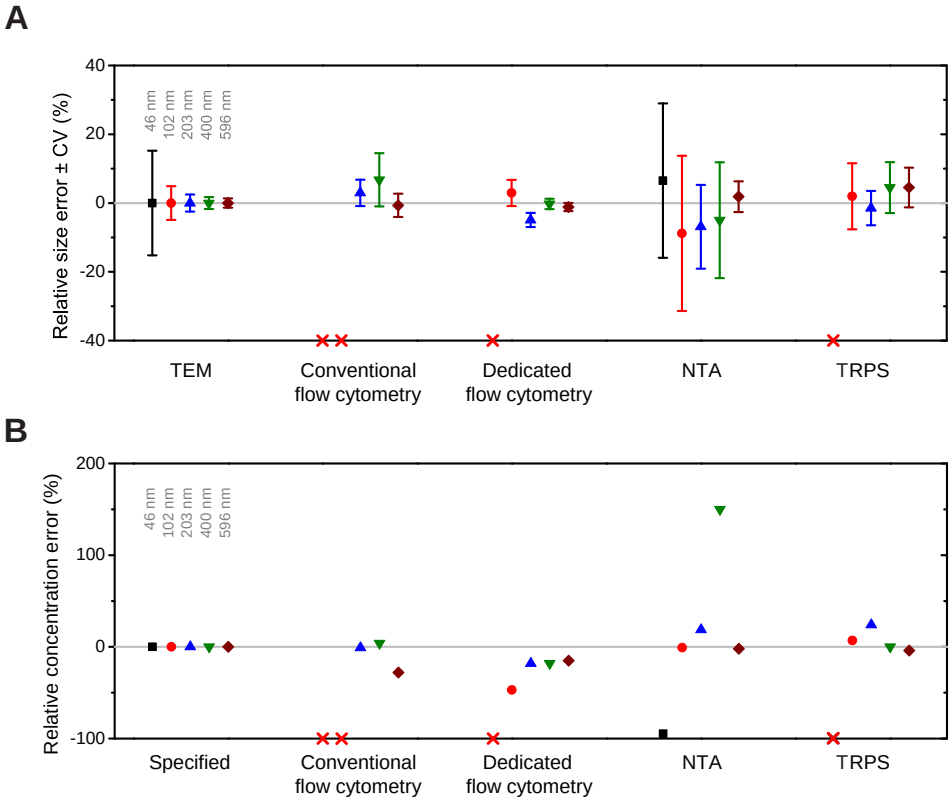

Figure 4.3: Relative error (symbols) and coefficient of variation (CV) (error bars) in determining the size (A) and concentration (B) of TEM, conventional flow cytometry, dedicated flow cytometry, nanoparticle tracking analysis (NTA) and tunable resistive pulse sensing (TRPS) for 46 nm beads (black), 102 nm beads (red), 203 nm beads (blue), 400 nm beads (green) and 596 nm beads (brown) from the reference mixture. Subpopulations that could not be detected are indicated by red crosses.

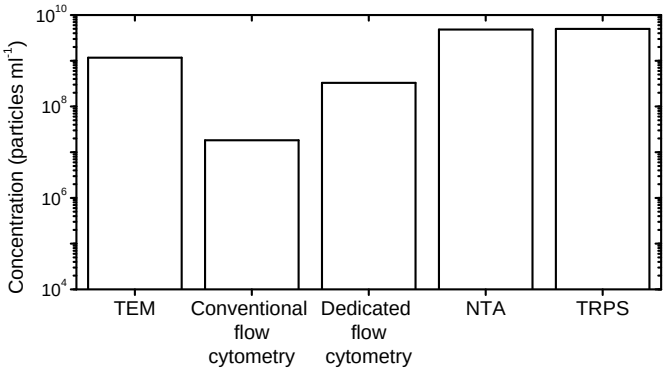

Figure 4.4: Total concentration (logarithmic scale) of vesicles detected by transmission electron microscopy (TEM), conventional flow cytometry, dedicated flow cytometry, nanoparticle tracking analysis (NTA), and tunable resistive pulse sensing (TRPS).

We attribute the low error of flow cytometry to the homogeneous refractive index of polystyrene and the strong relationship between size and scattering power (Fig. 4.2). The error of TRPS was limited because of specific measurement restrictions, as described in section 4.2. We attribute the relatively large error of NTA to the uncertainty in the measured diffusion coefficient.

The error bars in Fig. 4.3A indicate the CV, which is the percentage ratio between the standard deviation and the mean size, and is thus a measure of the width of the peaks in Fig. 4.1. Owing to the high resolution of TEM as compared with the measured standard deviation of the bead sizes, this standard deviation is a close approximation of the actual size of the beads. The lowest CVs were obtained by dedicated flow cytometry, followed by conventional flow cytometry, TRPS, and NTA.

Figure 4.3B shows the relative measurement error in determining the concentration of subpopulations of reference beads. TRPS was most accurate in determining the concentration of beads, followed by conventional flow cytometry, dedicated flow cytometry, and NTA. The error of TRPS was limited because of specific measurement restrictions. With flow cytometry, the concentration was derived from the flow rate, which has an uncertainty of 10 %. Dedicated flow cytometry underestimated the concentration of 102 nm beads, as these beads were close to the detection threshold. NTA was the least accurate method for determining the concentration of beads, possibly because of broadening of the PSD and crosstalk between 203 nm beads and 400 nm beads. The concentration of 46 nm beads was underestimated, as tracking of 46 nm beads was hindered by the presence of larger beads that saturated the camera.

4.3.8 Concentration of vesicles

Figure 4.4 shows the detected concentration of vesicles per technique. As compared with TRPS and NTA, conventional flow cytometry underestimates the concentration of vesicles almost 300-fold, whereas the more sensitive dedicated flow cytometer underestimates the vesicle concentration 15-fold. With TEM, the detected concentration was affected by sample preparation losses.

Table 4.3: Assessed capabilities of techniques for the detection of single vesicles in suspension

Method	Minimum detctable vesicle size (nm)	Size requirements and/or assumptions	Concentration requirements and/or assumptions	Additional features	Measurement time
TEM	∼1	No shrinkage, equivalent circular size	100 % surface binding, no centrifugation losses	Immunogold labeling	H
Conventional flow cytometry	270−600	Calibration with beads, spherical particle, $n = 1.40 \pm 0.02$	Q	Fluorescence	S
Dedicated flow cytometry	150−190	Calibration with beads, spherical particle, $n = 1.40 \pm 0.02$	Q	Fluorescence	S
NTA	70−90	T, η, ΔD, spherical particle	Calibration with beads $I_v(d, n) = I_b$	Zeta potential, fluorescence	M
TRPS	70−100	Calibration with beads, spherical particle, $\rho_v \ll \rho_m$	Calibration with beads Q dominated by Q_P	Zeta potential	M

NTA, nanoparticle tracking analysis; TRPS, tunable resistive pulse sensing; TEM, transmission electron microscopy. For each technique, the minimum detectable vesicle size, ability to measure the size and concentration and the requirements for this, ability to detect additional features, and measurement time are estimated. We derived the minimum detectable vesicle size of TRPS from six measurements performed with different NP100 pores. d is the vesicle diameter, ΔD is the uncertainty in the diffusion coefficient, I_v and I_b are the scattering intensities of a vesicle and a calibration bead, respectively, η is the viscosity of the solvent, n is the vesicle refractive index, Q is the flow rate, Q_P is the flow rate caused by external pressure, ρ_v are ρ_m are the electrical conductivities of a vesicle and the medium, respectively, and T is the temperature of the solvent. The measurement time is indicated by S, M, and H, meaning < 1 min, between 1 min and 1 h, and > 1 h, respectively.

4.4 Discussion and conclusion

In this chapter, we compared the abilities of five commonly used methods to determine the PSD of vesicles in suspension. A reference mixture of polystyrene beads with known PSD (Fig. 4.1A) and a vesicle standard from urine (Fig. 4.1B) were measured by each method. In agreement with our theoretical approach in Chapter 3, each technique gives a different PSD for the same sample. By comparing the vesicle PSDs and combining these results with the knowledge obtained from reference beads, however, many differences are now explained.

Throughout section 4.3, we have discussed the requirements and assumptions involved in the measured PSDs. Table 4.3 summarizes these requirements and assumptions, and also lists the minimum detectable vesicle size, the measurement times, and the capabilities to obtain functional information, such as fluorescence. In the next section, we will discuss our approach and the results in more detail.

4.4.1 TEM

To obtain the size of the reference beads (Fig. 4.1A), we used traceable TEM measurements of the manufacturer. Traceability means that the measurement result is related to SI units through an unbroken chain of comparisons with known uncertainties [202, 310]. To characterize beads, TEM is particularly useful, as beads are not affected by sample preparation, and the resolution of TEM is higher than the size of the beads. For comparison purposes, we set the relative size error of TEM to 0 (Fig. 4.3A). However, the relative size error of the reference beads ranges from 1.0 % for the 596 nm beads to 4.3 % for the 46 nm beads. The TEM data also provide the CV of the beads, which is a measure of the spread in bead sizes. Consequently, the error bars in Fig. 4.3A represent not only the imprecision of the instrument, i.e. the broadening of the reference bead PSD caused by the instrument, but also the CV of the reference beads.

We derived the reference bead concentrations from the manufacturer-specified mass concentration, density and size of the beads. Note that the concentration of submicrometer beads is not traceable, as uncertainties in the mass concentration and density of the beads are unknown. The mass concentration is often provided with single-digit precision, and the density of silica beads may range from 1.8 to $2.5\,\mathrm{g\,cm^{-3}}$. Consequently, the bead concentration and error thereof are unknown, and the relative concentration errors can only be mutually compared (Fig. 4.3B).

TEM analysis of vesicles involves two centrifugation steps and extensive sample preparation. To quantify the influence of these preanalytic variables on the obtained PSD (Fig. 4.1B), we overlapped the power-law functions of TEM and TRPS, which required horizontal and vertical stretching of the TRPS data with factors of 0.88 and 0.21, respectively. Considering TRPS to be the most reliable method for determining the PSD of vesicles, we hypothesize that vesicles shrink by 12 %, owing to fixation and dehydration, and that 21 % of the vesicles are recovered after centrifugation and binding to the formvar coating.

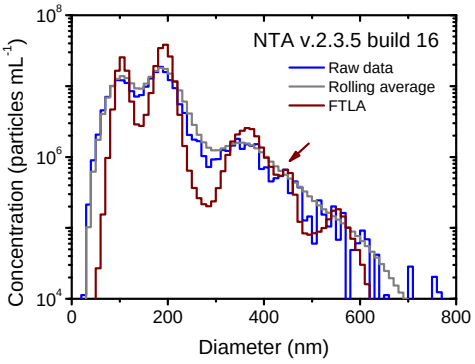

Figure 4.5: Particle size distribution (PSD) of the reference beads detected by nanoparticle tracking analysis (NTA) with low-sensitivity settings and processed by NTA v2.3.5.16 software (Nanosight). The bin width is 10 nm. The software provides raw data (blue line), a rolling average of the data (gray line), and data processed with the finite track length adjustment (FTLA) algorithm (brown line), resulting in different PSDs. The FTLA algorithm results in a peak (brown arrow) that is absent in the rolling average of the data.

4.4.2 Flow cytometry

To relate the measured light scattering to a particle size, we calibrated flow cytometers by using beads and Mie theory (Fig. 4.2), assuming spherical particles of known refractive index. As beads meet these criteria, Mie theory can be used to determine their PSD (Fig. 4.1C,E), resulting in dedicated flow cytometry being the most accurate in sizing beads (Fig. 4.3A). However, the refractive index of vesicles is probably heterogeneous and not exactly known [143], thereby affecting the PSD of vesicles obtained by flow cytometry (Fig. 4.1D,F). For example, under the assumption that the vesicle refractive index is 1.40 ± 0.02, the minimum detectable vesicle sizes are 270−600 nm for conventional flow cytometry and 150−190 nm for dedicated flow cytometry (Table 4.3). We attribute the high concentration of vesicles > 340 nm obtained by conventional flow cytometry relative to other techniques to background counts. An advantage of flow cytometry is knowledge of the analyzed sample volume, such that the particle concentration can be determined without calibration with beads.

4.4.3 NTA

The PSD of beads determined by NTA shows extensive broadening as compared with the other techniques (Figs. 4.1G and 4.3A). In addition, the determined concentration of vesicles requires careful interpretation. The manufacturer or user calibrates the instrument with beads to relate the mean number of scatterers in the field-of-view to the concentration [108]. This calibration is valid for a vesicle size that scatters the same amount of light as the calibration beads. The concentration of smaller vesicles is underestimated, whereas the concentration of larger vesicles is overestimated. Moreover, the concentration of beads is not traceable. To obtain the minimum detectable vesicle size of 70−90 nm, we related the scattering of 46 nm polystyrene beads, which were at the limit of detection, to the diameter of vesicles by using Mie theory.

Software often applies unknown and undesired operations to the data. For example, Fig. 4.5 shows the reference bead PSD detected by NTA with the low-

sensitivity settings and processed by NTA v2.3.5.16 (Nanosight). Analysis of the videos with this newer software results in a PSD (blue line) different from that in Fig. 4.1G (blue line). The software generates a batch summary file, wherein a rolling average is applied to the raw data, resulting in a smoother but less correct representation of the data (gray line). Application of finite track length adjustment (FTLA) results in narrower peaks, a decreased accuracy of the determined mean diameters, and the presence of an additional peak at 445 nm (brown line). As FTLA introduces artefacts, the application of FTLA to polydisperse samples is not recommended.

4.4.4 TRPS

Accurate sizing of vesicles by TRPS requires that the electrical conductivity of a particle is negligible as compared with the conductivity of the electrolyte [155, 158]. As polystyrene beads, cells and intact vesicles meet this requirement [209], we believe that the detected vesicle size is representative for urinary vesicles (Fig. 4.1J). However, our measurement restrictions made the TRPS measurements impractical. The major concerns with TRPS are pore clogging and pore stability. In the case of pore clogging, we reversed the pressure or temporarily applied a high pressure with a plunger. As the pores are stretchable, plunging may change the pore dimensions, as observed by a change in the baseline current. If the baseline current changed by $> 5\,\%$, we repeated the measurement and calibration, resulting in a measurement time of several hours.

The concentration is obtained by calibration with beads [158], which is inaccurate, because the concentration of the used beads is not traceable. As the flow rate is mainly determined by pressure across the pore, and not by electro-osmosis or electrophoresis, the differences between the zeta potentials of vesicles and calibration beads are negligible. Consequently, the accuracy in determining the vesicle concentration is expected to be comparable to that for the mixture of beads.

4.4.5 Single-vesicle detection as a biomarker

A biomarker based on vesicle enumeration should determine the concentration of a specific vesicle type. For this determination, the technique must obtain biochemical information to identify specific vesicles, and the measurement time should not exceed several minutes. Furthermore, size accuracy and precision are important, e.g. to distinguish vesicles from platelets. Our findings demonstrate that any reported concentration needs to be accompanied by the minimum detectable vesicle size. For example, the shaded area in Fig. 4.1J shows that a decrease in the minimum detectable vesicle size from 80 nm to 60 nm would result in a 2.4-fold increase in the obtained concentration. Therefore, we propose daily monitoring of the minimum detectable vesicle size, as day-to-day variation is expected for each instrument. Alternatively, a power-law fit may be applied to compare concentrations obtained with different minimum detectable vesicle sizes. An additional requirement for comparison of concentrations is traceable determination of both

size and concentration, which is problematic for techniques that calibrate the concentration with untraceable beads.

In conclusion, each technique gave a different PSD for the same vesicle sample. Differences between the detected vesicle concentrations are primarily caused by differences between the minimum detectable vesicle sizes. The minimum detectable vesicle sizes were 70−90 nm for NTA, 70−100 nm for TRPS, 150−190 nm for dedicated flow cytometry, and 270−600 nm for conventional flow cytometry. TEM could detect the smallest vesicles present, albeit after adhesion on a surface. Dedicated flow cytometry was most accurate in determining the size of reference beads, but is expected to be less accurate on vesicles, owing to heterogeneity of the refractive index of vesicles. A reliable estimate of the vesicle refractive index is required to convert the optical scatter signal detected by flow cytometry to size. Nevertheless, dedicated flow cytometry is relatively fast and allows multiplex fluorescence detection, making it most applicable to clinical research.

CHAPTER 5

Single versus swarm detection of extracellular vesicles by flow cytometry

Abstract

Background: Microvesicles and exosomes are cell-derived vesicles and potential biomarkers for disease. Recently, the Scientific Standardization Committee collaborative workshop of the International Society on Thrombosis and Haemostasis initiated standardization of vesicle detection by flow cytometry with polystyrene beads. Because polystyrene beads have different optical properties than vesicles, and because the mechanisms causing the detection signal are incompletely understood, there are contradictions between expected and observed results. *Objectives:* To develop a model with which to relate the detection signal of a flow cytometer to the diameter of vesicles and clarify observed discrepancies. *Methods:* We combined measurements of polystyrene and silica beads with an estimated refractive index of vesicles and performed Mie calculations of light scattering. *Results:* We established the relationship between measured light scattering and the diameter of vesicles. The Megamix gating strategy proposed by the Scientific Standardization Committee selects single vesicles and cells with diameters between 800 and 2,400 nm when applied on the forward-scattering detector of regular flow cytometers. Nevertheless, we demonstrated that, irrespective of the applied gating, multiple vesicles smaller than 220 nm or multiple 89 nm silica beads were counted as a single event signal at sufficiently high concentrations. *Conclusions:* Vesicle detection by flow cytometry is attributed to large single vesicles and swarm detection of smaller vesicles; that is, multiple vesicles are simultaneously illuminated by the laser beam and counted as a single event signal. Swarm detection allows the detection of smaller vesicles than previously thought possible, and explains the finding that flow cytometry underestimates the concentration of vesicles.

This chapter has been published as:

- E. van der Pol, M.J.C. van Gemert, A. Sturk , R. Nieuwland, and T.G. van Leeuwen. Single versus swarm detection of microparticles and exosomes by flow cytometry. *J. Thromb. Haemost.* **10**(5), 919-930 (2012)

5.1 Introduction

Microvesicles and exosomes are cell-derived vesicles present in body fluids that contribute to coagulation, inflammation, cellular homeostasis and survival, intercellular communication, and transport of waste materials [270, 217, 246]. The size, concentration, biochemical composition, and cellular origin of these biological vesicles contain clinically relevant information [30, 193, 247]. However, because of the small size of vesicles (30 nm to 1 µm), they are below the detection range of many currently used techniques [235]. Throughout this chapter, we will use 'vesicles' as a generic term for all types of extracellular, biological vesicle.

Approximately 75 % of laboratories apply flow cytometry to detect vesicles in clinical samples [179]. A flow cytometer guides cells and vesicles through a laser beam in a hydrodynamically focused fluid stream. One detector is placed in line with the laser beam, and measures the forward-scattered light (FSC). Other detectors measure the side-scattered light (SSC) and fluorescence intensity perpendicular to the beam. Light scattering by vesicles is essential, as scattering is generally used as the trigger signal telling the instrument that a vesicle is present.

A difficulty with flow cytometry is that the relationship between the measured light scattering and the diameter of vesicles is unknown, resulting in recent discussions about the standardization of vesicle detection [58, 212, 254] and in unexplained contradictions between the expected and observed measurement results. For example, according to the literature, the smallest polystyrene beads that can be detected by commercial flow cytometers typically have a diameter between 200 nm and 300 nm [58, 253, 227]. Because vesicles have a lower refractive index than polystyrene beads, they scatter light approximately 10-fold less efficiently than polystyrene beads [58]. Consequently, the smallest single vesicles that are detectable by flow cytometry must be larger than $\sim$ 500 nm. Using transmission electron microscopy (TEM) image analysis, we have recently shown that urinary vesicles are smaller than 500 nm [235], so we would not expect these vesicles to be detected by flow cytometry. Nevertheless, urinary vesicles are detectable by flow cytometry [320], although, from reference measurements with nanoparticle tracking analysis and atomic force microscopy, we now know that flow cytometry underestimates the concentration of vesicles by $\sim$ 1,000-fold [335, 124].

To resolve the contradictions in vesicle detection by flow cytometry, we will first present measurements on polystyrene beads and silica beads of known diameter, concentration, and refractive index. Combined with Mie calculations of the optical scattering power, this allows calibration of the flow cytometer, i.e. relating the detected scattering power to the diameter of single polystyrene or silica beads. On that basis, and using an estimated refractive index, we assess the diameter range of the smallest detectable single vesicles. In addition, we show that 89 nm silica beads, which have optical properties resembling those of vesicles, can be detected by regular flow cytometry, albeit at a higher concentration than used to detect single beads. Using dilution series of silica beads and cell-free urine, we elucidate the underlying mechanisms of vesicle detection.

Table 5.1: Diameter of polystyrene beads and silica beads and the efficiency with which single beads are detected by flow cytometry

Material	Diameter (nm)	Detection efficiency
Polystyrene	102 ± 5	
	203 ± 5	0.9 ± 0.2
	400 ± 7	1.0 ± 0.2
	596 ± 8	0.9 ± 0.2
	799 ± 5	1.0 ± 0.1
	994 ± 10	1.0 ± 0.1
	3005 ± 30	1.2 ± 0.2
Silica	89 ± 36	
	204 ± 35	0.6 ± 0.2
	389 ± 75	1.1 ± 0.3
	610 ± 101	1.0 ± 0.2
	732 ± 107	1.0 ± 0.2
	988 ± 132	1.2 ± 0.3
	2795 ± 472	1.1 ± 0.4

Diameter is expressed as mean ± standard deviation. The detection efficiency is defined as the ratio between the concentration as determined by the flow cytometer and the prepared concentration.

5.2 Methods

5.2.1 Samples

Beads

Table 5.1 summarizes the mean diameter and standard deviation of the used NIST-traceable polystyrene beads (Thermo Fisher Scientific, Waltham, MA, USA) and silica beads (Kisker Biotech, Steinfurt, Germany). At the illumination wavelength of our flow cytometer, which is 488 nm, the refractive indices of polystyrene and silica are 1.605 and 1.445, respectively. For comparison, the refractive index of water is 1.337 at this wavelength. As the refractive index of vesicles is assumed to be 1.38 inside the vesicle and 1.48 at the 10 nm-thick phospholipid membrane [309, 31, 102, 47], the optical properties of silica beads resemble those of vesicles better than those of polystyrene beads. To explore the detection limit of our flow cytometer (Figs. 5.4 and 5.5), beads were diluted in purified and deionized water (MilliPore, Billerica, MA, USA) to a concentration of 10^5 /mL. For this concentration, the expected count rate is 100 events s^{-1} at an estimated flow rate of 60 µL min^{-1}, which is within the recommended count rate for the flow cytometer. To explore the underlying mechanisms of vesicle detection (Fig. 5.7), dilution series of silica beads were prepared, in which the ratio of 89 nm and 610 nm silica beads was varied.

Vesicles

Cell-derived vesicles from human urine were used as a reference sample, because vesicles can be easily isolated without substantial contamination [235]. Fresh morning urine from five overnight-fasting healthy male subjects was collected, pooled, and centrifuged in 50 mL Falcon tubes for 10 min at 180 g and 4 °C (Mikro 200 R; Hettich, Tuttlingen, Germany) within 10 min after collection. The supernatant (45 mL) was collected and centrifuged for another 20 min at 1,550 g and 4 °C to remove the remaining cells. Aliquots of the supernatant (40 mL) were frozen in liquid nitrogen and stored at −80 °C. Samples were thawed on melting ice for 1 h, and centrifuged for 10 min at 1,550 g and 4 °C to remove precipitated amorphous salts.

5.2.2 TEM

For TEM analysis, vesicles were isolated by ultracentrifugation 60 min at 154,000 g and 4 °C), and washed once in phosphate-buffered saline (PBS)-citrate. Next, vesicles were resuspended in 0.2 % paraformaldehyde (w/v). After fixation for 24 h, vesicles were allowed to adhere to formvar-carbon coated 300 mesh grids (Electron Microscopy Sciences, Hatfield, PA, USA), stained with 1.75 % uranyl acetate (w/v), and imaged with a transmission electron microscope (CM-10; Philips, Eindhoven, The Netherlands) at 100 kV. From 1,000 vesicles, the surface area was determined by use of a custom-made Javascript with the Quick selection tool of Photoshop version 11.0.2 (Adobe Systems, San Jose, CA, USA). From the surface area, the diameter of each vesicle was calculated to create a size distribution.

5.2.3 Flow cytometry

FSC and SSC powers were measured for 1 min with a FACSCalibur (Becton Dickinson, Franklin Lakes, NJ, USA) at a high flow rate (60 µL min^{-1}). The flow cytometer has a linearly polarized 15 mW argon-ion laser emitting at 488 nm. The beam is elliptically focused to a cross-sectional area of $22 \times 66\,\mu m^2$, and at high flow rate the sample core diameter is 56 µm [68]. Consequently, the effective beam volume is $22 \cdot \pi \cdot 28^2 = 5.4 \cdot 10^4\,\mu m^3$ or 54 pL. The illumination intensity is $\sim 1.4 \cdot 10^7\,Wm^{-2}$ [114]. We selected SSC as the trigger signal to indicate to the instrument that a vesicle or bead is present. The following detector settings were used throughout this experiment. For SSC, the applied voltage was 400 V, the gain was 1, and the threshold was 0. For FSC, the amplification was 100, the gain was 1, and the threshold was 0. As no threshold was applied, optical, electronic and fluidic noise contribute to a considerable noise background [273]. However, in modern flow cytometers, both the dark current and stray light are electronically subtracted from the signal coming from the detector by the baseline restorer, resulting in a stable and relatively low noise background of $< 10{,}000$ counts/min in our case. To account for this remaining noise background, a background measurement was performed with purified and deionized water before and after each

Table 5.2: Parameters used for Mie calculations

Parameter	Value
Refractive index: polystyrene	1.605
Refractive index: silica	1.445
Refractive index: water	1.337
Refractive index: vesicle inside	1.38 ± 0.02
Refractive index: vesicle at the membrane	1.48
Vesicle membrane thickness (nm)	10
Illumination wavelength (nm)	488
Illumination intensity (Wm^{-2})	$1.4 \cdot 10^7$
Collection angle: FSC Becton Dickinson FACSCalibur (°)	0.5−7
Collection angle: SSC Becton Dickinson FACSCalibur (°)	47−133
Collection angle: FSC Apogee A40 (°)	1−70
Collection angle: FSC Beckman Coulter FC500 (°)	2−16

The refractive indices are provided for room temperature, atmospheric pressure, and an illumination wavelength of 488 nm. FSC, forward-scattered light; SSC, side-scattered light.

measurement series. The average SSC and FSC histograms of these background measurements were subtracted from each dataset.

5.2.4 Mie theory

The power of light scattered in a particular direction by a spherical particle, such as a bead or a vesicle, is calculated by Mie theory, and involves the diameter and refractive index of the particle, the refractive index of the surrounding medium, and the wavelength, polarization and intensity of light [40]. We selected Mie theory because, in contrast to Rayleigh scattering and Faunhofer diffraction, it is valid for any ratio of the diameter of the particle to the wavelength [235, 40]. All Mie calculations in this chapter are based on the MATLAB scripts of Mätzler [199], and are similar to the calculations of Fattaccioli et al. [97], but other free software is online available [184]. Data processing was performed with MATLAB (v.7.9.0.529), and graphs were plotted with OriginPro (v.8.0724). As input for the Mie calculations, we used the parameters listed in Table 5.2. Here, we assumed that urine has a refractive index equal to that of water, and that vesicles are spherical and have refractive indices of 1.38 ± 0.02 inside and 1.48 at the 10 nm-thick phospholipid membrane [309, 31, 102, 47]. Our estimation of the inner refractive index of vesicles is based on the measured inner refractive index of cells and bacteria [309]. As vesicles originate from their parent cell, we expected that vesicles would have an inner refractive index equal to that of their parent cell.

5.2.5 Flow cytometer calibration

Flow cytometry provides the detected scattering power in arbitrary units, implying that the relationship between the detected scattering power and the diameter of

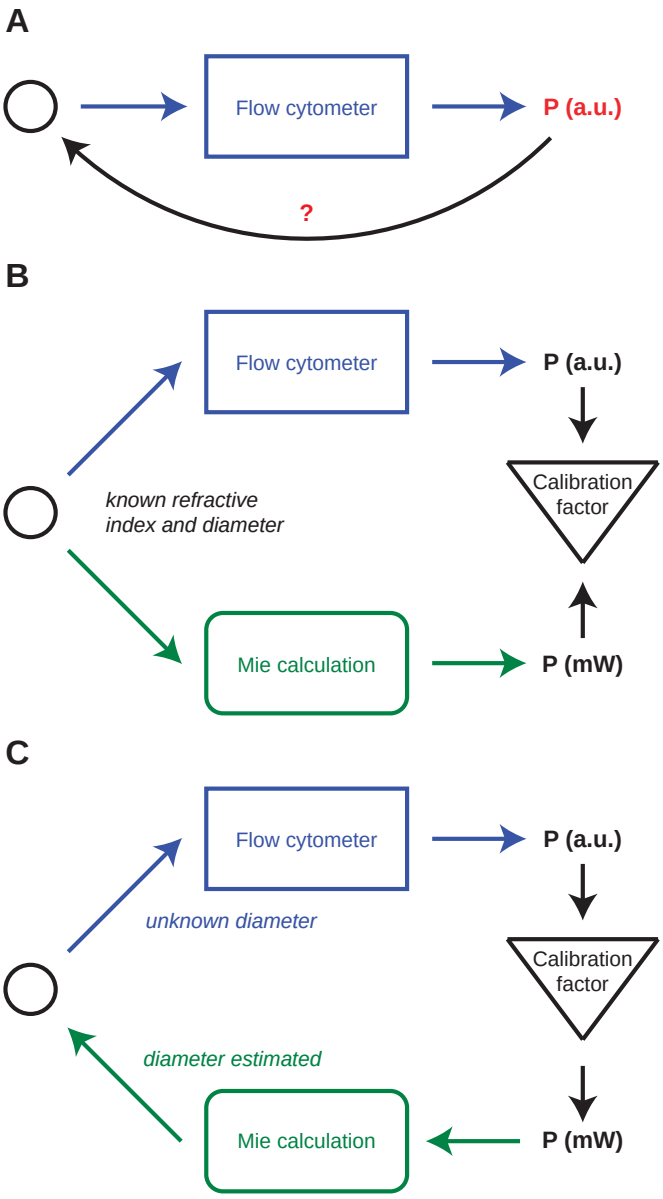

Figure 5.1: From detected scattering power to vesicle diameter. (A) The relationship between the vesicle (circle) diameter and the detected scattering power P in arbitrary units (a.u.) is unknown. (B) From beads (circle) with known diameter and refractive index, the scattering power P (a.u.) can be measured. In parallel, the true scattering power P (mW) can be calculated by Mie theory to obtain the calibration factor, which relates the detected scattering power to the calculated scattering power. (C) By use of the calibration factor, it is possible to convert the detected scattering power of any spherical particle to the scattering power and apply Mie calculations to estimate the particle diameter.

vesicles is unknown, as illustrated in Fig. 5.1A. To establish this relationship, we measured the relative power in arbitrary units (a.u.) and, in parallel, calculated the absolute power (mW) of light that scattered by beads of known diameter and refractive index in the direction of the detectors. Fig. 5.1B shows that this approach enables us to obtain a calibration factor that relates the detected to the calculated scattering power. The calibration factor is thus a property of the detector and the optical configuration of the instrument, and is independent of the sample. Fig. 5.1C shows that this calibration factor allows estimation of the true diameter of the particle. Note that the calculated scattering power depends on the estimated illumination intensity (Table 5.2). However, as the detected scattering power is fitted to the calculated scattering power by use of the calibration factor, the relationship between the detected scattering power and the diameter of vesicles remains similar for any value of the illumination intensity.

5.2.6 Tunable Resistive pulse sensing

To estimate the concentration of vesicles in cell-free urine, tunable resistive pulse sensing (Izon qNano, Christchurch, New Zealand) was applied. The thawed cell-free urine was diluted 1:10 with PBS. At least 1,000 vesicles were counted at a pressure of 6.9 mbar, using both NP100A and NP400A nanopores, which are optimized for the detection of particles with diameters ranging from 50 nm to 200 nm and 200 nm to 800 nm, respectively.

5.3 Results

5.3.1 Flow cytometry detects vesicles smaller than 220 nm

Fig. 5.2A shows a TEM image of vesicles from urine and Fig. 5.2B their determined size distribution. The largest vesicles had a diameter of 295 nm. As the diameter of the smallest polystyrene beads that can be detected by commercial flow cytometers is typically between 200 nm and 300 nm [58, 253, 227], and because vesicles have a lower refractive index than polystyrene beads, we would not expect these urinary vesicles to be detected by flow cytometry.

Fig. 5.3A,B shows the FSC and SSC histograms of the same urine sample measured with flow cytometry. Both histograms show a peak, indicating that vesicles were detected. To exclude the possibility that vesicles larger than 300 nm were present, urine was subsequently filtered with a 220 nm filter (MilliPore) before analysis. Fig. 5.3C,D shows that, after filtration, FSC and SSC histograms of vesicles were still obtained, although at fewer counts per minute than with the unfiltered sample. Thus, in contrast to our expectations, flow cytometry detected vesicles smaller than 220 nm.

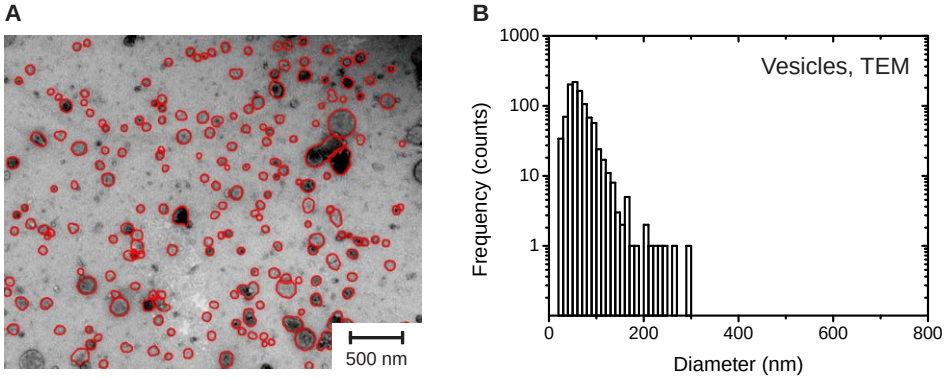

Figure 5.2: Vesicle detection by transmission electron microscopy (TEM). (A) TEM image of urinary vesicles. The red circles indicate the surface areas of spherical objects. (B) Size distribution (logarithmic vertical scale) of 1,000 vesicles determined from five TEM images. The plot shows a distribution with vesicle diameters between 25 nm and 295 nm, with a single peak at 55 nm.

5.3.2 Scattering power of beads

Fig. 5.4A,C shows FSC histograms of polystyrene beads and silica beads, respectively. The distributions of beads with a diameter smaller than 1,000 nm are broad and overlapping. Thus, FSC was unable to resolve the diameter of particles smaller than 1,000 nm. Fig. 5.4B,D shows the SSC histograms of polystyrene beads and silica beads, respectively. As the SSC distribution of light scattered by beads was narrow, they could be distinguished from each other. Thus, for our flow cytometer, SSC is more suitable than FSC for resolving particles with a diameter smaller than 1,000 nm. As the 102 nm polystyrene beads and the 89 nm silica beads could not be detected, the smallest detectable polystyrene beads and silica beads were 203 and 204 nm, respectively. However, not all 204 nm silica beads were detected. As the flow rate was known, the bead concentration could be calculated and compared with the true concentration. The ratio between the measured and the true concentration is defined as the detection efficiency. For the 204 nm silica beads, the detection efficiency was 0.6 ± 0.2. Table 5.1 shows that the detection efficiency of all other beads was close to 1, meaning that single polystyrene beads and silica beads with diameters of 203 and 389 nm, and larger, could be detected.

5.3.3 Smallest detectable single vesicles

To establish the relationship between the detected scattering power and the diameter of vesicles, the flow cytometer needs to be calibrated, as shown in Fig. 5.1. Therefore, the histograms from beads in Fig. 5.4 were fitted with a normal distribution to determine the mean scattering power and standard deviation for each bead diameter. The detected scattering power is provided in arbitrary units, and is proportional to the absolute scattering power (mW), which was calculated by

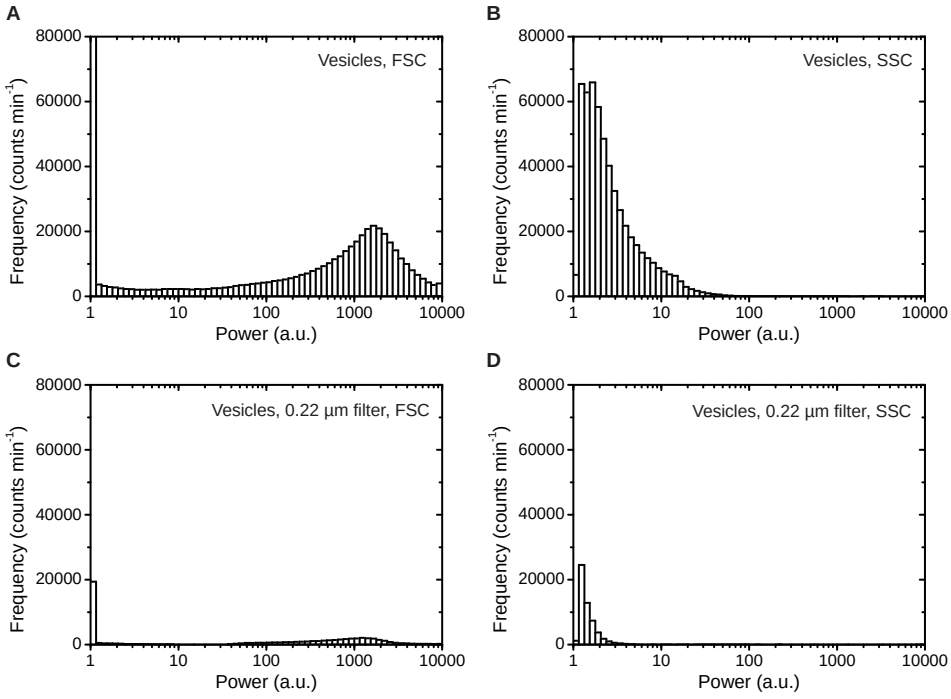

Figure 5.3: Vesicle detection by flow cytometry. (A) Forward-scattered light (FSC) histogram (logarithmic horizontal scale) of urinary vesicles. A flat peak is observed. In total, $5.5 \cdot 10^5$ events were counted during 1 min. (B) Side-scattered light (SSC) histogram of urinary vesicles. A single peak is observed. (C) FSC histogram of urinary vesicles filtered through a 220 nm filter. A flat peak is observed. In total, $5.7 \cdot 10^4$ events were counted during 1 min. (D) SSC histogram of urinary vesicles filtered through a 220 nm filter. A single peak is observed. a.u., arbitrary units.

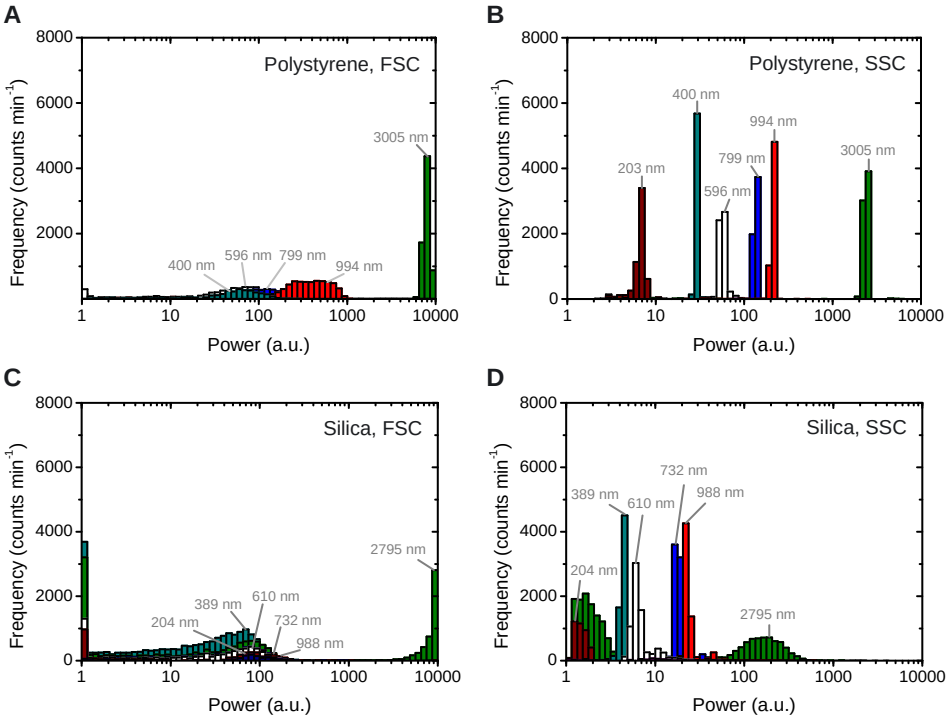

Figure 5.4: Forward-scattered light (FSC) and side-scattered light (SSC) histograms (logarithmic horizontal scale) for polystyrene beads (A, B) and silica beads (C, D) of known diameters and at a concentration $1 \cdot 10^5$ mL^{-1}. The FSC distributions from beads with a diameter smaller than 1,000 nm are broad and overlapping, whereas the SSC distributions for the same beads are narrow and can be distinguished from each other. a.u., arbitrary units.

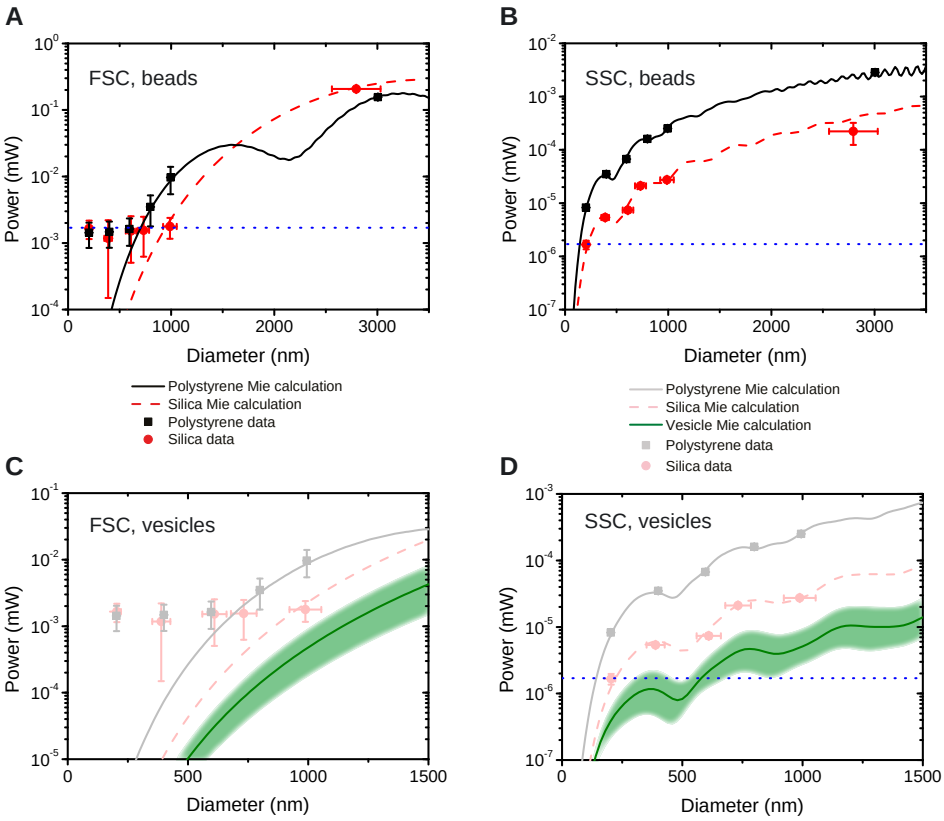

Figure 5.5: Relationship between the measured light-scattering power of beads and the diameter of vesicles. (A) Measured (symbols) and calculated (lines) forward-scattered light (FSC) power (logarithmic scale) vs. diameter for polystyrene beads (black) and silica beads (red). Data points corresponding to a power higher than $1.7 \cdot 10^{-3}$ mW (dotted blue line) are in agreement with theory. The trough at 2,140 nm for the calculation of polystyrene beads is caused by a Mie resonance. (B) Measured and calculated side-scattered light (SSC) power vs. diameter for polystyrene beads and silica beads. The power increases with increasing particle diameter and refractive index. The detection limit is $1.7 \cdot 10^{-6}$ mW (dotted blue line). (C) Measured and calculated FSC power vs. diameter for polystyrene beads (gray), silica beads (transparent red), and vesicles (green). The light green area around the Mie calculation for vesicles is a calculated confidence interval, which is based on an assumed inner refractive index of biological vesicles of 1.38 ± 0.02. The FSC power increases with increasing particle diameter, and is lower for vesicles than for beads. (D) Measured and calculated SSC power vs. diameter for polystyrene beads, silica beads, and vesicles. The intersection of the detection limit with the Mie calculation for vesicles gives the range of smallest single vesicles that can be detected by the FACSCalibur (blue dotted line), which is 300–700 nm. The calculation parameters are listed in Table 5.2.

Mie theory. For our instrument, the calibration factors that relate the measured to the calculated scattering power are $2.07 \cdot 10^5$ for the FSC detector and $1.26 \cdot 10^6$ for the SSC detector. Fig. 5.5A shows the measured and calculated FSC power vs. the diameter of polystyrene beads and silica beads. Data points corresponding to a power higher than $1.7 \cdot 10^{-3}$ mW are in agreement with the Mie calculations. Some beads from which the scattered power was below $1.7 \cdot 10^{-3}$ mW were detected by FSC, but the observed power was not related to the size of the beads. Fig. 5.5B shows the measured and calculated SSC power vs. diameter for polystyrene beads and silica beads. The power increased with increasing particle diameter and refractive index. The data are in excellent agreement with the Mie calculations, except for the 2,795 nm silica beads. We attribute the underestimation of the scattered power of 2,795 nm silica beads to a decreased refractive index resulting from porosity, as stated by the manufacturer. The effective refractive index of the porous 2,795 nm silica beads that matches with our measurement is 1.423 rather than 1.445. The power corresponding to the smallest detectable beads is defined as the detection limit, which is $1.7 \cdot 10^{-6}$ mW, meaning that each single vesicle for which the SSC power was equal to or higher than $1.7 \cdot 10^{-6}$ mW would be detected.

Now the diameter of the smallest detectable single vesicles by flow cytometry can be assessed. Fig. 5.5C is a close-up of the lower part of Fig. 5.5A, extended with the calculated FSC power of vesicles. Note that the vesicles scatter light less efficiently than beads, owing to their lower refractive index. As the exact refractive index of vesicles is unknown, the light green area represents an estimated confidence interval, which is based on an assumed inner refractive index of biological vesicles of 1.38 ± 0.02. Fig. 5.5D is a close-up of the lower part of Fig. 5.5B, extended with the calculated SSC power of vesicles. As the detection limit is $1.7 \cdot 10^{-6}$ mW, the estimated diameter range of the smallest detectable single vesicle is 300−700 nm, which contradicts our finding that vesicles smaller than 220 nm can be detected by flow cytometry (Fig. 5.3).

5.3.4 Detection of vesicles smaller than 220 nm and 89 nm silica beads

We hypothesize that the detection of vesicles smaller than 220 nm is a consequence of swarm detection; that is, multiple vesicles are simultaneously illuminated by the laser beam and counted as a single event signal. Fig. 5.6 shows an artist impression of swarm detection. As a proof of principle, silica beads with a diameter of 89 nm, significantly below the 203 nm of single detectable beads, were prepared at a concentration of 10^{10} /mL and successfully detected, as reflected by the SSC histogram shown in Fig. 5.7A. Thus, 89 nm beads with a refractive index close to that of vesicles can also be detected by flow cytometry at sufficiently high concentrations, owing to swarm detection.

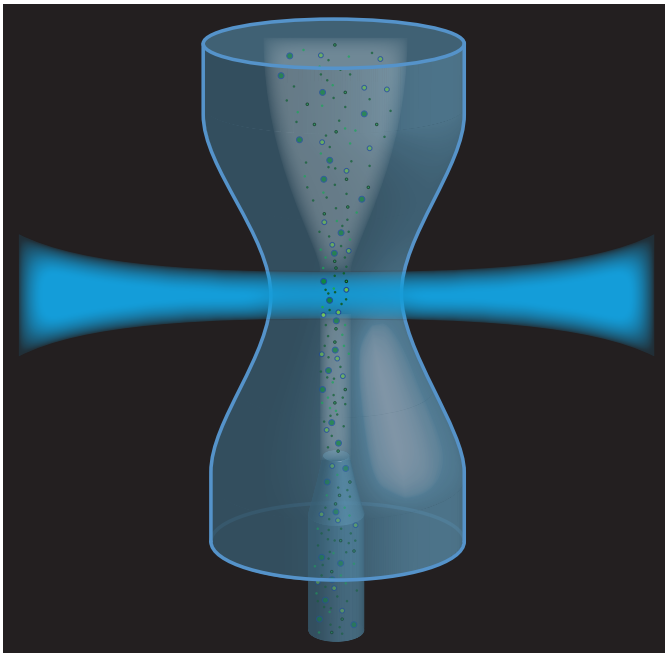

Figure 5.6: Artist impression of swarm detection. A flow cytometer guides vesicles (green dots) through a laser beam (horizontal blue cone) in a hydrodynamically focused fluid stream (vertical gray cone). Due to the small size and high concentration of vesicles relative to the dimensions of the laser beam, multiple vesicles are simultaneously illuminated.

5.3.5 Single bead detection versus swarm detection

For polydisperse samples, such as vesicles in plasma and urine, it is interesting to know whether a count is generated by one large particle or by multiple small particles present in the laser beam. Here, a large or a small particle is defined as a particle scattering more or less light, respectively, than the detection limit of the flow cytometer. Consequently, the presence of one large particle or of multiple small particles in the laser beam will both be counted as a single event signal. Fig. 5.7B shows the SSC histogram of a mixture of small 89 nm silica beads with a concentration of 10^{10} /mL and large 610 nm silica beads with a concentration of 10^5 /mL. The first peak is attributed to the high concentration of 89 nm beads, and the second peak is attributed to the 10^5-fold lower concentration of 610 nm beads. Considering the low concentration of 610 nm beads as compared with that of the 89 nm beads, it is clear that the count rate is dominated by the large particles.

Dilution series are used to investigate the relative contributions of large and small particles to the count rate of the flow cytometer. Fig. 5.7C shows the dilution curves of different ratios of 89 nm and 610 nm silica beads. The horizontal axis represents the sum of the prepared concentrations of 89 nm and 610 nm silica beads. The left vertical axis shows the count rate (frequency) as determined by the flow cytometer. As the flow rate was known, the concentration as determined by the flow cytometer was also calculated, and is shown on the right vertical axis. First, with large 610 nm beads only, the flow cytometer-determined concentration obviously equaled that of the prepared concentration, and, within the acquisition

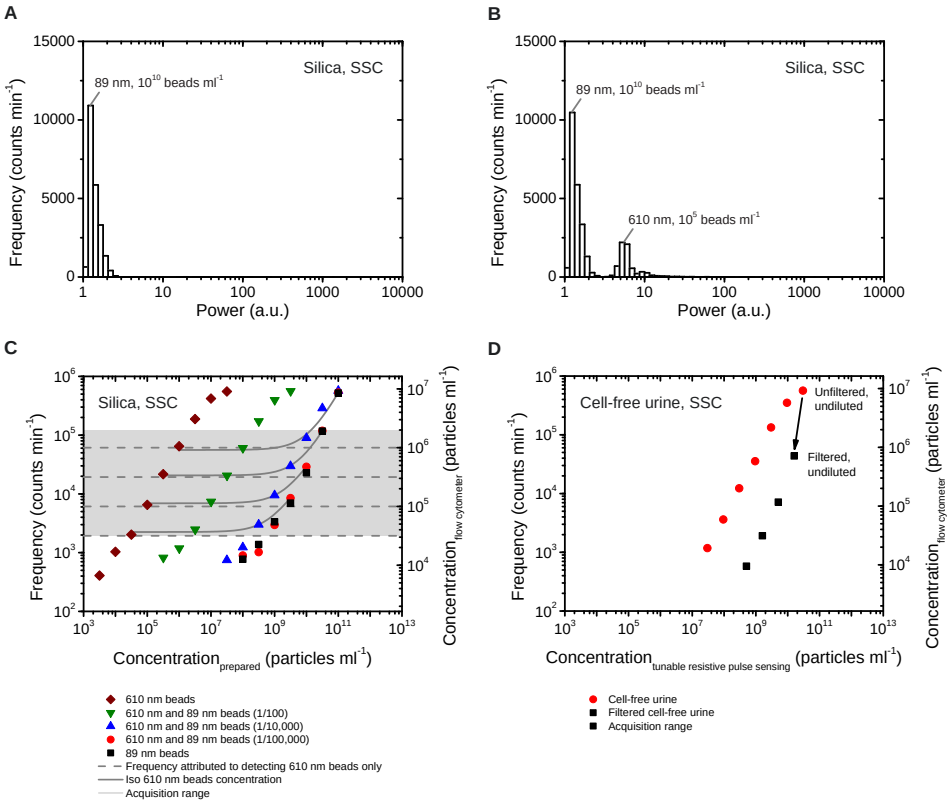

Figure 5.7: Relative contributions of mechanisms underlying vesicle detection. Side-scattered light (SSC) histogram (logarithmic horizontal scale) for (A) 89 nm silica beads at a concentration of $1 \cdot 10^{10}$ mL^{-1}, and (B) a mixture of 89 nm and 610 nm silica beads at concentrations of $1 \cdot 10^{10}$ mL^{-1} and $1 \cdot 10^{5}$ mL^{-1}, respectively. (C) Frequency or count rate vs. total concentration (logarithmic scales) of 610 nm silica beads (diamonds), 89 nm silica beads (squares), mixtures of 610 nm and 89 nm silica beads prepared at ratios of 1:100 (green triangles), 1:10,000 (blue triangles), and 1:100,000 (circles), and (D) cell-free urine and cell-free urine filtered (arrow) through a 220 nm filter. The right vertical axis shows the concentration as determined with the flow cytometer. Data points within the acquisition range (gray area) should be considered reliable. The error bars overlap with the symbols and are omitted to improve legibility. The dashed horizontal lines indicate the count rates corresponding to the detection of 610 nm silica beads at four different concentrations. The solid gray lines are exponential fits through data points with similar concentrations of 610 nm silica beads. a.u., arbitrary units.

range (gray area), the relationship between count rate and concentration was linear (dark red diamonds). Second, after addition of 100 beads of 89 nm to each 610 nm bead, the flow cytometer-determined concentration remained similar to that of the samples containing 610 nm beads only (dashed horizontal lines), meaning that, at this concentration, the 89 nm beads had no influence on the count rate (green triangles). Third, if we added 10,000 beads of 89 nm to each 610 nm bead, the flow cytometer-determined concentration increased by 40 %, on average, in comparison with the samples containing 610 nm beads only (blue triangles), and with addition of 100,000 beads of 89 nm to each 610 nm bead, the flow cytometer-determined concentration increased by 350 %, on average, in comparison with the samples containing 610 nm beads only (red circles). For the latter mixture, the relationship between count rate and prepared concentration is non-linear, as indicated by the increased slope, and the data overlap with those of the pure 89 nm beads (black squares), indicating that the count rate is dominated by the simultaneous presence of multiple 89 nm beads in the laser beam.

5.3.6 Single vesicle detection versus swarm detection

Fig. 5.7D shows the dilution curves of cell-free urine and cell-free urine filtered through a 220 nm filter. With tunable resistive pulse sensing (data not shown), the concentrations of vesicles in unfiltered and filtered cell-free urine were estimated to be $3.0{\cdot}10^{10}$ /mL and $1.6{\cdot}10^{10}$ /mL, respectively. For cell-free urine, the relationship between the count rate and the concentration is linear, meaning that the counts are predominantly caused by single large vesicles. However, the dilution curve of the filtered cell-free urine reveals that small vesicles also contribute to the count rate (Fig. 5.7D). The relationship between count rate and concentration of filtered cell-free urine is non-linear, as indicated by the increased slope, confirming that the counts are caused by swarm detection.

5.4 Discussion and conclusion

We have developed a model that relates the measured light scattering power to the diameter of single vesicles by combining measurements on polystyrene beads and silica beads with Mie calculations. Two mechanisms for vesicle detection by flow cytometry can be derived from the results. First, a single vesicle is counted if its diameter is larger than 300−700 nm, i.e. the smallest detectable single vesicle diameter estimated for our flow cytometer. Second, a swarm of multiple smaller vesicles is counted as a single event signal if the power of light scattered by all vesicles that are simultaneously present in the laser beam exceeds the detection limit. For polydisperse samples, such as vesicles in plasma and urine, counts are generated by a combination of single particle and swarm detection.

If large and small particles are defined as particles scattering more or less light than the detection limit of the flow cytometer, single particle detection is caused by large particles only. As every large particle is counted (Table 5.1), the concentra-

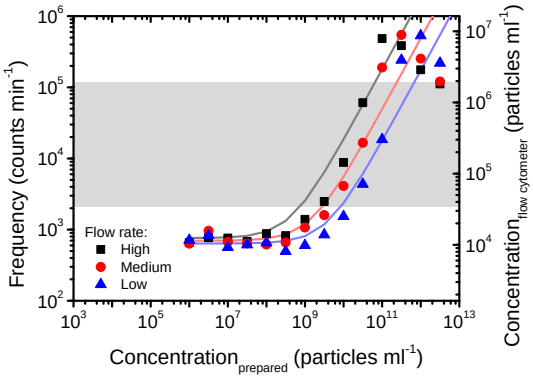

Figure 5.8: Flow rate dependency of swarm detection. Frequency or count rate vs. total concentration of 89 nm silica beads at high (63 µL min^{-1}; squares), medium (37 µL min^{-1}; circles) and low (12 µL min^{-1}; triangles) flow rates. The solid lines are linear fits through the data points below the maximum acquisition range. The right vertical axis shows the concentration as determined by the flow cytometer. Data points within the acquisition range (gray area) should be considered reliable. The error bars overlap with the symbols. SSC, side-scattered light.

5

tion as determined by the flow cytometer equals the prepared concentration, and a linear relationship between count rate and prepared concentration is obtained, as demonstrated with the use of large 610 nm silica beads only (Fig. 5.7C).

Swarm detection, on the other hand, is caused by the detection of small particles only. As multiple small particles have to be simultaneously present in the laser beam to generate a single event signal, the flow cytometer-determined concentration underestimates the real concentration, and the relationship between count rate and prepared concentration is non-linear. Although the diameters of the smallest detectable single polystyrene and silica beads are 203 nm and 204 nm, respectively, we demonstrated that we could detect high concentrations of 89 nm silica beads (Fig. 5.7A) and vesicles filtered through a 220 nm filter (Fig. 5.3C,D), owing to swarm detection. For both samples, the flow cytometer-determined concentration is more than 1,000-fold lower than the real concentration (Fig. 5.7C,D), and the relationship between count rate and concentration is non-linear. As the detection limit of the flow cytometer is $1.7 \cdot 10^{-6}$ mW and the mean SSC powers of an 89 nm silica bead and a urinary vesicle are $2.2 \cdot 10^{-8}$ mW and $1.1 \cdot 10^{-8}$ mW, respectively, at least 80 silica beads or 160 vesicles have to be simultaneously present in the laser beam to generate a signal. For both samples, this requirement was fulfilled, as the estimated volume of the laser beam is 54 pL and the concentrations of silica beads and vesicles are 10^{10} /mL and $1.6 \cdot 10^{10}$ /mL, respectively, so that, on average, 540 silica beads or 860 vesicles were simultaneously present in the beam. Fig. 5.8 shows the dilution curves of 89 nm silica beads for high, medium and low flow rates. Within the acquisition range (gray area), the established concentration underestimates the prepared concentration, and the relationship between count rate and prepared concentration is non-linear. As a lower flow rate yields a smaller cross-sectional area of the sample stream and thus a smaller effective beam volume [266], a higher concentration of 89 nm silica beads is required to generate

an event signal. Consequently, the dilution curves in Fig. 5.8 are shifted to the right with decreasing flow rates.

For samples containing a mixture of large and small particles, such as vesicles in plasma and urine, counts are generated by both single particle and swarm detection. If the concentration of small particles is lower than the threshold for generation of a signal, the count rate is dominated by large particles, and a linear relationship between count rate and concentration is obtained (Fig. 5.7C). However, if the concentration of small particles equals or exceeds the threshold for generation of a signal, the contribution of small and large particles to the count rate depends on the relative size and concentration of particles (Fig. 5.7C). For cell-free urine, we have shown that small vesicles contribute to the count rate by using a 220 nm filter. Without filtration, a fairly linear relationship between the count rate and the concentration is obtained, indicating that large vesicles, i.e. vesicles larger than 300−700 nm, are present. Vesicles larger than 295 nm were not observed by TEM imaging (Fig. 5.2), probably because the amount of imaged vesicles did not represent the full population, and because the diameter was affected by preanalytic factors, such as centrifugation, staining, fixation, and adhesion [333]. Note that the concentration as determined by the flow cytometer is 1,000-fold lower than the concentration estimated with tunable resistive pulse sensing, which was observed when flow cytometry was compared with other, novel detection methods [335, 124]. The presence of multiple vesicles in the laser beam explains why the concentration is underestimated 1,000-fold, but, more importantly, swarm detection allows the detection of smaller vesicles than previously thought possible.

5.4.1 Sensitivity increases with collection angle

Although it is often thought that FSC should be used to determine the size of vesicles [179, 58, 254, 298, 178], Fig. 5.4A–D shows that, for our flow cytometer, the SSC detector is more sensitive and has a higher capability to resolve the size of beads than the FSC detector, as confirmed by other groups using instruments with a similar optical layout [266, 298, 90]. In this section, we will explain this phenomenon. Fig. 5.9 shows the optical detection geometry of a flow cytometer (A) and how this affects the detection of light scattered by a cell (B), a microvesicle (C), or an exosome (D). Each cell, microvesicle or exosome is illuminated by a laser beam with a constant intensity, which we estimate to be $1.4 \cdot 10^7\,\mathrm{Wm}^{-2}$. The FSC detector is a photodiode that detects light which is scattered under an angle of approximately 0.5−7°, depending on the setup of the instrument. To prevent the laser directly illuminating the FSC detector, both the laser beam itself and the light scattered under an angle smaller than 0.5° are blocked by the so-called obscuration bar, as indicated by the interruption in the red line. The SSC detector is a photomultiplier tube, which is not only more sensitive than the photodiode of the FSC detector, but also detects scattered light over a much broader angle, i.e. 47−133°. The dashed blue lines inside the gray circular diagrams show how much light is scattered in each direction. Fig. 5.9B shows that a cell with a diameter of

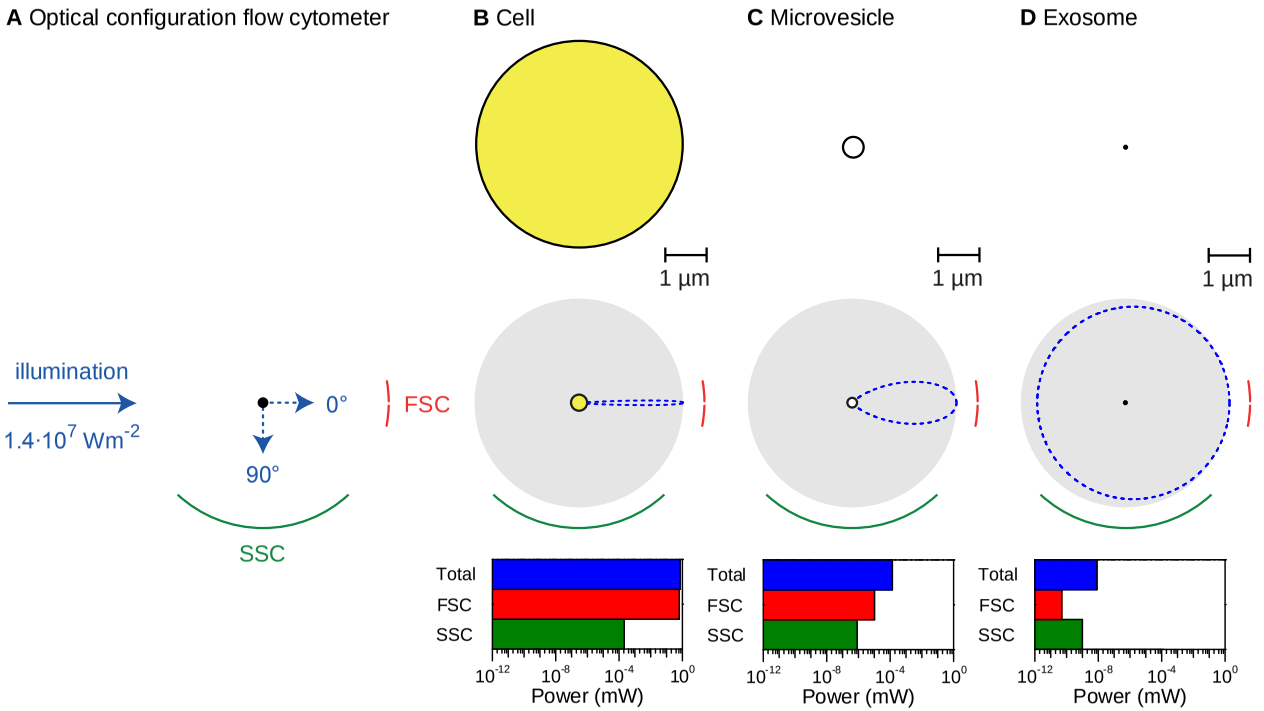

Figure 5.9: Optical detection geometry of the FACSCalibur and the angular intensity distribution of light scattered by a single cell, a microvesicle, or an exosome. (A) A particle (black dot) is illuminated by a laser beam (blue solid arrow). Forward-scattered light (FSC) and side-scatterered light (SSC) are collected between 0.5° and 7° (red lines) and between 47° and 133° (green line), respectively. The gray circular diagrams show the angular intensity distribution (blue dashed line) of perpendicularly polarized light scattered by a cell (yellow circle) with diameter 5 µm (B), a microvesicle (white circle) with diameter 500 nm, and an exosome (black dot) with diameter 50 nm (C). The scattering angle becomes wider for decreasing cell or vesicle diameters. The bar plots at the bottom show the power (logarithmic scale) scattered in all directions (blue), the power scattered in the FSC direction (red), and the power scattered in the SSC direction (green). The calculation parameters are listed in Table 5.2.

5 µm scatters light predominantly in the forward direction, which is in the direction of the FSC detector. Hence, FSC is associated with cell size. Fig. 5.9C shows that a microvesicle with a diameter of 500 nm scatters light differently than a cell, i.e. mainly under an angle of 0−10°. In comparison with the cell, the fraction of light scattered in the direction of the FSC detector has decreased, whereas the fraction of light scattered in the direction of the SSC detector has increased. Fig. 5.9D shows that an exosome with a diameter of 50 nm scatters light nearly isotropically. As a result, more light is scattered in the direction of the SSC detector than in the direction of the FSC detector. As organelles are of a similar size as microvesicles and exosomes, an increased SSC is commonly associated with the complex anatomy of cells. In fact, the SSC detector is optimized to detect scattering from multiple particles smaller than the wavelength. Thus, to increase the sensitivity for vesicle detection, it is beneficial to select the detector with the largest collection angle. For most regular flow cytometers, this implies using the SSC detector.

5.4.2 Implications and limitations

Our model explains several recent observations regarding vesicle detection with flow cytometry. In an effort to standardize vesicle detection, the Scientific Standardization Committee of the International Society on Thrombosis and Haemostasis (ISTH) proposed a protocol that used 500 nm and 900 nm polystyrene beads from Megamix to define a vesicle size gate [179]. They observed that flow cytometer-determined concentrations of vesicles appeared to be consistent among instruments measuring FSC with a relatively wide solid angle (1−19°; Beckman Coulter), but appeared to be inconsistent among instruments measuring FSC with a low solid angle (0.7−10°; Becton Dickinson). The low collection angle makes the detection limit strongly dependent on the width of the obscuration bar, which is specific for each individual instrument. As vesicle detection typically takes place near the detection limit, the results differed among the Becton Dickinson instruments.

Chandler et al. applied the Megamix gating strategy to detect platelet microparticles (PMPs) on the Apogee A40, which has an FSC collection angle of 1−70°, and showed that mainly platelets, which have an average diameter of 2,000−5,000 nm [324], were counted [58]. Unlike Chandler et al., Mullier et al. and Robert et al. [212, 254] could perfectly distinguish PMPs from platelets by using the same gating strategy on their flow cytometers, which all had an FSC collection angle below 19°. To explain this discrepancy and to show that our calibration procedure is generally applicable, we have determined the calibration factors for the FSC detectors of the Apogee A40 and the Beckman Coulter FC500 by using their data [58, 254]. Fig. 5.10A,B shows the diameters of single vesicles as selected by the Megamix gating strategy for the Apogee A40 and FC500, respectively. The range of diameters of single vesicles gated on theApogee A40 is 200 nm larger than the range gated on the FC500. Owing to the wider collection angle of the Apogee A40 than of the FC500, the Apogee A40 is more sensitive to the difference in refractive index between polystyrene beads and vesicles than the FC500. Nevertheless, single PMPs are not expected to appear in the gated range

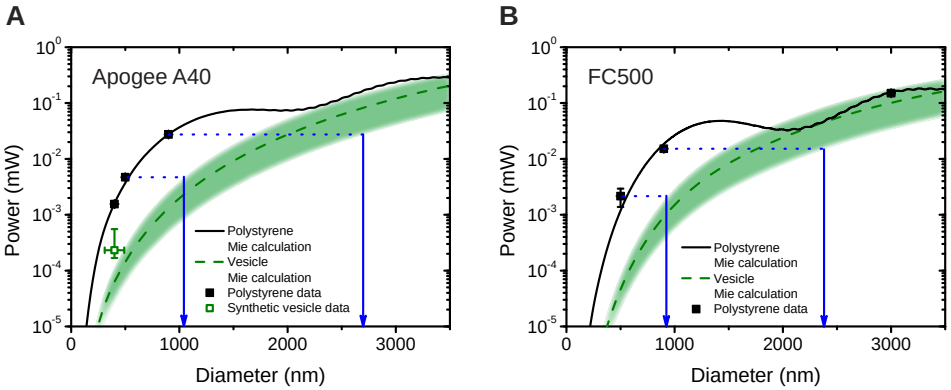

Figure 5.10: Selected vesicle diameter range obtained by applying the Megamix gating strategy on the Apogee A40 vs. the FC500. (A) Measured (symbols) and calculated (lines) forward-scattered light (FSC) power (logarithmic scale) vs. diameter for polystyrene beads (black) and vesicles (circle), for the Apogee A40. The measured data points are adopted from Chandler et al. [58]. The obtained calibration factor is $2.67 \cdot 10^6$. The Megamix gating strategy would select single vesicles with a diameter between 1,000 nm and 2,700 nm. (B) Measured and calculated FSC power vs. diameter for polystyrene beads and vesicles for the FC500. The measured data points are adopted from Robert et al. [254]. The obtained calibration factor is $5.18 \cdot 10^4$. The Megamix gating strategy would select single vesicles with a diameter between 800 nm and 2,400 nm. The calculation parameters are listed in Table 5.2.

for either the Apogee A40 or the FC500, as the measured PMP diameter is far below 500 nm [335, 124, 90]. Rather, it is the presence of multiple PMPs in the laser beam that makes them detectable by flow cytometry. From reference measurements with novel methods, we know that the concentration of PMPs exceeds 10^{10} /mL [90], which ensures that multiple vesicles are illuminated simultaneously and is sufficient to generate a single event signal.

For functional research on vesicles, the presence of multiple vesicles in the beam may have major consequences. For example, different fluorescence signals corresponding to a 'single event signal' may originate from multiple vesicles, each containing a different antibody, which may explain the colocalization of granulocyte (CD66e) and platelet (CD61) markers on tissue factor-exposing vesicles [84]. On the other hand, as all vesicles contribute to the signal, our findings explain why flow cytometry results often correlate with disease.

Our work may lead to a better understanding of vesicle detection by flow cytometry, increased sensitivity by optimizing the instrument-specific settings, and improvements in the standardization of measurements between laboratories, which involves at least four steps. First, the scattering power of beads should be measured for the detector with the largest collection angle and highest sensitivity. Second, the scattering power of beads should be calculated specifically for the used detector by Mie theory. Third, the calibration factor should be determined to quantify the detection signal. Fourth, a gate should be selected on the basis of the quantified optical power. For improved standardization, the relationship between the detected scattering power from multiple vesicles, the volume of the laser beam and the flow rate requires further investigation. For improved vesicle detection, we suggest modification of the hardware of the flow cytometer [278], and study of the refractive index of vesicles and the medium. In addition, as many studies also use fluorescence to identify vesicles, we suggest performing a detailed analysis on fluorescent beads, although many non-trivial practical and theoretical problems will have to be solved before a comparable study based on fluorescence can be performed [235]. In spite of its limitations, flow cytometry will still have to be the present method of choice, because we do not yet have validated methods for quantitative enumeration and establishment of the cellular source of vesicles.

In conclusion, we have established a model that relates the detected scattering power to the diameter of single vesicles. The gating strategy proposed by the ISTH Scientific Standardization Committee collaborative workshop selects single vesicles and cells with diameters between 800 nm and 2,400 nm when applied on the FSC detector of regular flow cytometers. However, vesicle detection by regular flow cytometry relies on two different mechanisms: (1) detection of single, relatively large, vesicles that scatter more light than the detection limit, and (2) swarm detection - that is, multiple relatively small vesicles are simultaneously illuminated by the laser beam and counted as a single event signal. Swarm detection allows the detection of smaller vesicles than previously thought possible. It explains the finding that flow cytometry underestimates the concentration of vesicles, and it clarifies several observations published by the ISTH Scientific Standardization Committee collaborative workshop on vesicle detection.

CHAPTER 6

Refractive index determination of nanoparticles in suspension using nanoparticle tracking analysis

Abstract

The refractive index (RI) dictates interaction between light and nanoparticles, and therefore is important to health, environmental and materials sciences. Using nanoparticle tracking analysis, we have determined the RI of heterogeneous particles $< 500\,\text{nm}$ in suspension. We demonstrate feasibility of distinguishing silica and polystyrene beads based on their RI. The hitherto unknown RI of extracellular vesicles from human urine was determined at 1.37 (mean) at a wavelength of 405 nm. This method enables differentiation of single nanoparticles based on their RI.

This chapter has been published as:

- E. van der Pol, F.A.W. Coumans, A. Sturk, R. Nieuwland, and T.G. van Leeuwen. Refractive index determination of nanoparticles in suspension using nanoparticle tracking analysis. *Nano Lett.* **14**(11), 6195-6201 (2014)

6.1 Introduction

The refractive index (RI) of nanoparticles is an indispensable property in a wide range of applications and studies, but is difficult to measure [167]. The RI depends on the wavelength, and is defined as the ratio of speed of light in vacuum to speed of light in the material. It relates light scattering to the size, shape, and chemical composition of a nanoparticle [40] and it defines the magnitude of the optical force that an electromagnetic field exerts on nanoparticles [28, 250]. Determination of the RI may be utilized to differentiation between different components of samples. For example, in atmospheric particulate matter, pollen (RI $\approx$ 1.53) [62] could be distinguished from cement dust (RI $\approx$ 1.70) [99] and fly ash (RI = 1.55−1.60) [149]. In clinical samples, it may be possible to distinguish vesicles from similar-sized lipoproteins (RI = 1.45−1.60) [206], which are abundantly present in blood [108, 90]. Potential differentiation of other nanoparticles by RI include soda lime, borosilicate, calcium carbonate, aluminum oxide, aluminum silicate, diamond, gold, nickel, polymethylmethacrylate (PMMA), polytetrafluoroethylene (PTFE), bacteria, viruses, and yeast. Thus, the RI dictates the interaction between light and nanoparticles in diverse applications spanning environmental science (e.g. the effect of aerosols on climate [105, 205]), or the carbon content of plankton [282]), health (drug delivery [191, 145, 118], or photodynamic therapy [174, 257]), and materials science (nanoparticles in paint [176, 15], or solar cells [338]).

Table 6.1 shows the capabilities of current techniques for determining the RI of particles. For polydisperse particles with homogeneous RI, the most applied technique is RI matching the medium to the particles [23, 126]. However, RI matching cannot be applied to particles of biological origin due to osmotic effects. Moreover, a sample with heterogeneous RI analyzed with a technique suitable only for homogeneous RI may result in artifacts. For monodisperse particles of known size and concentration, the RI can be determined by measuring the optical extinction coefficient of multiple particles simultaneously [205, 190, 181]. Sorting on size may allow these techniques to determine the RI of polydisperse particles. However, size-based fractionation of particles $< 500\,\text{nm}$ is difficult [310] and may introduce artifacts. For samples with heterogeneous RI and unknown size distribution, the RI can be derived from single particles by measuring angle or wavelength resolved scattering, Fraunhofer diffraction, or the stiffness of an optical trap [167, 24, 64, 230, 169, 8, 168, 89, 303]. These techniques, however, have only been applied to particles $> 500\,\text{nm}$. Thus, currently no method is capable of determining RI of single nanoparticles ($< 500\,\text{nm}$) in suspension.

Consequently, the RI of extracellular vesicles $< 500\,\text{nm}$, such as exosomes, is unknown. Extracellular vesicles are biological nanoparticles that are released by cells to transport waste and exchange intercellular messages, such as DNA, RNA, or surface receptors [231]. Body fluids, but also seawater, contain typically 10^5 to 10^{10} of these vesicles per mL [90, 46, 232, 34]. Since most vesicles have specialized functions and contribute to homeostatic processes, clinical applications of vesicles are in development [231]. Fig. 6.1A shows a transmission electron microscopy

Table 6.1: Capabilities and requirements of methods to determine the refractive index (RI) of particles.

Method	References	In suspension	Diameter (µm)	Single particles	Heterogeneous diameter[1]	Heterogeneous RI[1]	Requirements
RI matching	[23, 126, 22]	+	All	−	+	−	Altering the medium
Optical extinction coefficient	[190]	+	All	−	−	−	Particle concentration and diameter
	[205, 181]	−					
Angle/wavelength resolved scattering, diffraction, optical force	[24, 64, 230]	−	> 3.0				
	[169, 8, 168]	+	> 0.5	+	+	+	
	[167, 89, 303]	+	> 1.0				

A method that is incapable or capable of providing information on the RI of single particles, particles with a heterogeneous size or RI distribution, or particles in suspension is indicated by − and +, respectively. [1] *+ heterogeneous and homogeneous possible, − only homogeneous possible.*

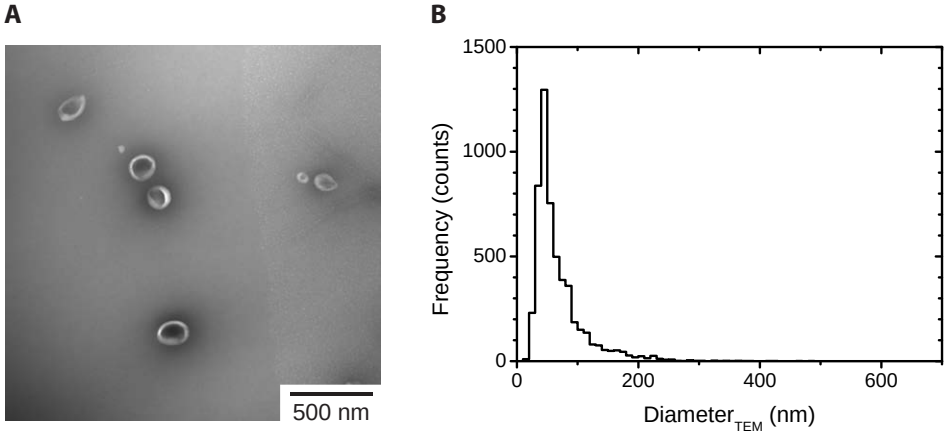

Figure 6.1: Size and morphology of urinary vesicles by transmission electron microscopy (TEM). (A) TEM image of urinary vesicles. The vesicles have a characteristic cup-shaped morphology. (B) Particle size distribution of 2,000 vesicles determined from 25 TEM images. The distribution ranges from 15 nm to 485 nm and has a single peak at 45 nm.

(TEM) image of vesicles from human urine. Sample preparation for TEM analysis and TEM analysis are extensively described in section 4.2.4. Urine contains a relatively high concentration of vesicles with low contamination of similar-sized non cell-derived particles [235]. Fig. 6.1B shows the particle size distribution (PSD) of urinary vesicles based on TEM data. The PSD ranges from 25 nm to 485 nm with a mode diameter of 45 nm. The small size and large heterogeneity of vesicles are characteristic of biological fluids and hamper their detection [232]. Please note that other biological fluids, such as blood, contain many components $< 1\,\mu$m with different RI, including protein aggregates (RI = 1.59−1.64) [206, 201], lipoproteins (RI = 1.45−1.60) [206], and viruses (RI = 1.52−1.57) [268, 221].

Currently, various optical techniques, such as flow cytometry, nanoparticle tracking analysis (NTA), and Raman microspectroscopy, are employed and improved to study vesicles in suspension [90, 235, 234, 287]. An essential property in these studies is the RI of vesicles. For example, RI determines the smallest detectable vesicle in NTA and flow cytometry, RI determines the smallest vesicle size that can be trapped with Raman microspectroscopy, and RI determines the relationship between size and scatter in flow cytometry [232]. In flow cytometry, the RI of vesicles has (accidentally) been assumed to be similar to polystyrene beads. This resulted in a gating strategy that selected vesicles with diameters from 800−2,400 nm, rather than the intended 500−900 nm [234]. The aim of this chapter is to develop a method to determine the RI of single nanoparticles in suspension and, as a proof of principle, apply the method to estimate the RI of extracellular vesicles.

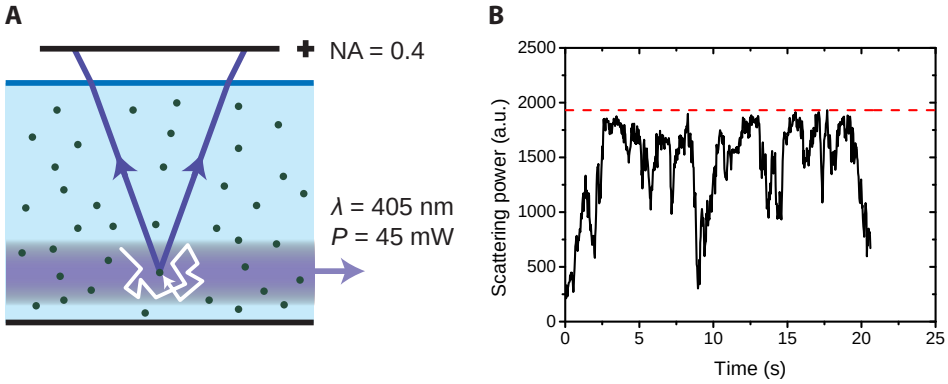

Figure 6.2: Detection of light scattered by particles undergoing Brownian motion. (A) Schematic representation of the nanoparticle tracking analysis (NTA) setup. A laser beam (purple) with a wavelength (λ) of 405 nm and a power (P) of 45 mW illuminates particles (spheres) in suspension. The particles are undergoing Brownian motion, which is the random motion (white arrow) resulting from collisions with molecules in the suspension. Light scattered by a particle is collected by a microscope objective with a numerical aperture (NA) of 0.4. (B) Scattering power versus time of a 203 nm polystyrene bead (solid) and the maximum scattering power (dashed). Due to Brownian motion the particle moves through the focal plane and the laser beam, causing the scattering power to fluctuate.

6.2 Methods and results

6.2.1 Approach

We have determined the RI by independently measuring diameter and light scattering power of individual particles with NTA and solving the inverse scattering problem with Mie theory. Fig. 6.2A schematically depicts the operating principle of the NTA. We visualized scattered light from particles illuminated by a 45 mW 405 nm laser by a dark-field microscope (NS500, Nanosight, UK). Due to Brownian motion, each particle moved randomly through the suspension. We used the trajectory of each particle in the lateral direction relative to the microscope objective to determine the diffusion coefficient, which we related to the particle diameter via the Stokes-Einstein equation [90, 46, 108]. Because the detected scattering power depends on the axial position of a particle, which changed due to Brownian motion, the detected scattering power fluctuated.

Fig. 6.2B shows a typical measurement of the scattering power versus time for a polystyrene bead with a diameter of 203 nm. Since we focused the objective onto the optical axis of the laser beam, the maximum scattering power was measured when the particle was in focus. To derive the RI, we described the measured (maximum) scattering power P from particles in focus by the theoretical scattering cross section σ_{Mie} from Mie theory [40] using the measured particle diameter as input to the calculation. Mie theory, extensively described by Bohren and Huffman

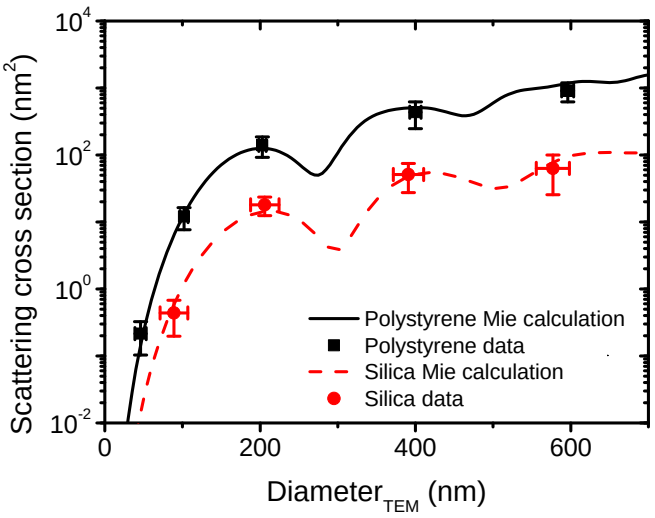

Figure 6.3: Measured (symbols) and calculated (lines) scattering cross section versus diameter for polystyrene beads (black) and silica beads (red). The scattering cross section increases with increasing particle diameter and refractive index. The particle diameters are determined by transmission electron microscopy (TEM). Error bars indicate one standard deviation of the mean.

[40], provides an analytical solution of Maxwell's equations and describes light scattering of spheres of all size parameters. However, Mie theory does not reduce these variables to a single equation, since the solution to Maxwell's equations are infinite series expansions of the electromagnetic fields. We use the Matlab Mie scripts of Mätzler [199] to calculate the infinite series and obtain the amplitude scattering matrix elements, which describe the relation between the incident and scattered field amplitudes of a sphere. Our model incorporates particle diameter and RI, RI of the medium, and wavelength, polarization, and collection angles of the microscope (see Appendix D).

6.2.2 Calibration

To calibrate the NTA instrument, we measured the scattering power of polystyrene beads P_{PS} of known size and calculated the scattering cross section of polystyrene spheres σ_{Mie}^{PS}. The RI of bulk polystyrene is 1.633 at 405 nm [161]. We measured P_{PS} for monodisperse populations of beads (Nanosphere, Thermo Fisher, MA) with a mean diameter of 46 nm, 102 nm, 203 nm, 400 nm, and 596 nm and a concentration of 10^8 beads/mL. For each diameter, 5 videos of 30 s were captured with NTA v2.3.0.17 software (Nanosight) and at least 100 particles were tracked. Since the scattering power of the beads differs more than 3 orders of magnitude, each sample required different camera settings (see Appendix C) to prevent pixel saturation. The videos contain 8-bit images of 640 by 480 pixels, which were processed with scripts by Blair and Dufresne [38] in Matlab (v7.13.0.564) to track the particles (see Appendix C). From the trajectory of each particle, we calculated the mean square displacement and diffusion coefficient and related it to particle diameter via the Stokes-Einstein equation. Furthermore, the script determined the maximum scattering power of each particle within its trajectory and corrected

for the applied shutter time and camera gain. An increase in minimum tracklength increases the precision of the measured diameter and scattering power, but also reduces the number of analyzed particles. After the analysis described in Appendix C, we required a minimum tracklength of 30 frames. We performed all measurements at 22.0 °C and assumed a medium viscosity of 0.95 cP. To take into account the illumination irradiance and transmission efficiency, the median of P_{PS} was scaled onto σ_{Mie}^{PS} by a least square fit. The resulting scaling factor is 0.067, which is a property of the instrument that we will use throughout this chapter to scale P to σ. Fig. 6.3 shows P_{PS} and σ_{Mie}^{PS} versus particle diameter. The data and theory show good agreement, with a coefficient of determination $R^2 = 0.997$.

6.2.3 Validation

To validate our approach, we have measured the scattering cross section of monodisperse populations of silica beads (Kisker Biotech, Germany) with a diameter of 89 nm, 206 nm, 391 nm, and 577 nm and a concentration of 10^8 beads/mL, as shown in Fig. 6.3. Since the RI of silica beads (RI_{Si}) is not exactly known, we performed a least square fit between the scattering cross section of silica beads σ_{Mie}^{Si} and the data. We found a RI_{Si} of 1.432, which is in between 1.43 and 1.45 of previous estimates [167, 127], confirming that NTA can be used to determine the RI of nanoparticles.

To further validate the method, we determined the PSD and RI distribution of a mixture of 203 nm polystyrene beads and 206 nm silica beads with a concentration of 10^8 beads/mL for both populations. We captured 20 videos of 30 s to track at least 1,000 particles. Data were processed as described above. Fig. 6.4A shows the measured σ versus bead diameter. Each dot represents a single particle, and two populations of beads are clearly discernible. As a reference, the grey lines show σ_{Mie} for seven RIs between 1.35 and 1.65. Fig. 6.4B shows the bead mixture PSD obtained by NTA fitted by a Gaussian distribution, which resulted in a size of 213 ± 25 nm (mean ± standard deviation). As a reference, the vertical bar shows the diameter of the silica beads determined by TEM, which is 206 ± 18 nm. We attribute the overestimation of the mean diameter to the uncertainty in the measured diffusion coefficient and to the difference between the hydrodynamic diameter measured by NTA and the physical diameter measured by TEM.

Fig. 6.4C shows the RI distribution of the bead mixture and a fit of two Gaussian distributions. We could clearly distinguish silica beads from similar-sized polystyrene beads. We obtained an RI_{Si} of 1.447 ± 0.021 (mean ± standard deviation), which is close to 1.432 as derived from Fig. 6.3 and in between 1.43 and 1.45 of previous estimates [167, 127]. For the RI of polystyrene beads (RI_{PS}) we obtained 1.665 ± 0.046, which is between 1.59 and 1.68 of previous estimates [205, 161]. Previous estimates with other techniques resulted in standard deviations of RI_{PS} between 0.011 and 0.027, [167, 205, 181] which is lower than our result. However, those techniques could not detect single particles < 500 nm, nor particles with a heterogeneous RI. The precision of RI_{PS} measurements with NTA is approximately 2-fold larger than literature values. We expect that the precision

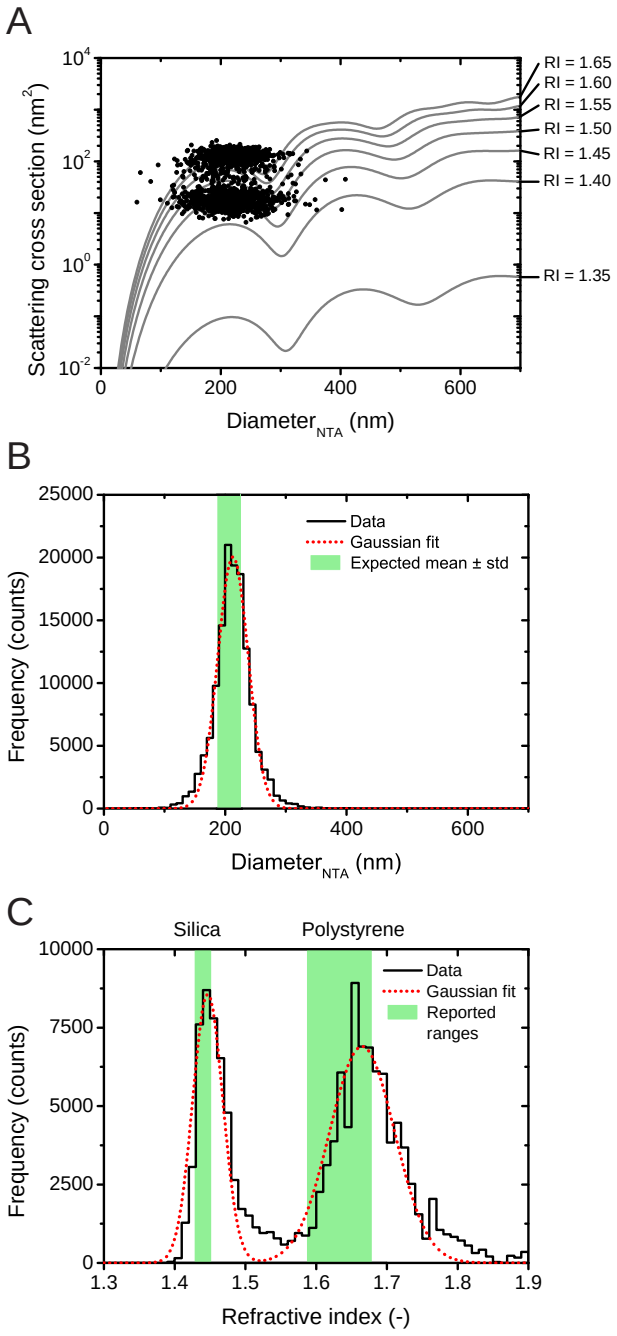

Figure 6.4: Size and refractive index (RI) determination of a mixture of 203 nm polystyrene beads and 206 nm silica beads in water by nanoparticle tracking analysis (NTA). (A) Scattering cross section versus diameter calculated by Mie theory (lines) and measured for the bead mixture (dots). (B) Particle size distribution of the bead mixture (solid line) fitted by a Gaussian function (dotted line; offset $f_0 = 0$, mean $\mu = 213$ nm, standard deviation $SD = 25$ nm, area $A = 1.26 \cdot 10^6$). The vertical green bar indicates $\mu \pm SD$ of the 206 nm silica beads measured by TEM. (C) RI distribution of the bead mixture (solid line) fitted by a sum of two Gaussian functions (dotted line; $f_1 = 0$, $\mu_1 = 1.447$, $SD_1 = 0.021$, $A_1 = 458$, $\mu_2 = 1.665$, $SD_2 = 0.046$, $A_2 = 793$). The vertical green bars indicate the range of reported RIs from literature.

of RI will be reduced for particles with a lower RI than polystyrene, as σ becomes more dependent on the RI for such particles. This may partly explain why the standard deviation of RI_{Si} was 0.021. Moreover, since the standard deviation of the diameter scales with $1/\sqrt{\text{tracklength}}$, [203] increasing the tracklength will reduce the standard deviation of the diameter, σ and RI. Technical modifications required to dramatically increase the tracklength without reducing the number of particles tracked have been demonstrated [54]. To further reduce the standard deviation of σ, we propose to improve the illumination homogeneity of the microscope.

6.2.4 Application

As a proof of principle, we applied NTA for the determination of the RI of urinary vesicles from a healthy male individual. After collection, urine was centrifuged twice (50 mL, 4 °C, 10 min, 180 g; and 20 min, 1,550 g) to remove cells, and diluted 100-fold in 50 nm-filtered (Nucleopore, GE Healthcare, IL) phosphate-buffered saline (PBS). Fig. 6.5A shows σ versus the diameter of urinary vesicles measured by NTA. We captured 20 videos of 30 s to track at least 1,000 vesicles. Since the scattering power of the vesicles differs more than 3 orders of magnitude, we used three different camera settings: gain 100, 350, and 470. The gains were selected such that the range of detectable scattering cross sections overlapped. Data processing was performed as described above. The grey lines again show the relationship between σ and the diameter for seven RIs between 1.35 and 1.65, taking into account that the RI of PBS is 0.002 higher than the RI of water [166]. Fig. 6.5B shows the measured PSD of urinary vesicles. The PSD ranges from 45 nm to 865 nm with a mode diameter of 115 nm. Similar to TEM, the right-hand side of the PSD shows a decreasing concentration with increasing diameter, but vesicles smaller than ∼100 nm are below the detection limit for the settings used. Fig. 6.5C shows the measured RI distribution of urinary vesicles, with a mean RI of 1.37. The RI of urinary vesicles is lower compared to a previous estimate of plasma vesicles > 500 nm, which have an RI distribution ranging from 1.34 to 1.50 with a peak at 1.40 [169]. However, in contrast to urine, plasma of non-fasting subjects contains chylomicrons [231], which are lipoprotein particles with an RI between 1.45 and 1.60 [206]. In addition, plasma vesicles may differ in composition from urinary vesicles. Moreover, our estimated RI of urinary vesicles falls within the range of estimates [235, 234, 58] based on the RI of cells [309, 31, 102]. The true RI of vesicles may differ from our estimate for four reasons. First, the scaling factor that relates scattering power to σ is obtained with polystyrene beads for which the RI uncertainty is 2.7 % [205]. Second, the heterogeneous sample required different camera settings. Therefore, we have corrected detected scattering power for non-linear camera gain response, which may change over time. Third, NTA determines the hydrodynamic diameter and therefore overestimates the physical diameter of a particle. Since σ increases with diameter for particles < 200 nm, an overestimation of the particle diameter causes an underestimation of the RI. Fourth, we have modeled vesicles as spheres with a uniform RI distribution. In

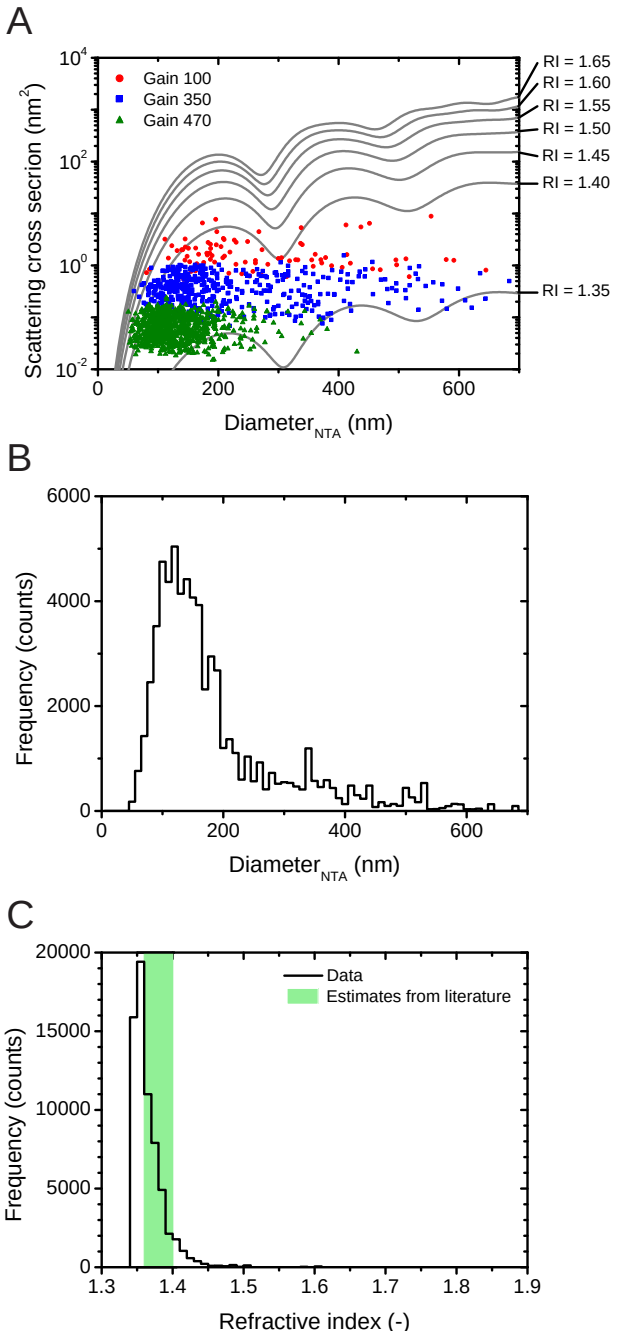

Figure 6.5: Size and refractive index (RI) determination of urinary vesicles in phosphate-buffered saline by nanoparticle tracking analysis (NTA). (A) Scattering cross section versus diameter calculated by Mie theory (lines) and measured for urinary vesicles with camera gain 100 (red circles), 350 (blue squares), and 470 (green triangles). (B) Particle size distribution (black line) of urinary vesicles. (C) RI distribution of urinary vesicles (black) and the range of estimates from literature (vertical green bar).

practice, however, a vesicle consists of a low RI core enclosed by a several nm thick phospholipid shell with an RI of 1.46 ± 0.06 [309, 31]. With Mie theory, σ of a shelled particle can be analytically described. Oscillations of σ as a function of the diameter are likely to shift for a shelled particle compared to a solid particle, which warrants further investigation, since such a shift should be measurable with NTA.

6.3 Conclusion

In conclusion, we have demonstrated the first use of NTA to determine the RI of individual nanoparticles in suspension. A major advantage of this single particle RI determination over bulk RI measurements, is that this method will give accurate RI measurements even if particles with different RI are present in the sample. Further, this method may be applied to differentiate between populations in a sample based on RI. We found that the mean RI of extracellular vesicles < 500 nm is 1.37 at 405 nm. This hitherto unknown property of vesicles is essential to data interpretation and standardization of clinical research on vesicles. We expect that determination of the RI of nanoparticles with NTA will become an important tool in biomedical diagnostics, materials science, and oceanography, as well as other fields where the optical characterization of nanoparticles is of critical importance.

CHAPTER 7

Reproducible extracellular vesicle size and concentration determination with tunable resistive pulse sensing

Abstract

Introduction: The size of extracellular vesicles (EVs) can be determined with a tunable resistive pulse sensor (TRPS). Because the diameter of the sensing pore varies from pore to pore, the minimum detectable diameter also varies. The aim of this chapter is to determine and improve the reproducibility of TRPS measurements. *Methods:* Experiments were performed with the qNano system (Izon) using beads and a standard urine vesicle sample. With a combination of voltage and stretch that yields a high blockade height, we investigate whether the minimum detected diameter is more reproducible when we configure the instrument targeting (1) fixed stretch and voltage, or (2) fixed blockade height. *Results:* Daily measurements with a fixed stretch and voltage (n = 102) on a standard urine sample show a minimum detected vesicle diameter of 128 ± 19 nm [mean ± standard deviation; coefficient of variation (CV) 14.8 %]. The vesicle concentration was $2.4 \pm 3.8 \cdot 10^9$ vesicles mL^{-1} (range $1.4 \cdot 10^8 - 1.8 \cdot 10^{10}$). When we compared setting a fixed stretch and voltage to setting a fixed blockade height on 3 different pores, we found a minimum detected vesicle diameter of 118 nm (CV 15.5 %, stretch), and 123 nm (CV 4.5 %, blockade height). The detected vesicle concentration was $3.2 - 8.2 \cdot 10^8$ vesicles mL^{-1} with fixed stretch and $6.4 - 7.8 \cdot 10^8$ vesicles mL^{-1} with fixed blockade height. *Conclusion:* Pore-to-pore variability is the cause of the variation in minimum detected size when setting a fixed stretch and voltage. The reproducibility of the minimum detectable diameter is much improved by setting a fixed blockade height.

This chapter has been published as:

- F.A.W. Coumans, E. van der Pol, A.N. Böing, N. Hajji, A. Sturk, T.G. van Leeuwen, and R. Nieuwland. Reproducible extracellular vesicle size and concentration determination with tunable resistive pulse sensing. *J. Extrecell. Vesicles* **3**: 25922 (2014)

7.1 Introduction

To establish whether there is any clinical value in the particle size distribution (PSD) of extracellular vesicles (EVs), reproducible measurements are a prerequisite. In Chapter 4, we have determined the PSD of urinary vesicles by transmission electronmicroscopy, flow cytometry, nanoparticle tracking analysis, and tunable resistive pulse sensing (TRPS) [232]. We found that TRPS, commercialized as the qNano (Izon, Christchurch, New Zealand), is the most accurate technique to determine the PSD of vesicles in suspension. However, we did not investigate the reproducibility of TRPS measurements. Moreover, standard procedures for determining the PSD of vesicles by TRPS are absent.

7.1.1 TRPS operating principle

The operating principle of TRPS is illustrated in Fig. 7.1. In TRPS, the resistance of a small pore filled with conductive medium is continuously measured [144, 82]. To measure the pore resistance, a voltage is applied across the pore, and the electric current through the pore is measured. The resistance R of a cylindrical pore is given in eqn. 7.1, with the conductivity of the medium ρ, the length of the pore L, and the diameter of the pore D:

$$R_{pore} = \frac{4\rho L}{\pi D^2} \tag{7.1}$$

Fig. 7.1B shows a cartoon of the signal from a vesicle moving through the pore. To drive vesicles through the pore, TRPS uses a combination of electrophoretic and convective flow induced by the applied voltage and an external pressure across the pore, respectively [326]. The influence of diffusion and electro-osmosis on the flow rate is typically negligible [326, 171]. While the vesicle is moving through the pore, the pore resistance is increased. This resistive pulse is observed as a transient decrease of the current. The magnitude of the dip in current is called the blockade height in the qNano system. From this dip in current, the resistive pulse is derived, which is proportional to the vesicle volume [171]:

$$\Delta R = \frac{4\rho}{\pi D^4} d^3 \tag{7.2}$$

Eqn. 7.2 was derived for a spherical vesicle with diameter d inside a cylindrical pore. Because D is unknown, calibration with beads of known diameter is required to find $4\rho/\pi D^4$. If D changes, the calibration needs to be repeated. The user can adjust D by stretching the pore, but D is also affected by factors that are beyond control of the user, such as the Mullins effect (stress induced softening) [314] and accumulation of high-molecular-weight proteins on the pore, such as fibrinogen or von Willebrand Factor. To limit the impact of variation in ρ and D throughout an experiment, the change in resistance ΔR relative to the resistance of the pore R is used for analysis (analysis in $\Delta I/I$ mode). Although the qNano has a conical

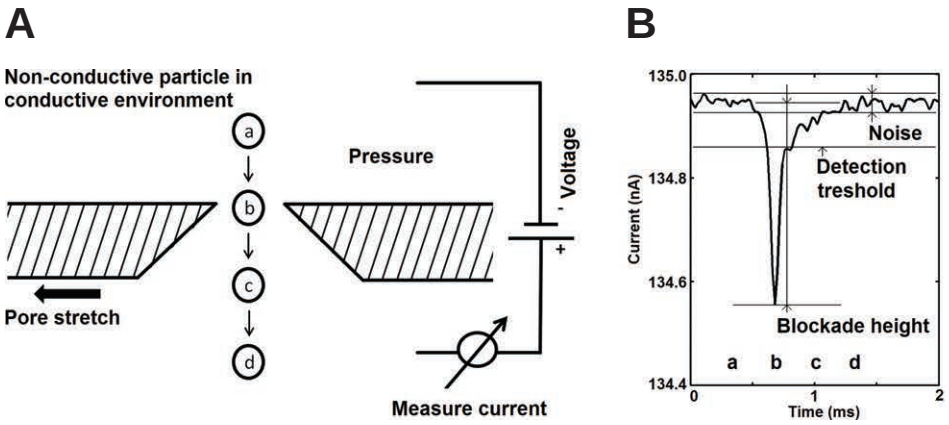

Figure 7.1: Operating principle of tunable resistive pulse sensing. When a non-conductive vesicle in a conductive medium passes through a pore, it causes a brief increase in electrical resistance of the pore. This is measured by monitoring the electrical current through the pore. (A) Schematic representation of a pore with a vesicle passing from position a−d. (B) Current from a particle moving through the pore. The letters a−d correspond to vesicle positions a−d in (A).

instead of cylindrical pore geometry [171], eqn. 7.1 and 7.2 are sufficient to describe the principle of sizing with TRPS.

The vesicle concentration is derived from the count rate, which is also calibrated with reference beads. The diameter of the pore used in the qNano system can be tuned by changing the stretch of the pore holder, hence the name tunable resistive pulse sensing. Fig. 7.2 shows a picture of the qNano system.

7.1.2 Size limits of TRPS

The diameter of cell-derived vesicles in body fluids such as urine typically ranges from 30 to 1,000 nm. Since TRPS cannot detect the smallest vesicles, it is important to know what the smallest detectable size by TRPS is, especially because the smallest detectable vesicle size strongly affects the main parameters of a PSD, such as mean size, median size, standard deviation and concentration [232]. From eqn. 7.1 and 7.2 it becomes clear that the smallest detectable size of TRPS is limited by the pore size, conductivity of the medium, stability of the baseline current and noise of the detection electronics [82, 131]. A smaller pore will increase the magnitude of the resistive pulse and therefore decrease the smallest detectable vesicle size. A change in pore size also affects the stability of the baseline current. Thus, a reproducible and stable pore size is required to have reproducible measurements. To distinguish resistive pulses from noise and eliminate the impact of noise, a detection threshold is set below the noise by the analysis software (see Fig. 7.1B).

Particles larger than the pore cannot be measured with TRPS, because these

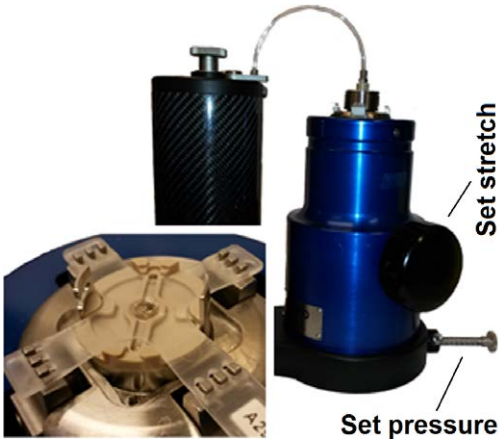

Figure 7.2: Tunable resistive pulse sensing commercialized as the qNano system. Left: air-based variable pressure module (VPM). Right: qNano system. The pore and fluid cells are contained within the green square. The insert shows the bottom fluid cell and the crucifix containing the pore mounted on the stretching mechanism.

particles cause pore clogging (described as pore blockages in other papers). If pore clogging occurs, the measurement has to be paused to unclog the pore, which may alter the dimensions of the pore.

7.1.3 Goals

Our goals are to determine and improve the reproducibility of TRPS measurements.

7

7.2 Methods

7.2.1 Approach

We performed 3 experiments to reach our goal. (I) To determine the reproducibility of TRPS, we measured the PSD of a standard population of vesicles 102 times at fixed settings of the voltage and stretch and determine the variation in minimum detectable vesicle size and concentration. (II) To improve sensitivity, we investigated how the set voltage, stretch, and pressure affect the measured baseline current and blockade height. (III) Using insights from experiment I and II, we studied how a fixed blockade height may improve the reproducibility of TRPS.

7.2.2 Standard population of vesicles and reference beads

To obtain a standard population of vesicles with low contamination by lipoproteins, platelets and protein aggregates [235], we selected vesicles from urine as our standard sample. Urine from 1 healthy male individual was collected, pooled, centrifuged twice to remove the cells (10 mL at 180 g, 4 °C, and 20 min at 1,550 g, 4 °C), and filtered with a 0.45 µm filter (MilliPore, Amsterdam, The Netherlands). Aliquots of 150 µL cell-free filtered urine were snap frozen in liquid nitrogen and

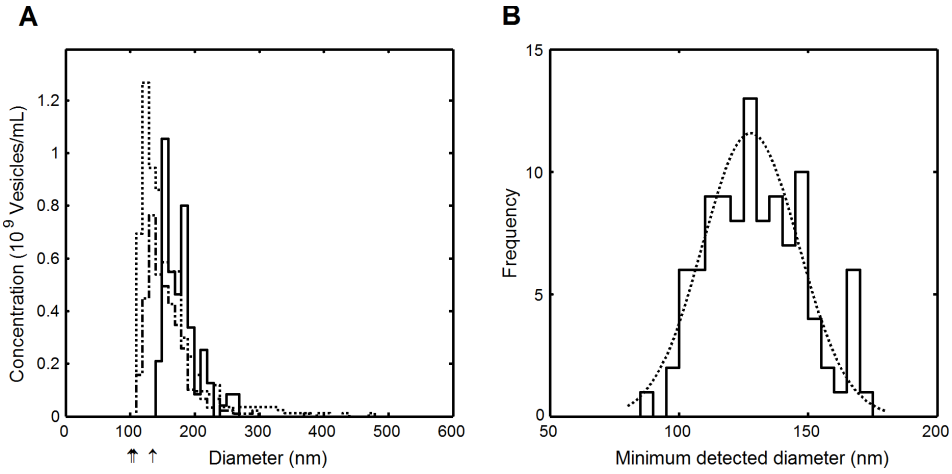

Figure 7.3: (A) Particle size distribution obtained from 3 measurement of the standard sample. The size distribution is shown as a histogram with bin width 10 nm. The minimum detected size for these 3 distributions is indicated with vertical arrows below the x-axis. (B) Histogram of the minimum detected size of the standard sample for 102 consecutive measurements measured on 102 days. The dashed line shows a fit of a normal distribution with a mean size of 127 nm and standard deviation of 19 nm.

stored at −80 °C. Before analysis, samples were thawed in 37 °C water to dissolve amorphous salts, and diluted 1:1 in 0.22 µm filtered (Millipore) phosphate buffered saline (PBS; 9.0 g NaCl, 0.22 g $Na_2HPO_4.2H_2O$ and 0.032 g $NaH_2PO_4.2H_2O$, per L de-ionized water) .

To calibrate the size and concentration and to find the relationship between the voltage, stretch, pressure, baseline current, and blockade height, we prepared polystyrene beads with a mode diameter of 203 nm (Izon) and a concentration of $2.0 \cdot 10^9$ particles mL^{-1}. To prevent aggregation of the beads, 0.6 mM sodium dodecyl sulphate (SDS) was added to the bead PBS. Prior to use, the beads were sonicated for 5 min and vortexed for 10 s.

7.2.3 Instrument settings and analysis

Reproducibility at fixed stretch and voltage (I)

To determine the reproducibility of TRPS, we measured the PSD of a standard population of vesicles. A measurement requires selection of electrolyte, nanopore, stretch, voltage and pressure. For the electrolyte, we selected PBS to prevent osmotic effects on vesicle size. Pores with different diameters are available for the qNano. The 3 pore types applicable to the measurement range of 50−1,000 nm are the NP100, NP200 and NP400. The naming of the pore types is not related to the diameter of the pore. Each pore type has a different measurement range with some overlap between the measurement ranges. The NP200 is most frequently

used in our lab because it is the most sensitive pore with an acceptable pore clogging rate on our samples. Pores were stretched 10 times from 43 to 47 mm to eliminate the influence of the Mullins effect [314]. Since standard procedures for measuring vesicles were unavailable at the time we started this experiment, we followed manufacturers' recommendations at the time and set the stretch at 45 mm, the voltage at 0.34 V, and the pressure at 7.5 mbar.

For each experiment, particles were measured for 10 min or until 1,000 particles were counted. We repeated the measurement if (1) the baseline current drifted by more than 5 %, (2) the RMS (root mean square) noise exceeded 10 pA or (3) the R^2-correlation of cumulative counts versus time was less than 0.999. The R^2-correlation and the baseline current drift are indirect indicators that a change in D may have occurred, which would reduce the size accuracy. Measurement and analysis were performed with Izon Control Suite v2.2.2.44 software. Summary of the data and graphical representation of the data was done in MATLAB 2010b (Mathworks, Natick, MA). Since the detection threshold (Fig. 7.1B) is set by the analysis software at 50 pA from the mean baseline current, the smallest detectable vesicle size can be calculated from the mean blockade height from beads of known size. Variation in the smallest detectable size was expressed as the coefficient of variation (CV), which is defined as the ratio of the standard deviation to the mean.

Optimal settings for detecting small sizes (II)

Experiment I was performed with manufacturer recommended settings. A systematic study of the selected measurement parameters is needed. To find the optimal settings for detecting small sizes, we determined the relationship between stretch, voltage, baseline current, and blockade height by testing combinations of stretch (43, 44, ..., 47 mm) and voltage (0.1, 0.2, ..., 0.8 V). For each experiment, we measured 1,000 beads or for 10 min, whichever came first. We repeated the measurement if (1) the baseline current drifted by more than 5 %, (2) the RMS noise exceeded 10 pA or (3) the R^2-correlation of cumulative counts versus time was less than 0.999. All data from this experiment were acquired with 3 pores at a constant pressure of 7.5 mbar. Settings that resulted in maximum blockade height, but without frequent pore clogging and without instability in the detection electronics due to excessive current, we appointed the optimal settings for detecting small sizes. These settings were then used to study the influence of pressure during measurement. We measured the bead and the vesicle sample with 3 pores at 0, 2.5, 5.0, ..., 15 mbar applied pressure. For selection of the optimal pressure, we considered the impact of pressure on the blockade height, and on the number of particles measured per minute.

Procedures to improve reproducibility (III)

Based on the optimal settings for detecting small sizes from experiment II, we evaluated whether setting a fixed blockade height improved the reproducibility of TRPS. To set the stretch, we set a voltage and adjusted the pore stretch until the

target current was achieved. According to eqn. 7.1, this is expected to improve the reproducibility of the pore size (D) and particle rate between pores. We did not exceed 47.5 mm stretch to prevent damage to the pore. Next, we adjusted the voltage to achieve a fixed mode blockade height on the calibration beads. This sets the minimum detected size directly, because the detection threshold (Fig. 7.1B) directly relates to the blockade height for a bead of known size to the smallest detected size. This method was compared to fixed stretch and voltage by repeated measurements on a single pore, and single measurements on multiple pores, referred to as inter-pore and intra-pore in the rest of the text. The inter-pore and intra-pore measurements were performed on different days. The pore was loaded onto the qNano, and calibration was performed for each measurement. For the 2 configuration methods, we compared the reproducibility of the particle rate, the minimum detected size and the concentration of the standard vesicle sample.

7.3 Results

7.3.1 Reproducibility at fixed stretch and voltage (I)

We have determined the PSD of a standard population of urinary vesicles 102 times using a fixed stretch and voltage. Three randomly selected PSDs are shown in Fig. 7.3A. While the overall shape of the distributions is similar, the minimum detected diameter was 106, 109 and 138 nm. The distribution of minimum detected sizes on the 102 measurements is shown in Fig. 7.3B. The minimum detected size ranged from 89 to 165 nm (average 128 nm, standard deviation 19 nm). From the shape of the PSD, it is expected that the change in minimum detectable size affects the determined concentration [232]. The mean urinary vesicle concentration is $2.4 \cdot 10^9$ vesicles mL^{-1} with a standard deviation of $3.8 \cdot 10^9$ (CV 158 %). Due to the large variability in minimum detected size and the skewed PSD, it is meaningless to describe PSDs with statistical parameters like mean, mode, median, nor to report a concentration without restricting size range.

Since (1) the baseline current is determined by the pore dimensions, (2) different pores have different baseline currents at similar settings, (3) the baseline current fluctuates over time (up to 5 % in 1 h, data not shown), and (4) the pore is made from polyurethane, which is a flexible material, we hypothesize that the variations in the minimum detectable vesicle size are caused by variations in the pore dimensions. However, minimizing the impact of the variations in the pore dimensions by optimizing the settings requires a thorough understanding and optimization of the measurement parameters.

7.3.2 Optimal settings for detection of small vesicles (II)

Optimal voltage and stretch

To find the optimal settings for detection of small vesicles, we investigated the relationship between the set voltage, stretch, and pressure, the baseline current

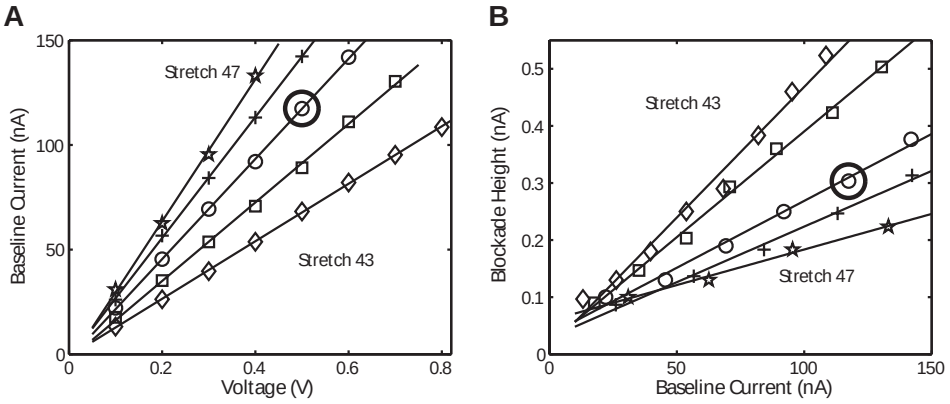

Figure 7.4: Effect of set voltage and stretch on baseline current and blockade height. Each point represents the average of 3 pores. Lines are linear fits to the data. (A) Relationship between baseline current, stretch, and voltage. (B) Relationship between blockade height and baseline current. The combination of parameters selected for further optimization is indicated with a bold circle.

and blockade height. For these experiments, we have determined the average baseline current and blockade height of 203 nm beads using 3 pores. Fig. 7.4A shows the baseline current versus voltage for different values of the pore stretch. Each data point has a CV between 11 and 22 %. The baseline current shows a linear relationship with the voltage, as expected from Ohm's law. In addition, a linear relationship between baseline current and stretch was found. For all combinations of the voltage and the stretch, the average RMS noise was 7.6 pA (SD 0.8 pA, range 6.0−9.4 pA). This is sufficiently smaller than the 50 pA detection threshold configured in the analysis software to guard against false positive events due to noise.

A higher blockage height for 203 nm beads means that smaller particles can be detected. Fig. 7.4B shows the relationship between the blockade height and the baseline current. The maximum blockade height was found for small stretch and high baseline current. However, a stretch of 43 and 44 mm resulted in frequent pore clogging, and baseline currents in excess of 140 nA occasionally had high RMS noise, making them unsuited for measurements. At 45 mm stretch, the highest blockade was achieved with 0.5 V. Thus, at 7.5 mbar of pressure, settings that are generally applicable to all NP200 pores and optimized for small particle detection are 0.5 V, 45 mm stretch, resulting in a mean current and blockade height of 117 nA and 0.30 nA for 203 nm beads, respectively.

Optimal pressure

The effect of pressure on blockade height and particle rate was determined on 3 pores for beads and urine measured with 45 mm stretch and 0.5 V. An increased

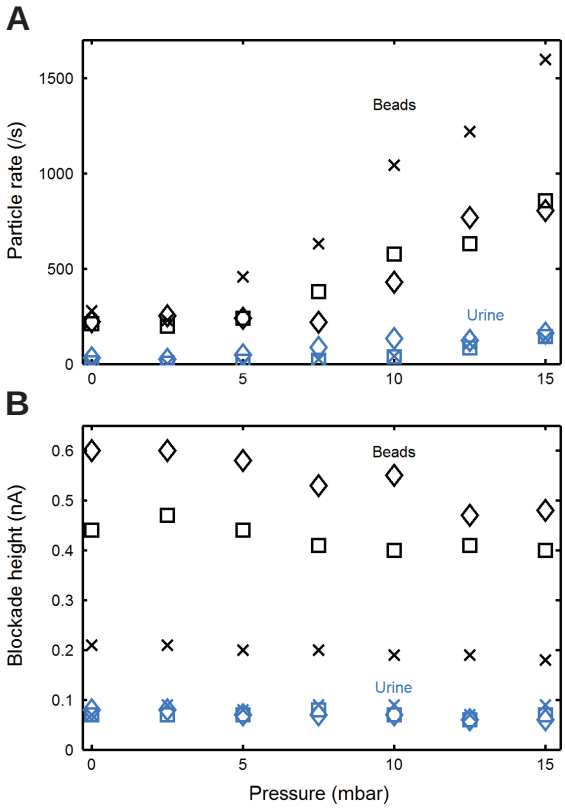

Figure 7.5: Impact of pressure on measurement. The data from 3 pores are shown for beads (black markers) and urine (blue markers). (A) Particle rate versus pressure. (B) Blockade height versus pressure.

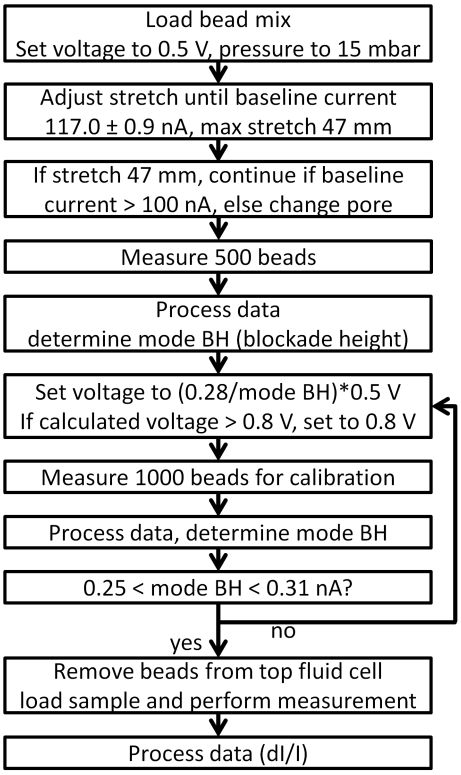

Figure 7.6: Flow chart for fixed blockade height method.

pressure resulted in an increased particle rate (Fig. 7.5A) and a reduced blockade height (Fig. 7.5B) for both beads and urine vesicles. Increasing the pressure from 7.5 mbar to 15 mbar approximately resulted in a 2-fold increase in particle rate, a 2-fold decrease in time needed to measure 1,000 particles, a 7 % reduction in blockade height, and only a 2 % increase of the smallest detectable vesicle. Given this large reduction in measurement time relative to the low loss in sensitivity, we selected 15 mbar as the optimal pressure for urinary vesicles. Consequently, the optimized settings for detecting small size were: 0.5 V, 45 mm stretch, 117 nA baseline current, 15 mbar pressure, and 0.28 nA blockade height for 203 nm beads.

7.3.3 Procedures to improve reproducibility (III)

In experiment I, we found that a fixed stretch and voltage results in poor reproducibility due to variations in the minimal detectable size. In experiment II, we found that 0.5 V, 45 mm stretch, and 15 mbar pressure are optimal settings for urinary vesicle measurements with the NP200 pore. At these optimized settings, however, the current and blockade height for 203 nm beads differ between NP200 pores due to variations in pore dimensions. An alternative approach to fixed voltage and stretch may be to set a fixed blockade height on reference beads, which

Table 7.1: Particles rate and average minimum and median detected diameter for 2 methods to configure TRPS measurements.

Method	Fixed stretch	Fixed blockade height
Inter-pore		
Particle rate (min^{-1})	67	136
Minimum diameter (nm)	96 ± 3.6	121 ± 4.3
Median diameter (nm)	130 ± 2.8	160 ± 4.7
Intra-pore		
Particle rate (min^{-1})	115	199
Minimum diameter (nm)	118 ± 15.5	123 ± 4.5
Median diameter (nm)	156 ± 15.6	166 ± 4.7

Diameter is expressed as mean ± coefficient of variation (CV).

directly determines the minimum detectable size through the detection threshold (Fig. 7.1B). Here, we will evaluate both approaches.

For fixed blockade height, first we set a voltage of 0.5 V, and then adjusted the pore stretch until a baseline current of 117±0.9 nA was achieved. Next, we adjusted the voltage to achieve a fixed mode blockade height of 0.28±0.03 nA on the calibration beads. See Fig. 7.6 for a flow diagram of the fixed blockade method. The target settings were taken from the optimized settings found earlier. The tolerances on current and stretch are achievable in a single iteration of configuring the instrument. The tolerance on the blockade height is expected to contribute up to 3.5 percentage point to the minimum detected size.

We measured the standard vesicle sample in triplicate with a single pore (inter-pore) and with 3 different pores (intra-pore). The results of these measurements are shown in Fig. 7.7 and in Table 7.1. Fig. 7.7A shows the average particle rate, Fig. 7.7B the minimum detectable diameter, and Fig. 7.7C the concentration using a single pore (left; inter-pore) and multiple pores (right; intra-pore) for fixed stretch and voltage, and fixed blockade height. With the intra-pore comparison, the particle rate again was lowest with fixed stretch (115 min^{-1}) compared to fixed blockade height (199 min^{-1}). The minimum detected diameter (% CV) was 118 (15.4 %) with fixed stretch, and 123 (4.5 %) with fixed blockade height. The minimum detected diameter CV on fixed blockade height remained comparable between inter- and intra-pore, while the CV with fixed stretch was substantially larger in the intra-pore measurement. This suggests that the fixed blockade height is more effective at standardizing the minimum detected diameter. With the inter-pore comparison, the detected concentration (Fig. 7.7C) has similar spread (range $6.2{-}8.6{\cdot}10^8$ vesicles mL^{-1} with fixed stretch, range $5.0{-}7.2{\cdot}10^8$ vesicles mL^{-1} with fixed blockade height). For multiple pores, the detected concentration (Fig. 7.7C) is most repeatable for fixed blockade height (range $6.4{-}7.8{\cdot}10^8$ vesicles mL^{-1} versus $3.2{-}8.2{\cdot}10^8$ vesicles mL^{-1} with fixed stretch and voltage). The 9 % difference in average detected concentration between inter- and intra-pore measurements may be attributable to sample thawing losses, since these experiments were performed on different days.

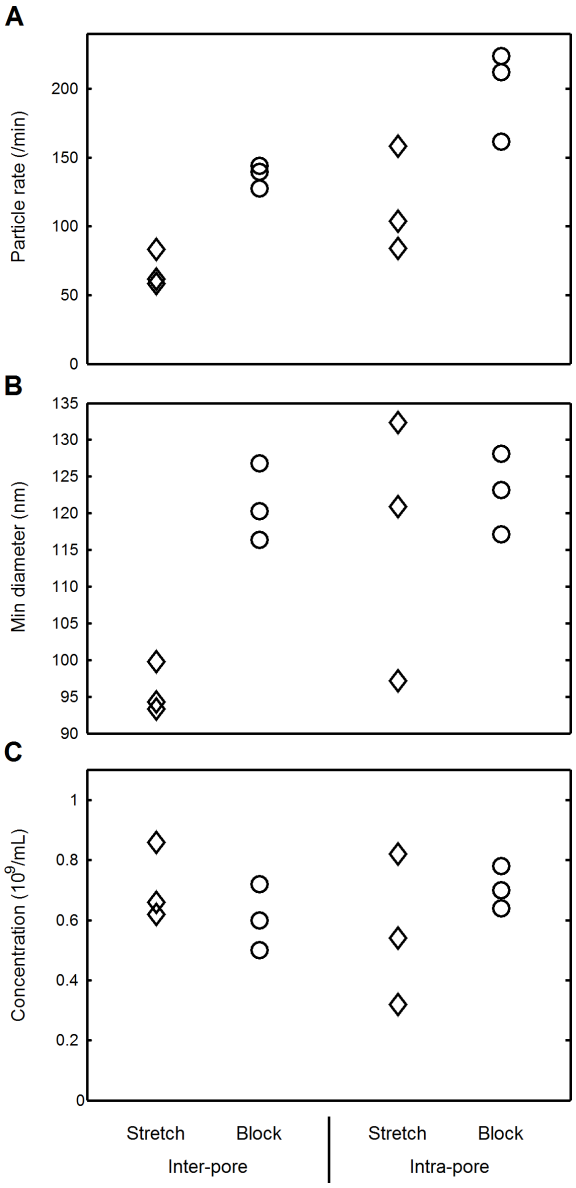

Figure 7.7: Inter- and intra-pore reproducibility (both n = 3) of particle rate (A), minimum detected diameter (B) and concentration (C) for 2 configuration methods. Labels below (C) refer to the methods fixed stretch and voltage and fixed blockade height.

7.4 Discussion

TRPS allows size determination of non-conducting particles in conducting media [232]. Since vesicles are relatively non-conducting, TRPS is a suitable technique to study vesicles. However, the vesicle size distribution of different samples cannot be compared rigorously if the size distributions cannot be parameterized. Because the PSD of vesicles extends below the minimum detection limit of the qNano system, and because the vesicle concentration increases with decreasing detectable vesicle size in biological fluids, a reproducible minimum detected size is required for this parameterization. The simplest approach to achieve this would be to truncate the data below a certain size. Fig. 7.3 demonstrates that this size cutoff with a NP200 pore would need to be approximately 160−170 nm, which would dramatically reduce the utility of a TRPS measurement because the vast majority of vesicles would go undetected. Therefore, a solution that improves the reproducibility of the minimum detected size is preferred.

7.4.1 Optimal settings for detection of small vesicles

To find settings for detection of the smallest vesicles, we varied voltage to determine the blockade height on beads of known size. We found that low stretch and high current results in high blockade height (Fig. 7.4) and thus improved minimum detected diameter. The minimum applicable stretch is limited by the increased incidence of pore clogs, and the maximum voltage was limited by the instability in the detection electronics above a baseline current of 140 nA. Increasing the pressure reduces the blockade height. However, the number of particles in the urinary samples was so low that we had to select the highest possible pressure of 15 mbar. As optimal settings for detection of small sizes we obtained a stretch of 45 mm, a voltage of 0.5 V, and a pressure of 15 mbar, corresponding to a current of 117 nA and a blockade height of 0.28 nA for 203 nm beads. Much smaller vesicles can be detected if the detection threshold of 50 pA is reduced, for example, by application of digital signal processing techniques which should even allow detection of pulses smaller than the RMS noise.

7.4.2 Procedure to improve reproducibility

The obtained optimal settings for detection of small sizes were close to the settings that we applied to study the reproducibility of the size and concentration of vesicles in 102 urine samples from the same pool. However, in this study we obtained concentrations in a range of 2 orders of magnitude and a minimum detectable vesicles size CV of 15 %. We compared the fixed stretch and voltage strategy that led to this to a fixed blockade height strategy. The latter strategy results in a more reproducible pore size, as can be seen in the reduced CV on the particle rate. The most reproducible minimum detected size (CV 4.5 %), as well as concentration, is found with the fixed blockade height. These reproducibilities are much better than what was measured on the 102 samples with fixed stretch and voltage; however, a

much larger sample than 3 experiments is needed to determine whether these gains are durable. If not, addition of beads to the sample can improve concentration reproducibility, but will not allow detection of vesicles with the same size as the beads [316].

7.4.3 Minimum detected size would be more reproducible with a tighter tolerance pore

A more reproducible pore could allow a simpler procedure than our proposed solution. Because the tunable pores are made of polyurethane, both the tolerances on the molding process as well as on the fabrication of the pore itself are a challenge. Rejection of pores that deviate from the desired size would reduce this issue, but a very high rejection rate would be cost prohibitive. A cheaper solution would be to produce the pores with, for example, silicon lithography, where tolerances of a few percent on both pore diameter and thickness are feasible. This direction would eliminate the tunable aspect of the TRPS system, which may be convenient as it eliminates the need for setting the stretch parameter.

7.4.4 Applicability to other vesicle types

We used urine vesicles for the selection of the optimal instrument configuration method. We expect the result to be applicable to other vesicle samples as well, provided the preparation of these samples did not induce high levels of large contaminants. Samples with higher vesicle concentrations should be measured at a lower pressure. Isolation by a Sepharose 2B column [42] could be used to minimize the presence of proteins in the sample.

7.5 Summary

Experiments to optimize a TRPS protocol with high sensitivity and reproducibility were performed. We demonstrated that the pore diameter can be controlled by adjusting stretch until a certain baseline current is achieved. The minimum detected size was made reproducible by adjusting the voltage to set the blockade height. With a standard urine vesicle sample, we demonstrated that the variation in detected particle rate, diameters and concentration is primarily caused by variation between pores. Until more reproducible pores become available, we will apply the following steps for the most reproducible results: (1) set the instrument stretch to achieve a fixed current, (2) set the instrument voltage to achieve a fixed blockade height on beads of known size, (3) allow the system to stabilize for 3 min before calibration, (4) measure your samples, repeat the measurement if the baseline current drifts by more than 5 %, or the particle rate is not constant ($R^2 < 0.99$), and (6) analyze the data in $\Delta I/I$ mode.

CHAPTER 8

Single-step isolation of extracellular vesicles by size-exclusion chromatography

Abstract

Background: Isolation of extracellular vesicles from plasma is a challenge due to the presence of proteins and lipoproteins. Isolation of vesicles using differential centrifugation or density-gradient ultracentrifugation results in co-isolation of contaminants such as protein aggregates and incomplete separation of vesicles from lipoproteins, respectively. *Aim*: To develop a single-step protocol to isolate vesicles from human body fluids. *Methods*: Platelet-free supernatant, derived from platelet concentrates, was loaded on a sepharose CL-2B column to perform size-exclusion chromatography (SEC; $n = 3$). Fractions were collected and analysed by nanoparticle tracking analysis, tunable resistive pulse sensing, flow cytometry and transmission electron microscopy. The concentrations of high-density lipoprotein cholesterol (HDL) and protein were measured in each fraction. *Results*: Fractions 9−12 contained the highest concentrations of particles larger than 70 nm and platelet-derived vesicles (46 ± 6 % and 61 ± 2 % of totals present in all collected fractions, respectively), but less than 5 % of HDL and less than 1 % of protein (4.8 ± 1.0 % and 0.65 ± 0.3 %, respectively). HDL was present mainly in fractions 18−20 (32 ± 2 % of total), and protein in fractions 19−21 (36 ± 2 % of total). Compared to the starting material, recovery of platelet-derived vesicles was 43 ± 23 % in fractions 9−12, with an 8-fold and 70-fold enrichment compared to HDL and protein. *Conclusions*: SEC efficiently isolates extracellular vesicles with a diameter larger than 70 nm from platelet-free supernatant of platelet concentrates. Application SEC will improve studies on the dimensional, structural, and functional properties of extracellular vesicles.

This chapter has been published as:

- A.N. Böing, E. van der Pol, A.E. Grootemaat, F.A.W. Coumans, A. Sturk, and R. Nieuwland. Single-step isolation of extracellular vesicles by size-exclusion chromatography. *J. Extracell. Vesicles* **3**: 23430 (2014)

8.1 Introduction

The scientific and clinical interest in plasma-derived vesicles is tremendous, since these vesicles may contain clinically relevant information [188, 288, 292, 308, 340]. Isolation of vesicles from plasma with good recovery and without contamination of proteins and lipoproteins, however, is a challenge. Thus far, most isolation protocols are based on differential centrifugation. After removal of cells in the first low-speed centrifugation step, vesicles are isolated using centrifugal accelerations of 19,000−100,000 g [294]. Unfortunately, protein aggregates are generated at high velocities of ∼ 100,000 g, [21, 120, 256] and vesicles may clump. Isolation of vesicles from plasma is further hampered by the viscosity and density of plasma, and by the presence of lipoprotein particles with a density and diameter similar to the extracellular vesicles of interest [294, 249, 231]. Consequently, isolation of vesicles from plasma or serum by density-gradient ultracentrifugation results in co-isolation of high-density lipoprotein (HDL), and isolation of HDL results in co-isolation of vesicles (as described in the response of Yuana Y. and Nieuwland R. to [317] and by Vickers K.C. et al. [312]). Thus, there is an urgent need for a simple and fast protocol to isolate vesicles from human plasma.

In platelet research, two different protocols are commonly applied to isolate platelets from platelet-rich plasma, that is, to replace the plasma by buffer. In one procedure, platelets are isolated from the plasma by centrifugation and washing [71, 339]. In the other procedure, platelets are isolated by size-exclusion chromatography (SEC), also known as "gel filtration" [339, 180]. SEC has also been used previously to isolate vesicles from sera, ascites and saliva, and was shown to separate vesicles from proteins [291, 289, 274, 220]. Whether SEC separates vesicles from HDL, however, has never been investigated. In this Chapter, we investigate the efficacy of single-step SEC for isolation of extracellular vesicles from human platelet-free supernatant of platelet concentrates and we studied the separation of vesicles by SEC from HDL and proteins.

8.2 Material and methods

8.2.1 Platelet concentrates

Platelet concentrates were from Sanquin (Amsterdam, The Netherlands). Buffy coats from 5 whole blood units are pooled together with one plasma unit of one of these donors. Subsequently, this pool was gently centrifuged. The resulting platelet rich plasma was slowly extracted using an automated separator via leukocyte reduction filter to a PVC-citrate storage bag. Platelet concentrates ($n = 3$, 9−12 days old, < 1 leukocyte $/\, 3 \cdot 10^8$ platelets) were stored with agitation at room temperature until use.

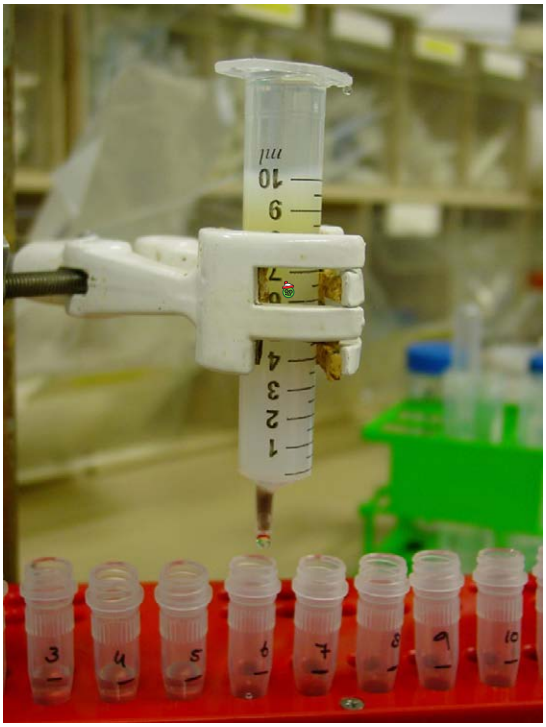

Figure 8.1: Image of size-exclusion chromatography column. A 10 mL syringe stacked with sepharose CL-2B for isolation of vesicles from platelet-free supernatant of platelet concentrates.

8.2.2 Platelet-depleted plasma

Platelet concentrate (30 mL) was diluted 1:1 with filtered phosphate-buffered saline [PBS; 1.54 mol/L NaCl, 12.4 mmol L^{-1} Na_2HPO_4, 2.05 mmol L^{-1} NaH_2PO_4, pH 7.4; 0.22 µm-filter (Merck chemicals BV, Darmstadt, Germany)]. Next, 12 mL acid citrate dextrose (ACD; 0.85 mol L^{-1} trisodiumcitrate, 0.11 mol L^{-1} D-glucose and 0.071 mol L^{-1} citric acid) was added and the suspension was centrifuged for 20 min at 800 g, 20 °C. Thereafter, the vesicle-containing supernatant was isolated and centrifuged (20 min at 1,550 g, 20 °C) to remove remaining platelets. This centrifugation procedure was repeated for 3 cycles, to ensure complete removal of platelets.

8.2.3 SEC column

Sepharose CL-2B (30 mL, GE Healthcare; Uppsala, Sweden) was washed with PBS containing 0.32 % trisodiumcitrate (pH 7.4, 0.22 µm-filtered). Subsequently, the tip of a 10 mL plastic syringe [Becton Dickinson (BD), San Jose, CA] was stuffed with nylon stocking (20 denier, Hema, Amsterdam, The Netherlands), and the syringe was stacked with 10 mL washed sepharose CL-2B to create a column with a diameter of 1.6 cm and a height of 6.2 cm (Fig. 8.1).

8.2.4 Collection of fractions

Platelet-free supernatant of a platelet concentrate (1.5 mL) was loaded on the column, followed by elution with PBS/citrate (0.32 %, pH 7.4, 0.22 µm filtered). The eluate was collected in 26 sequential fractions of 0.5 mL (Fig. 8.1). For each fraction, the number of particles was determined by nanoparticle tracking analysis (NTA), tunable resistive pulse sensing (TRPS) and flow cytometry. In addition, HDL cholesterol and protein concentrations were measured for each fraction. Of each fraction, $\sim$ 200 µL was frozen in liquid nitrogen and stored at −80 °C for subsequent transmission electron microscopy (TEM) on thawed fractions.

8.2.5 Nanoparticle tracking analysis

The concentration and size distribution of particles in collected fractions was measured with NTA (NS500; Nanosight, Amesbury, UK), equipped with an EMCCD camera and a 405 nm diode laser. Silica beads (100 nm diameter; Microspheres-Nanospheres, Cold Spring, NY) were used to configure and calibrate the instrument. Fractions were diluted 10−1,000-fold in PBS to reduce the number of particles in the field of view below 200 per image. Of each fraction, 10 videos with a duration of 30 s were captured with the camera shutter set at 33.3 ms and the camera gain set at 400. All fractions were analysed using the same threshold, which was calculated by custom-made software (MATLAB v.7.9.0.529). Analysis was performed by the instrument software (NTA 2.3.0.15).

8.2.6 Tunable resistive pulse sensing

The concentration and size distribution of particles was measured with TRPS (qNano; Izon Science, Christchurch, New Zealand) using an NP200A nanopore. This nanopore was suitable for the detection of 100−400 nm particles. Samples were measured with 7 mbar pressure, 45 mm stretch and 0.34 V. Samples were analysed for 5 min or until 1,000 vesicles were counted, whichever came first. To calibrate size and concentration, carboxylated polystyrene beads (Izon Science) were sonicated for 10 s, diluted in PBS with 0.3 mM sodium dodecyl sulphate and analysed immediately after dilution.

8.2.7 Flow cytometry

To detect platelet vesicles, 20 µL of each fraction was incubated for 15 min with an antibody against glycoprotein IIIa (CD61), which is a subunit of the platelet fibrinogen receptor and also known as integrin β_3 [phycoerythrin (PE)-conjugated CD61; 5 µL 1:10 prediluted in PBS/citrate, Pharmingen, San Diego, CA]. IgG_1-PE (BD) was used as control antibody. To detect all vesicles, 20 µL of each fraction was labelled with lactadherin (fluorescein isothiocyanate-conjugated, 5 µL 1:10 prediluted in PBS/citrate). After incubation, 300 µL PBS/citrate was added and samples were analysed on a FACSCalibur (BD, Cellquest version 4.0.2) for 1 min at a flow rate of 60 µL min^{-1}. The trigger was set on FSC at E00, the SSC voltage at

329 V, and the thresholds at FSC 30 and SSC 0. No gates were used to determine extracellular vesicles.

8.2.8 Transmission electron microscopy

After thawing, samples from all fractions, both undiluted and 50-fold diluted in PBS, were subjected to overnight fixation, in 0.1 % final concentration (v/v) paraformaldehyde (Electron Microscopy Science, Hatfield, PA). Then, a 200-mesh formvar and carbon coated copper grid (Electron Microscopy Science) was placed on a 10 µL droplet to allow adherence of particles to the grid (7 min, room temperature). Thereafter, the grid was transferred onto drops of 1.75 % uranyl acetate (w/v) for negative staining. Each grid was studied using a transmission electron microscope (Fei, Tecnai-12; Eindhoven, the Netherlands) operated at 80 kV using a Veleta 2,000×2,000 side-mounted CCD camera and Imaging Solutions software (Olympus, Tokyo, Japan).

8.2.9 Protein

The protein concentration was determined using a Bradford protein assay according to the manufacturer's instructions (Pierce, Rockford, IL). The absorbance was measured at 595 nm on a Spectramax Plus (Molecular Devices, Sunnyvale, CA). In addition, to directly visualize the relative presence of proteins in the collected fractions, in a single experiment, 10 µL of each fraction was mixed with 10 µL 2-fold concentrated reducing sample buffer, boiled for 5 min and loaded on an 8−16 % gradient gel (BioRad, Hercules, CA). Proteins were stained with Bio-Safe Coomassie G-250 Stain (BioRad).

8.2.10 Western blot

Proteins from all fractions (800 µL) were precipitated using trichloroacetic acid (20 % final concentration; Sigma-Aldrich, St. Louis, MO). From each fraction, equal amounts of protein (4 µg) were dissolved in non-reducing sample buffer, boiled and loaded on 8−16 % gradient PAGE gels (Biorad), and proteins were transferred to PVDF membrane (Millipore, Billerica, MA). Blots were incubated with anti-CD63 (BD, clone H5C6) or anti-CD9 (BD, clone M-L13), extensively washed and then incubated with a goat-anti-mouse (GAM)-horseradish peroxidase (Dako, Glostrup, Denmark). Subsequently, the PVDF membranes were incubated with a 5-fold diluted peroxidase substrate (LumiLight, Roche Diagnostics, Almere, The Netherlands) for 5 min, followed by analysis of luminescence using a LAS4000 luminescence image analyser (Fuji, Valhalla, NY).

8.2.11 High density lipoprotein

HDL cholesterol was determined using the colorimetric reagent HDL-Cholesterol Plus third generation (Roche Diagnostics, Almere, The Netherlands) on a Cobas

C8000 analyser (Roche) as per manufacturer's instructions. This assay specifically detects HDL-associated cholesterol [283]. Furthermore, a specific protein present in HDL, apo lipoprotein A1 (APO A1), was measured on an Architect (Abbott, Abbott Park, IL) according to manufacturer's instructions.

8.2.12 Recovery and enrichment

Recovery was defined as the total number of CD61-exposing vesicles in all fractions combined divided by the total number of CD61-exposing vesicles in the starting material. Recovery in a limited number of fractions is the total number in those fractions divided by the total number in the starting material.

The enrichment factor of vesicles to protein or HDL in fraction X is the ratio of CD61-exposing vesicles to protein or HDL in fraction X compared to the ratio of vesicles to protein or HDL in the starting material. Results from 3 independent experiments are presented as the mean ± standard deviation.

8.3 Results

8.3.1 Particles by NTA

The concentration of particles was determined by NTA in both starting material and fractions. Particles detected by NTA are not necessarily extracellular vesicles. With our settings, NTA will detect single particles with a diameter larger than ∼ 70 nm, which may include not only vesicles, but also protein aggregates, chylomicrons (size range 100−2,000 nm [67]) and very low density lipoproteins (VLDL; 27−200 nm [67]). NTA will not detect HDL (7−12 nm [67]), low density lipoproteins ([LDL; 18−23 nm [67]) and intermediate density lipoproteins (IDL; 23−27 nm [67]). After SEC, the highest concentration of particles was found in fractions 9−12 (Fig. 8.2A). The recovery of particles measured by NTA was 76 ± 38 %, and 46 ± 6 % of the recovered particles were present in fractions 9−12.

8.3.2 Particles by TRPS

The concentration of particles was determined by TRPS in both the starting material and in the fractions. Also particles detected by TRPS are not necessarily vesicles. With our settings, TRPS can detect single particles with a diameter of ∼ 100−400 nm, which will include vesicles, protein aggregates, chylomicrons and VLDL. TRPS will not detect HDL, LDL, or IDL. After SEC, the highest concentrations of particles were present in fractions 9−12 (Fig. 8.2B). The recovery of particles measured by TRPS was 60 ± 10 %, and 72 ± 1 % of the recovered particles were present in fractions 9−12 (Fig. 8.2B).

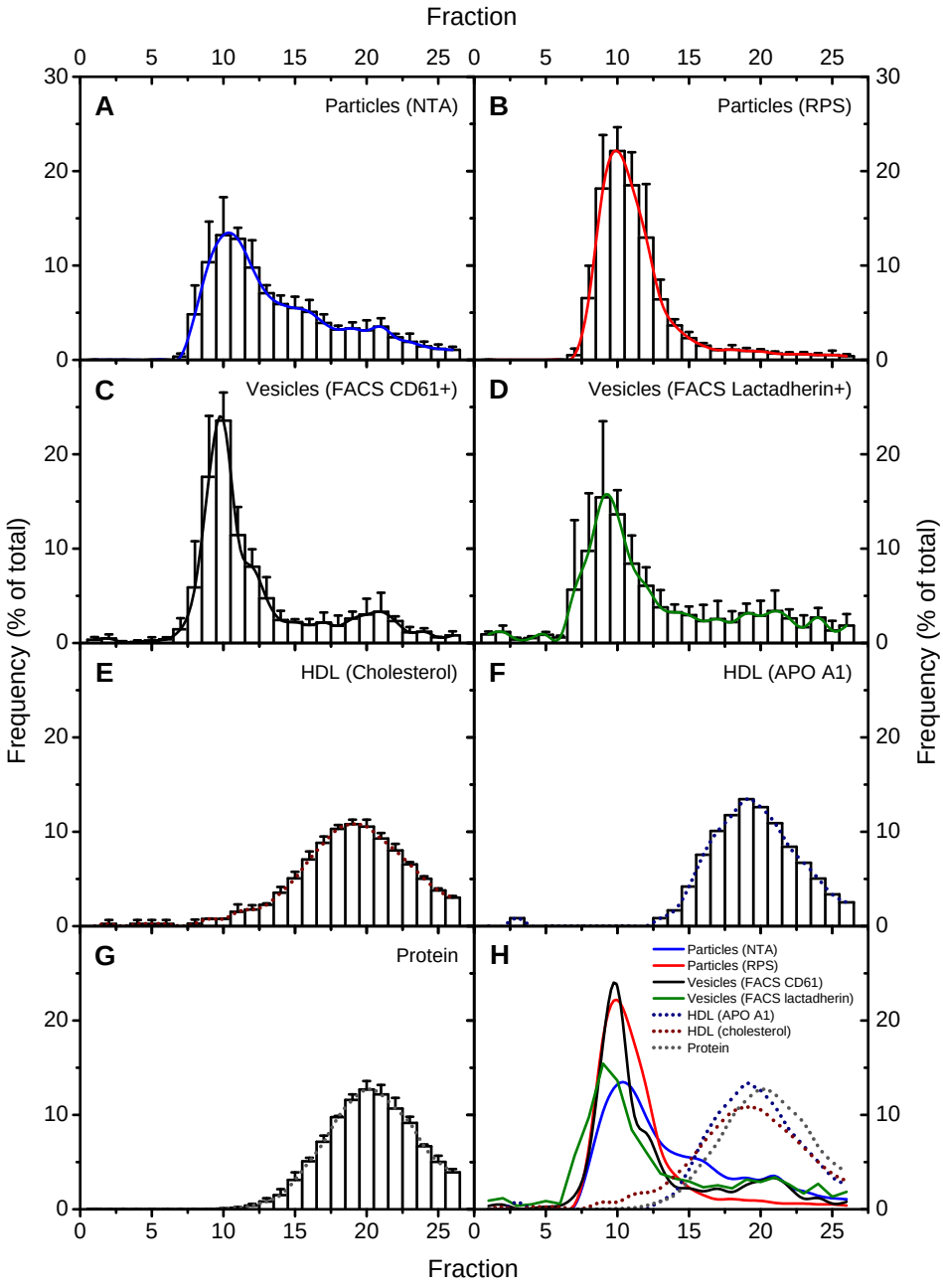

Figure 8.2: Presence of vesicles, protein, and lipoproteins per fraction. Each bar shows the number present in a fraction as % of the total number that passed the column. The height of the bar represents the mean, the error bars the standard deviation from 3 experiments. (continued)

Figure 8.2: (A) Particles (larger than 70 nm) measured by NTA. (B). Particles (100−400 nm) measured by tunable resistive pulse sensing (TRPS). (C) CD61+ vesicles measured by flow cytometry. (D) Lactadherin− vesicles measured by flow cytometry. (E) HDL (cholesterol) concentration measured by a colorimetric assay. (F) HDL (APO A1) concentration measured by a turbidimetric assay. (G) Protein concentration measured by a Bradford protein assay. (H) Overview of all measured results.

8.3.3 Detection of platelet-derived vesicles

Since the particles detected in fractions 9−12 by both NTA and TRPS are not necessarily vesicles, we applied flow cytometry to distinguish vesicles from lipoprotein particles. Because the studied extracellular vesicles originated from platelets, we used CD61 and lactadherin as vesicle markers. With our settings, the flow cytometer detects vesicles with a diameter larger than 500 nm. The recovery of CD61-exposing vesicles by flow cytometry was 71 ± 35 %, and 61 ± 2 % of the recovered vesicles were present in fractions 9−12 (Fig. 8.2C). The recovery of CD61-exposing vesicles in fractions 9−12 was 43 ± 23 % of the starting material. The recovery of lactadherin-binding vesicles was 163 ± 55 %, and 44 ± 5 % of the recovered vesicles were present in fractions 9−12 (Fig. 8.2D). The recovery of lactadherin-binding vesicles in fractions 9−12 was 73 ± 31 % of the starting material.

8.3.4 Lipoproteins and protein

The recovery of HDL cholesterol was 103 ± 11 %, and fractions 18−20 contained 32 ± 2 % of total recovered HDL (Fig. 8.2E). Although the HDL cholesterol assay is specific for HDL, we confirmed these measurement results by also measuring APO A1, a specific HDL protein, in a control experiment. The recovery of HDL APO A1 was 72 % and fractions 18−20 contained 38 % of total recovered HDL APO A1 (Fig. 8.2F). The recovery of protein was 95 ± 17 %, and fractions 19−21 contain 36 ± 2 % of total recovered protein (Fig. 8.2G). Fractions 9−12 contained the majority of vesicles and additionally contained 4.8 ± 1.0 % of total recovered HDL cholesterol, whereas HDL APO A1 was below the detection limit ($0.01\,\mathrm{g\,L^{-1}}$) in these fractions. Fractions 9−12 contained 0.65 ± 0.30 % of total recovered protein.

8.3.5 Overview of detected parameters

Figure 8.2H shows an overlay of the percentage of particles (NTA, TRPS), vesicles (CD61-exposing, lactadherin-binding), HDL (cholesterol, APO A1) and protein per fraction. Particles and vesicles showed a peak at fraction 10, whereas HDL (cholesterol and APO A1) and protein showed a peak at fraction 19 and 20, respectively. Thus, it is clear that vesicles can be separated from protein and lipoproteins by SEC.

8.3.6 Presence of proteins per fraction

To directly visualize the efficacy of SEC to separate vesicles from plasma proteins, a control experiment was performed in which similar volumes from all collected fractions (as described in section 8.2) were compared for the presence of plasma protein after gel electrophoresis. The starting material, platelet-free supernatant of a platelet concentrate (1.5 mL), contained very high concentrations of proteins including albumin (66 kDa) when applied directly to gel electrophoresis (3 and 20 µL, 8.3A right gel). Evidently, after SEC low levels of protein become detectable from fraction 8 or 9 onwards, but the bulk of the protein elutes from fraction 15 onwards. Thus, vesicles, which are mainly present in fractions 9−12, are clearly separated from the bulk of soluble plasma proteins by SEC.

8.3.7 Presence of CD63 and CD9 per fraction

To confirm the detection of vesicles by flow cytometry, we performed a control experiment to study the presence of CD63 and CD9, both vesicle-associated tetraspanins, by Western blot. CD63 and CD9 were both detectable in fractions 9 and 10 (Fig. 8.3B and C, respectively), confirming the presence of vesicles in these fractions.

8.3.8 Visualization of vesicles, lipoproteins, and proteins

TEM was used to confirm the presence of vesicles or lipoprotein particles. Fig. 8.4 shows representative images of the starting material and fractions 5, 9−11, and 17−20 (Fig. 8.4A−I). In the starting material, vesicles were not visible due to the abundant presence of lipoproteins and proteins (Fig. 8.4A). To improve the visualization of the contents of the starting material and fractions 17−20, we also performed TEM on 50-fold diluted samples (Fig. 8.5A−E). In the diluted starting material, vesicles (cup shaped) as well as lipoproteins (white spheres) and proteins (white ragged structures) were visible (Fig. 8.5A). In fraction 5, no vesicles or lipoproteins are detectable (Fig. 8.4B), which confirms the results of NTA, TRPS and flow cytometry. As expected, in fraction 9 the vesicles were clearly visible, but also visible were low numbers of lipoproteins (Fig. 8.4C). Vesicles were also visible in fractions 10 and 11 (Fig. 8.4D−E), but the number of lipoprotein particles was increased compared to fraction 9. The vesicles in fractions 9−11 range in diameter from 70 to 500 nm. Very few vesicles and an abundance of proteins and lipoprotein particles were visible in fractions 17−20 (Figs. 8.4F−I and 8.5B−E). Thus, TEM confirms that SEC separates vesicles from proteins and lipoproteins.

8.3.9 Recovery and enrichment

As mentioned, most particles and vesicles were present in fractions 9−12. To gain insight into the extent of purification of the vesicles, we calculated the recovery of CD61-exposing vesicles, protein, and HDL cholesterol of fractions 9−12 compared to the starting material (Fig 8.6A). In fraction 9, the recovery of vesicles was 14 ±

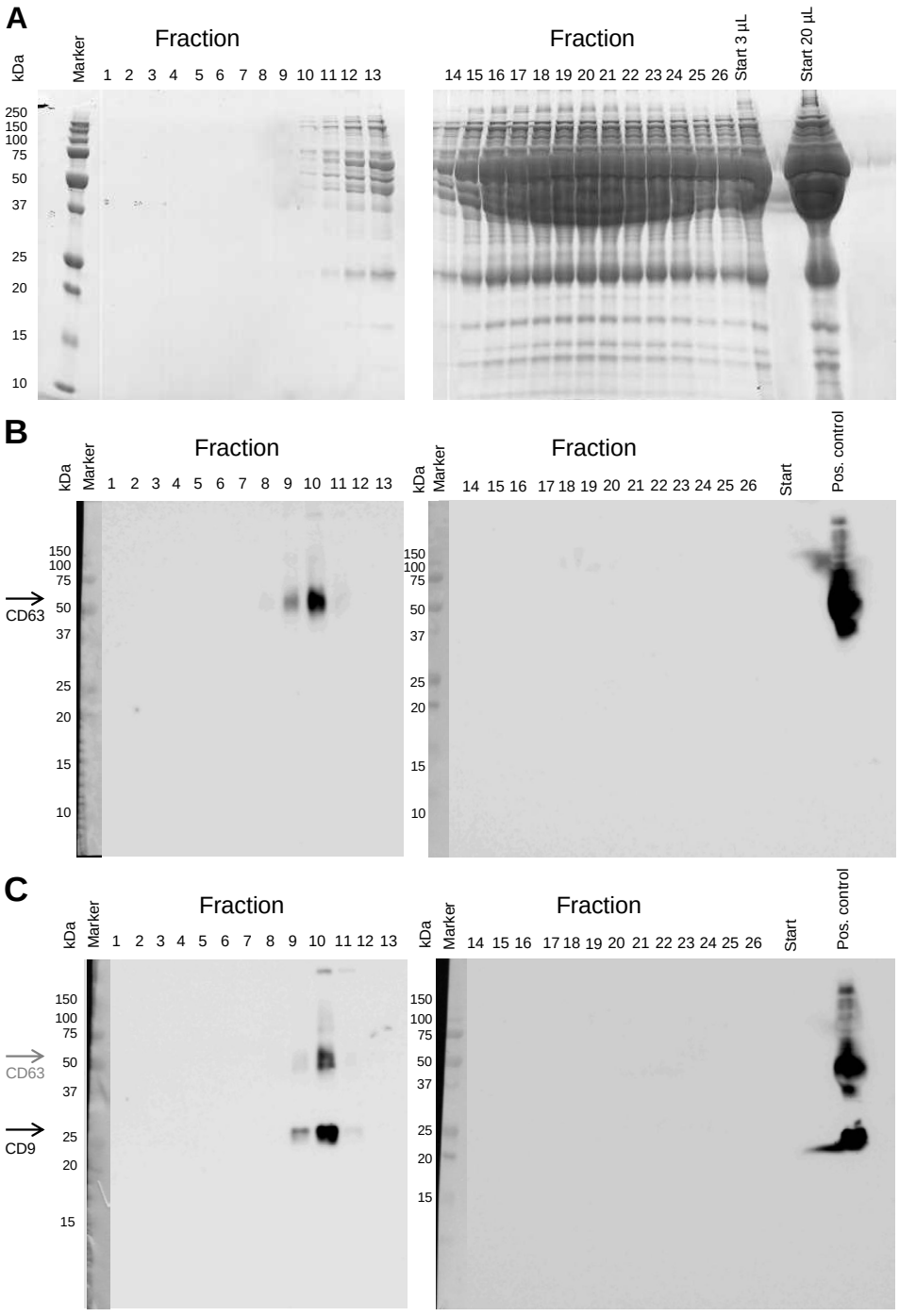

Figure 8.3: Presence of proteins, CD63, and CD9 in collected fractions. (continued)

Figure 8.3: (A) The presence of proteins in each fraction determined by loading 20 µL on PAGE gels. The molecular weight of albumin is 66 kDa. (B,C) Presence of tetraspanins in the different fractions was studied by Western blot, with 4 µg protein used per fraction. First, the presence of CD63 was shown (53 kDa, panel B), and next the presence of CD9 was shown (24 kDa, panel C). The tetraspanin bands are indicated by arrows in panels B and C. Platelet lysate was used as positive control.

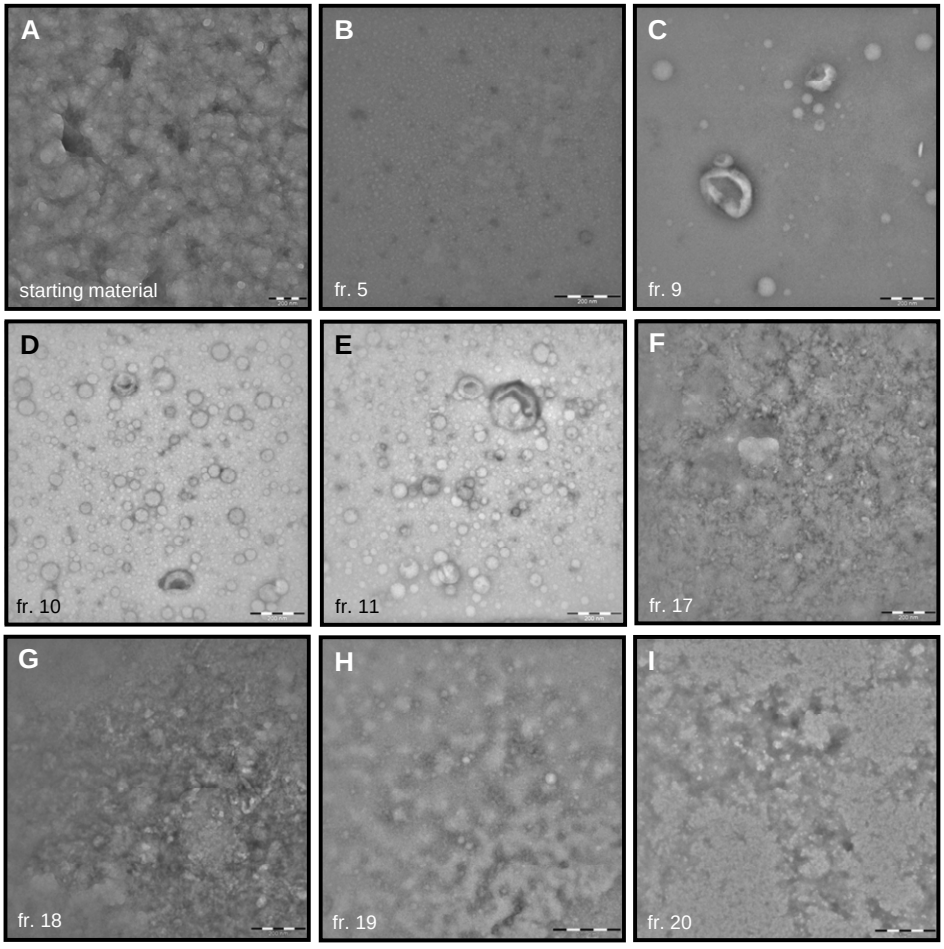

Figure 8.4: Transmission electron microscopy images of starting material (A), fraction 5 (B), fractions 9−11 (C-E), and fractions 17−20 (F-I). All samples were undiluted. Scale bars are 200 nm (A−G), 500 nm (H), and 1 µm (I).

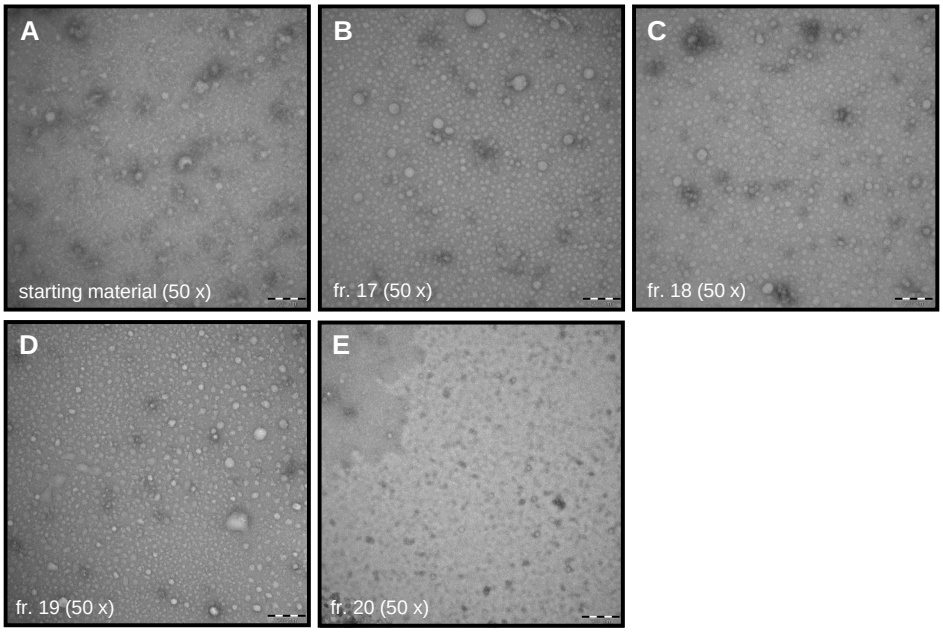

Figure 8.5: Transmission electron microscopy images of starting material (A), and fractions 17–20 (B-E). All samples were diluted 50-fold in PBS prior to fixation. Scale bars are 200 nm.

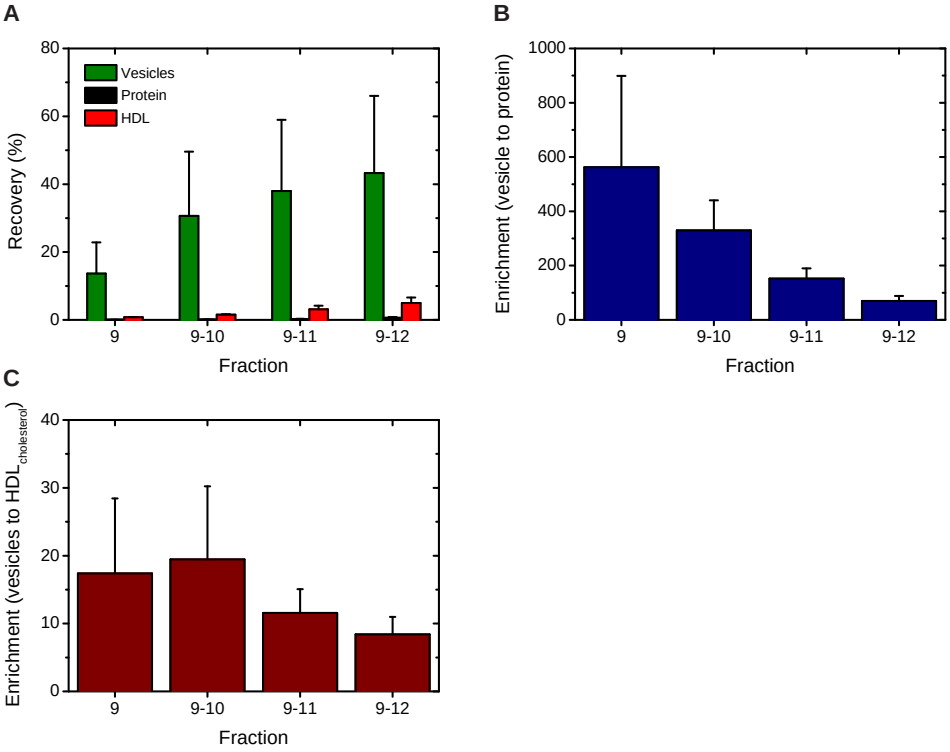

Figure 8.6: Recovery and enrichment in the vesicle-containing fractions (9, 9−10, 9−11, 9−12) relative to the starting material. (A) Recovery of vesicles, protein, and HDL (cholesterol) in the vesicle-containing fractions. (B) Enrichment factor of vesicle to protein. (C) Enrichment factor of vesicle to HDL (cholesterol).

8

9 % and the recoveries of protein and HDL cholesterol were low, 0.023 ± 0.010 % and 0.80 ± 0.07 %, respectively. Thus, sepharose CL-2B SEC results in a 560 ± 340-fold enrichment of vesicles compared to proteins in the starting material (Fig. 8.6B), and a 17 ± 11-fold enrichment of vesicles compared to HDL cholesterol (Fig. 8.4C).

When fractions 9 and 10 were combined, the recovery of vesicles was 31 ± 19 %, but this increase was at the expense of an increased contamination with protein and HDL cholesterol compared to fraction 9 alone (Fig. 8.6A). Nevertheless, combining fractions 9 and 10 gives a 330 ± 110-fold enrichment of vesicles compared to protein (Fig. 8.6B), and a 19 ± 11-fold enrichment of vesicles compared to HDL cholesterol (Fig. 8.6C). Combining fractions 9−11 recovered 38 ± 21 % of the vesicles from the starting material and results in a 150 ± 40-fold enrichment of vesicles compared to protein (Fig. 8.6B), and a 12 ± 4-fold enrichment of vesicles compared to HDL cholesterol (Fig. 8.4C). Combining fractions 9−12 recovered 43 ± 23 % of vesicles from the starting material and give a 70 ± 19-fold enrichment of vesicles

compared to protein (Fig. 8.6B), and a 8 ± 3-fold enrichment of vesicles compared to HDL cholesterol (Fig. 8.6C). Thus, it is clear that the recovery of vesicles can be improved by combining fractions 9−11 or 9−12, but this result is at the expense of more contamination by protein and HDL cholesterol (Fig. 8.6A).

8.4 Discussion

We demonstrate that vesicles can be purified from human platelet-free supernatant of platelet concentrates by sepharose CL-2B SEC. With this approach, vesicles can be easily separated from proteins and HDL. We also isolated vesicles from human plasma with SEC, which resulted in similar recoveries of vesicles, proteins, and lipoproteins in fractions 9−12 (data not shown).

SEC has several major advantages compared to differential centrifugation and density-gradient ultracentrifugation, which are the most widely applied protocols for vesicle isolation. Compared to differential centrifugation, there is no risk of protein complex formation and vesicle aggregation. In addition, the high viscosity of plasma affects the recovery of vesicles isolated by differential centrifugation [208, 219], but does not affect the recovery of vesicles by SEC.

Compared to density-gradient ultracentrifugation, buffers with physiological osmolarity and viscosity can be used. The most commonly applied density gradient for the isolation of vesicles, sucrose [294, 21, 5, 162, 223, 237, 245], may have some additional downsides. For example, isolation of organelles by sucrose density-gradient ultracentrifugation is detrimental, since these gradients are "highly viscous and grossly hyperosmotic, leading to slow sedimentation rates for small particles and loss of water from subcellular organelles" [104]. Furthermore, whereas several investigators reported a loss of biological function when vesicles are isolated by sucrose density-gradient ultracentrifugation (International Society for Extracellular Vesicles meeting Budapest, October 2013), vesicles from saliva isolated by SEC are still fully functional with regard to their capacity to induce coagulation (data not shown, personal communication C.M. Hau), indicating that the biological properties of vesicles seem unaffected after isolation by SEC. Moreover, by density-gradient ultracentrifugation, contaminants with overlapping densities cannot be isolated. For example, the density of HDL considerably overlaps with vesicles [294, 249].

The recovery of vesicles isolated with SEC is 43 ± 23 %, when combining fractions 9−12. Similar recoveries are reported after isolation of vesicles by (ultra) centrifugation and detection by flow cytometry, namely 50−80 % [147]. Furthermore, Momen-Heravi showed a recovery of 2 % of plasma vesicles after ultracentrifugation as measured by NTA [208]. In both studies, however, contamination by proteins and lipoproteins was not studied. When combining fractions 9−12, a reduction of 70-fold in the protein to vesicle ratio and 8-fold in the HDL to vesicle ratio is found. To our knowledge, it is unknown to which extent HDL and protein are reduced in the vesicle fraction after a (sucrose gradient) ultracentrifugation protocol. However, despite the reduced contamination after isolation of vesicles

with SEC, we recommend the use of blood samples collected from fasting subjects, to minimize potential contamination by chylomicrons and VLDL.

The principle of SEC is separation based on a difference in size. The sepharose beads in the column have pores with a diameter of approximately 75 nm [330, 122], and a tortuous path through the bead. A particle that can enter the beads is delayed due to the increased path length. All particles larger than $\sim$ 75 nm, including lipoproteins, cannot enter the beads and can only travel along with the void volume fluid. Based on our TEM results, the smallest vesicles that are present in fraction 9−12 have a diameter of 70 nm or larger, which confirms the theoretical separation of components below and above 75 nm.

Because the size distribution of vesicles, as measured by TRPS and NTA, does not change between the starting material and fraction 9−12 (data not shown), there seems to be no separation of vesicles in the size range from 70 to 500 nm. We confirmed this by making a mixture of 100 and 400 nm silica beads. After application of SEC, 45−48 % of both sizes of beads were recovered in fractions 9−12, confirming no separation within this size range (data not shown).

Vesicles smaller than $\sim$ 75 nm are probably present in the fractions high in HDL, that is fractions 18−20. From the size distributions of vesicles in urine [235] and erythrocyte concentrates (Y. Yuana, personal communication), we estimate that approximately 50 % of all vesicles are larger than 75 nm. It is unknown whether vesicles smaller than 75 nm harbour different clinical information than the larger vesicles. Sepharose CL-2B has relatively large pores. Choice of a sepharose with smaller pores may allow the isolation of vesicles smaller than 75 nm, albeit with higher contamination by lipoproteins.

We used sepharose CL-2B in a 10 mL plastic syringe (Fig. 8.1), which has a diameter of 1.6 cm and a height of 6.2 cm. We expect that the column height, column diameter and sample volume can be optimized to improve separation of vesicles from contaminants and the recovery of vesicles. For example, a longer, narrower column with the same volume of sepharose may result in an improved separation of protein and vesicles. A narrower column with a smaller volume of sepharose and the same length, on the other hand, may result in a higher recovery of vesicles. Investigators should optimize those parameters to their own experimental needs.

Because the size distribution of vesicles does not vary between fractions 9 and 12, we assume that the vesicles in each fraction are comparable. Fraction 9 is the purest vesicle fraction, but contains only 14 % of the vesicles in the starting material. The method used for further analysis determines whether it is best to collect only fraction 9 or to combine multiple fractions. For example, for proteomics the lowest possible contamination with protein is essential and the use of fraction 9 only may be optimal. For TEM imaging, the background is much improved when comparing fractions 9−11 to the starting material (Fig. 8.4A−D). Combining multiple fractions may result in a higher density of vesicles on the TEM grid, speeding up the analysis. For flow cytometry, we prefer a higher concentration of vesicles if this does not lead to swarm detection [218, 234], and thus fractions 9−12 would be combined.

In conclusion, this chapter shows that vesicles of a diameter larger than 75 nm can be isolated from complex body fluids, such as plasma, by single-step SEC. Purification of vesicles in combined fractions 9−12 relative to protein and HDL is 70- and 8-fold, respectively. Recovery of vesicles with sepharose CL-2B SEC is 43 % compared to 2−80 % with ultracentrifugation. Thus, compared to ultracentrifugation, SEC results in a good recovery of vesicles with almost complete removal of contaminants. Furthermore, vesicle isolation by sepharose CL-2B SEC takes less than 20 min, compared to 2−96 h for ultracentrifugation, thus vesicle samples can be prepared for analysis on the same day of collection. In addition, sepharose CL-2B SEC components cost approximately €15,- and no expensive equipment is needed. Thus, isolation of vesicles by SEC is quick, cheap, and easy.

CHAPTER 9

Beyond the state of the art: detection of extracellular vesicles by specialized techniques

Abstract

Cell-derived or extracellular vesicles, including microvesicles and exosomes, are abundantly present in body fluids such as blood. Although such vesicles have gained strong clinical and scientific interest, their detection is difficult because many vesicles are extremely small with a diameter of less than 100 nm, and, moreover, these vesicles have a low refractive index and are heterogeneous in both size and composition. In this chapter, we focus on four methods that are not commercially available: Raman microspectroscopy, micro nuclear magnetic resonance, small-angle X-ray scattering (SAXS), and anomalous SAXS. These methods are currently being explored to study vesicles and are likely to offer novel information for future developments.

Parts of this chapter have been published as:

- E. van der Pol E., F.A.W. Coumans, Z. Varga, M. Krumrey, and R. Nieuwland. Innovation in detection of microparticles and exosomes. *J. Thromb. Haemost.* **11**(Suppl. 1), 36−45 (2013)

9.1 Introduction

Cell-derived (extracellular) vesicles contain a phospholipid bilayer and have diameters ranging from 50 nm to 5 µm [231]. We will use the term "vesicles" for all vesicles in human body fluids and culture media because no consensus exists on nomenclature and classification [231]. The scientific and clinical interest in vesicles is increasing as they contribute to health and disease processes and are potentially useful as biomarkers and therapeutic agents.

The detection of vesicles is extremely challenging because many vesicles have a diameter of less than 100 nm, have a low refractive index, are highly heterogeneous [235], and are sensitive to collection and handling conditions [235, 333, 177, 336, 236, 70]. Detection limitations have practical consequences because methods such as flow cytometry have been pushed to their limits, resulting not only in improved detection but also in measurement of artefacts.

Vesicles have been studied extensively by electron microscopy and functional (coagulation) assays since the 1950's. Many investigators, including ourselves, have used flow cytometry for the detection of vesicles since the 1990's, but owing to the use of novel technologies, such as nanoparticle tracking analysis (NTA), dynamic light scattering (DLS), and tunable resistive pulse sensing (TRPS), we have learned that many vesicles are too small to be detected as single vesicles by flow cytometry. Since then, the detection of vesicles has gained considerable interest, and at present, a plethora of detection methods are being explored and no gold standard exists for the detection of vesicles. In parallel, attempts are being made to standardize vesicle measurements and pre-analytical variables.

To illustrate the presence and dimensions of vesicles in body fluids, Fig. 9.1A shows a size distribution of vesicles in 1 mL platelet-free plasma after a single freeze/thaw cycle, measured with NTA (Nanosight, Amesbury, UK). The total number of particles/vesicles in this sample is $7.3 \cdot 10^{10}$ mL^{-1}, with a total surface area of 22 cm^2 (Fig. 9.1B) and a total volume of 73 nL (Fig. 9.1C). Thus, the total volume of the particles/vesicles is approximately 85-fold less than of leukocytes in 1 mL of blood, whereas the total surface area is comparable.

Please also note that the size of vesicles is within a range of easily detectable contaminants such as immune complexes [120, 132, 16], calcium-phosphate microprecipitates [182], liposomes and other particles [90], and fluorescent antibody aggregates [6], which may introduce artefacts in any of the techniques described in this chapter. For example, we can erroneously reproduce the finding that 'platelet-derived microvesicles' are present in synovial fluid, but only when we do not remove the fluorescent antibody aggregates before labeling of the vesicles [29, 41]. The distributions shown in Fig. 9.1 may be affected by the presence of contaminants. Nevertheless, Fig. 9.1 illustrates that vesicle measurements require instruments capable of detecting the majority of such particles/vesicles in a large size range.

In this chapter, we focus on four methods, which are not yet commercially available, but are likely to offer new and relevant information and directions for future research.

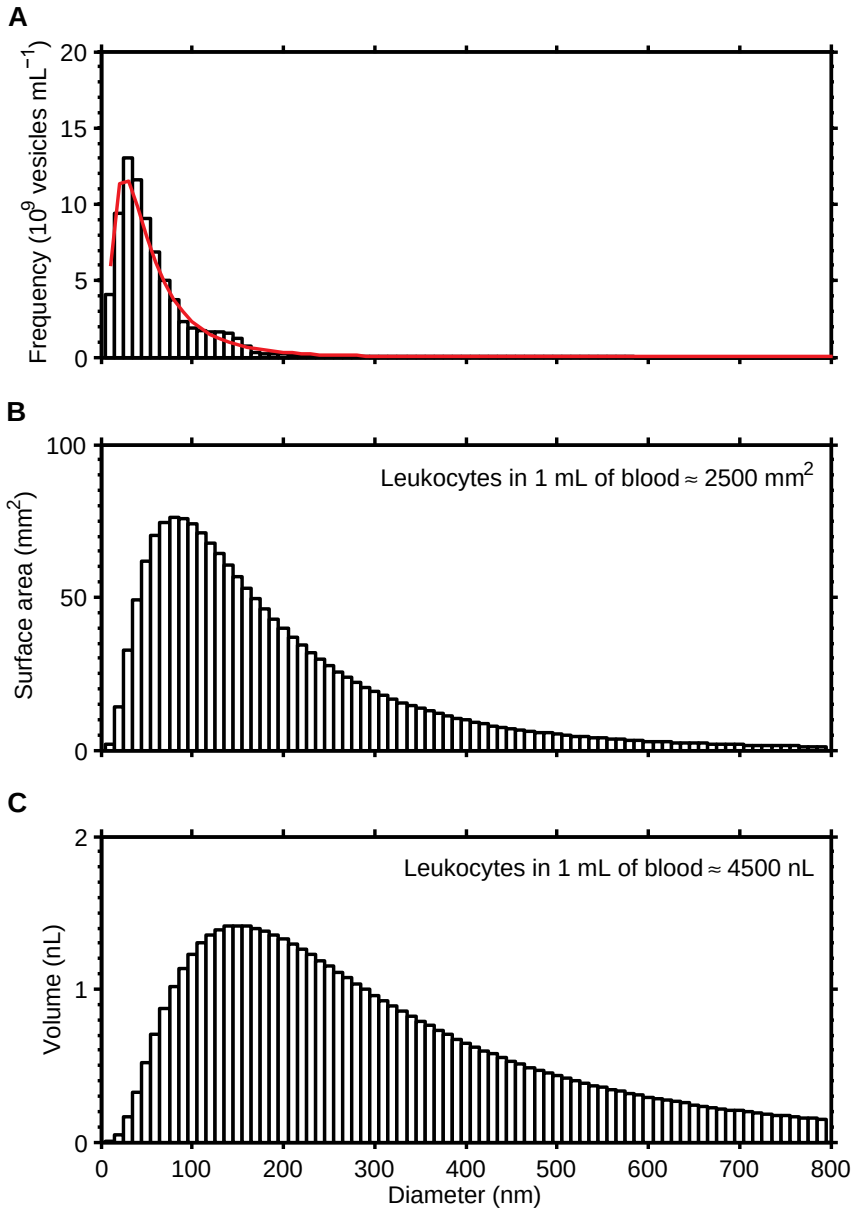

Figure 9.1: Properties of vesicles in plasma. (A) Distribution of particle/vesicle sizes present in 1 mL plasma (histogram bin width 10 nm) and a log-normal distribution that was least squares fit to the data (red line). The log-normal fit was used to derive the distribution of vesicle surface area (B) and total vesicle volume (C) per 10 nm bin. For comparison, the total surface area and total volume of $5 \cdot 10^6$ leukocytes is shown in panels B and C, respectively.

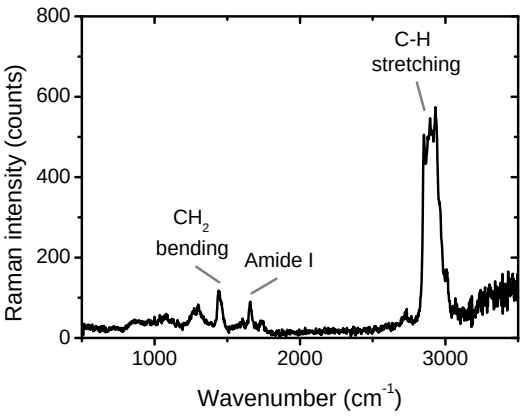

Figure 9.2: Raman spectrum of a single erythrocyte-derived vesicle. The Raman spectrum of a single erythrocyte vesicle is shown in suspension after subtraction of the background spectrum of the medium. The peaks reveal specific chemical bonds, which are present in this vesicle. For instance, the peak at 1,654 cm^{-1} is characteristic for Amide I, the peak at 1,440 cm^{-1} is characteristic for methylene (CH_2) bending, and the peak at 2,947 cm^{-1} is characteristic for hydrocarbon (C–H) stretching.

9.2 Beyond state of the art: detection of vesicles by specialized techniques

9.2.1 Raman microspectroscopy

Raman spectroscopy is based on the detection of inelastic light scattering and is used to study the structure and chemical composition of macromolecules inside single living cells [242]. The sample is illuminated by monochromatic laser light. When the light is inelastically scattered by the sample, the wavelength shifts due to an energy gain or loss associated with molecular vibrations in the sample. Because this wavelength shift is molecule specific, Raman spectroscopy allows label-free examination. With Raman microspectroscopy, the probe volume is typically $< 1\,\mu m^3$, which overlaps with the dimension of vesicles. Fig. 9.2 shows the Raman spectrum of a single vesicle isolated from an erythrocyte concentrate by differential centrifugation. This spectrum was obtained using a confocal Raman microspectrometer, in which a 647 nm laser with a power of 100 mW was focused on a probe volume of $0.3\,\mu m^3$ [240]. Due to the high irradiance, the vesicle was optically trapped in the laser beam. The peaks in the spectrum are specific to the chemical bonds and symmetry of the molecules. Because the amplitude of the signal is linearly proportional to the number of molecules, Raman microspectroscopy is a quantitative technique. Recently, Raman microspectroscopy was applied to study vesicles of Dictyostelium discoideum, a convenient model to study eukaryotic vesicles [287]. Without labeling, at least two different types of vesicles were identified, illustrating that Raman microspectroscopy allows label-free distinction between single vesicles of different composition.

Applicability and limitations

Raman microspectroscopy is a relatively expensive and specialized method with limited availability. In addition, a measurement takes considerable time, because

trapping is a stochastic process and because the intensity of Raman scattering is weak compared with Rayleigh scattering. Consequently, acquisition times in the order of seconds per vesicle are required. Thus, with the current state of the art, obtaining Raman spectra from 1,000 vesicles would take hours.

New developments

To obtain simultaneous information on the size, concentration, and chemical composition of single vesicles in suspension without fluorescence antibody labeling, we will combine Raman microspectroscopy with TRPS (qNano). The sample stream in the qNano will force vesicles through the focused laser beam to reduce measurement time.

9.2.2 Micro nuclear magnetic resonance (μNMR)

Nuclear magnetic resonance (NMR) can be used to measure the magnetic susceptibility of a sample, that is, the degree of sample magnetization in response to an applied magnetic field. In general, biological samples have negligible magnetic susceptibility [265], but using magnetic nanoparticles conjugated to an antibody, the presence of an antigen exposed on a vesicle can be detected. The miniaturized micro nuclear magnetic resonance (μNMR) system [142] is a lab-on-a-chip NMR device capable of measuring the large contrast in magnetic susceptibility between biological samples and magnetic nanoparticles. Vesicles with a diameter of 50−150 nm are loaded into multiple parallel chambers, each chamber containing a 50 nm pore size filter to prevent the vesicles from leaving the chamber while allowing reagents to pass through the chamber. Each chamber is labeled with a different antibody conjugated to 38 nm ferrite nanoparticles [264]. The number of vesicles present in a chamber is estimated by labeling vesicles in one of the chambers with an antibody directed against CD63, a tetraspanin exposed on many vesicles. The magnetic susceptibility detected in the parallel sample chambers is normalized for the CD63 signal to account for variations in the number of vesicles in each chamber. The μNMR system detects the presence of magnetic nanoparticles in the sample chamber with great sensitivity. For example, the CD63 signal from 10^4 vesicles could be detected, which is claimed to be a 1,000-fold more sensitive than ELISA. The sample size is 1 μL per chamber and the measurement time approximately 1 h.

Applicability and limitations

The μNMR has been applied to detect glioblastome multiforme (GBM) vesicles in plasma of mice and humans [142]. μNMR provides no information on single vesicles. Nevertheless, the high sensitivity of this method beholds great promise to detect rare vesicles, such as tumor-derived vesicles in plasma samples. For example, in GBM, vesicles may be a new serological biomarker in a field where the currently available biomarkers are insensitive and expensive to measure [142]. The number of different antigens that can be detected can be expanded by loading

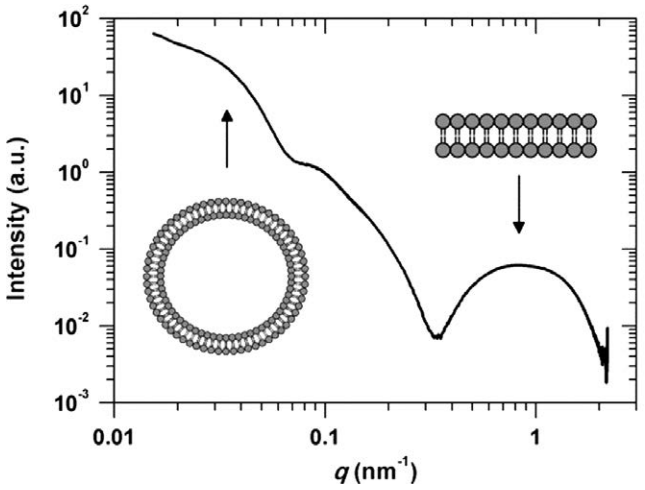

Figure 9.3: Scattered intensity of phospholipid vesicles by SAXS. The scattering intensity curve of 100 nm phospholipid vesicles provides information about the size (low q) and bilayer thickness (high q) of the vesicles. The relevant physical quantity for the dimensional characterization is the momentum transfer q, which is related to wavelength λ and scattering angle θ by $q = 4\pi/\lambda \sin\theta$.

and labeling more sample chambers. Changing the filter pore sizes used for sample preparation may allow biochemical characterization of vesicles of different sizes.

9.2.3 Small-angle X-ray scattering (SAXS)

Small-angle X-ray scattering is based on the elastic scattering of X-ray photons at low angles. In contrast to protein crystallography, where the atomic structure of macromolecules is determined by collecting the scattering pattern at wide angles, SAXS can provide structural information on nanomaterials, for example, the bilayer thickness of vesicles, in the 1 nm to 100 nm size range. For sufficiently monodisperse nanoparticles, a traceable size determination is possible [113, 175]. SAXS measurements require monochromatic X-rays with a wavelength below 1 nm, which is perfectly suited to probe nanomaterials. The forward scattered radiation from the sample is recorded at small angles (typically up to about 3°) with a large area pixel detector placed at variable distance (typically 1 m to 4 m) from the sample. The one-dimensional scattering curves as function of the scattering angle are obtained by radial averaging of the two-dimensional scattering pattern. The momentum transfer depends on the scattering angle and wavelength, and provides information for dimensional characterization.

SAXS was already applied to describe the organization of the lipid bilayer of various vesicles of synthetic and natural origin [45, 49, 133, 57], for example, Castorph et al. studied the structure of synaptic vesicles using SAXS and obtained detailed information on size, density, and composition [57]. Because extracellular vesicles are enclosed by a phospholipid bilayer membrane, SAXS can provide detailed information on their phospholipid bilayer structure and embedded transmembrane proteins, which are both in the nm range. In the case of objects such as vesicles with overall diameter below 100 nm, the scattering of the whole vesicle appears at low momentum transfer, enabling the characterization of the vesicle

size and shape. These features can be demonstrated for synthetic phospholipid vesicles, which are commonly used as model systems for biological membranes and as drug delivery vehicles. The scattered intensity of a liposome system with a diameter of 100 nm is shown in Fig. 9.3.

Applicability and limitations

While SAXS has been applied in soft matter science, two main limitations have to be considered. The scattered intensity relates to the sixth power of the radius in the case of spherical particles, causing large differences in the scattering signal from particles with different sizes. As a consequence, the scattering from samples containing vesicles with large differences in diameter may lead to ambiguous determination of the size distribution. As small-angle scattering results from electron density discontinuities, the second limitation is the decrease in the scattered intensity with decreasing (electron) density contrast. Therefore, SAXS characterization of biological materials that have a low electron density contrast relative to the aqueous media requires very intense monochromatic X-rays, which are usually available only at synchrotron radiation facilities. Fig. 9.4A shows the electron storage ring BESSY II with 250 m circumference in Berlin, together with the laboratory of PTB [26]. Beamline 2a in this figure is the 40 m long four-crystal monochromator beamline. The SAXS set-up of Helmholtz-Zentrum Berlin is installed at this beamline as shown in Fig. 9.4B. The monochromatized and collimated X-ray beam interacts with the sample placed in a vacuum chamber.

9.2.4 Anomalous small-angle X-ray scattering (ASAXS)

Biological samples exhibit complex small-angle scattering curves due to their multicomponent nature and hierarchical structural characteristics. Identifying each scattering contribution is the main challenge in the interpretation of SAXS curve of samples such as vesicles. Separation of the scattering contributions of the different constituents of this complex system can be achieved using anomalous small-angle X-ray scattering (ASAXS). Because every chemical element has characteristic X-ray absorption edges, the presence of each element can be detected by recording scattering curves at appropriate wavelengths. In case of vesicles, ASAXS can identify the contribution from proteins (sulfur), phospholipids, and nucleic acids (phosphorus). For example, the distribution of proteins between the inner and outer side of the phospholipid bilayer can be determined, as well as the thickness of the bilayer. Because the absorption edges of relevant elements of vesicles are at photon energies below 3 keV, where the penetration length of X-rays is limited, the commonly used glass capillaries have to be replaced by a dedicated sample cell with thin ($< 1\,\mu m$) silicon nitride windows. The sample cell and the detector have to be placed in vacuum. A vacuum-compatible large area X-ray detector has become only recently available and will be used to study vesicles present in human body fluids in the METVES project (`www.metves.eu`) [88].

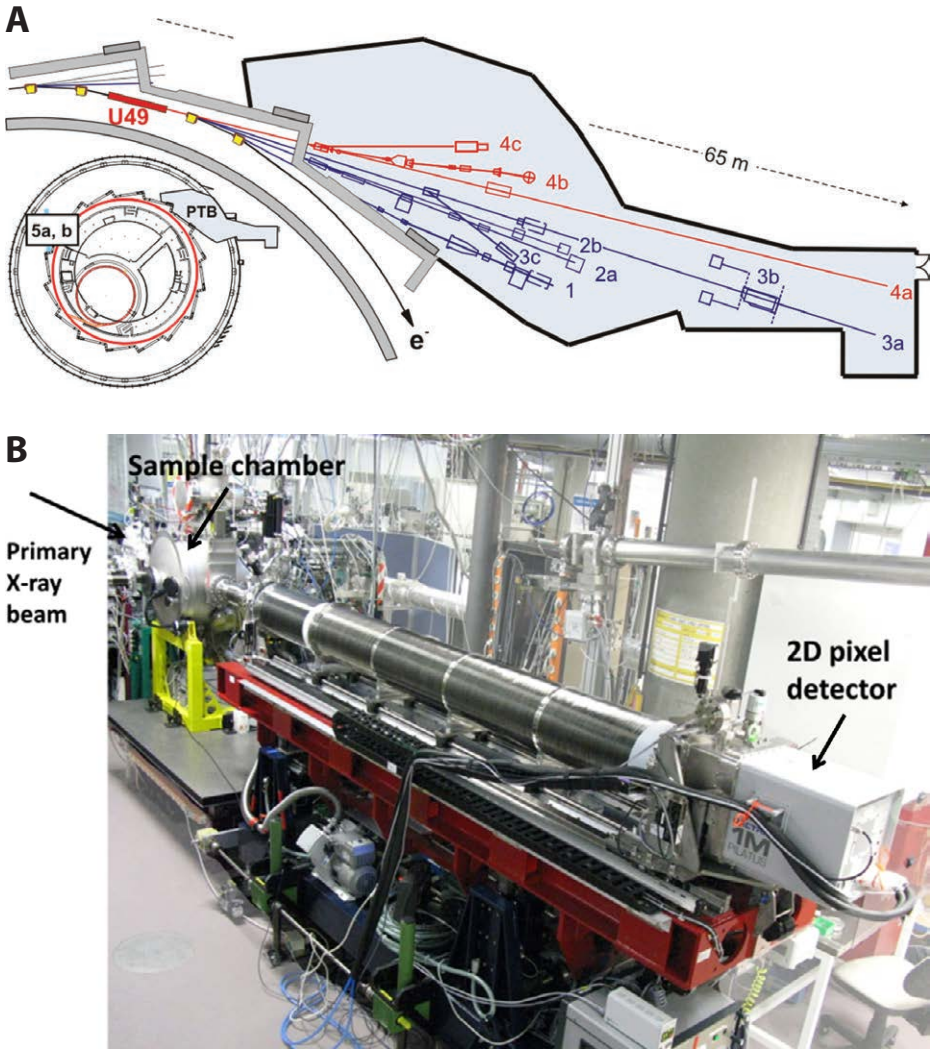

Figure 9.4: Measuring vesicles by Small-Angle X-ray Scattering. (A) The layout of the PTB laboratory at the BESSY II synchrotron radiation facility in Berlin (Germany). The ring circumference is 250 m. (B) The generated X-ray photons pass the four-crystal monochromator beamline.

9.3 Discussion

Vesicles have become firmly established entities, a fact illustrated by founding of the International Society for Extracelluar Vesicles (`www.isev.org`). Only recently it has become apparent, however, by application of novel commercially available technologies such as NTA and TRPS, that many vesicles are extremely small with a diameter of less than 100 nm. The straightforward detection of such vesicles is hampered by their small size, high concentration, low refractive index, and heterogeneity in size, composition, and morphology.

We have also shown that exciting attempts are now being made to explore the cutting edge of physical and biochemical know-how to improve the detection of vesicles. Some of the methods, such as SAXS, can provide the absolute size or size distribution of vesicles in suspension, whereas other methods, such as Raman microspectroscopy, have the potential to obtain biochemical information, such as cellular origin, on the level of single vesicles directly in suspension without labeling.

For the vesicle field to leap forward, the detection limits of existing technologies need to be pushed further or the detection limits need to be improved by combining technologies and developing new technologies. With more sensitive technology, we expect to gain a growing insight into the composition, biological and clinical relevance of vesicles in health and disease.

CHAPTER 10

Discussion and outlook

The topic of this thesis is the detection of extracellular vesicles as biomarkers for disease. To give an example of biomarkers, Table 10.1 shows normal hematology values of blood cells. Such tables are used in hospitals to recognize abnormal values and diagnose patients. In the future, extracellular vesicles will become part of hematology tables, as their concentration correlate with disease. For this future to materialize, vesicle science will need a solid foundation. Prerequisites for the development of vesicle biomarkers are: (1) knowledge of physical properties of vesicles, (2) insight into capabilities and limitations of detection techniques, (3) availability of techniques with the capability of deriving the cellular origin and function of vesicles and with improved sensitivity compared to current state-of-art technology, and (4) standardization of measurements.

10.1 Impact of the physical properties of vesicles on their detection

From a biological and clinical perspective, the most relevant properties of extracellular vesicles are their cellular origin and function (*Chapter 2*). However, the cellular origin can only be measured indirectly, whereas a functional test, such as the fibrin generation test, requires isolation of numerous vesicles. Physical detectable properties of vesicles are size, concentration, refractive index, composition (e.g. lipids, DNA, RNA, antigens, and other proteins), morphology, density, and zeta potential (*Chapter 3*). From these properties the cellular origin of vesicles may be deduced. In this thesis we focus primarily on the size, concentration, and RI of vesicles, since these three properties play a key role in vesicle detection.

Table 10.1: Normal hematology values of the most abundant blood cells in male adults [4].

Hematology parameter	Concentration (cells mL^{-1})
Platelet count	$1.50 - 4.00 \cdot 10^8$
Erythrocyte count	$4.50 - 5.50 \cdot 10^9$
Reticulocyte count	$2.5 - 10.0 \cdot 10^7$
Leukocyte count	$4.0 - 10.5 \cdot 10^6$
Total cell count	$4.7 - 6.0 \cdot 10^9$

10.1.1 Particle size distribution and concentration

Similar to others, we show that vesicles are heterogeneous in size and that their diameter ranges from 30 nm to 1 µm. We found concentrations in the order of 10^{10} vesicles/mL in urine (diameter 70−800 nm, *Chapter 4*). We demonstrate that the concentration of vesicles decreases with increasing diameter, and that this relationship can be accurately described by the power-law function. From tunable resistive pulse sensing (TRPS) and nanoparticle tracking analysis (NTA) measurements it follows that $> 80\,\%$ of the vesicles is < 100 nm in diameter. At a concentration of 10^{10} vesicles/mL, the total volume of vesicles is approximately 85-fold less than of all leukocytes in 1 mL of blood, whereas the total surface area is comparable. We speculate that the number of receptors exposed on a vesicle is proportional to the surface area, whereas the amount of cargo a vesicle can transport is proportional to the volume. Given the equal total surface area and small total volume of vesicles relative to leukocytes, we hypothesize that surface receptors are important candidates to reveal the cellular origin and potential functions of vesicles.

Several techniques, such as dynamic light scattering and small-angle X-ray scattering, measure scattering from multiple vesicles simultaneously. Due to the broad particle size distribution (PSD) of vesicles, these techniques are prone to artifacts, since scattering is dominated by the presence of a few larger vesicles (Fig. 3.1E). In addition, the distinction between coexisting vesicle types is difficult if not impossible with such bulk measurements (*Chapter 2*). To resolve coexisting vesicle types, single vesicle detection is preferred.

Flow cytometers detect single particles, but given their limited sensitivity and the power-law distribution of the vesicle PSD, the majority of vesicles are below the detection limit of common flow cytometers. However, due to the high vesicle concentration, multiple vesicles are simultaneously illuminated by the laser beam and erroneously counted as a single event signal (*Chapter 5*). We christened this phenomenon swarm detection to distinguish it from coincidence detection. With swarm detection, tens or hundreds of vesicles are continuously present in the detection volume, while coincidence detection refers to the occasional presence of two cells in the detection volume.

The most important implication of the power-law function is the strong dependence of the detected vesicle concentration on the minimum detectable vesicle size (*Chapter 4*). For example, a decrease in the minimum detectable vesicle size of only 20 nm may result in a 2.4-fold increase in the obtained vesicle concentration (Fig. 4.1). This finding emphasizes the need to quantify and monitor the minimum detectable vesicle size. For four techniques we have determined the minimum detectable vesicle size, which is 70−90 nm for nanoparticle tracking analysis (NTA), 70−100 nm for TRPS, 150−190 nm for a flow cytometer dedicated to the detection of submicrometer particles, and 270−600 nm for conventional flow cytometry. These differences in minimum detectable vesicle size contribute for $> 60\,\%$ to the 300-fold difference in concentration between these techniques (Appendix B). In addition, the differences in the minimum detectable vesicle size explains why the reported concentrations of vesicles in human plasma from healthy individuals

range from 10^4 to 10^{12} vesicles/mL [37, 316, 90, 335]. Thus, the vesicle size is not only important to distinguish vesicle types (Table 2.1), but is also an important quality parameter of vesicle concentration measurements. From now on, any reported vesicle concentration should include the detected size range.

10.1.2 Refractive index

The refractive index (RI) determines how efficiently a vesicle scatters light, which is essential to data interpretation and comparison. For urinary vesicles we obtained a mean RI of 1.37 at 405 nm, with an RI below 1.40 for 95 % of vesicles (*Chapter 6*). This RI is much lower than the frequently and often unintentionally assumed values between 1.45 and 1.63 [179, 313, 253]. To illustrate the optical impact of this finding: a 100 nm vesicle (RI=1.37) scatters approximately 90-fold less light than a similar-sized polystyrene bead (RI=1.63). The low RI of vesicles relative to water (1.34 at 405 nm) is consistent with their structure and falls within the range of estimates [235, 234, 58] based on the RI of cells [309, 31, 102, 47]. Due to the low RI, a 30 nm vesicle with a physical cross section of 700 vesicles/mL has an optical scattering cross section of only $0.02\,\mathrm{nm}^2$. Needless to say, detecting scattering from vesicles demands a sensitive detector.

We used the vesicle RI to establish the relationship between the vesicle diameter and light scattering measured by flow cytometry, which is presently the most frequently applied technique for single vesicle detection. We demonstrated that the gating strategy proposed by the Scientific Standardization Committee (SSC) collaborative workshop of the International Society on Thrombosis and Haemostasis (ISTH) selects single vesicles and cells with diameters ranging from 800−2,400 nm instead of the envisioned 500−900 nm (*Chapter 5*). Thus, for over a decade, we and others have unintentionally studied particles with diameters > 800 nm. Our finding and recent cryo-electron microscopy data suggest that these particles are empty blood cells instead of extracellular vesicles [19].

10.1.3 Applicability to other vesicle samples

We have developed a toolbox to determine vesicle properties, which we applied to urinary vesicles, since urine contains a relatively high concentration of vesicles with low contamination of similar-sized non cell-derived particles, such as lipoproteins. In other samples, we have found vesicle properties comparable to urinary vesicles. For example, the power-law function was also applicable to fit the PSD of vesicles from plasma (Fig. B.2), blood bank concentrates, and cultured cell medium (data not shown). Nevertheless, a rigorous determination of vesicle properties in other samples is still needed but challenging, since samples like plasma contain different vesicle types and similar-sized non cell-derived particles. Tools that can determine the vesicle size and concentration, as well as identify different vesicles types and distinguish vesicles from other particles need to be developed.

10.2 Outlook

In this section, the future of vesicle detection will be discussed based on the physical properties of vesicles and insight into capabilities and limitations of detection techniques.

10.2.1 Novel detection techniques

Requirements

A biomarker based on vesicle enumeration should determine the concentration of a specific vesicle type within minutes. To realize this, detection techniques need to become sufficiently sensitive to identify the cellular origin of single vesicles with diameters of 50 nm and larger. In addition, detection techniques need to be able to distinguish vesicles from impurities. To provide valuable information on the vesicle concentration, the detection volume and minimum detectable vesicle size need to be quantified. Ultimately, single vesicles are sorted to perform functional tests on subpopulations of vesicles.

Cellular origin of vesicles

Current techniques will soon meet the requirements to determine the vesicle size and concentration. Therefore, the next step is to determine the cellular origin of single vesicles. The origin of vesicles could be derived by detecting their antigen expression, for example, erythrocyte vesicles with glycophorin A (CD235), platelet vesicles with glycoprotein IIIa (CD61), or tumor vesicles with Epithelial cell adhesion molecule (EpCAM; CD326).

The number of antigens per vesicle is unknown. We can provide an initial estimate by assuming that the antigen density in the membrane of a vesicle is similar to the density in the cell membrane. In this case, a 100 nm vesicle would have 300 glycophorin A molecules (erythrocyte [81]), 100 CD61 molecules (platelet [228]), or 0−20 EpCAM molecules (T24 and SKBR3 breast cancer cell lines [79]). For comparison, a 2 µm platelet typically has 50,000 CD61 molecules. Hence, the fluorescent signals from labeled vesicles are weak. A vesicle detection technique will require quantification of the minimum detectable number of dye molecules, and determination of the efficiency with which these few receptors are labeled. Potentially, labeling efficiency can be studied by optically trapping single vesicles in the evanescent field of an optical resonator (Optofluidics, Philadelphia, PA, USA) and imaging fluorescently labeled receptors with stimulated emission depletion microscopy.

A technology leap is still needed before current immunofluorescence techniques are sufficiently sensitive to differentiate between our hypothetical 100 nm vesicles. Alternative to the antigen based identification, we could pursue vesicle differentiation based on “bulk” chemical composition measured by Raman microscopectroscopy, or differentiate based on morphology.

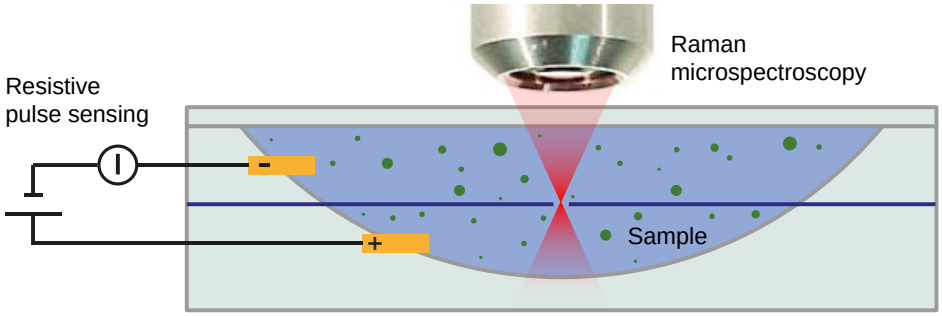

Figure 10.1: Schematic representation of hybrid resistive pulse sensing - Raman microspectroscopy. Resistive pulse sensing consists of two fluid cells divided by a non-conductive membrane (blue horizontal line). A voltage is applied by two electrodes (yellow) to flow an electrical current (I) through the pore. When a vesicle (green dots) passes through the pore, this will result in an increase of the pore resistance and a decrease of the measured current. The change in current can be related to the vesicle size. After passing through the pore, the vesicle will be optically trapped by a focused laser beam to measure the elastic scattering intensity and Raman spectrum of the vesicle.

ExoFlow

The exosome flow cytometer, or "ExoFlow", is a flow cytometer tailored to detect and characterize sub-micrometer vesicles. Due to the capability of measuring size, concentration, and multiple fluorescence signals on thousands of vesicles per second, flow cytometry is the workhorse for single vesicle detection. However, (1) size determination of vesicles by flow cytometry is inaccurate and imprecise because the vesicle RI is heterogeneous, (2) the presence of impurities reduces specificity of measurements, and (3) the sensitivity to detect vesicles $< 150-190$ nm is lacking. To overcome these problems we will integrate TRPS into the flow cell of the ExoFlow and improve the scatter sensitivity. We will use the combination of vesicle sizing by TRPS and the improved scatter sensitivity to determine the RI of all detected particles in the sample. Since the RI of urinary and plasma vesicles is 1.37 ± 0.03 (*Chapter 6*) and 1.39 ± 0.04 [169], respectively, we expect that this RI determination can be used to distinguish vesicles from protein aggregates (RI between $1.45-1.60$) [330] and bulk proteins (RI between 1.61 ± 0.02) [201].

Hybrid resistive pulse sensing - Raman microspectroscopy

TRPS can determine the size, concentration, and zeta potential of vesicles $>$ 70 nm in suspension (*Chapters 4* and *7*). While these parameters are valuable, it is unlikely that the cellular origin of a vesicle can be deduced from its size and zeta potential. This can be overcome by complementing TRPS with Raman microspectroscopy. Raman microspectroscopy can provide chemical characteristics of single vesicles (9), such as the presence of proteins, lipids, organic compounds, and genetic content, which may identify the parent cell (*Chapter 9*).

Fig. 10.1 shows a schematic representation of the hybrid resistive pulse sensing - Raman microspectroscopy system. A vesicle is driven through the TRPS nanopore by electrophoresis to determine its diameter and zeta potential. Next, the vesicle is trapped by a focused laser beam, and its backscattering and Raman signature is probed. The backscattering and size of the vesicle are used to determine the vesicle RI from Mie theory.

We are in the process of constructing this setup using a customized TRPS device (qNano, Izon, Oxford, UK) and a custom-built Raman microspectrometer. The spectrometer has a spectral range of -27 to 3,490 cm^{-1} and a spectral resolution of 4.0 cm^{-1}, which enables the identification of spectral features characteristic of phospholipid vesicles [63, 287]. After the Raman peaks that are characteristic of the origin of vesicles are known, coherent anti-Stokes Raman scattering (CARS) can be applied to increase measurement speed.

Blinking tubes measured with NTA

A study of plasma vesicles by cryo-electron microscopy [19, 143, 334] demonstrated the existence of a vesicle sub-population ($< 5\,\%$ of total) that is not round but tubular. The tubular morphology may contain information on the cellular origin of these vesicles. Since the scattering cross section of tubular particles depends on the particle orientation, and these vesicles will rotate freely in suspension, the scatter signal from these tubular vesicles will appear to blink when observed by NTA [54].

10.2.2 Standardization

In addition to novel detection techniques, clinical studies on vesicles require data comparison. Currently, data comparison on vesicles in clinical samples is hampered by the application of varying vesicle isolation procedures and different instruments. Since the minimum detectable vesicle size and thus the detected vesicle concentration is instrument dependent, there is a high demand for standardization of vesicle measurements.

Flow cytometry standardization through vesicle size approximation

We are developing a standardization procedure to improve the reproducibility of the measured concentration of vesicles by flow cytometry. Without standardization, the reproducibility of vesicles concentration measurements has an 80 % coefficient of variation (CV). The proposed standardization strategy by the SSC collaborative workshop of the ISTH improved the reproducibility to a CV of 60 %, but excluded the worst performing instruments. The main reasons for the poor performance of current standardization strategies are that differences between optical configurations of flow cytometers and differences between the RI of vesicles and beads are not taken into account.

Our solution encompasses a mixture of traceable reference beads (`www.metves.eu`) and software (`www.exometry.com`). The reference beads need to be measured

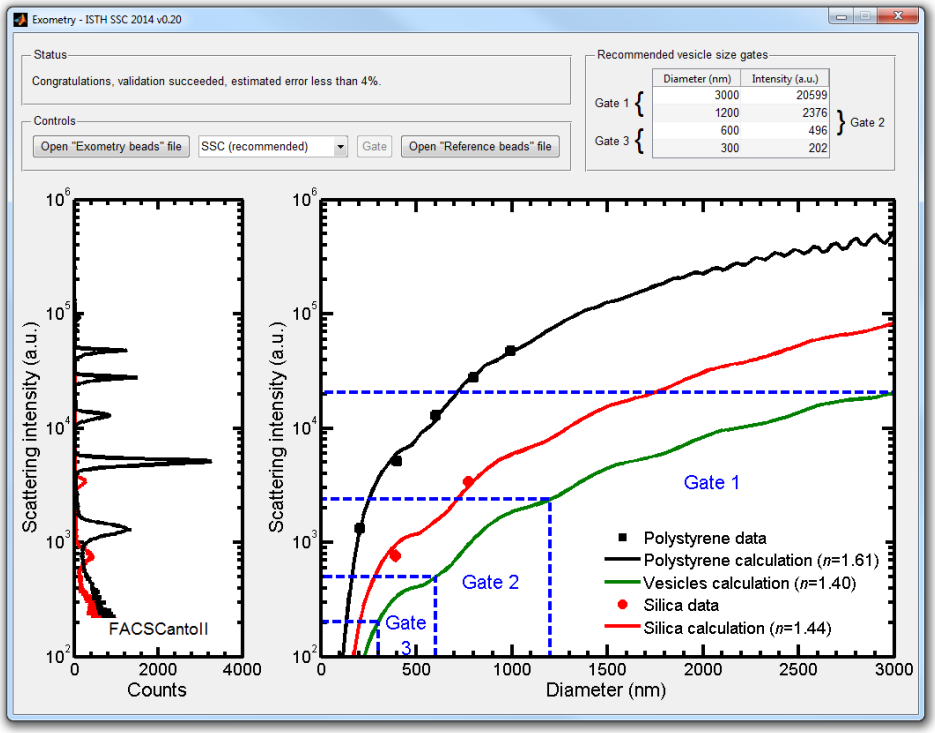

Figure 10.2: Screenshot of the software developed for flow cytometry standardization through vesicle size approximation.

Table 10.2: Fictive hematology values of the most abundant extracellular vesicles in male adults.

Hematology parameter	Concentration (vesicles mL^{-1})
Platelet vesicle count	$2.3 - 6.2 \cdot 10^9$
Erythrocyte vesicle count	$7.0 - 8.6 \cdot 10^{10}$
Reticulocyte vesicle count	$3.9 - 15.6 \cdot 10^8$
Leukocyte vesicle count	$6.2 - 16.4 \cdot 10^7$
Total vesicle count	$7.3 - 9.4 \cdot 10^{10}$

once a day and are automatically recognized by the software. The software establishes the relationship between particle diameter, RI and light scattering, which is specific for the optical configuration of the flow cytometer. Next, the software provides a vesicle size gate, which the user can apply to its own data analysis application to determine the concentration of vesicles within a predefined size range. Fig. 10.2 shows a screenshot of the software.

The standardization project is sponsored by the SSC of ISTH and involves 62 different flow cytometers in 32 clinical laboratories worldwide. The final results are expected at the ISTH 2015 congress.

10.2.3 Vesicle-based diagnostics have high potential

Our ambition is to add vesicles to the reference hematology values of blood cells in Table 10.1. An important question is how much sample would need to be analyzed to perform a vesicle-based hematology test. To make a first assessment, we assumed that the relative frequency of hematological vesicles is the same as the relative frequency of their cells of origin. Combined with a total concentration of $7 \cdot 10^{10}$ vesicles per mL blood, this resulted in the fictive hematology values of blood vesicles in Table 10.2. To count 1,000 vesicles (Poisson error $\leq 3\,\%$) of the least frequent vesicle type, we would need to analyze 100 nL blood and thus count 7.3 million vesicles. This sample volume can be perfectly handled by microfluidic chips, which may shift our single step isolation of vesicles from plasma (*Chapter 8*) to single step isolation of vesicles from whole blood [76], thereby solving several pre-analytical issues [333]. A major advantage of the vesicle hematology test would be the small sample volume. The small sample volume would lighten the phlebotomy burden on sensitive patient groups, such as neonates [44], and in addition, it might enable continuous monitoring of hematology values.

Other rare vesicles of clinical interest are tumor-derived vesicles. For prostate cancer, the median concentration of circulating tumor cells (CTCs) is 7 per 7.5 mL blood. Under the assumption that CTCs have a diameter of 30 µm [73] and break up in vesicles with a PSD that resembles the power-law distribution, the concentration of tumor-derived vesicles is $\sim 10^7\,mL^{-1}$. Blood of these patients contained 250 tumor microparticles with a diameter of 2−4 µm per 7.5 mL [73]. Extrapolating the power-law PSD from 2−4 µm particles to tumor-derived vesicles < 1 µm results in a concentration of $\sim 10^8\,mL^{-1}$. Although these numbers warrant further

investigation, they are in the same order of magnitude as the estimated leukocyte-derived vesicles in Table 10.1.

In conclusion, we have obtained a solid insight into the physical properties of vesicles and the capabilities of current detection techniques. We are developing techniques that are capable of deriving the cellular origin and function of single vesicles. These techniques will have improved sensitivity compared to current state-of-art. Standardization and rigorous characterization of the measurement techniques are essential. These are important steps towards vesicle-based diagnostics, allowing us to live healthier ever after.

APPENDIX A

Mathematical model to predict the measured vesicle size distribution

This appendix contains a mathematical model to predict the measured size distribution for a given vesicle population. In addition, this appendix contains assumptions involved in both the mathematical model and Table 3.1 of Chapter 3.

A.1 Model

To compare the performance of the various methods on size detection, we made a model which predicts the detected size distribution for a given vesicle population. The model considers the detection limit and the size resolvability of each method. With the detection limit we mean the smallest and largest biological vesicle that can be detected due to physical limitations of the applied detection technique. With size resolvability we refer to the ability of a method to resolve two populations with different particle size. The size distributions are generated without considering noise.

To account for the detection limit, the model simply rejects vesicles from the input population that cannot be detected because they are too small or too large to be detected by that method. Table A.1 shows the detection limit for each method as used by our model. For commercial flow cytometers based on light scattering, nanoparticle tracking analysis (NTA), fluorescence nanoparticle tracking analysis (F-NTA), and Coulter counters, the detection limit is provided by the references. The lower detection limit of dynamic light scattering(DLS) and fluorescence correlation spectroscopy (F-CS) depends on the polydispersity of the sample. Since large vesicles scatter more light or show more fluorescence than small vesicles, smaller vesicles cannot be detected. For DLS, we assume that all vesicles, for which the scattering coefficient per diameter range is smaller than 2^8 times the maximum detectable scattering coefficient, cannot be detected. The factor 2^8 was chosen by considering a 12-bits detector that due to noise effectively uses 8-bits to measure intensity fluctuations in the signal. With F-CS, the amount of fluorescence is assumed to be proportional to the surface area of the vesicles. All diameters for which the surface area times the concentration is smaller than 2^8 times the maximum are rejected. For stimulated emission depletion microscopy (STED), X-ray microscopy, transmission electron microscopy (TEM), and atomic force microscopy (AFM) the detection limit is supposed to be equal to the imaging resolution.

Table A.1: Detection limit, size resolvability, and full width at half maximum (FWHM) of the Gaussian function as used to calculate the size distribution of the detection methods.

Method	Detection limit (nm)	Size resolvability	Gaussian FHWM	References
Scattering flow cytometry	300	280 nm	280 nm	[253, 227, 322]
DLS	70	$F = 2$	$2/3\ d$	[137, 48, 170, 101]
NTA	50−1000	$F = 4/3$	$2/7\ d$	[56]
STED microscopy	16	16 nm	16 nm	[322]
F-CS	30	$F = 2$	$2/3\ d$	[276]
F-NTA	1	$F = 4/3$	$2/7\ d$	[56]
X-ray microscopy	12	12 nm	12 nm	[59]
TEM, AFM	1	1 nm	1 nm	[36]
Impedance-based flow cytometry	300	$F = 1.1$	$2/21\ d$	[144, 259, 340]

AFM, atomic force microscopy; DLS, dynamic light scattering; F: size resolvability factor; F-CS, fluorescence correlation spectroscopy; F-NTA, fluorescence nanoparticle tracking analysis; NTA, nanoparticle tracking analysis; STED, stimulated emission depletion; TEM, transmission electron microscopy.

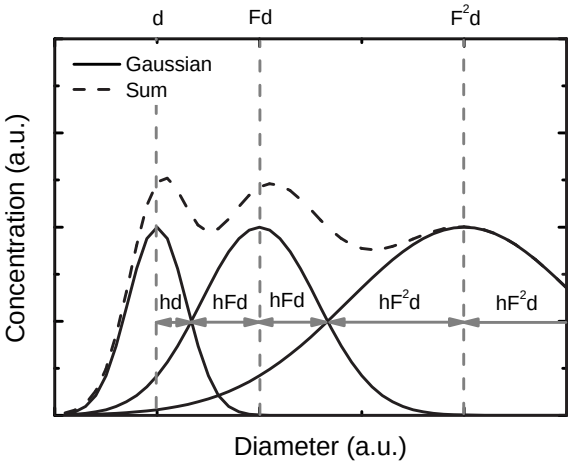

Figure A.1: Concentration vs. diameter for three Gaussian distributions centered at diameter d, dF and dF^2 (solid line) and the sum of the three Gaussian distributions (dashed line). The full width at half maximum (FWHM) of the Gaussian distributions do not overlap. Therefore, the Gaussian distributions can be resolved from their sum.

Table A.2: Wavelength (λ) and numerical aperture (NA) as used to calculate the resolution of optical microscopy, nanoparticle tracking analysis (NTA), fluorescence microscopy, and fluorescence nanoparticle tracking analysis (F-NTA).

Method	λ(nm)	NA	Resolution (nm)
Optical microscopy	532	1.4	200
NTA	635	0.4	1000
Fluorescence microscopy	532	1.4	200
F-NTA	405	0.4	600

After rejecting vesicles from the input population by considering the detection limit, the remaining size distribution is convolved with a Gaussian function to account for the size resolvability. Applying a Gaussian convolution to a size distribution is comparable to applying a Gaussian blur filter to an image. The larger the full width at half of the maximum (FWHM) of the Gaussian function, the more the image is blurred and the more difficult it is to resolve details from the image. Table A.1 shows the size resolvability and the FWHM of the Gaussian function for each method as used by our model. For commercial flow cytometers based on light scattering, a size resolvability of 280 nm is used [253, 227]. For all microscopy methods, the FWHM of the Gaussian function is defined by the imaging resolution. Due to the physical nature of many non-imaging methods, the size resolvability is often expressed as a factor F in size difference that can be resolved. For example, for DLS the mean size of two sub populations can only be resolved from the autocorrelation of the intensity fluctuations if the size difference between the particles is roughly a factor 2 [137, 48, 170, 101]. So in case of DLS, a sub population of vesicles with 200 nm in diameter can potentially be resolved from a sub population of 400 nm vesicles, but a sub population of 400 nm vesicles cannot be resolved from a sub population of 600 nm vesicles. We account for this by increasing the FWHM of the Gaussian function during convolution. Figure A.1 shows how we calculated the FWHM of the Gaussian function as function of the diameter d and the size resolvability factor F. The solid black curves are Gaussian distributions at position d, Fd, and F^2d. By definition, two Gaussian distributions can be resolved from their sum if their FWHM do not overlap. Mathematically this can be expressed as follows:

$$d + hd \leq Fd - hFd \tag{A.1}$$

where hd is the half width at half of the maximum of the Gaussian distribution. Solving Eqn. A.1 for the FWHM gives:

$$\mathrm{FWHM}(d) = 2hd \leq 2\frac{F-1}{F+1}d \tag{A.2}$$

By using Eqn. A.2 to calculate the FWHM of the Gaussian function as function of d, the sum of the three Gaussian functions from Fig. A.1 can still be resolved, as shown by the dashed curve.

A.2 Assumptions involved in model and table 3.1

A.2.1 Resolution

The resolution of optical microscopy, NTA, fluorescence microscopy, and F-NTA are determined using Eqn. 3.1. Table A.2 summarizes the used values for λ and NA. Values for F-NTA are obtained from the product specifications of a commercialized system [56]. The resolution is rounded off to 100 nm, since that is approximately the order of accuracy. For the other methods described in Chapter 3, the resolution is provided by the references.

A.2.2 Measurement time

In Table 3.1, the measurement time for all microscopy methods for imaging 10,000 particles is estimated at 1 h or longer. We assume that one image contains on average 100 particles. Although recent technological developments yield an image acquisition time faster than 1 s for each method [323, 332, 160, 141], taking 100 images within 100 s is currently not feasible since several actions have to be performed before an image can be acquired. For example, the region of interest has to be selected and for some methods the focal distance must be set. Sample regions might be damaged or simply contain no vesicles, which requires human intervention in case of automated microscopes. Therefore, assuming a measurement time of 1 min per image is more realistic, resulting in a total measurement time of 1 h or longer. For routine clinical use, imaging of vesicles requires dedicated image analysis software to process the data quickly and accurately.

The measurement time for Raman spectroscopy on 10,000 particles is estimated at 3 h or longer, based on the setup of Dr. C. Otto. In this setup, vesicle tracing is automated using scanning electron microscopy (SEM) and high-speed nanometer resolution positioning stages. The time to measure the Raman spectrum of a single vesicle is assumed to be 1 s, so the measurement time of 10,000 particles is in the order of 3 h. For the other methods described in Chapter 3, the measurement time is provided by the references.

A.2.3 Hydrodynamic diameter

Table 3.1 states that DLS, NTA, F-CS, and F-NTA provide the particle diameter under the assumption of $d = d_h$. Instead of determining the diameter d of a particle, the methods determine the hydrodynamic diameter d_h. That is the diameter of a perfect solid sphere that has the same translational diffusion properties as the particle being measured. We assume that d equals the d_h.

APPENDIX B

Mathematical function to fit the particle size distribution of vesicles

In Chapter 4, we have used a mathematical function to describes the relationship between the concentration and diameter of vesicles. To select the mathematical function that optimally describes the particle size distribution (PSD), we have fitted the PSD of the vesicle standard as measured by transmission electron microscopy (TEM) and tunable resistive pulse sensing (TRPS) with six empirical functions that are frequently used to describe PSDs of particles in suspension [155]: the exponential function, the Gamma function, the Lorentzian function, the power-law function, the Weibull distribution, and the log-normal distribution. We selected TEM and TRPS as the most accurate methods to determine the PSD of vesicles. The exponential function is given by

$$C(d) = ce^{-bd} \tag{B.1}$$

where C is the concentration of vesicles as function of the diameter d, c is a scale factor for the particle concentration, and b is a fit parameter. The exponential function becomes a Gamma function by adding an extra slope parameter a:

$$C(d) = cd^a e^{-bd} \tag{B.2}$$

The Lorentzian function is given by

$$C(d) = \frac{2C_{tot}}{\pi} \frac{w}{4(d-d_c)^2 + w^2} \tag{B.3}$$

where C_{tot} is the total concentration, and d_c and w specify the location of the peak and the full width at half maximum of the distribution, respectively. The power-law function is given by

$$C(d) = k \left(\frac{d}{d_0} \right)^{-m} \tag{B.4}$$

where k has the same dimension as C and m is a non-dimensional constant. Parameter $d_0 \equiv 1$ and has the same dimension as d to create a dimensionally homogeneous equation. The Weibull distribution is given by

$$C(d) = \frac{ca}{b} \left(\frac{d-d_s}{b} \right)^{a-1} \exp\left[-\left(\frac{d-d_s}{b} \right)^a \right] \tag{B.5}$$

where c is a scale factor for the particle concentration, a is a non-dimensional constant, and d_s is the smallest particle diameter of the distribution. Parameter b has the same dimension as d to create a dimensionally homogeneous equation. The log-normal distribution is given by

$$C(d) = \frac{C_{tot}}{\sqrt{2\pi}\sigma d} \exp - \frac{\ln(d/\mu)^2}{2\sigma^2} \tag{B.6}$$

where C_{tot} is the total concentration, and μ and σ are the mean and standard deviation of the natural logarithm of the distribution, respectively.

The PSD of vesicles is an asymmetrical distribution, but the Lorentzian function is symmetrical, the exponential function, Gamma function, and power-law function diverge as the particle size tends to 0, and the Weibull distribution diverges as the particles size tends to d_s. Thus, the shape of these functions differs from the shape of the PSD of vesicles. However, these functions can still be used to describe a part of the PSD. In fact, for all methods except TEM the full PSD is not measured due to the presence of vesicles that are smaller than the lower detection limit. Therefore, functions are fitted to data on the right-hand side of the peaks only. Fitting was done by taking the natural logarithm of both the function and the data and performing a least square fit. Fig. B.1 shows the PSD of the vesicle standard measured by TEM and TRPS fitted by an exponential function, a Gamma function, a Lorentzian function, a power-law function, and a Weibull distribution. Fig. B.2A shows the PSD of the vesicle standard measured by TEM fitted by a log-normal distribution. Due to the "long tail" at the right-hand side of the log-normal distribution, the fit did not converge for data on he right-hand side of the peak. Therefore, the log-normal distribution is fitted to the full PSD obtained by TEM only, since the PSD by TEM is not affected by the lower detection limit. The obtained fit parameters are listed in Table B.1. To determine the goodness-of-fit, the reduced χ^2 and the adjusted R^2 were calculated for each fit and listed in Table B.2 .

Best fits were obtained with the Gamma function, power-law function, and the Weibull distribution. For further analysis, we selected the power-law function, since it is least susceptible to the minimal detectable vesicle size and it has the least fit parameters. To show that the power-law function is not only applicable to fit the PSD of the vesicle standard, we have applied it to vesicles from plasma. Fig. B.2B shows that also the PSD of vesicles from platelet poor plasma as measured by TRPS can be well-described by a power-law function.

To show that the detected concentrations of vesicles in Fig. 4.4 where primarily determined by the minimum detectable vesicle size, we have calculated the vesicle concentration of the power-law fit of TRPS between the minimum detectable vesicle size of each method and 800 nm. Table B.3 shows the actual detected vesicle concentration and the concentration expected from the minimum detectable vesicle size. For all methods except TEM, the expected concentration was within 40% of the detected concentration, confirming that the detected concentrations were primarily determined by the minimum detectable vesicle size. With TEM, the detected concentration is affected by the binding efficiency.

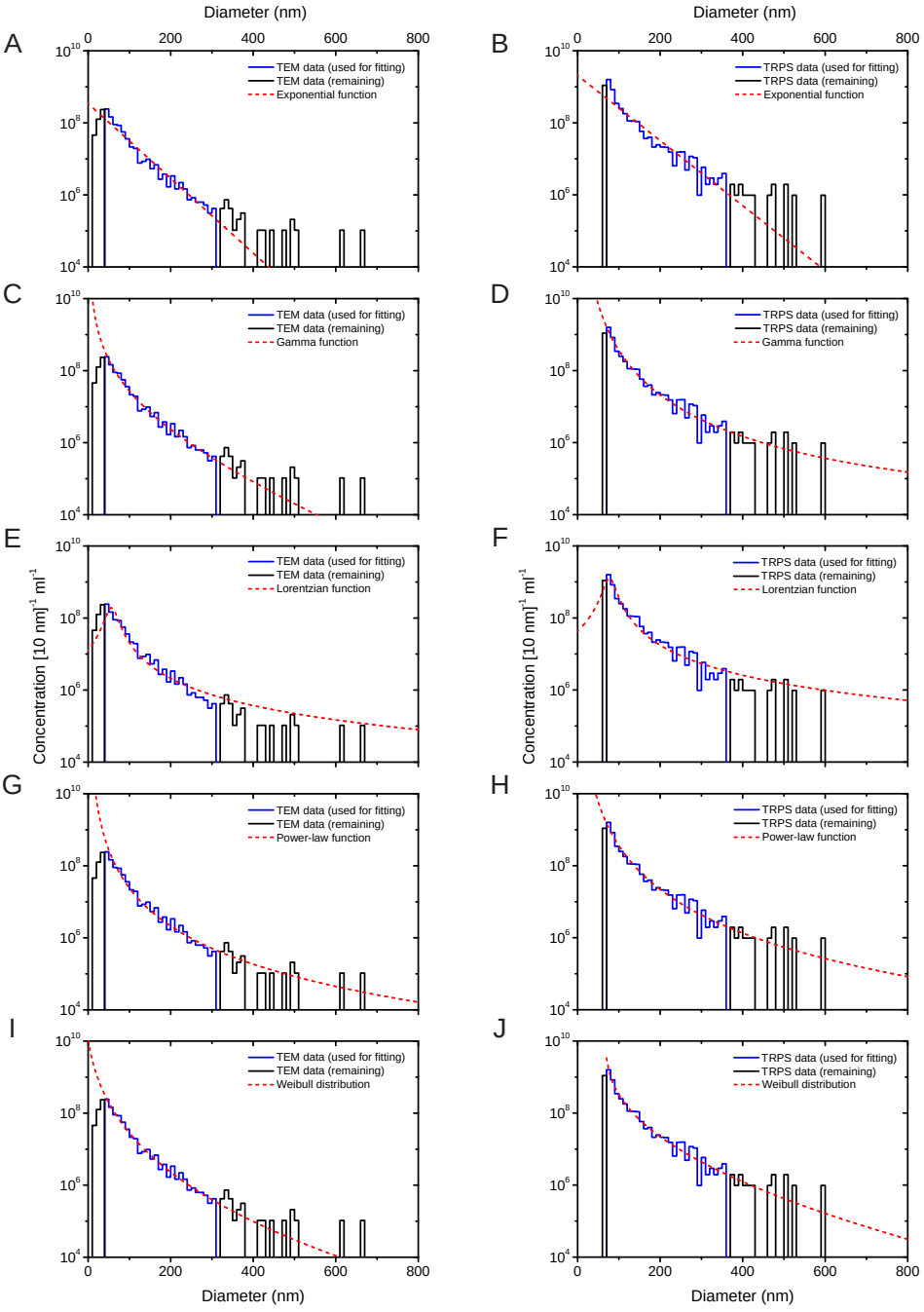

Figure B.1: Particle size distribution of the vesicle standard measured by transmission electron microscopy (TEM) and tunable resistive pulse sensing (TRPS) fitted by (A,B) an exponential function, (C,D) a Gamma function, (E,F) a Lorentzian function, (G,H) a power-law function, and (I,J) a Weibull distribution.

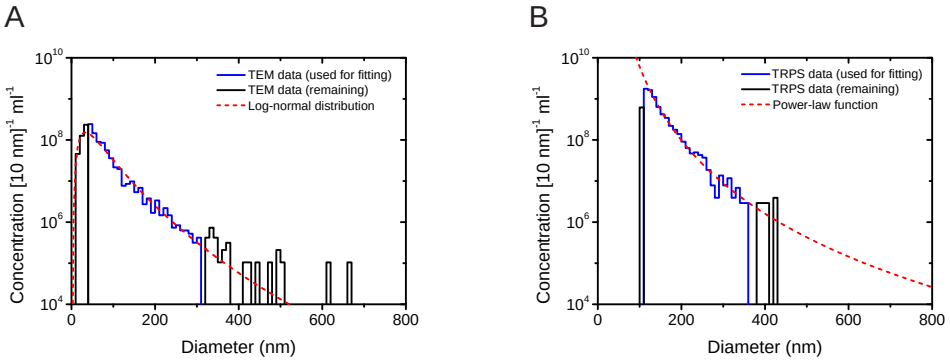

Figure B.2: (A) Particle size distribution of the vesicle standard measured by transmission electron microscopy (TEM) and fitted by a log-normal distribution. (B) Particle size distribution of vesicles from platelet poor plasma measured by tunable resistive pulse sensing (TRPS) and fitted by a power-law function using fit parameters $k = 4.520 \cdot 10^{21}$ *and* $m = 5.938$*, giving a* χ^2_{red} *of 0.14 and a* R^2_{adj} *of 0.97.*

Table B.1: Parameters used to fit the particle size distribution of the vesicle standard measured by transmission electron microscopy (TEM) and tunable resistive pulse sensing (TRPS) with an exponential function, a Gamma function, a Lorentzian function, a power-law function, a Weibull distribution, and a log-normal distribution.

Function	Parameter	TEM	TRPS
Exponential function	b	$2.389 \cdot 10^{-2}$	$2.079 \cdot 10^{-2}$
	c	$3.416 \cdot 10^{8}$	$2.050 \cdot 10^{9}$
Gamma function	a	-2.229	-4.371
	b	$9.040 \cdot 10^{-3}$	$-1.870 \cdot 10^{-3}$
	c	$1.929 \cdot 10^{12}$	$1.666 \cdot 10^{17}$
Lorentzian function	C_{tot}	$9.201 \cdot 10^{9}$	$5.824 \cdot 10^{10}$
	d_c	30.04	77.34
	w	56.43	28.95
Power-law function	k	$2.494 \cdot 10^{14}$	$3.992 \cdot 10^{16}$
	m	3.508	4.024
Weibull distribution	a	$6.199 \cdot 10^{12}$	$7.279 \cdot 10^{10}$
	b	0.1977	10.05
	c	0.3400	0.5294
	d_s	-13.18	66.28
Log-normal distribution	C_{tot}	$9.676 \cdot 10^{9}$	
	μ	0.6284	
	σ	48.99	

Parameters are explained throughout the text.

Table B.2: Results of goodness-of-fit tests applied to fitting a function to the PSD of the vesicle standard as measured by transmission electron microscopy (TEM) and tunable resistive pulse sensing (TRPS).

	TEM		TRPS	
Function	χ^2_{red}	R^2_{adj}	χ^2_{red}	R^2_{adj}
Exponential function	0.16	0.96	0.39	0.89
Gamma function	0.07	0.98	0.23	0.93
Lorentzian function	0.20	0.95	0.30	0.92
Power-law function	0.10	0.97	0.23	0.94
Weibull distribution	0.07	0.98	0.24	0.93
Log-normal distribution	0.20	0.97		

χ^2_{red}, *reduced* χ^2; R^2_{adj}, *adjusted* R^2.

Table B.3: Total concentration of vesicles from urine as detected by transmission electron microscopy (TEM), conventional flow cytometry, dedicated flow cytometry, nanoparticle tracking analysis (NTA), and tunable resistive pulse sensing (TRPS) and the expected concentration calculated by bounding the power-law fit of TRPS on urine vesicles between the minimum detectable vesicle size and 800 nm.

Method	Smallest detectable vesicle size (nm)	Detected concentration (vesicles mL^{-1})	Expected concentration (vesicles mL^{-1})	Ratio (-)
TEM	40	$1.2 \cdot 10^9$	$1.8 \cdot 10^{10}$	0.1
Conventional flow cytometry	340	$1.6 \cdot 10^7$	$2.7 \cdot 10^7$	0.6
Dedicated flow cytometry	160	$3.3 \cdot 10^8$	$2.8 \cdot 10^8$	1.2
NTA	70	$4.6 \cdot 10^9$	$3.4 \cdot 10^9$	1.3
TRPS	60	$5.0 \cdot 10^9$	$5.5 \cdot 10^9$	0.9

APPENDIX C

Optimal settings for refractive index determination with nanoparticle tracking analysis

This appendix contains the optimal particle tracking parameters and camera settings for refractive index determination of single vesicles with NTA (Chapter 6).

C.1 Particle tracking parameters

Each measurement comprises videos of scattering particles undergoing Brownian motion. The videos contain 8-bit images of 640 by 480 pixels, which are processed with scripts by Blair and Dufresne [38] in MATLAB (v7.13.0.564) to track the particles. The script basically performs five tasks.

First, a spatial band-pass filter is applied to each image to suppress pixel noise up to 2 pixels and long-wavelength image variations down to 25 pixels. Second, a threshold of 5 is applied to each image to find local maxima to pixel level accuracy. If multiple peaks are found within a radius of 13 pixels, only the position of the brightest peak is stored. Third, each local maximum is enclosed by a window with a diameter of 25 pixels to obtain the scattering power and the centroid to sub-pixel accuracy. The scattering power is the sum of all pixel intensities within the window divided by the shutter time and camera gain response and the centroid is calculated by taking the weighted average. Particles that cause pixel saturation are omitted. Fourth, 2-dimensional trajectories are calculated from the list of particles coordinates at discrete times. The maximum allowed jump distance of a particle between two successive frames is set to 23 pixels, which corresponds to 3.9 µm. The minimum tracklength of a particle is set to 30 frames, which will be discussed in the next paragraph. From the trajectory of each particle, we calculated the mean square displacement and diffusion coefficient and relate it to particle diameter via the Stokes-Einstein equation.

C.1.1 Minimum tracklength

The tracklength determines to what precision the diameter and scattering power are measured. A longer tracklength will increase the precision of both parameters. However, a longer tracklength also means that fewer particles are tracked, which reduces the correlation between the sample and the sampled population. Thus, the minimum tracklength determines a trade-off between precision and the number of particles included in the analysis.

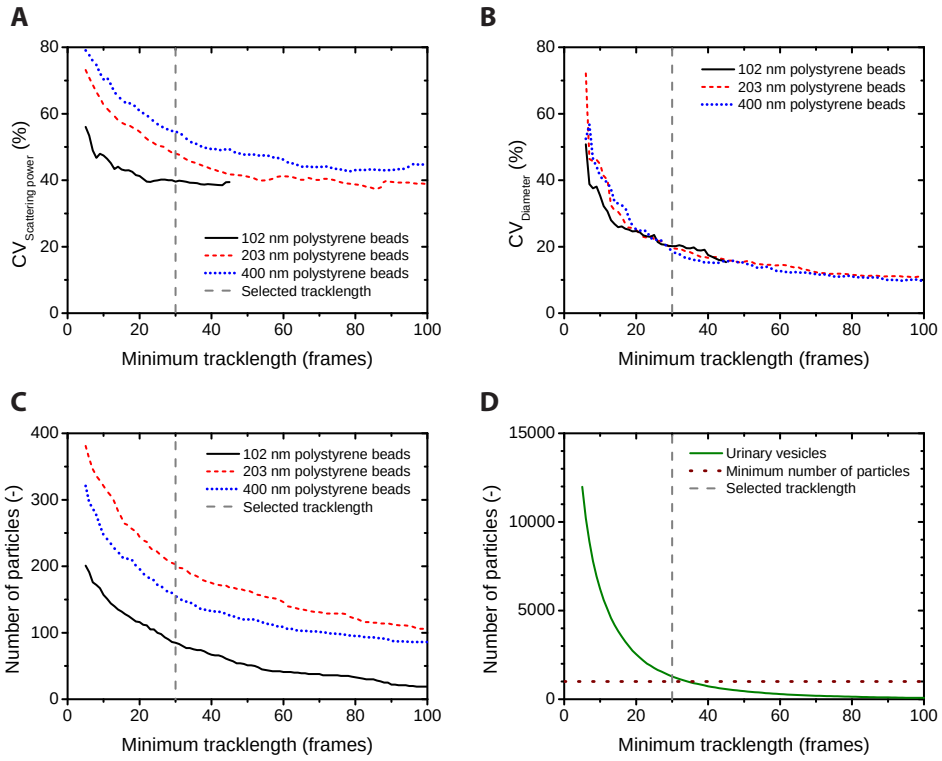

Figure C.1: Impact of the minimum tracklength on the accuracy of nanoparticle tracking analysis. (A) Coefficient of variation (CV) of the scattering power, (B) CV of the diameter, (C) and number of particles versus tracklength for 102 nm (solid black line), 203 nm (dashed red line), and 400 nm (dotted blue line) polystyrene beads. CV is defined as standard deviation divided by mean. (D) Number of particles versus tracklength for urinary vesicles. An increase of the minimum tracklength reduces the CV on scattering power and diameter, but also reduces the number of analyzed particles. To have a Poisson error ≤ 3 %, the minimum required number of analyzed particles is 1,000 (horizontal dotted line). Therefore, we selected a minimum tracklength of 30 frames (vertical dashed lines).

To select the optimal minimum tracklength, we determine the relationship between tracklength and scattering power, diameter, and number of analyzed particles. The coefficient of variation (CV), which is the percentage ratio between the standard deviation and the mean, is used to express the reproducibility of scattering power and diameter. Fig. C.1A shows the CV of the scattering power versus the minimum tracklength for 102 nm, 203 nm, and 400 nm polystyrene beads (sample 2, 3, and 4 in Table C.1). To eliminate the impact of the number of analyzed particles on the CV, we determined the CV for a fixed number of beads that were at least tracked for 45 (102 nm beads) or 100 (203 nm and 400 nm beads) frames. Increasing the minimum tracklength increases the probability that a particle is in focus. Since beads are monodisperse, the mean scattering power increases and converges, whereas the standard deviation decreases. Consequently, the scattering power CV decreases with increasing minimum tracklength. Smaller beads diffuse faster than larger beads, and therefore require less tracks to converge. The average scattering power CV is 55, 47, and 43 % for tracklenghts of 15, 30, and 45 frames, respectively.

Fig. C.1B shows the CV of the determined diameter versus the minimum tracklength for the same beads. Because the standard deviation of the determined diameter scales with $1/\sqrt{\text{tracklength}}$, the diameter CV decreases with increasing minimum tracklength. The diameter CV is 30, 19, and 16 % for tracklenghts of 15, 30, and 45 frames, respectively.

Fig. C.1C shows that the number of analyzed beads decreases with minimum tracklength. This is because particles that diffuse outside the field-of-view of the microscope before the minimum required tracklength is reached, are rejected from the analysis. Since smaller beads have a larger diffusion coefficient, smaller particles diffuse faster outside the field-of-view and are therefore more prone to rejection than larger particles. Fig. C.1D shows that the number of analyzed urinary vesicles (sample 11, 12, 13 in Table C.1) also decreases with tracklength. The number of events is 3,843, 1,280, and 567 for tracklenghts of 15, 30, and 45, respectively. A minimum tracklength of 30 frames is selected for further analysis, because the errors in diameter and illumination power are close to the best achievable (especially for vesicles < 150 nm, which is 53 % of the total), while a representative sample is still analyzed.

C.2 Camera settings

Since the scattering power of the particles in the samples differs more than 3 orders of magnitude, each sample required different camera settings. Table C.1 shows the applied camera settings.

Table C.1: Sample characteristics, applied camera settings, and number of valid tracks.

Sample	d (nm)	C (ml^{-1})	Shutter time (ms)	Gain (-)	Valid tracks
1. Polystyrene beads	46	10^8	23.3	425	136
2. Polystyrene beads	102	10^8	30.0	1	134
3. Polystyrene beads	203	10^8	2.67	1	235
4. Polystyrene beads	400	10^8	0.83	1	226
5. Polystyrene beads	596	10^8	0.50	1	231
6. Silica beads	89	10^8	23.3	370	297
7. Silica beads	206	10^8	35.0	1	98
8. Silica beads	391	10^8	10.0	1	286
9. Silica beads	577	10^8	4.67	1	233
10. Beads mixture	203 & 206	$2 \cdot 10^8$	5.00	1	1744
11. Urinary vesicles			35.0	100	93
12. Urinary vesicles			35.0	350	446
13. Urinary vesicles			35.0	470	741

d, diameter; C, concentration.

APPENDIX D

Light scattering calculations

Electromagnetic fields, such as light, can be mathematically described by Maxwell's equations. Mie theory provides an analytical solution of Maxwell's equations and describes light scattering of spheres and shells of all size parameters. Mie theory is extensively described by Bohren and Huffman [40]. The formulations by Bohren and Huffman are implemented in Matlab by Mätzler [199]. Throughout this thesis, we have used the scripts of Mätzler to calculate the scattering properties of beads, cells, and vesicles.

D.1 Total scattering cross section

The total scattering cross section $C_{sca,tot}$ is a hypothetical area describing the probability of light with unit incident irradiance being scattered (in all directions) by the particle. Therefore, the scattering cross section is proportional to the quantity of light scattered by a particle. In Chapter 3, we used the scripts of Mätzler to calculate the scattering efficiency Q, which is related to $C_{sca,tot}$ and the particle cross section as follows:

$$Q = \frac{4C_{sca,tot}}{\pi d^2} \tag{D.1}$$

where d is the particle diameter. We calculated the scattering cross section of a gold sphere ($n_p = 0.40 + 2.54i$) with 200 nm diameter in water ($n_w = 1.33$) using an illumination wavelength of 532 nm to be $1.13 \cdot 10^5$ nm^2. The character i is mathematically defined as $i = \sqrt{-1}$ and represents the absorption losses of the material. The scattering cross section for a 200 nm polystyrene sphere ($n_p = 1.60$) is $4.22 \cdot 10^3$ nm^2, which is 27 times smaller than the scattering cross section of a 200 nm gold sphere. The scattering cross section for a 200 nm vesicle ($n_p = 1.38$) that contains a 10 nm thick shell ($n_s = 1.46$), e.g. a phospholipid membrane, is 283 nm^2, which is 15 times smaller than the scattering cross section of a 200 nm polystyrene sphere and 399 times smaller than that of a 200 nm gold sphere.

D.2 Aperture-weighted scattering cross section

The detection methods used in Chapters 4, 5, and 6 collect scattered light under specific angles. To take into account the optical configuration of these instruments, the differential scattering cross section has to be integrated over the collection

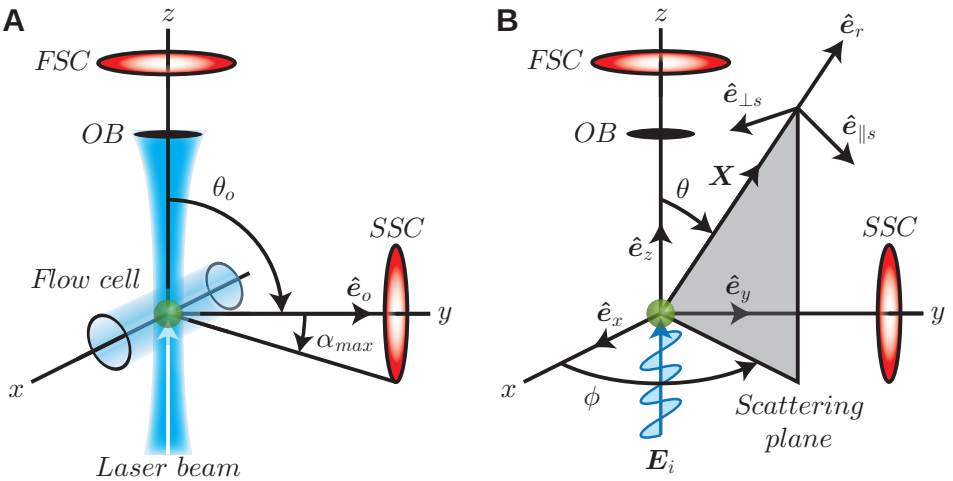

Figure D.1: Optical configuration of the (A) FACSCalibur flow cytometer and (B) coordinate system and variables used to calculate the scattering intensity of a spherical particle that is illuminated by a laser beam. Symbols are explained throughout the text.

angles of the instrument. In Chapter 5, we followed the approach of Fattaccioli et al. [97] to calculate the forward and side scattered light from beads and vesicles for the BD FACSCalibur (Becton Dickinson, Franklin Lakes, NJ, USA). However, Fattaccioli et al. did not take into account that the transmission efficiency of a lens decreases with increasing propagation angle relative to the optical axis.

In the next section, we will discuss the approach that we used in Chapters 4 and 6 to calculate the light scattering intensity for particles measured by nanoparticle tracking analysis (NTA; NS500, Nanosight, UK) and flow cytometry.

D.2.1 Optical configuration FACSCalibur

Fig. D.1A shows a schematic of the optical configuration of the FACSCalibur. A linearly polarized 15 mW argon-ion laser emitting at 488 nm is elliptically focused to illuminate cells or vesicles, which are hydrodynamically focused in the flow cell. Forward scattered light (FSC) is measured in line with the laser beam. To prevent the laser directly illuminating the photodiode, the laser beam is blocked by the obscuration bar (OB). Side scattered light (SSC) is collected by an objective with a numerical aperture (NA) of 1.2, which is placed perpendicular to the beam. NA characterizes the range of angles over which the objective collects light and is defined as $\mathrm{NA} = n_m \sin \alpha_{max}$, where n_m is the refractive index of the medium and α_{max} is the maximum propagation angle. The SSC detector is a photomultiplier tube (PMT), which is not only more sensitive than the photodiode of the FSC detector, but also detects scattered light over a much broader angle. Therefore, we select SSC as the trigger signal and measure SSC from vesicles to derive their particle size distribution (PSD).

D.2.2 Optical configuration NS500

The optical configuration of the Nanosight NS500 is comparable to the detection of SSC in the FACSCalibur. A linearly polarized 45 mW diode laser emitting at 405 nm is collimated in a flow cell and illuminates vesicles. Light is collected in the SSC direction by an objective with an NA of 0.4.

D.2.3 Model

Fig. D.1B shows a spherical particle with diameter d and refractive index n_p that is illuminated by a plane electromagnetic wave propagating along the z direction and polarized in the x direction:

$$\boldsymbol{E}_i = E_{0,x} e^{i(kz-\omega t)} \hat{\boldsymbol{e}}_x \tag{D.2}$$

with $E_{0,x}$ the electric field amplitude, ω the angular frequency, t the time, $\hat{\boldsymbol{e}}_x$ the orthonormal basis vector in the direction of the positive x axis, $k = 2\pi n_m/\lambda$ the wave number, and λ is the wavelength of the incident light in vacuum. The total scattering cross section is given by:

$$C_{sca} = \int_0^{2\pi} \int_0^{\pi} \frac{|\boldsymbol{X}|^2}{k^2} \sin\theta d\theta d\phi \tag{D.3}$$

with θ the polar angle, ϕ the azimuthal angle, and $\boldsymbol{X}$ the vector scattering amplitude. In a flow cytometer, θ and ϕ are limited by the optical aperture of the microscope objective, and since the detected scattering power P is in arbitrary units, a scalar F is introduced to scale the calculations to the data:

$$P = F \int_{\phi_1}^{\phi_2} \int_{\theta_1}^{\theta_2} \frac{\eta|\boldsymbol{X}|^2}{k^2} \sin\theta d\theta d\phi \tag{D.4}$$

where η is the angle dependent transmission efficiency of the objective. For SSC on the FACSCalibur, θ is integrated from $\theta_1 = \theta_o - \alpha_{max}$ to $\theta_2 = \theta_o + \alpha_{max}$, with θ_o the angle between the optical axis of the objective and the propagation direction of the incoming wave $\hat{\boldsymbol{e}}_z$. Since the objective has a circular geometry, ϕ_1 is expressed in terms of θ as follows :

$$\phi_1 = \arcsin\left(\frac{\sin(\frac{1}{2}\pi - \alpha_{max})}{\sin(\frac{1}{2}\pi - \theta_o + \theta)}\right) \tag{D.5}$$

and $\phi_2 = \pi - \phi_1$. The number of steps over which θ and ϕ are integrated is 50. For a spherical particle, the vector scattering amplitude $\boldsymbol{X}$ is related to the amplitude scattering matrix elements S_j as follows:

$$\boldsymbol{X} = (S_2 \cos\phi)\hat{\boldsymbol{e}}_{\parallel s} + (S_1 \sin\phi)\hat{\boldsymbol{e}}_{\perp s} \tag{D.6}$$

where the basis vector $\hat{\boldsymbol{e}}_{\parallel s}$ is parallel and $\hat{\boldsymbol{e}}_{\perp s}$ is perpendicular to the scattering plane, which is defined by the scattering direction $\hat{\boldsymbol{e}}_r$ and the propagation direction

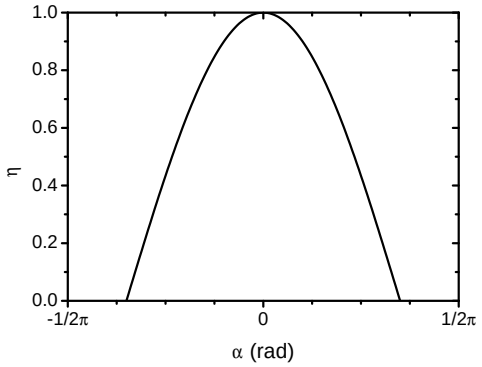

Figure D.2: Transmission efficiency versus angle of propagation for a high NA objective.

of the wave $\hat{\boldsymbol{e}}_z$. The parameters S_1 and S_2 depend on d, n_p, n_m, k, and θ, and are calculated using the Matlab routines of Mätzler. Since $\hat{\boldsymbol{e}}_{\parallel s}$ and $\hat{\boldsymbol{e}}_{\perp s}$ are orthogonal, the term $|\boldsymbol{X}|^2$ can be written as

$$|\boldsymbol{X}|^2 = |S_2|^2 \cos^2\phi + |S_1|^2 \sin^2\phi \tag{D.7}$$

Equation D.7 is used to calculate the scattering power for SSC on the NS500. In the FACSCalibur, however, SSC is filtered by a 90/10 beam splitter placed under the Brewster angle, such that only the scattered component parallel to $\hat{\boldsymbol{e}}_x$ is measured [97]. Under these conditions, the term $|\boldsymbol{X}\cdot\hat{\boldsymbol{e}}_x|^2$ is to be considered and can be written as

$$|\boldsymbol{X}|^2 = |S_2|^2 \cos^4\phi\cos^2\theta + |S_1|^2 \sin^4\phi + (S_1 S_2^* + S_1^* S_2)\cos^2\phi\sin^2\phi\cos\theta \tag{D.8}$$

Since the transmission efficiency η of light propagating through a high NA objective decreases with increasing propagation angle α with respect to $\hat{\boldsymbol{e}}_o$ (see Fig. D.1A), a sine function was chosen empirically as a weighting function for η:

$$\eta = \sin\left(\frac{\pi\alpha}{2\alpha_{max}} + \frac{1}{2}\pi\right) \tag{D.9}$$

Fig. D.2 shows an example of the weighting function for $\alpha_{max} = 0.35\pi$, which is close to an NA of 1.2. To calculate α, it is expressed in terms of θ and ϕ by using the inner product between $\hat{\boldsymbol{e}}_r$ and $\hat{\boldsymbol{e}}_o$ and taking $\phi_o = \frac{1}{2}\pi$, where ϕ_o denotes the angle between $\hat{\boldsymbol{e}}_o$ and $\hat{\boldsymbol{e}}_x$, resulting in

$$\alpha = \arccos[\sin\phi\cos(\theta_o - \theta)] \tag{D.10}$$

To find the optimal values for unknown values of F, NA, θ_o, and θ_s, a least square fit was applied on data from beads of known size and refractive index. Since the NS500 is equipped with a low NA objective, no weighting function was applied.

APPENDIX E

Wound scabs protect regenerating tissue against harmful ultraviolet radiation

This appendix contains a draft manuscript which is not related to the topic of this thesis. The authors are E. van der Pol, Y.D. Mudde, F.A.W. Coumans, T.G. van Leeuwen, A. Sturk, and R. Nieuwland.

Abstract

Benefits attributed to wound scabs include prevention of blood loss and protection against infection. However, when formation of a wound scab is prevented the risk of infection is reduced. Moreover, in the absence of a wound scab, wounds heal faster and scar formation is reduced. The question arises why we develop a wound scab. Here we show that wound scabs inhibit transmission of ultraviolet radiation (UVR). We compared the UVR transmittance of human wound scabs to sunscreen by measuring the sun protection factor (SPF) with diffuse transmittance spectroscopy. Three wound scabs showed SPFs of 70, 84, and 300, which is more effective than the most protective commercially available sun block. Our results demonstrate that a wound scab offers natural protection against UVR, thereby likely to reduce the risk of DNA damage during regeneration of wound tissue exposed to sunlight.

E.1 Introduction

Wound healing is a complex interplay between haemostasis, inflammation, formation of new tissue, and tissue remodelling [195, 119, 33]. Haemostasis involves formation of a platelet plug, thereby limiting blood loss and reducing the risk of infection. Concurrently, leukocytes are recruited, granulation tissue, new blood vessels and an extracellular matrix are formed, damaged tissue is removed, and tissue remodelling starts that can last for more than a year [195, 119]. A hallmark of dermal wound healing is the formation of a dry wound scab, which consists of blood cells such as platelets and erythrocytes, and proteins such as fibrin [321]. Wound scabs contain higher numbers of microorganisms than the underlying tissue [115], suggesting that one of the functions of wound scabs is to trap pathogens, thereby reducing the risk of infection. However, a wound in the oral cavity is not covered by a scab, and usually heals without infection despite the abundant

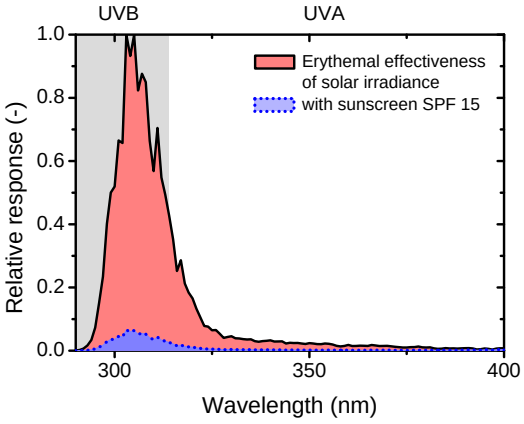

Figure E.1: Erythemal response to solar irradiance. Erythemal spectral effectiveness relative to the reference solar spectral irradiance for the Caucasian skin with and without sunscreen of sun protection factor (SPF) 15. Erythema is mainly induced by ultraviolet radiation B (UVB, grey area) and is considerably reduced for skin protected with SPF 15 sunscreen. UVA: ultraviolet radiation A.

presence of pathogens [115, 255]. In fact, when formation of a dry wound scab is prevented, the risk of infection is reduced, wounds heal faster, and scar formation is reduced [115, 255, 328, 103, 327]. Taken together, no beneficial trait is consistently attributed to wound scabs. Because the intact skin protects underlying tissue from ultraviolet radiation (UVR), we hypothesize that wound scabs, which temporarily replace the skin, may also inhibit transmission of UVR, thereby reducing the risk of sunlight-induced DNA damage to vulnerable cells in the wound area during regeneration of tissue.

In order to study the UVR protection of wound scabs, we measured their UVR transmittance, calculated their sun protection factor (SPF), and compared these to values for sunscreen. In vivo, the SPF is defined as the amount of UVR required to produce erythema on protected skin relative to unprotected skin [2]. Fig. E.1 shows that erythema of the Caucasian skin induced by solar irradiance is mainly caused by the ultraviolet radiation B (UVB) region of the spectrum (280−315 nm), with a maximum near 305 nm [2, 1, 281]. Fig. E.1 also shows that erythema is considerably reduced when the skin is protected by SPF 15 sunscreen, as measured by diffuse transmittance spectroscopy. In vitro, SPF is defined as the ratio of the areas under the two curves [86].

E.2 Methods

E.2.1 Sample preparation

By micropipetting, 4 µL/cm^2 sunscreen (private label SPF 15 and SPF 50, Etos, The Netherlands) was applied between two quartz slides to obtain a spatially homogeneous distribution by capillary attraction. The quartz slides were removed from each other in lateral direction, resulting in two quartz slides coated with 2 µL/cm^2 sunscreen each [2], which was immediately covered with medical tape (Transpore, 3M company, MN, USA) to imitate the texture of human skin [86].

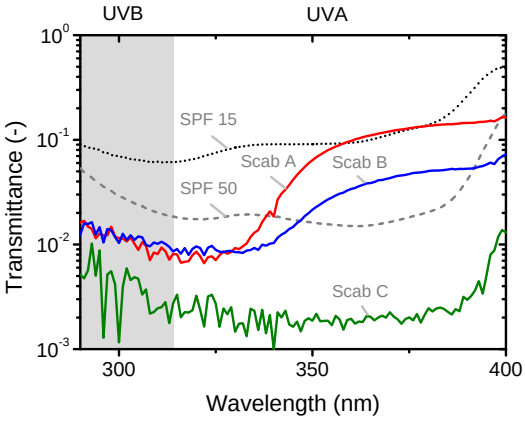

Figure E.2: Ultraviolet radiation (UVR) transmittance of sunscreen and wound scabs. UVR transmittance of sunscreen with sun protection factor (SPF) 15 and SPF 50 and three wound scabs, revealing that wound scabs effectively attenuate UVR transmission and transmit less ultraviolet radiation B (UVB) radiation than SPF 50 sunscreen. UVA: ultraviolet radiation A.

After 30 min, the samples were mounted on an aluminium plate containing a 10.4 mm aperture, with the samples covering the aperture. Wound scabs were collected anonymously from healthy individuals and mounted on a plate containing a 3.0 mm aperture.

E.2.2 Diffuse transmittance UVR spectroscopy

The samples were placed in the opening of an integrating sphere (70672, Newport, CA, USA). Light from a fibre-coupled Xenon lamp (E7536, Hamamatsu, Japan) was spectrally filtered (UG11, Schott, Germany) and collimated to a beam with a diameter of 13.0 mm, resulting in an irradiance of 24 Wm^{-2}. The output port of the integrating sphere is connected to a fiber, guiding the light to a thermo-electrically cooled CCD (S10141-1108S, Hamamatsu, Japan) mounted on a 284 mm focal length imaging spectrograph (M266, Solar Laser Systems, Russia) with a grating of 2,200 grooves mm^{-1}. An Hg(Ar) lamp (6035, Oriel cooperation, CA, USA) was used for spectral calibration. The acquisition time was 3.5 s for SPF 15 sunscreen and 35 s for the other samples. All data are reported as the mean ± standard deviation of 5 measurements. Data processing and data representation were done with MATLAB (v.7.14, MathWorks, MA, USA) and ORIGINPRO (v.8.0724, OriginLab, MA, USA), respectively. After subtracting the dark current and binning the data (bin width 1 nm), the transmittance $T(\lambda)$ was calculated and used to evaluate the SPF14:

$$\mathrm{SPF} = \frac{\int_{290\mathrm{nm}}^{400\mathrm{nm}} E(\lambda)S(\lambda)d\lambda}{\int_{290\mathrm{nm}}^{400\mathrm{nm}} E(\lambda)S(\lambda)T(\lambda)d\lambda} \tag{E.1}$$

where $E(\lambda)$ is the erythemal spectral effectiveness as defined by the International Commission on Illumination [1], $S(\lambda)$ the reference solar spectral irradiance [2], and λ the wavelength of light.

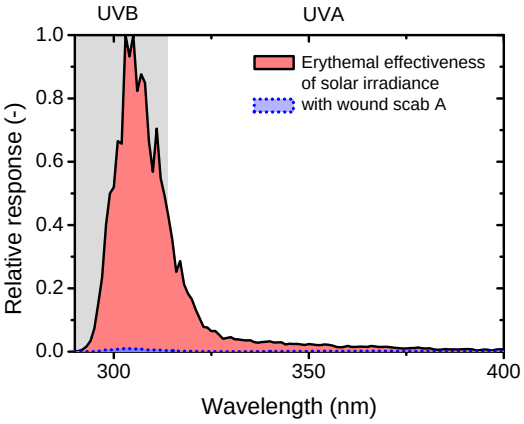

Figure E.3: Erythemal response to solar irradiance of skin covered by a wound scab. Erythemal spectral effectiveness of the reference solar spectral irradiance in the absence and presence of a wound scab. Erythema is inhibited for skin protected by a wound scab. UVA: ultraviolet radiation A; UVB: ultraviolet radiation B.

E.3 Results

The diffuse transmittance spectra of sunscreen with SPF 15 and SPF 50 and three human wound scabs are shown in Fig. E.2. The transmittance spectra of sunscreen with SPF 15 and SPF 50 are the mean transmittance spectra of 5 independent measurements and result in an SPF of 15 ± 4 and 45 ± 11, respectively. All wound scabs inhibit the transmission of UVB more effectively than SPF 50 sunscreen. The measured SPFs of the studied wound scabs are 84, 70, and 300 for wound scab A, B, and C, respectively.

Fig. E.3 shows the erythemal spectral effectiveness of solar irradiance in the absence and presence of wound scab A. In the presence of wound scab A, solar irradiance induces erythema 84 times slower than uncovered skin, illustrating that a wound scab effectively protects underlying tissue from UVR.

E.4 Discussion and conclusion

We demonstrate that a human wound scab is an excellent sun block against UVR. Exposure of the skin to sunlight results in absorption of UVR, leading to direct UVB-induced DNA damage and indirect ultraviolet radiation A-induced DNA damage via generation of reactive oxygen species [150]. It is mainly the UVB-induced release of photo-damaged DNA fragments that leads to erythema and triggers DNA repair mechanisms [91, 12, 80].

When DNA damage is not or insufficiently repaired, the remaining mutations increase the risk of developing skin cancer, including melanoma [80, 92]. Because a wound scab effectively inhibits exposure to UVR, coverage of a wound by a scab protects the otherwise exposed cells from UVR-induced DNA damage. Since extensive cell migration, proliferation and differentiation occur in a healing wound, which is not protected from UVR by melanin, inhibition of UVR by a wound scab is essential and is likely to reduce the risk of skin cancer.

Our present finding is supported by two lines of circumstantial evidence. First, after removal of a wound scab the underlying tissue is characterized by hypopigmentation ("white scarring"), illustrating that the newly formed skin is protected from UVR-induced DNA damage and thus lacks melanin production. Second, wounds formed on locations not exposed to UVR, such as wounds within the hand palm or at the underside of the foot, tend not to develop a wound scab.

Taken together, we postulate that a main biological function of human wound scabs is to inhibit the exposure to UVR, thus protecting otherwise exposed and vulnerable cells in a wound from UVR-induced DNA damage. Future research comprises the provision of epidemiological evidence that in the absence of a wound scab people have an increased risk of skin cancer.

Bibliography

1. *Erythema reference action spectrum and standard erythema dose* CIE S007/E-1998 Commission Internationale de l'Eclairage, CIE Central Bureau, Vienna, Austria (1998).
2. *Experimentelle in vivo-Bewertung des Erythemschutzes von externen Sonnenschutzmitteln für die menschliche Haut.* DIN 67501 Deutsches Institut für Normung (DIN), Berlin, Germany (2010).
3. Query: [TITLE: (exosome* OR (cell$ AND microvesicle$) OR (cell$ AND nanovesicle$) OR "extracellular *vesicle$" OR "cell-derived *vesicle$" OR "cell-derived microparticle$")] (2014) URL `http://apps.webofknowledge.com`.
4. *Reference haematology values* Academic Medical Center, University of Amsterdam, Amsterdam, The Netherlands (2014).
5. Aalberts M., van Dissel-Emiliani F.M.F., van Adrichem N.P.H., van Wijnen M., Wauben M.H.M., Stout T.A.E. and Stoorvogel W. Identification of distinct populations of prostasomes that differentially express prostate stem cell antigen, annexin A1, and GLIPR2 in humans *Biol. Reprod.* **86**(3), 82–90 (2012).
6. Aass H.C.D., Øvstebø R., Trøseid A.M.S., Kierulf P., Berg J.P. and Henriksson C.E. Fluorescent particles in the antibody solution result in false TF- and CD14-positive microparticles in flow cytometric analysis *Cytom. Part A* **79**(12), 990–999 (2011).
7. Abid Hussein M.N., Nieuwland R., Hau C.M., Evers L.M., Meesters E.W. and Sturk A. Cell-derived microparticles contain caspase 3 in vitro and in vivo *J. Thromb. Haemost.* **3**(5), 888–896 (2005).
8. Ackleson S.G. and Spinrad R.W. Size and refractive index of individual marine participates: a flow cytometric approach *Appl. Opt.* **27**(7), 1270–1277 (1988).
9. Ade H. and Stoll H. Near-edge X-ray absorption fine-structure microscopy of organic and magnetic materials *Nat. Mater.* **8**(4), 281–290 (2009).
10. Ade H., Zhang X., Cameron S., Costello C., Kirz J. and Williams S. Chemical contrast in X-ray microscopy and spatially resolved XANES spectroscopy of organic specimens *Science* **258**(5084), 972–975 (1992).
11. Admyre C., Grunewald J., Thyberg J., Gripenbäck S., Tornling G., Eklund A., Scheynius A. and Gabrielsson S. Exosomes with major histocompatibility complex class II and co-stimulatory molecules are present in human BAL fluid *Eur. Respir. J.* **22**(4), 578–583 (2003).
12. Agar N. and Young A.R. Melanogenesis: a photoprotective response to DNA damage? *Mutat. Res.* **571**(1), 121–132 (2005).

13. Al-Nedawi K., Meehan B., Micallef J., Lhotak V., May L., Guha A. and Rak J. Intercellular transfer of the oncogenic receptor EGFRvIII by microvesicles derived from tumour cells *Nature* **10**(5), 619–624 (2008).
14. Allan D. and Raval P. Some morphological consequences of uncoupling the lipid bilayer from the plasma membrane skeleton in intact erythrocytes *Biomed. Biochim. Acta* **42**(11-12), S11–6 (1983).
15. Allen N.S., Edge M., Ortega A., Liauw C.M., Stratton J. and McIntyre R.B. Behaviour of nanoparticle (ultrafine) titanium dioxide pigments and stabilisers on the photooxidative stability of water based acrylic and isocyanate based acrylic coatings *Polym. Degrad. Stab.* **78**(3), 467–478 (2002).
16. Amabile N., Renard J.M., Caussin C. and Boulanger C.M. Circulating immune complexes do not affect microparticle flow cytometry analysis in acute coronary syndrome *Blood* **119**(9), 2174–2175 (2012).
17. Andaloussi S.E.L., Mäger I., Breakefield X.O. and Wood M.J.A. Extracellular vesicles: biology and emerging therapeutic opportunities *Nat. Rev. Drug Discovery* **12**(5), 347–357 (2013).
18. André F., Chaput N., Schartz N.E., Flament C., Aubert N., Bernard J., Lemonnier F., Raposo G., Escudier B., Hsu D.H., Tursz T., Amigorena S., Angevin E. and Zitvogel L. Exosomes as potent cell-free peptide-based vaccine. I. Dendritic cell-derived exosomes transfer functional MHC class I/peptide complexes to dendritic cells *J. Immunol.* **172**(4), 2126–2136 (2004).
19. Arraud N., Linares R., Tan S., Gounou C., Pasquet J.M., Mornet S. and Brisson A.R. Extracellular vesicles from blood plasma: determination of their morphology, size, phenotype and concentration *J. Thromb. Haemost.* **12**(5), 614–627 (2014).
20. Babst M. A protein's final ESCRT *Traffic* **6**(1), 2–9 (2005).
21. Bard M.P., Hegmans J.P., Hemmes A., Luider T.M., Willemsen R., Severijnen L.A.A., van Meerbeeck J.P., Burgers S.A., Hoogsteden H.C. and Lambrecht B.N. Proteomic analysis of exosomes isolated from human malignant pleural effusions *Am. J. Respir. Cell Mol. Biol.* **31**(1), 114–121 (2004).
22. Barer R. Refractometry and interferometry of living cells *J. Opt. Soc. Am.* **47**(6), 545–556 (1957).
23. Barer R. and Tkaczyk S. Refractive index of concentrated protein solutions *Nature* **173**, 821–822 (1954).
24. Barnes M.D., Lermer N., Whitten W.B. and Ramsey J.M. A CCD based approach to high-precision size and refractive index determination of levitated microdroplets using Fraunhofer diffraction *Rev. Sci. Instrum.* **68**(6), 2287–2291 (1997).
25. Baumgarth N. and Roederer M. A practical approach to multicolor flow cytometry for immunophenotyping *J. Immunol. Methods* **243**(1), 77–97 (2000).
26. Beckhoff B., Gottwald A., Klein R., Krumrey M., Müller R., Richter M., Scholze F., Thornagel R. and Ulm G. A quarter-century of metrology using synchrotron radiation by PTB in Berlin *Phys. Status Solidi* **B246**(7), 1415–1434 (2009).

27. van Beers E.J., Schaap M.C.L., Berckmans R.J., Nieuwland R., Sturk A., van Doormaal F.F., Meijers J.C.M. and Biemond B.J. Circulating erythrocyte-derived microparticles are associated with coagulation activation in sickle cell disease *Haematologica* **94**(11), 1513–1519 (2009).
28. Bendix P.M. and Oddershede L.B. Expanding the optical trapping range of lipid vesicles to the nanoscale *Nano Lett.* **11**(12), 5431–5437 (2011).
29. Berckmans R.J., Nieuwland R., Tak P.P., Böing A.N., Romijn F.P.H.T., Kraan M.C., Breedveld F.C., Hack C.E. and Sturk A. Cell-derived microparticles in synovial fluid from inflamed arthritic joints support coagulation exclusively via a factor VII–dependent mechanism *Arthritis Rheum.* **46**(11), 2857–2866 (2002).
30. Berckmans R.J., Sturk A., Schaap M.C. and Nieuwland R. Cell-derived vesicles exposing coagulant tissue factor in saliva *Blood* **117**(11), 3172–3180 (2011).
31. Beuthan J., Minet O., Helfmann J., Herrig M. and Müller G. The spatial variation of the refractive index in biological cells *Phys. Med. Biol.* **41**(3), 369–382 (1996).
32. Beyer C. and Pisetsky D.S. The role of microparticles in the pathogenesis of rheumatic diseases *Nat. Rev. Rheumatol.* **6**(1), 21–29 (2010).
33. Bielefeld K.A., Amini-Nik S. and Alman B.A. Cutaneous wound healing: recruiting developmental pathways for regeneration *Cell. Mol. Life Sci.* **70**(12), 2059–2081 (2013).
34. Biller S.J., Schubotz F., Roggensack S.E., Thompson A.W., Summons R.E. and Chisholm S.W. Bacterial vesicles in marine ecosystems *Science* **343**(6167), 183–186 (2014).
35. Bilyy R.O., Shkandina T., Tomin A., Muñoz L.E., Franz S., Antonyuk V., Kit Y.Y., Zirngibl M., Fürnrohr B.G., Janko C., Lauber K., Schiller M., Schett G., Stoika R.S. and Herrmann M. Macrophages discriminate glycosylation patterns of apoptotic cell-derived microparticles *J. Biol. Chem.* **287**(1), 496–503 (2012).
36. Binnig G., Quate C.F. and Gerber C. Atomic force microscope *Phys. Rev. Lett.* **56**(9), 930 (1986).
37. Biro E., Sturk-Maquelin K.N., Vogel G.M.T., Meuleman D.G., Smit M.J., Hack C.E., Sturk A. and Nieuwland R. Human cell-derived microparticles promote thrombus formation in vivo in a tissue factor-dependent manner *J. Thromb. Haemost.* **1**(12), 2561–2568 (2003).
38. Blair D. and Dufresne E. Matlab particle tracking code repository (2008) URL `http://physics.georgetown.edu/matlab/`.
39. Bobrie A., Colombo M., Raposo G. and Théry C. Exosome secretion: molecular mechanisms and roles in immune responses *Traffic* **12**(12), 1659–1668 (2011).
40. Bohren C.F. and Huffman D.R. *Absorption and scattering of light by small particles* Wiley, New York, NY (1983).

41. Boilard E., Nigrovic P.A., Larabee K., Watts G.F., Coblyn J.S., Weinblatt M.E., Massarotti E.M., Remold-O'Donnell E., Farndale R.W., Ware J. et al. Platelets amplify inflammation in arthritis via collagen-dependent microparticle production *Science* **327**(5965), 580–583 (2010).
42. Böing A.N., van der Pol E., Grootemaat A.E., Coumans F.A.W., Sturk A. and Nieuwland R. Single-step isolation of extracellular vesicles by size-exclusion chromatography *J. Extracell. Vesicles* **3**, 23430 (2014).
43. Booth A.M., Fang Y., Fallon J.K., Yang J.M., Hildreth J.E. and Gould S.J. Exosomes and HIV Gag bud from endosome-like domains of the T cell plasma membrane *J. Cell Biol.* **172**(6), 923–935 (2006).
44. Bosschaart N. *Quantitative and localized spectroscopy for non-invasive bilirubinometry in neonates* Ph.D. thesis University of Amsterdam Amsterdam, The Netherlands (2012).
45. Bouwstra J.A., Gooris G.S., Bras W. and Talsma H. Small angle X-ray scattering: possibilities and limitations in characterization of vesicles *Chem. Phys. Lipids* **64**(1), 83–98 (1993).
46. Braeckmans K., Buyens K., Bouquet W., Vervaet C., Joye P., Vos F.D., Plawinski L., Doeuvre L., Angles-Cano E., Sanders N.N., Demeester J. and De Smedt S.C. Sizing nanomatter in biological fluids by fluorescence single particle tracking *Nano Lett.* **10**(11), 4435–4442 (2010).
47. Briggs C., Harrison P. and Samuel J.M. *Platelet counting* chap. 24, 475–483 Platelets 2nd edn. Academic Press, San Diego, CA (2006).
48. Bryant G. and Thomas J.C. Improved particle size distribution measurements using multiangle dynamic light scattering *Langmuir* **11**(7), 2480–2485 (1995).
49. Brzustowicz M.R. and Brunger A.T. X-ray scattering from unilamellar lipid vesicles *J. Appl. Crystallogr.* **38**(1), 126–131 (2005).
50. Burnier L., Fontana P., Kwak B.R., Angelillo-Scherrer A. et al. Cell-derived microparticles in haemostasis and vascular medicine *Thromb. Haemost.* **101**(3), 439–451 (2009).
51. Buschow S.I., Liefhebber J.M.P., Wubbolts R. and Stoorvogel W. Exosomes contain ubiquitinated proteins *Blood Cells Mol. Dis.* **35**(3), 398–403 (2005).
52. Buschow S.I., Van Niel G., Pols M.S., Ten Broeke T., Lauwen M., Ossendorp F., Melief C.J., Raposo G., Wubbolts R., Wauben M.H. and Stoorvogel W. MHC II in Dendritic Cells is Targeted to Lysosomes or T Cell-Induced Exosomes Via Distinct Multivesicular Body Pathways *Traffic* **10**(10), 1528–1542 (2009).
53. Caby M.P., Lankar D., Vincendeau-Scherrer C., Raposo G. and Bonnerot C. Exosomal-like vesicles are present in human blood plasma *Int. Immunol.* **17**(7), 879–887 (2005).
54. Cachau R.E., Braden B.C., Collins J.R. and Casas-Finet J.R. Nanoparticles characterization using HDR-NTA image analysis in *SPIE Photonics West* 8954-34 (2014).
55. Canault M., Leroyer A.S., Peiretti F., Leseche G., Tedgui A., Bonardo B., Alessi M.C., Boulanger C.M. and Nalbone G. Microparticles of human

atherosclerotic plaques enhance the shedding of the tumor necrosis factor-α converting enzyme/ADAM17 substrates, tumor necrosis factor and tumor necrosis factor receptor-1 *Am. J. Pathol.* **171**(5), 1713–1723 (2007).

56. Carr R., Smith J., Hole P., Malloy A., Nelson P. and Warren J. The real-time visualisation and size analysis of nanoparticles in liquids - nanoparticle tracking analysis. Tech. rep. Nanosight Ltd. Salisbury, UK (2008).
57. Castorph S., Riedel D., Arleth L., Sztucki M., Jahn R., Holt M. and Salditt T. Structure parameters of synaptic vesicles quantified by small-angle x-ray scattering *Biophys* **98**(7), 1200–1208 (2010).
58. Chandler W.L., Yeung W. and Tait J.F. A new microparticle size calibration standard for use in measuring smaller microparticles using a new flow cytometer *J. Thromb. Haemost.* **9**(6), 1216–1224 (2011).
59. Chao W., Kim J., Rekawa S., Fischer P. and Anderson E.H. Demonstration of 12 nm resolution Fresnel zone plate lens based soft x-ray microscopy *Opt. Express* **17**(20), 17669–17677 (2009).
60. Chaput N. and Théry C. Exosomes: immune properties and potential clinical implementations in *Semin. Immunopathol.* vol. 33 419–440 (2011).
61. Chargaff E. and West R. The biological significance of the thromboplastic protein of blood *J. Biol. Chem.* **166**(1), 189–197 (1946).
62. Charrière F., Marian A., Montfort F., Kuehn J., Colomb T., Cuche E., Marquet P. and Depeursinge C. Cell refractive index tomography by digital holographic microscopy *Opt. Lett.* **31**(2), 178–180 (2006).
63. Cherney D.P., Myers G.A., Horton R.A. and Harris J.M. Optically Trapping Confocal Raman Microscopy of Individual Lipid Vesicles: Kinetics of Phospholipase A2-Catalyzed Hydrolysis of Phospholipids in the Membrane Bilayer *Anal. Chem.* **78**(19), 6928–6935 (2006).
64. Chylek P., Ramaswamy V., Ashkin A. and Dziedzic J.M. Simultaneous determination of refractive index and size of spherical dielectric particles from light scattering data *Appl. Opt.* **22**(15), 2302–2307 (1983).
65. Clark N.A., Lunacek J.H. and Benedek G.B. A study of Brownian motion using light scattering *Am. J. Phys.* **38**(5), 575–585 (1970).
66. Cocucci E., Racchetti G. and Meldolesi J. Shedding microvesicles: artefacts no more *Trends Cell Biol.* **19**(2), 43–51 (2009).
67. Colhoun H.M., Otvos J.D., Rubens M.B., Taskinen M.R., Underwood S.R. and Fuller J.H. Lipoprotein subclasses and particle sizes and their relationship with coronary artery calcification in men and women with and without type 1 diabetes *Diabetes* **51**(6), 1949–1956 (2002).
68. Collier J.L. Flow cytometry and the single cell in phycology *J. Phycol.* **36**(4), 628–644 (2000).
69. Conde-Vancells J., Rodriguez-Suarez E., Embade N., Gil D., Matthiesen R., Valle M., Elortza F., Lu S.C., Mato J.M. and Falcon-Perez J.M. Characterization and Comprehensive Proteome Profiling of Exosomes Secreted by Hepatocytes *J. Proteome Res.* **7**(12), 5157–5166 (2008).

70. Connor D.E., Exner T., Ma D.D.F. and Joseph J.E. The majority of circulating platelet-derived microparticles fail to bind annexin V, lack phospholipid-dependent procoagulant activity and demonstrate greater expression of glycoprotein Ib *Thromb. Haemost.* **103**(5), 1044 (2010).
71. Copley A.L. and Houlihan R.B. Studies on platelets; the isolation of platelets from human and dog blood *Blood* **1**, 170–181 (1947).
72. Coumans F.A.W., van Dalum G., Beck M.G. and Terstappen L.W.M.M. Filter characteristics influencing circulating tumor cell enrichment from whole blood *PLoS ONE* **8**(4), e61770 (2013).
73. Coumans F.A.W., Doggen C.J.M., Attard G., De Bono J.S. and Terstappen L.W.M.M. All circulating EpCAM+ CK+ CD45- objects predict overall survival in castration-resistant prostate cancer *Ann. Oncol.* **21**(9), 1851–1857 (2010).
74. Couzin J. Cell biology: The ins and outs of exosomes. *Science* **308**(5730), 1862–1863 (2005).
75. Crawford N. The presence of contractile proteins in platelet microparticles isolated from human and animal platelet-free plasma *Br. J. Haematol.* **21**(1), 53–69 (1971).
76. Crowley T.A. and Pizziconi V. Isolation of plasma from whole blood using planar microfilters for lab-on-a-chip applications *Lab Chip* **5**(9), 922–929 (2005).
77. Dalli J., Norling L.V., Renshaw D., Cooper D., Leung K.Y. and Perretti M. Annexin 1 mediates the rapid anti-inflammatory effects of neutrophil-derived microparticles *Blood* **112**(6), 2512–2519 (2008).
78. Dalton A.J. Microvesicles and vesicles of multivesicular bodies versus "virus-like" particles *J. Natl. Cancer Inst.* **54**(5), 1137–1148 (1975).
79. Dalum G., Lenferink A.T.M. and Terstappen L.W.M.M. Detection of EpCAM negative circulating tumor cells in CellSearch waste *Cancer Res.* **73**(Suppl. 1), 1459 (2013).
80. De Gruijl F.R. Skin cancer and solar UV radiation *Eur. J. Cancer* **35**(14), 2003–2009 (1999).
81. Dean L. The MNS blood group in *Blood groups and red cell antigens* National Center for Biotechnology Information, Bethesda, MD (2005).
82. Deblois R.W., Bean C.P. and Wesley R.K.A. Electrokinetic measurements with submicron particles and pores by the resistive pulse technique *J. Colloid Interf. Sci.* **61**(2), 323–335 (1977).
83. Deregibus M.C., Cantaluppi V., Calogero R., Iacono M.L., Tetta C., Biancone L., Bruno S., Bussolati B. and Camussi G. Endothelial progenitor cell–derived microvesicles activate an angiogenic program in endothelial cells by a horizontal transfer of mRNA *Blood* **110**(7), 2440–2448 (2007).
84. Diamant M., Nieuwland R., Pablo R.F., Sturk A., Smit J.W. and Radder J.K. Elevated numbers of tissue-factor exposing microparticles correlate with components of the metabolic syndrome in uncomplicated type 2 diabetes mellitus *Circulation* **106**(19), 2442–2447 (2002).

85. Dieckmann Y., Cölfen H., Hofmann H. and Petri-Fink A. Particle size distribution measurements of manganese-doped ZnS nanoparticles *Anal. Chem.* **81**(10), 3889–3895 (2009).
86. Diffey B.L. and Robson J. A new substrate to measure sunscreen protection factors throughout the ultraviolet spectrum *J. Soc. Cosmet. Chem.* **40**(3), 127–133 (1989).
87. van Dijk M.A., Lippitz M. and Orrit M. Far-field optical microscopy of single metal nanoparticles *Acc. Chem. Res.* **38**(7), 594–601 (2005).
88. Donath T., Brandstetter S., Cibik L., Commichau S., Hofer P., Krumrey M., Lüthi B., Marggraf S., Müller P., Schneebeli M. et al. Characterization of the PILATUS photon-counting pixel detector for X-ray energies from 1.75 keV to 60 keV in *J. Phys. Conf. Ser.* vol. 425 062001 IOP Publishing (2013).
89. Doornbos R.M.P., Schaeffer M., Hoekstra A.G., Sloot P., de Grooth B.G. and Greve J. Elastic light-scattering measurements of single biological cells in an optical trap *Appl. Opt.* **35**(4), 729–734 (1996).
90. Dragovic R.A., Gardiner C., Brooks A.S., Tannetta D.S., Ferguson D.J.P., Hole P., Carr B., Redman C.W.G., Harris A.L., Dobson P.J., Harrison P. and Sargent I.L. Sizing and phenotyping of cellulars vesicles using Nanoparticle Tracking Analysis *Nanomed. Nanotechnol. Biol. Med.* **7**(6), 780–788 (2011).
91. Eller M.S., Ostrom K. and Gilchrest B.A. DNA damage enhances melanogenesis *Proc. Natl. Acad. Sci. USA* **93**(3), 1087–1092 (1996).
92. Elwood J.M. and Jopson J. Melanoma and sun exposure: an overview of published studies *Int. J. Cancer* **73**(2), 198–203 (1997).
93. Escola J.M., Kleijmeer M.J., Stoorvogel W., Griffith J.M., Yoshie O. and Geuze H.J. Selective enrichment of tetraspan proteins on the internal vesicles of multivesicular endosomes and on exosomes secreted by human B-lymphocytes *J. Biol. Chem.* **273**(32), 20121–20127 (2010).
94. Faber D.J., Aalders M.C.G., Mik E.G., Hooper B.A., van Gemert M.J.C. and van Leeuwen T.G. Oxygen saturation-dependent absorption and scattering of blood *Phys. Rev. Lett.* **93**(2), 028102 (2004).
95. Faber D.J., van der Meer F., Aalders M.C.G. and van Leeuwen T.G. Quantitative measurement of attenuation coefficients of weakly scattering media using optical coherence tomography *Opt. Express* **12**(19), 4353–4365 (2004).
96. Fang Y., Wu N., Gan X., Yan W., Morrell J.C. and Gould S.J. Higher-order oligomerization targets plasma membrane proteins and HIV gag to exosomes *PLoS Biol.* **5**(6), e158 (2007).
97. Fattaccioli J., Baudry J., Émerard J.D., Bertrand E., Goubault C., Henry N. and Bibette J. Size and fluorescence measurements of individual droplets by flow cytometry *Soft Matter* **5**(11), 2232–2238 (2009).
98. Fauré J., Lachenal G., Court M., Hirrlinger J., Chatellard-Causse C., Blot B., Grange J., Schoehn G., Goldberg Y., Boyer V., Kirchhoff F., Raposo G., Garin J. and Sadoul R. Exosomes are released by cultured cortical neurones *Mol. Cell. Neurosci.* **31**(4), 642–648 (2006).

99. Ferraris C.F., Guthrie W., Avilés A.I., Haupt R. and MacDonald B.S. Certification of SRM 114q: Part I Tech. Rep. 260-161 National Institute of Standards and Technology Gaithersburg, MD (2005).
100. Ferris M.M. and Rowlen K.L. Detection and enumeration of single nanometric particles: A confocal optical design for fluorescence flow cytometry *Rev. Sci. Instrum.* **73**(6), 2404–2410 (2002).
101. Filella M., Zhang J.W., Newman M.E. and Buffle J. Analytical applications of photon correlation spectroscopy for size distribution measurements of natural colloidal suspensions: Capabilities and limitations *Colloid Surface A* **120**(1), 27–46 (1997).
102. Foladori P., Quaranta A. and Ziglio G. Use of silica microspheres having refractive index similar to bacteria for conversion of flow cytometric forward light scatter into biovolume *Water Res.* **42**(14), 3757–3766 (2008).
103. Fonder M.A., Mamelak A.J., Lazarus G.S. and Chanmugam A. Occlusive wound dressings in emergency medicine and acute care *Emerg. Med. Clin. North Am.* **25**(1), 235–242 (2007).
104. Ford T., Graham J. and Rickwood D. Iodixanol: a nonionic iso-osmotic centrifugation medium for the formation of self-generated gradients *Anal. Biochem.* **220**(2), 360–366 (1994).
105. Forster P., Ramaswamy V., Artaxo P., Berntsen T., Betts R., Fahey D.W., Haywood J., Lean J., Lowe D.C., Myhre G., Nganga J., Prinn R., Raga G., Schultz M. and Van Dorland R. Changes in atmospheric constituents and in radiative forcing in Solomon S., Qin D., Manning M., Chen Z., Marquis M., Averyt K., Tignor M. and Miller H. (eds.), *Climate Change 2007. The Physical Science Basis.* chap. 2, 129–234 Cambridge University Press, Cambridge, UK (2007).
106. Freyssinet J.M. Cellular microparticles: what are they bad or good for? *J. Thromb. Haemost.* **1**(7), 1655–1662 (2003).
107. Freyssinet J.M.R. and Toti F. Membrane microparticle determination: at least seeing what's being sized! *J. Thromb. Haemost.* **8**(2), 311–314 (2010).
108. Gardiner C., Ferreira Y.J., Dragovic R.A., Redman C.W.G. and Sargent I.L. Extracellular vesicle sizing and enumeration by nanoparticle tracking analysis *J. Extracell. Vesicles* **2**, 1–11 (2013).
109. de Gassart A., Géminard C., Février B., Raposo G. and Vidal M. Lipid raft-associated protein sorting in exosomes *Blood* **102**(13), 4336–4344 (2003).
110. George J.N., Potterf R.D., Lewis P.C. and Sears D.A. Studies on platelet plasma membranes. I. Characterization of surface proteins of human platelets labeled with diazotized (125i)-diiodosulfanilic acid *J. Lab. Clin. Med.* **88**(2), 232–246 (1976).
111. George J.N., Thoi L.L., McManus L.M. and Reimann T.A. Isolation of human platelet membrane microparticles from plasma and serum *Blood* **60**(4), 834–840 (1982).
112. Giesen P.L.A., Rauch U., Bohrmann B., Kling D., Roqué M., Fallon J.T., Badimon J.J., Himber J., Riederer M.A. and Nemerson Y. Blood-borne tissue

factor: another view of thrombosis *Proc. Natl. Acad. Sci. USA* **96**(5), 2311–2315 (1999).

113. Gleber G., Cibik L., Haas S., Hoell A., Müller P. and Krumrey M. Traceable size determination of PMMA nanoparticles based on Small Angle X-ray Scattering (SAXS) in *J. Phys. Conf. Ser.* vol. 247 012027 IOP Publishing (2010).
114. Goddard G., Martin J.C., Naivar M., Goodwin P.M., Graves S.W., Habbersett R., Nolan J.P. and Jett J.H. Single particle high resolution spectral analysis flow cytometry *Cytom. Part A* **69**(8), 842–851 (2006).
115. Goss A.N. Intra-uterine healing of fetal rat oral mucosal, skin and cartilage wounds *J. Oral Pathol. Med.* **6**(1), 35–43 (1977).
116. Grdisa M., Mathew A. and Johnstone R. Expression and loss of the transferrin receptor in growing and differentiating HD3 cells *J. Cell Physiol.* **155**(2), 349–357 (1993).
117. de Grooth B.G., Terstappen L.W.M.M., Pupples G.J. and Greve J. Light-scattering polarization measurements as a new parameter in flow cytometry *Cytometry* **8**(6), 539–544 (1987).
118. Gujrati V., Kim S., Kim S.H., Min J.J., Choy H.E., Kim S.C. and Jon S. Bioengineered bacterial outer membrane vesicles as cell-specific drug-delivery vehicles for cancer therapy *ACS Nano* **8**(2), 1525–1537 (2014).
119. Gurtner G.C., Werner S., Barrandon Y. and Longaker M.T. Wound repair and regeneration *Nature* **453**(7193), 314–321 (2008).
120. György B., Módos K., Pállinger É., Pálóczi K., Pásztói M., Misják P., Deli M.A., Sipos Á., Szalai A., Voszka I., Polgár A., Tóth K., Csete M., Nagy G., Gay S., Falus A., Kittel A. and Buzás E.I. Detection and isolation of cell-derived microparticles are compromised by protein complexes resulting from shared biophysical parameters *Blood* **117**(4), e39–e48 (2011).
121. György B., Szabó T.G., Pálóczi M., Pál Z., Misják P., Aradi B., László V., Pállinger E., Pap E., Kittel A., Nagy G., Falus A. and Buzás E.I. Membrane vesicles, current state-of-the-art: emerging role of extracellular vesicles *Cell. Mol. Life Sci.* **68**(16), 2667–2688 (2011).
122. Hagel L., Östberg M. and Andersson T. Apparent pore size distributions of chromatography media *J. Chrom. A* **743**(1), 33–42 (1996).
123. Harding C., Heuser J. and Stahl P. Receptor-mediated endocytosis of transferrin and recycling of the transferrin receptor in rat reticulocytes. *J. Cell Biol.* **97**(2), 329–339 (1983).
124. Harrison P., Dragovic R., Albanyan A., Lawrie A.S., Murphy M. and Sargent I. Application of dynamic light scattering to the measurement of microparticles *J. Thromb. Haemost.* **7**(Suppl. 2) (2009).
125. Harrison P. and Gardiner C. Invisible vesicles swarm within the iceberg *J. Thromb. Haemost.* **10**(5), 916–918 (2012).
126. Hart S.J. and Leski T.A. Refractive index determination of biological particles Tech. Rep. ADA454180 Naval Research Laboratory Washington, DC (2006).

127. Hart S.J. and Terray A.V. Refractive-index-driven separation of colloidal polymer particles using optical chromatography *Appl. Phys. Lett.* **83**(25), 5316–5318 (2003).
128. Haugland R.P., Spence M.T.Z. and Johnson I.D. *The handbook: A Guide to Fluorescent Probes and Labeling Technologies* Molecular probes, Stockton, CA (2005).
129. Heijnen H.F.G., Schiel A.E., Fijnheer R., Geuze H.J. and Sixma J.J. Activated platelets release two types of membrane vesicles: Microvesicles by surface shedding and exosomes derived from exocytosis of multivesicular bodies and alpha-granules *Blood* **94**(11), 3791–3799 (1999).
130. Hein B., Willig K.I. and Hell S.W. Stimulated emission depletion (STED) nanoscopy of a fluorescent protein-labeled organelle inside a living cell *Proc. Natl. Acad. Sci. USA* **105**(38), 14271–14276 (2008).
131. Heins E.A., Siwy Z.S., Baker L.A. and Martin C.R. Detecting single porphyrin molecules in a conically shaped synthetic nanopore *Nano Lett.* **5**(9), 1824–1829 (2005).
132. Hexley P., Robinson C.T., Osterburg A.R. and Babcock G.F. Circulating microparticles do not all share biophysical light scatter properties with immune complexes when analyzed by flow cytometry *Blood* **120**(7), 1528–1529 (2012).
133. Hirai M., Iwase H., Hayakawa T., Koizumi M. and Takahashi H. Determination of asymmetric structure of ganglioside-DPPC mixed vesicle using SANS, SAXS, and DLS *Biophys. J.* **85**(3), 1600–1610 (2003).
134. Hoekstra A.G., Maltsev V. and Videen G. *Optics of Biological Particles* vol. 238 of *Proceedings of the NATO advanced research workshop on fluorescence and other optical properties of biological particles for biological warfare agent sensors* Springer, Dordrecht, The Netherlands (2007).
135. Hoekstra A.G. and Sloot P. *Light Scattering by Nonspherical Particles, Theory, Measurements, and Applications* chap. Biophysical and biomedical applications of non-spherical scattering, 585–602 Academic Press, San Diego, CA (2000).
136. Holmgren L., Szeles A., Rajnavölgyi E., Folkman J., Klein G., Ernberg I. and Falk K.I. Horizontal transfer of DNA by the uptake of apoptotic bodies *Blood* **93**(11), 3956–3963 (1999).
137. Hoo C.M., Starostin N., West P. and Mecartney M.L. A comparison of atomic force microscopy (AFM) and dynamic light scattering (DLS) methods to characterize nanoparticle size distributions *J. Nanopart. Res.* **10**(1), 89–96 (2008).
138. Hristov M., Erl W., Linder S. and Weber P.C. Apoptotic bodies from endothelial cells enhance the number and initiate the differentiation of human endothelial progenitor cells in vitro *Blood* **104**(9), 2761–2766 (2004).
139. Hsu C., Morohashi Y., Yoshimura S.i., Manrique-Hoyos N., Jung S., Lauterbach M.A., Bakhti M., Grønborg M., Möbius W., Rhee J., Barr F.A. and Simons M. Regulation of exosome secretion by Rab35 and its GTPase-activating proteins TBC1D10A–C *J. Cell Biol.* **189**(2), 223–232 (2010).

140. van de Hulst H.C. *Light scattering by small particles* Wiley, New York (1957).
141. Humphris A.D.L., Miles M.J. and Hobbs J.K. A mechanical microscope: high-speed atomic force microscopy *Appl. Phys. Lett.* **86**(3), 034106 (2005).
142. Issadore D., Min C., Liong M., Chung J., Weissleder R. and Lee H. Miniature magnetic resonance system for point-of-care diagnostics *Lab Chip* **11**(13), 2282–2287 (2011).
143. Issman L., Brenner B., Talmon Y. and Aharon A. Cryogenic transmission electron microscopy nanostructural study of shed microparticles *PLoS ONE* **8**(12), e83680 (2013).
144. Ito T., Sun L., Henriquez R.R. and Crooks R.M. A carbon nanotube-based Coulter nanoparticle counter *Acc. Chem. Res.* **37**(12), 937–945 (2004).
145. Jang S.C., Kim O.Y., Yoon C.M., Choi D.S., Roh T.Y., Park J., Nilsson J., Lötvall J., Kim Y.K. and Gho Y.S. Bioinspired exosome-mimetic nanovesicles for targeted delivery of chemotherapeutics to malignant tumors *ACS Nano* **7**(9), 7698–7710 (2013).
146. Jänicke R.U., Sprengart M.L., Wati M.R. and Porter A.G. Caspase-3 is required for DNA fragmentation and morphological changes associated with apoptosis *J. Biol. Chem.* **273**(16), 9357–9360 (1998).
147. Jayachandran M., Miller V.M., Heit J.A. and Owen W.G. Methodology for isolation, identification and characterization of microvesicles in peripheral blood *J. Immunol. Methods* **375**(1), 207–214 (2012).
148. Jensen O.A., Prause J.U. and Laursen H. Shrinkage in preparatory steps for SEM: a study on rabbit corneal endothelium *A. Graef. Arch. Klin. Exp. Ophthalmol.* **215**(4), 233–242 (1981).
149. Jewell R.B. and Rathbone R.F. Optical properties of coal combustion byproducts for particle-size analysis by laser diffraction *Coal Combust. Gasific. Prods.* **1**, 1–7 (2009).
150. Jhappan C., Noonan F.P. and Merlino G. Ultraviolet radiation and cutaneous malignant melanoma *Oncogene* **22**(20), 3099–3112 (2003).
151. Johnstone R.M. Maturation of reticulocytes: formation of exosomes as a mechanism for shedding membrane proteins *Biochem. Cell Biol.* **70**(3-4), 179–190 (1992).
152. Johnstone R.M., Adam M., Hammond J.R., Orr L. and Turbide C. Vesicle formation during reticulocyte maturation. Association of plasma membrane activities with released vesicles (exosomes). *J. Biol. Chem.* **262**(19), 9412–9420 (1987).
153. Johnstone R.M., Bianchini A. and Teng K. Reticulocyte maturation and exosome release: transferrin receptor containing exosomes shows multiple plasma membrane functions *Blood* **74**(5), 1844–1851 (1989).
154. Johnstone R.M., Mathew A., Mason A.B. and Teng K. Exosome formation during maturation of mammalian and avian reticulocytes: evidence that exosome release is a major route for externalization of obsolete membrane proteins *J. Cell Physiol.* **147**(1), 27–36 (1991).

155. Jonasz M. and Fournier G. *Light Scattering by Particles in Water: Theoretical and Experimental Foundations* 1st edn. Academic Press, London, UK (2007).
156. Joop K., Berckmans R., Nieuwland R., Berkhout J., Romijn F.P.H.T., Hack C.E. and Sturk A. Microparticles from patients with multiple organ dysfunction syndrome and sepsis support coagulation through multiple mechanisms *Thromb. Haemost.* **85**(5), 810–820 (2001).
157. Jy W., Horstman L.L., Jimenez J.J. and Ahn Y.S. Measuring circulating cell-derived microparticles *J. Thromb. Haemost.* **2**(10), 1842–1843 (2004).
158. Kachel V. *Electrical resistance pulse sizing (Coulter sizing)* 45–80 2nd edn. Wiley-Liss, New York, NY (1990).
159. Kang D.J., Oh S., Ahn S.M., Lee B.H. and Moon M.H. Proteomic analysis of exosomes from human neural stem cells by flow field-flow fractionation and nanoflow liquid chromatography-tandem mass spectrometry *J. Proteome Res.* **7**(8), 3475–3480 (2008).
160. Kanno T., Yamada T., Iwabuki H., Tanaka H., Kuroda S., Tanizawa K. and Kawai T. Size distribution measurement of vesicles by atomic force microscopy *Anal. Biochem.* **309**(2), 196–199 (2002).
161. Kasarova S.N., Sultanova N.G., Ivanov C.D. and Nikolov I.D. Analysis of the dispersion of optical plastic materials *Opt. Mater.* **29**(11), 1481–1490 (2007).
162. Keller S., Ridinger J., Rupp A.K., Janssen J. and Altevogt P. Body fluid derived exosomes as a novel template for clinical diagnostics *J. Transl. Med.* **9**(86), 1–9 (2011).
163. Keller S., Sanderson M.P., Stoeck A. and Altevogt P. Exosomes: from biogenesis and secretion to biological function *Immunol. Lett.* **107**(2), 102–108 (2006).
164. Kerr J.F.R., Wyllie A.H. and Currie A.R. Apoptosis: a basic biological phenomenon with wide-ranging implications in tissue kinetics *Br. J. Cancer* **26**(4), 239 (1972).
165. Kesimer M., Scull M., Brighton B., DeMaria G., Burns K., O'Neal W., Pickles R.J. and Sheehan J.K. Characterization of exosome-like vesicles released from human tracheobronchial ciliated epithelium: a possible role in innate defense *FASEB J.* **23**(6), 1858–1868 (2009).
166. Kindt J.D. *Optofluidic intracavity spectroscopy for spatially, temperature, and wavelength dependent refractometry* Ph.D. thesis Colorado State University Fort Collins, CO (2012).
167. Knöner G., Parkin S., Nieminen T.A., Heckenberg N.R. and Rubinsztein-Dunlop H. Measurement of the index of refraction of single microparticles *Phys. Rev. Lett.* **97**(15), 157402 (2006).
168. Kolesnikova I.V., Potapov S.V., Yurkin M.A., Hoekstra A.G., Maltsev V.P. and Semyanov K.A. Determination of volume, shape and refractive index of individual blood platelets *J. Quant. Spectrosc. Radiat. Transfer* **102**(1), 37–45 (2006).

169. Konokhova A.I., Yurkin M.A., Moskalensky A.E., Chernyshev A.V., Tsvetovskaya G.A., Chikova E.D. and Maltsev V.P. Light-scattering flow cytometry for identification and characterization of blood microparticles *J. Biomed. Opt.* **17**(5), 0570061–0570068 (2012).
170. Korgel B.A., van Zanten J.H. and Monbouquette H.G. Vesicle size distributions measured by flow field-flow fractionation coupled with multiangle light scattering *Biophys. J.* **74**(6), 3264–3272 (1998).
171. Kozak D., Anderson W., Vogel R., Chen S., Antaw F. and Trau M. Simultaneous size and ζ-potential measurements of individual nanoparticles in dispersion using size-tunable pore sensors *ACS nano* **6**(8), 6990–6997 (2012).
172. Krämer-Albers E.M., Bretz N., Tenzer S., Winterstein C., Möbius W., Berger H., Nave K.A., Schild H. and Trotter J. Oligodendrocytes secrete exosomes containing major myelin and stress-protective proteins: Trophic support for axons? *Proteomics Clin. Appl.* **1**(11), 1446–1461 (2007).
173. Kroonenberg S. *De menselijke maat* Atlas Contact (2012).
174. Krpetic Z., Nativo P., Sée V., Prior I.A., Brust M. and Volk M. Inflicting controlled nonthermal damage to subcellular structures by laser-activated gold nanoparticles *Nano Lett.* **10**(11), 4549–4554 (2010).
175. Krumrey M., Gleber G., Scholze F. and Wernecke J. Synchrotron radiation-based x-ray reflection and scattering techniques for dimensional nanometrology *Meas. Sci. Technol.* **22**(9), 094032 (2011).
176. Kumar A., Vemula P.K., Ajayan P.M. and John G. Silver-nanoparticle-embedded antimicrobial paints based on vegetable oil *Nat. Mater.* **7**(3), 236–241 (2008).
177. Lacroix R., Judicone C., Poncelet P., Robert S., Arnaud L., Sampol J. and Dignat-George F. Impact of pre-analytical parameters on the measurement of circulating microparticles: towards standardization of protocol *J. Thromb. Haemost.* **10**(3), 437–446 (2012).
178. Lacroix R., Robert S., Poncelet P. and Dignat-George F. Overcoming limitations of microparticle measurement by flow cytometry *Semin. Thromb. Hemost.* **36**(8), 807–818 (2010).
179. Lacroix R., Robert S., Poncelet P., Kasthuri R.S., Key N.S. and Dignat-George F. Standardization of platelet-derived microparticle enumeration by flow cytometry with calibrated beads: results of the International Society on Thrombosis and Haemostasis SSC Collaborative workshop *J. Thromb. Haemost.* **8**(11), 2571–2574 (2010).
180. Lages B., Scrutton M.C. and Holmsen H. Studies on gel-filtered human platelets: isolation and characterization in a medium containing no added Ca2+, Mg2+, or K+. *J. Lab. Clin. Med.* **85**(5), 811–825 (1975).
181. Lang-Yona N., Rudich Y., Segre E., Dinar E. and Abo-Riziq A. Complex refractive indices of aerosols retrieved by continuous wave-cavity ring down aerosol spectrometer *Anal. Chem.* **81**(5), 1762–1769 (2009).
182. Larson M.C., Luthi M.R., Hogg N. and Hillery C.A. Calcium-phosphate microprecipitates mimic microparticles when examined with flow cytometry *Cytom. Part A* **83**(2), 242–250 (2013).

183. Lauri A., Brunet T., Handberg-Thorsager M., Fischer A.H., Simakov O., Steinmetz P.R.H., Tomer R., Keller P.J. and Arendt D. Development of the annelid axochord: Insights into notochord evolution *Science* **345**(6202), 1365–1368 (2014).
184. Laven P. MiePlot (2011) URL `http://www.philiplaven.com/mieplot.htm`.
185. Lawrie A.S., Albanyan A., Cardigan R.A., Mackie I. and Harrison P. Microparticle sizing by dynamic light scattering in fresh-frozen plasma *Vox Sang.* **96**(3), 206–212 (2009).
186. Le Pecq J.B. Dexosomes as a therapeutic cancer vaccine: from bench to bedside *Blood Cells Mol. Dis.* **35**(2), 129–135 (2005).
187. Lenassi M., Cagney G., Liao M., Vaupotič T., Bartholomeeusen K., Cheng Y., Krogan N.J., Plemenitaš A. and Peterlin B.M. HIV Nef is secreted in exosomes and triggers apoptosis in bystander CD4+ T cells *Traffic* **11**(1), 110–122 (2010).
188. Li J., Sherman-Baust C.A., Tsai-Turton M., Bristow R.E., Roden R.B. and Morin P.J. Claudin-containing exosomes in the peripheral circulation of women with ovarian cancer *BMC cancer* **9**(1), 244–255 (2009).
189. Loomis R.J., Holmes D.A., Elms A., Solski P.A., Der C.J. and Su L. Citron kinase, a RhoA effector, enhances HIV-1 virion production by modulating exocytosis *Traffic* **7**(12), 1643–1653 (2006).
190. Ma X., Lu J.Q., Brock R.S., Jacobs K.M., Yang P. and Hu X.H. Determination of complex refractive index of polystyrene microspheres from 370 to 1610 nm *Phys. Med. Biol.* **48**(24), 4165–4172 (2003).
191. Mackowiak S.A., Schmidt A., Weiss V., Argyo C., von Schirnding C., Bein T. and Bräuchle C. Targeted drug delivery in cancer cells with red-light photoactivated mesoporous silica nanoparticles *Nano Lett.* **13**(6), 2576–2583 (2013).
192. Mallat Z., Benamer H., Hugel B., Benessiano J., Steg P.G., Freyssinet J.M. and Tedgui A. Elevated levels of shed membrane microparticles with procoagulant potential in the peripheral circulating blood of patients with acute coronary syndromes *Circulation* **101**(8), 841–843 (2000).
193. Manly D.A., Wang J.G., Glover S.L., Kasthuri R., Liebman H.A., Key N.S. and Mackman N. Increased microparticle tissue factor activity in cancer patients with Venous Thromboembolism *Thromb. Res.* **125**(6), 511–512 (2010).
194. Marsh M. and van Meer G. No ESCRTs for exosomes *Science* **319**(5867), 1191–1192 (2008).
195. Martin P. Wound healing - aiming for perfect skin regeneration *Science* **276**(5309), 75–81 (1997).
196. Marzesco A.M., Janich P., Wilsch-Brauninger M., Dubreuil V., Langenfeld K., Corbeil D. and Huttner W.B. Release of extracellular membrane particles carrying the stem cell marker prominin-1 (CD133) from neural progenitors and other epithelial cells *J. Cell Sci.* **118**(13), 2849–2858 (2005).
197. Mathivanan S., Ji H. and Simpson R.J. Exosomes: extracellular organelles important in intercellular communication *J. Proteomics* **73**(10), 1907–1920 (2010).

198. Matsuo H., Chevallier J., Mayran N., Le Blanc I., Ferguson C., Fauré J., Blanc N.S., Matile S., Dubochet J., Sadoul R., Parton R.G. and Vilbois F. Role of LBPA and Alix in multivesicular liposome formation and endosome organization *Science* **303**(5657), 531–534 (2004).

199. Mätzler C. MATLAB functions for Mie scattering and absorption Report (2002).

200. McCarthy D.A. Fluorochromes and fluorescence in Macey M. (ed.), *Flow Cytometry: Principles and Applications* 59–112 Humana Press (2007).

201. McMeekin T.L., Wilensky M. and Groves M.L. Refractive indices of proteins in relation to amino acid composition and specific volume *Biochem. Biophys. Res. Commun.* **7**(2), 151–156 (1962).

202. Meli F., Klein T., Buhr E., Frase C.G., Gleber G., Krumrey M., Duta A., Duta S., Korpelainen V., Bellotti R., Picotto G., Boyd R. and Cuenat A. Traceable size determination of nanoparticles, a comparison among European metrology institutes *Meas. Sci. Technol.* **23**(12), 125005 (2012).

203. Michalet X. and Berglund A.J. Optimal diffusion coefficient estimation in single-particle tracking *Phys. Rev. E* **85**(6), 061916 (2012).

204. Michelet X., Djeddi A. and Legouis R. Developmental and cellular functions of the ESCRT machinery in pluricellular organisms *Biol. Cell* **102**(3), 191–202 (2010).

205. Miles R.E., Rudić S., Orr-Ewing A.J. and Reid J.P. Measurements of the wavelength dependent extinction of aerosols by cavity ring down spectroscopy *Phys. Chem. Chem. Phys.* **12**(15), 3914–3920 (2010).

206. Mills G.L., Lane P.A. and Weech P.K. *A guidebook to lipoprotein techniques* Elsevier, Amsterdam, The Netherlands (2000).

207. Möbius W., Ohno-Iwashita Y., van Donselaar E.G., Oorschot V.M., Shimada Y., Fujimoto T., Heijnen H.F., Geuze H.J. and Slot J.W. Immunoelectron microscopic localization of cholesterol using biotinylated and non-cytolytic perfringolysin O *J. Histochem. Cytochem.* **50**(1), 43–55 (2002).

208. Momen-Heravi F., Balaj L., Alian S., Trachtenberg A.J., Hochberg F.H., Skog J. and Kuo W.P. Impact of biofluid viscosity on size and sedimentation efficiency of the isolated microvesicles *Front Physiol.* **3**, 162–167 (2012).

209. Montesinos E., Esteve I. and Guerrero R. Comparison between direct methods for determination of microbial cell volume: electron microscopy and electronic particle sizing *Appl. Environ. Microbiol.* **45**(5), 1651–1658 (1983).

210. Morel O., Jesel L., Freyssinet J.M. and Toti F. Cellular mechanisms underlying the formation of circulating microparticles *Arterioscler. Thromb. Vasc. Biol.* **31**(1), 15–26 (2011).

211. Mosk A.P., Blum C., Cesa Y., van den Broek J.M., Vos W.L. and Subramaniam V. Controlling Fluorescent Proteins by Manipulating the Local Density of Photonic States in *Frontiers in Optics* FWS6 Optical Society of America (2009).

212. Mullier F., Bailly N., Chatelain C., Dogné J.M. and Chatelain B. More on: calibration for the measurement of microparticles: needs, interests, and limitations of calibrated polystyrene beads for flow cytometry-based quantification of biological microparticles *J. Thromb. Haemost.* **9**(8), 1679–1681 (2011).
213. Mullier F., Dogné J.M., Bailly N., Cornet Y., Robert S. and Chatelain B. Accurate quantification of microparticles by flow cytometry: important issues *J. Thromb. Haemost.* **7**(Suppl. 2) (2009).
214. Nieuwland R., Berckmans R.J., McGregor S., Böing A.N., Romijn F.P.H.T., Westendorp R.G.J., Hack C.E. and Sturk A. Cellular origin and procoagulant properties of microparticles in meningococcal sepsis *Blood* **95**(3), 930–935 (2000).
215. Nieuwland R., Berckmans R.J., Rotteveel-Eijkman R.C., Maquelin K.N., Roozendaal K.J., Jansen P.G.M., ten Have K., Eijsman L., Hack C.E. and Sturk A. Cell-derived microparticles generated in patients during cardiopulmonary bypass are highly procoagulant *Circulation* **96**(10), 3534–3541 (1997).
216. Nieuwland R., van der Pol E., Gardiner C. and Sturk A. *Platelets* chap. Platelet-derived microparticles, 453–467 3rd edn. Academic Press, San Diego, CA (2012).
217. Nieuwland R. and Sturk A. Why do cells release vesicles? *Thromb. Res.* **125**(Suppl 1), S49–S51 (2010).
218. Nolan J.P. and Stoner S.A. A trigger channel threshold artifact in nanoparticle analysis *Cytom. Part A* **83**(3), 301–305 (2013).
219. O'Brien J.R. Cell membrane damage, platelet stickiness and some effects of aspirin *Br. J. Haematol.* **17**(6), 610–611 (1969).
220. Ogawa Y., Kanai-Azuma M., Akimoto Y., Kawakami H. and Yanoshita R. Exosome-like vesicles with dipeptidyl peptidase IV in human saliva *Biol. Pharm. Bull.* **31**(6), 1059–1062 (2008).
221. Oster G. Two-phase formation in solutions of tobacco mosaic virus and the problem of long-range forces *J. Gen. Physiol.* **33**(5), 445–473 (1950).
222. Ostrowski M., Carmo N.B., Krumeich S., Fanget I., Raposo G., Savina A., Moita C.F., Schauer K., Hume A.N., Freitas R.P., Goud B., Benaroch P., Hacohen N., Fukuda M., Desnos C., Seabra M.C., Darchen F., Amigorena S., Moita L.F. and Théry C. Rab27a and Rab27b control different steps of the exosome secretion pathway *Nat. Cell Biol.* **12**(1), 19–30 (2009).
223. Palma J., Yaddanapudi S.C., Pigati L., Havens M.A., Jeong S., Weiner G.A., Weimer K.M.E., Stern B., Hastings M.L. and Duelli D.M. MicroRNAs are exported from malignant cells in customized particles *Nucleic Acids Res.* **40**(18), 9125–9138 (2012).
224. Pan B.T., Teng K., Wu C., Adam M. and Johnstone R.M. Electron microscopic evidence for externalization of the transferrin receptor in vesicular form in sheep reticulocytes. *J. Cell Biol.* **101**(3), 942–948 (1985).
225. Parkinson D.Y., McDermott G., Etkin L.D., Le Gros M.A. and Larabell C.A. Quantitative 3-D imaging of eukaryotic cells using soft X-ray tomography *J. Struct. Biol.* **162**(3), 380–386 (2008).

226. Patil C.A., Bosschaart N., Keller M.D., van Leeuwen T.G. and Mahadevan-Jansen A. Combined Raman spectroscopy and optical coherence tomography device for tissue characterization *Opt. Lett.* **33**(10), 1135–1137 (2008).

227. Perez-Pujol S., Marker P.H. and Key N.S. Platelet microparticles are heterogeneous and highly dependent on the activation mechanism: studies using a new digital flow cytometer *Cytom. Part A* **71**(1), 38–45 (2007).

228. Peter K. Platelet Integrins and Signaling in *Platelet Function* 21–42 Springer, New York, NY (2005).

229. Pisitkun T., Shen R.F. and Knepper M.A. Identification and proteomic profiling of exosomes in human urine *Proc. Natl. Acad. Sci. USA* **101**(36), 13368–13373 (2004).

230. Pluchino A.B., Goldberg S.S., Dowling J.M. and Randall C.M. Refractive-index measurements of single micron-sized carbon particles *Appl. Opt.* **19**(19), 3370–3372 (1980).

231. van der Pol E., Böing A.N., Harrison P., Sturk A. and Nieuwland R. Classification, functions and clinical relevance of extracellular vesicles *Pharmacol. Rev.* **64**(3), 676–705 (2012).

232. van der Pol E., Coumans F.A.W., Grootemaat A.E., Gardiner C., Sargent I.L., Harrison P., Sturk A., van Leeuwen T.G. and Nieuwland R. Particle size distribution of exosomes and microvesicles by transmission electron microscopy, flow cytometry, nanoparticle tracking analysis, and resistive pulse sensing *J. Thromb. Haemost.* **12**, 1–11 (2014).

233. van der Pol E., Coumans F.A.W., Varga Z., Krumrey M. and Nieuwland R. Innovation in detection of microparticles and exosomes *J. Thromb. Haemost.* **11**(s1), 36–45 (2013).

234. van der Pol E., van Gemert M.J.C., Sturk A., Nieuwland R. and van Leeuwen T.G. Single versus swarm detection of microparticles and exosomes by flow cytometry *J. Thromb. Haemost.* **10**(5), 919–930 (2012).

235. van der Pol E., Hoekstra A.G., Sturk A., Otto C., van Leeuwen T.G. and Nieuwland R. Optical and non-optical methods for detection and characterization of microparticles and exosomes *J. Thromb. Haemost.* **8**(12), 2596–2607 (2010).

236. van der Pol E., Leeuwen T.G. and Nieuwland R. *Extracellular Vesicles in Health and Disease* chap. An overview of novel and conventional methods to detect extracellular vesicles, 107–138 1st edn. Pan Standford Publishing, Singapore (2014).

237. Poliakov A., Spilman M., Dokland T., Amling C.L. and Mobley J.A. Structural heterogeneity and protein composition of exosome-like vesicles (prostasomes) in human semen *Prostate* **69**(2), 159–167 (2009).

238. Prado N., Marazuela E.G., Segura E., Fernández-García H., Villalba M., Théry C., Rodríguez R. and Batanero E. Exosomes from bronchoalveolar fluid of tolerized mice prevent allergic reaction *J. Immunol.* **181**(2), 1519–1525 (2008).

239. Pully V.V., Lenferink A. and Otto C. Hybrid Rayleigh, Raman and two-photon excited fluorescence spectral confocal microscopy of living cells *J. Raman Spectrosc.* **41**(6), 599–608 (2010).
240. Pully V.V., Lenferink A.T.M. and Otto C. Time-lapse Raman imaging of single live lymphocytes *J. Raman Spectrosc.* **42**(2), 167–173 (2011).
241. Puppels G.J., Colier W., Olminkhof J.H.F., Otto C., De Mul F.F.M. and Greve J. Description and performance of a highly sensitive confocal Raman microspectrometer *J. Raman Spectrosc.* **22**(4), 217–225 (1991).
242. Puppels G.J., De Mul F.F.M., Otto C., Greve J., Robert-Nicoud M., Arndt-Jovin D.J. and Jovin T.M. Studying single living cells and chromosomes by confocal Raman microspectroscopy *Nature* **347**(6290), 301–303 (1990).
243. Radbruch A. *Flow Cytometry and Cell Sorting* 2nd edn. Springer, New York (2000).
244. Rao S.K., Huynh C., Proux-Gillardeaux V., Galli T. and Andrews N.W. Identification of SNAREs involved in synaptotagmin VII-regulated lysosomal exocytosis *J. Biol. Chem.* **279**(19), 20471–20479 (2004).
245. Raposo G., Nijman H.W., Stoorvogel W., Leijendekker R., Harding C.V., Melief C.J.M. and Geuze H.J. B lymphocytes secrete antigen-presenting vesicles *J. Exp. Med.* **183**(3), 1161–1172 (1996).
246. Ratajczak J., Wysoczynski M., Hayek F., Janowska-Wieczorek A. and Ratajczak M.Z. Membrane-derived microvesicles: important and underappreciated mediators of cell-to-cell communication *Leukemia* **20**(9), 1487–1495 (2006).
247. Rautou P.E., Leroyer A.S., Ramkhelawon B., Devue C., Duflaut D., Vion A.C., Nalbone G., Castier Y., Leseche G., Lehoux S., Tedgui A. and Boulanger C.M. Microparticles From Human Atherosclerotic Plaques Promote Endothelial ICAM-1-Dependent Monocyte Adhesion and Transendothelial Migration *Circ. Res.* **108**(3), 335–343 (2011).
248. Record M., Subra C., Silvente-Poirot S. and Poirot M. Exosomes as intercellular signalosomes and pharmacological effectors *Biochem. Pharmacol.* **81**(10), 1171–1182 (2011).
249. Redgrave T.G., Roberts D.C.K. and West C.E. Separation of plasma lipoproteins by density-gradient ultracentrifugation *Anal. Biochem.* **65**(1), 42–49 (1975).
250. Righini M., Ghenuche P., Cherukulappurath S., Myroshnychenko V., García de Abajo F.J. and Quidant R. Nano-optical trapping of Rayleigh particles and Escherichia coli bacteria with resonant optical antennas *Nano Lett.* **9**(10), 3387–3391 (2009).
251. van Rijn C.J.M. *Nano and micro engineered membrane technology* vol. 10 of *Membrane Science and Technology Series* 1st edn. Elsevier Science, Amsterdam, The Netherlands (2004).
252. Robert S., Lacroix R., Poncelet P., Harhouri K., Bouriche T., Judicone C., Wischhusen J., Arnaud L. and Dignat-George F. High-sensitivity flow cytometry provides access to standardized measurement of small-size microparticles *Arterioscler. Thromb. Vasc. Biol.* **32**(4), 1054–1058 (2012).

253. Robert S., Poncelet P., Lacroix R., Arnaud L., Giraudo L., Hauchard A., Sampol J. and Dignat-George F. Standardization of platelet-derived microparticle counting using calibrated beads and a Cytomics FC500 routine flow cytometer: a first step towards multicenter studies? *J. Thromb. Haemost.* **7**(1), 190–197 (2009).

254. Robert S., Poncelet P., Lacroix R., Raoult D. and Dignat-George F. More on: calibration for the measurement of microparticles: value of calibrated polystyrene beads for flow cytometry-based sizing of biological microparticles *J. Thromb. Haemost.* **9**(8), 1676–1678 (2011).

255. Robinson B.W. and Goss A.N. Intra-uterine healing of fetal rat cheek wounds *Cleft Palate J.* **18**(4), 251–255 (1981).

256. Rood I.M., Deegens J.K.J., Merchant M.L., Tamboer W.P., Wilkey D.W., Wetzels J.F.M. and Klein J.B. Comparison of three methods for isolation of urinary microvesicles to identify biomarkers of nephrotic syndrome *Kidney Int.* **78**(8), 810–816 (2010).

257. Rozhkova E.A., Ulasov I., Lai B., Dimitrijevic N.M., Lesniak M.S. and Rajh T. A high-performance nanobio photocatalyst for targeted brain cancer therapy *Nano Lett.* **9**(9), 3337–3342 (2009).

258. Safaei R., Larson B.J., Cheng T.C., Gibson M.A., Otani S., Naerdemann W. and Howell S.B. Abnormal lysosomal trafficking and enhanced exosomal export of cisplatin in drug-resistant human ovarian carcinoma cells *Mol. Cancer Ther.* **4**(10), 1595–1604 (2005).

259. Saleh O. and Sohn L.L. Quantitative sensing of nanoscale colloids using a microchip Coulter counter *Rev. Sci. Instrum.* **72**(12), 4449–4451 (2001).

260. Savina A., Fader C.M., Damiani M.T. and Colombo M.I. Rab11 promotes docking and fusion of multivesicular bodies in a calcium-dependent manner *Traffic* **6**(2), 131–143 (2005).

261. Savina A., Furlán M., Vidal M. and Colombo M.I. Exosome release is regulated by a calcium-dependent mechanism in K562 cells *J. Biol. Chem.* **278**(22), 20083–20090 (2003).

262. Sebbagh M., Renvoizé C., Hamelin J., Riché N., Bertoglio J. and Bréard J. Caspase-3-mediated cleavage of ROCK I induces MLC phosphorylation and apoptotic membrane blebbing *Nat. Cell Biol.* **3**(4), 346–352 (2001).

263. Shah M.D., Bergeron A.L., Dong J.F. and López J.A. Flow cytometric measurement of microparticles: pitfalls and protocol modifications *Platelets* **19**(5), 365–372 (2008).

264. Shao H., Chung J., Balaj L., Charest A., Bigner D.D., Carter B.S., Hochberg F.H., Breakefield X.O., Weissleder R. and Lee H. Protein typing of circulating microvesicles allows real-time monitoring of glioblastoma therapy *Nat. Med.* **18**(12), 1835–1840 (2012).

265. Shao H., Yoon T.J., Liong M., Weissleder R. and Lee H. Magnetic nanoparticles for biomedical NMR-based diagnostics *Beilstein J. Nanotechnol.* **1**(1), 142–154 (2010).

266. Shapiro H.M. and Leif R.C. *Practical flow cytometry* 4th edn. John Wiley & Sons, Inc., NJ (2003).
267. Shet A.S., Aras O., Gupta K., Hass M.J., Rausch D.J., Saba N., Koopmeiners L., Key N.S. and Hebbel R.P. Sickle blood contains tissue factor–positive microparticles derived from endothelial cells and monocytes *Blood* **102**(7), 2678–2683 (2003).
268. Shih S.J., Yagami M., Tseng W.J. and Lin A. Validation of a quantitative method for detection of adenovirus aggregation *Bioprocess. J.* **9**(2), 25–33 (2011).
269. Siedlecki C.A., Wen Wang I., Higashi J.M., Kottke-Marchant K. and Marchant R.E. Platelet-derived microparticles on synthetic surfaces observed by atomic force microscopy and fluorescence microscopy *Biomaterials* **20**(16), 1521–1529 (1999).
270. Simons M. and Raposo G. Exosomes - vesicular carriers for intercellular communication *Curr. Opin. Cell Biol.* **21**(4), 575–581 (2009).
271. Sims P.J., Faioni E.M., Wiedmer T. and Shattil S.J. Complement proteins C5b-9 cause release of membrane vesicles from the platelet surface that are enriched in the membrane receptor for coagulation factor Va and express prothrombinase activity. *J. Biol. Chem.* **263**(34), 18205–18212 (1988).
272. Sims P.J., Wiedmer T.H., Esmon C.H.T., Weiss H.J. and Shattil S.J. Assembly of the platelet prothrombinase complex is linked to vesiculation of the platelet plasma membrane. Studies in Scott syndrome: an isolated defect in platelet procoagulant activity. *J. Biol. Chem.* **264**(29), 17049–17057 (1989).
273. Snow C. Flow cytometer electronics *Cytom. Part A* **57**(2), 63–69 (2004).
274. Sokolova V., Ludwig A.K., Hornung S., Rotan O., Horn P.A., Epple M. and Giebel B. Characterisation of exosomes derived from human cells by nanoparticle tracking analysis and scanning electron microscopy *Colloid Surface B* **87**(1), 146–150 (2011).
275. Song Y., Hoang B.Q. and Chang D.D. ROCK-II-induced membrane blebbing and chromatin condensation require actin cytoskeleton *Exp. Cell Res.* **278**(1), 45–52 (2002).
276. Starchev K., Buffle J. and Perez E. Applications of fluorescence correlation spectroscopy: Polydispersity measurements *J. Colloid Interf. Sci.* **213**(2), 479–487 (1999).
277. Stavis S.M., Edel J.B., Samiee K.T. and Craighead H.G. Single molecule studies of quantum dot conjugates in a submicrometer fluidic channel *Lab Chip* **5**(3), 337–343 (2005).
278. Steen H.B. Flow cytometer for measurement of the light scattering of viral and other submicroscopic particles *Cytom. Part A* **57**(2), 94–99 (2004).
279. Stegmayr B. and Ronquist G. Promotive effect on human sperm progressive motility by prostasomes *Urol. Res.* **10**(5), 253–257 (1982).
280. Stenmark H. Rab GTPases as coordinators of vesicle traffic *Nat. Rev. Mol. Cell Biol.* **10**(8), 513–525 (2009).

281. Sterenborg H.J.C.M. *Investigations on the action spectrum of tumorigenesis by ultraviolet radiation* Ph.D. thesis University of Utrecht Utrecht, The Netherlands (1987).
282. Stramski D. Refractive index of planktonic cells as a measure of cellular carbon and chlorophylla content *Deep-Sea Res. Pt. I* **46**(2), 335–351 (1999).
283. Sugiuchi H., Uji Y., Okabe H., Irie T., Uekama K., Kayahara N. and Miyauchi K. Direct measurement of high-density lipoprotein cholesterol in serum with polyethylene glycol-modified enzymes and sulfated alpha-cyclodextrin. *Clin. Chem.* **41**(5), 717–723 (1995).
284. Sun D., Zhuang X., Xiang X., Liu Y., Zhang S., Liu C., Barnes S., Grizzle W., Miller D. and Zhang H.G. A novel nanoparticle drug delivery system: the anti-inflammatory activity of curcumin is enhanced when encapsulated in exosomes *Mol. Ther.* **18**(9), 1606–1614 (2010).
285. Tamai K., Tanaka N., Nakano T., Kakazu E., Kondo Y., Inoue J., Shiina M., Fukushima K., Hoshino T., Sano K., Uenob Y., Shimosegawab T. and Sugamuraa K. Exosome secretion of dendritic cells is regulated by Hrs, an ESCRT-0 protein *Biochem. Biophys. Res. Commun.* **399**(3), 384–390 (2010).
286. Tanimura A., McGregor D.H. and Anderson H.C. Matrix vesicles in atherosclerotic calcification *Proc. Soc. Exp. Biol. Med.* **172**(2), 173–177 (1983).
287. Tatischeff I., Larquet E., Falcón-Pérez J.M., Turpin P.Y. and Kruglik S.G. Fast characterisation of cell-derived extracellular vesicles by nanoparticles tracking analysis, cryo-electron microscopy, and Raman tweezers microspectroscopy *J. Extracell. Vesicles* **1**, 1–11 (2012).
288. Tavoosidana G., Ronquist G., Darmanis S., Yan J., Carlsson L., Wu D., Conze T., Ek P., Semjonow A., Eltze E. et al. Multiple recognition assay reveals prostasomes as promising plasma biomarkers for prostate cancer *Proc. Natl. Acad. Sci. USA* **108**(21), 8809–8814 (2011).
289. Taylor D.D., Chou I.N. and Black P.H. Isolation of plasma membrane fragments from cultured murine melanoma cells *Biochem. Biophys. Res. Commun.* **113**(2), 470–476 (1983).
290. Taylor D.D. and Gercel-Taylor C. Tumour-derived exosomes and their role in cancer-associated T-cell signalling defects *Br. J. Cancer* **92**(2), 305–311 (2005).
291. Taylor D.D., Zacharias W. and Gercel-Taylor C. Exosome isolation for proteomic analyses and RNA profiling in *Serum/plasma proteomics* vol. 728 of *Methods in Molecular Biology* 235–246 Springer (2011).
292. Tesselaar M.E.T., Romijn F.P.H.T., Van Der Linden I.K., Prins F.A., Bertina R.M. and Osanto S. Microparticle-associated tissue factor activity: a link between cancer and thrombosis? *J. Thromb. Haemost.* **5**(3), 520–527 (2007).
293. Theos A.C., Truschel S.T., Tenza D., Hurbain I., Harper D.C., Berson J.F., Thomas P.C., Raposo G. and Marks M.S. A lumenal domain-dependent pathway for sorting to intralumenal vesicles of multivesicular endosomes involved in organelle morphogenesis *Dev. Cell* **10**(3), 343–354 (2006).

294. Théry C., Amigorena S., Raposo G. and Clayton A. Isolation and characterization of exosomes from cell culture supernatants and biological fluids *Curr. Protoc. Cell Biol.* **Ch. 3**, Unit 3.22 (2006).

295. Théry C., Boussac M., Véron P., Ricciardi-Castagnoli P., Raposo G., Garin J. and Amigorena S. Proteomic analysis of dendritic cell-derived exosomes: a secreted subcellular compartment distinct from apoptotic vesicles *J. Immunol.* **166**(12), 7309–7318 (2001).

296. Théry C., Ostrowski M. and Segura E. Membrane vesicles as conveyors of immune responses *Nat. Rev. Immunol.* **9**(8), 581–593 (2009).

297. Théry C., Zitvogel L. and Amigorena S. Exosomes: composition, biogenesis and function *Nat. Rev. Immunol.* **2**(8), 569–579 (2002).

298. Tocchetti E.V., Flower R.L. and Lloyd J.V. Assessment of in vitro-generated platelet microparticles using a modified flow cytometric strategy *Thromb. Res.* **103**(1), 47–55 (2001).

299. Trajkovic K., Hsu C., Chiantia S., Rajendran L., Wenzel D., Wieland F., Schwille P., Brügger B. and Simons M. Ceramide triggers budding of exosome vesicles into multivesicular endosomes *Science* **319**(5867), 1244–1247 (2008).

300. Trams E.G., Lauter C.J., Norman Salem J. and Heine U. Exfoliation of membrane ecto-enzymes in the form of micro-vesicles *Biochim. Biophys. Acta* **645**(1), 63–70 (1981).

301. Tsutsui H. and Ho C.M. Cell separation by non-inertial force fields in microfluidic systems *Mech. Res. Commun.* **36**(1), 92–103 (2009).

302. Turiák L., Misják P., Szabó T.G., Aradi B., Pálóczi K., Ozohanics O., Drahos L., Kittel Á., Falus A., Buzás E.I. and Vékey K. Proteomic characterization of thymocyte-derived microvesicles and apoptotic bodies in BALB/c mice *J. Proteomics* **74**(10), 2025–2033 (2011).

303. Ulanowski Z., Greenaway R.S., Kaye P.H. and Ludlow I. Laser diffractometer for single-particle scattering measurements *Meas. Sci. Technol.* **13**(3), 292–296 (2002).

304. Ungureanu C., Rayavarapu R.G., Manohar S. and van Leeuwen T.G. Discrete dipole approximation simulations of gold nanorod optical properties: choice of input parameters and comparison with experiment *J. Appl. Phys.* **105**(10), 102032 (2009).

305. Uzunbajakava N., Lenferink A., Kraan Y., Volokhina E., Vrensen G., Greve J. and Otto C. Nonresonant confocal Raman imaging of DNA and protein distribution in apoptotic cells *Biophys. J.* **84**(6), 3968–3981 (2003).

306. Valadi H., Ekström K., Bossios A., Sjöstrand M., Lee J.J. and Lötvall J.O. Exosome-mediated transfer of mRNAs and microRNAs is a novel mechanism of genetic exchange between cells *Nature* **9**(6), 654–659 (2007).

307. Van Apeldoorn A.A., Aksenov Y., Stigter M., Hofland I., De Bruijn J.D., Koerten H.K., Otto C., Greve J. and Van Blitterswijk C.A. Parallel high-resolution confocal Raman SEM analysis of inorganic and organic bone matrix constituents *J. R. Soc. Interface* **2**(2), 39–45 (2005).

308. Van Doormaal F., Kleinjan A., Berckmans R.J., Mackman N., Manly D., Kamphuisen P.W., Richel D.J., Büller H.R., Sturk A. and Nieuwland R. Coagulation activation and microparticle-associated coagulant activity in cancer patients. An exploratory prospective study. *Thromb. Haemost.* **108**(1), 160–165 (2012).
309. Van Manen H.J., Verkuijlen P., Wittendorp P., Subramaniam V., Van den Berg T.K., Roos D. and Otto C. Refractive index sensing of green fluorescent proteins in living cells using fluorescence lifetime imaging microscopy *Biophys. J.* **94**(8), L67–L69 (2008).
310. Varga Z., Yuana Y., Grootemaat A.E., van der Pol E., Gollwitzer C., Krumrey M. and Nieuwland R. Towards traceable size determination of extracellular vesicles *J. Extracell. Vesicles* **3**, 1–10 (2014).
311. Vella L.J., Greenwood D.L.V., Cappai R., Scheerlinck J.P.Y. and Hill A.F. Enrichment of prion protein in exosomes derived from ovine cerebral spinal fluid *Vet. Immunol. Immunopathol.* **124**(3), 385–393 (2008).
312. Vickers K.C., Palmisano B.T., Shoucri B.M., Shamburek R.D. and Remaley A.T. MicroRNAs are transported in plasma and delivered to recipient cells by high-density lipoproteins *Nat. Cell Biol.* **13**(4), 423–433 (2011).
313. van der Vlist E.J., Aalberts M., Mertens H.C.H., Bosch B.J., Bartelink W., Mastrobattista E., van Gaal E.V.B., Stoorvogel W., Arkesteijn G.J.A. and Wauben M.H.M. Quantitative and qualitative flow cytometric analysis of nano-sized cell-derived membrane vesicles *Nanomed. Nanotechnol. Biol. Med.* **8**(5), 712–720 (2011).
314. Vogel R., Willmott G., Kozak D.M., Roberts G.S., Anderson W., Groenewegen L., Glossop B., Barnett A., Turner A. and Trau M. Quantitative sizing of nano/microparticles with a tunable elastomeric pore sensor *Anal. Chem.* **83**(9), 3499–3506 (2011).
315. Von Mollard G.F., Mignery G.A., Baumert M., Perin M.S., Hanson T.J., Burger P.M., Jahn R. and Südhof T. Rab3 is a small GTP-binding protein exclusively localized to synaptic vesicles *Proc. Natl. Acad. Sci. USA* **87**(5), 1988–1992 (1990).
316. de Vrij J., Maas S.L.N., van Nispen M., Sena-Esteves M., Limpens R.W.A., Koster A.J., Leenstra S., Lamfers M.L. and Broekman M.L.D. Quantification of nanosized extracellular membrane vesicles with scanning ion occlusion sensing *Nanomedicine* **8**(9), 1443–1458 (2013).
317. Wagner J., Riwanto M., Besler C., Knau A., Fichtlscherer S., Röxe T., Zeiher A.M., Landmesser U. and Dimmeler S. Characterization of levels and cellular transfer of circulating lipoprotein-bound microRNAs *Arterioscler. Thromb. Vasc. Biol.* **33**(6), 1392–1400 (2013).
318. Walker J.D., Maier C.L. and Pober J.S. Cytomegalovirus-infected human endothelial cells can stimulate allogeneic CD4+ memory T cells by releasing antigenic exosomes *J. Immunol.* **182**(3), 1548–1559 (2009).
319. Webb W.W. Applications of fluorescence correlation spectroscopy *Q. Rev. Biophys.* **9**(01), 49–68 (1976).

320. Welton J.L., Khanna S., Giles P.J., Brennan P., Brewis I.A., Staffurth J., Mason M.D. and Clayton A. Proteomics analysis of bladder cancer exosomes *Mol. Cell Proteomics* **9**(6), 1324–1338 (2010).
321. Wester J., Sixma J.J., Geuze J.J. and Heijnen H.F. Morphology of the hemostatic plug in human skin wounds: transformation of the plug *Lab. Invest.* **41**(2), 182–192 (1979).
322. Westphal V. and Hell S.W. Nanoscale resolution in the focal plane of an optical microscope *Phys. Rev. Lett.* **94**(14), 143903 (2005).
323. Westphal V., Rizzoli S.O., Lauterbach M.A., Kamin D., Jahn R. and Hell S.W. Video-rate far-field optical nanoscopy dissects synaptic vesicle movement *Science* **320**(5873), 246–249 (2008).
324. White I., Bailey L., Aghakhani M., Moss S. and Futter C. EGF stimulates annexin 1-dependent inward vesiculation in a multivesicular endosome subpopulation *EMBO J.* **25**(1), 1–12 (2006).
325. Willig K.I., Rizzoli S.O., Westphal V., Jahn R. and Hell S.W. STED microscopy reveals that synaptotagmin remains clustered after synaptic vesicle exocytosis *Nature* **440**(7086), 935–939 (2006).
326. Willmott G.R. and Bauerfeind L.H. Detection of polystyrene sphere translocations using resizable elastomeric nanopores *arXiv* (1002.0611), 1–30 (2010).
327. Winter G.D. Formation of the scab and the rate of epithelization of superficial wounds in the skin of the young domestic pig *Nature* **193**, 293–294 (1962).
328. Winter G.D. Some factors affecting skin and wound healing *J. Tissue Viabil.* **16**(2), 20–23 (2006).
329. Wolf P. The nature and significance of platelet products in human plasma *Br. J. Haematol.* **13**(3), 269–288 (1967).
330. Wu C. *Column handbook for size exclusion chromatography* Academic Press, Orlando. FL (1999).
331. Wubbolts R., Leckie R.S., Veenhuizen P.T.M., Schwarzmann G., Möbius W., Hoernschemeyer J., Slot J.W., Geuze H.J. and Stoorvogel W. Proteomic and biochemical analyses of human B cell-derived exosomes. Potential implications for their function and multivesicular body formation. *J. Biol. Chem.* **278**(13), 10963–10972 (2003).
332. Yamamoto Y. and Shinohara K. Application of X-ray microscopy in analysis of living hydrated cells *Anat. Rec.* **269**(5), 217–223 (2002).
333. Yuana Y., Bertina R.M. and Osanto S. Pre-analytical and analytical issues in the analysis of blood microparticles *Thromb. Haemost.* **105**(3), 396–408 (2011).
334. Yuana Y., Koning R.I., Kuil M.E., Rensen P.C.N., Koster A.J., Bertina R.M. and Osanto S. Cryo-electron microscopy of extracellular vesicles in fresh plasma *J. Extracell. Vesicles* **2**, 1–7 (2013).
335. Yuana Y., Oosterkamp T.H., Bahatyrova S., Ashcroft B., Garcia R.P., Bertina R.M. and Osanto S. Atomic force microscopy: a novel approach to the detection of nanosized blood microparticles *J. Thromb. Haemost.* **8**(2), 315–323 (2010).

336. van der Zee P.M., Biró É., Ko Y., de Winter R.J., Hack C.E., Sturk A. and Nieuwland R. P-selectin-and CD63-exposing platelet microparticles reflect platelet activation in peripheral arterial disease and myocardial infarction *Clin. Chem.* **52**(4), 657–664 (2006).
337. Zhang Q., Li Y. and Tsien R.W. The dynamic control of kiss-and-run and vesicular reuse probed with single nanoparticles *Science* **323**(5920), 1448–1453 (2009).
338. Zhang W., Saliba M., Stranks S.D., Sun Y., Shi X., Wiesner U. and Snaith H.J. Enhancement of perovskite-based solar cells employing core–shell metal nanoparticles *Nano Lett.* **13**(9), 4505–4510 (2013).
339. Zucker W.H., Shermer R.W. and Mason R.G. Ultrastructural comparison of human platelets separated from blood by various means *Am. J. Pathol.* **77**(2), 255–267 (1974).
340. Zwicker J.I., Liebman H.A., Neuberg D., Lacroix R., Bauer K.A., Furie B.C. and Furie B. Tumor-derived tissue factor–bearing microparticles are associated with venous thromboembolic events in malignancy *Clin. Cancer Res.* **15**(22), 6830–6840 (2009).

Summary

Extracellular vesicles

The human body is made up of cells. Cells release small sacks filled with fluid, which are called "extracellular vesicles". The diameter of extracellular vesicles (EV) typically ranges from 30 nm to 1 µm, the smallest being some 100-fold smaller than the smallest cells of the human body. Because cells release EV into their environment, our body fluids, such as blood, saliva, and urine, contain numerous EV.

Detection hampers clinical applications of EV

Cells release EV to remove waste, and to transport and deliver cargo, such as receptors and genetic information, to other cells. Since the size, concentration, cellular origin, and composition of EV in body fluids change during disease, EV have promising clinical applications, such as diagnosis of cancer and monitoring the efficacy of therapy. However, clinical applications of EV are not realized yet, because currently used detection techniques lack the sensitivity to detect the majority of EV.

Aim of this thesis

The aim of this thesis is to improve the detection of EV by (1) obtaining insights into physical properties of EV, and (2) gaining a profound understanding of techniques to detect EV.

Physical properties of EV

Detection is the act of perceiving "something". To specify "something", physically detectable properties of EV are defined in *Chapter 2*. Examples of these properties are size, concentration, density, morphology, biochemical composition, refractive index, zeta potential and deformability. This thesis focuses on the properties size, concentration and refractive index of EV, since these three properties play a key role in the optical detection of EV.

Gaining understanding of detection techniques

In *Chapter 3*, an overview of currently available and potentially applicable techniques to detect the size and concentration of EV is provided. The working principle of all techniques is briefly discussed, as well as their capabilities and limitations based on the underlying physical parameters of the technique. To compare the precision in determining the size of EV between the discussed techniques, a mathematical model is developed to calculate the expected size distribution for a reference EV population. In *Chapter 4*, the most applicable techniques of Chapter 3 are selected for an experimental evaluation. For these techniques, the accuracy and precision in measuring the EV size and concentration are determined. Although each technique gives a different size distribution and concentration for the reference EV population, all techniques indicate that the concentration of EV decreases with increasing diameter. Consequently, the minimum detectable EV size of a technique affects the measured concentration. Differences between the minimum detectable EV size of techniques explain the 100,000,000-fold difference in the reported concentrations of EV in human blood plasma. The relationship between the concentration of EV and their diameter can be described by the power-law function.

EV detection by flow cytometry

Chapter 5 addresses EV detection by flow cytometry, which is the most widely used technique to study single EV. Due to their small size and high concentration, however, multiple EV are simultaneously illuminated by the laser beam of the flow cytometer, and therefore are counted as a single event signal. This phenomenon is christened "swarm detection". In addition, the relationship between light scattering and the diameter of EV is modeled using Mie theory. This relationship is used to demonstrate that a currently widely applied standardization procedure for EV detection selects EV and cells with a diameter of 800−2,400 nm instead of the envisioned 500−900 nm. Consequently, in many studies other particles than the envisioned EV were studied.

Refractive index of EV

A variable of Mie theory is the refractive index of EV, which determines how efficiently a EV scatters light. In *Chapter 6*, a method based on nanoparticle tracking analysis is developed to determine the size and refractive index of single EV and other nanoparticles. For urinary EV a mean refractive index of 1.37 at 405 nm was obtained, which is much lower than the frequently and often unintentionally assumed values between 1.45 and 1.63. The low refractive index of EV implies that EV scatter light less efficiently than calibration beads. Consequently, detecting scattering from EV demands a sensitive detector. The determined refractive

index of EV can be used to relate scattering to diameter, which is useful for data interpretation and calibration.

EV detection by tunable resistive pulse sensing

Tubable resistive pulse sensing is a technique to measure the size and concentration of EV in suspension. In *Chapter 7*, a protocol is developed to determine and improve the reproducibility of tunable resistive pulse sensing.

Single-step isolation of EV

Because body fluids contain many particles other than EV, EV require isolation prior to detection. Isolation of EV particularly from plasma is challenging due to the presence of proteins and lipoproteins. In *Chapter 8*, a single-step protocol to isolate EV from human body fluids is developed. The protocol is based on size-exclusion chromatography and has excellent recovery and enrichment.

The future of EV-based diagnostics

In the future, EV will be included in reference tables, such as hematology reference tables, as their physical properties are expected to correlate with disease. Prerequisites to establish EV as clinical biomarkers are: (1) knowledge of physical properties of EV, (2) insight into capabilities and limitations of detection techniques, (3) availability of techniques with the capability of deriving the cellular origin and function of EV and with improved sensitivity compared to current state-of-art technology, and (4) standardization of measurements. Standardization is important for data comparison between laboratories. In *Chapter 9*, the applicability of EV detection by techniques that are beyond the current state-of-art is discussed. *Chapter 10* enlightens the future of EV-based diagnostics.

This thesis provides solid insight into (1) the physical properties of EV and (2) the capabilities and limitations of current detection techniques. This knowledge is the onset to (3) the development of novel detection techniques and (4) improved standardization procedures, which are important steps towards EV-based diagnostics.

Samenvatting

Celblaasjes

Het menselijk lichaam is opgebouwd uit cellen. Cellen snoeren ronde blaasjes af, die "celblaasjes" worden genoemd. Deze celblaasjes zijn kleiner dan een duizendste millimeter. De kleinste celblaasjes zijn maar liefst duizend keer kleiner dan de dikte van een mensenhaar. Omdat cellen blaasjes afsnoeren, bevatten onze lichaamsvloeistoffen, zoals bloed, speeksel en urine, talrijke celblaasjes.

Klinische toepassingen van celblaasjes

Cellen snoeren blaasjes af om afval te verwijderen en om te communiceren met andere cellen. Omdat de grootte, concentratie, herkomst en samenstelling van celblaasjes in lichaamsvloeistoffen verandert tijdens ziekte, heeft het meten van celblaasjes veelbelovende klinische toepassingen, zoals kanker diagnostiek en het monitoren van de effectiviteit van therapie. Klinische toepassingen van celblaasjes zijn er echter nog niet, met name omdat de meeste celblaasjes te klein zijn voor de huidige meettechnieken.

Doel van dit proefschrift

Het doel van dit proefschrift is om het meten van celblaasjes te verbeteren. Dit doel wordt bereikt door (1) het verkrijgen van inzicht in de natuurkundige eigenschappen van celblaasjes, en (2) het verkrijgen van inzicht in technieken die gebruikt worden om celblaasjes te meten.

Natuurkundige eigenschappen van celblaasjes

Meten is de waarde van een natuurkundige eigenschap bepalen. In *Hoofdstuk 2* worden de natuurkundige eigenschappen van celblaasjes gedefinieerd. Voorbeelden van deze eigenschappen zijn de de diameter, concentratie, dichtheid, vorm, biochemische samenstelling, brekingsindex, oppervlaktelading en vervormbaarheid. In dit proefschrift ligt de nadruk op de eigenschappen diameter, concentratie en brekingsindex van celblaasjes, omdat deze drie eigenschappen een belangrijke rol spelen bij het meten van celblaasjes met behulp van optische technieken.

Het verkrijgen van inzicht in de meettechnieken

Hoofdstuk 3 geeft een overzicht van momenteel gebruikte en mogelijk toepasbare technieken voor het meten van de diameter en concentratie van celblaasjes. Het werkingsprincipe, de mogelijkheden en de beperkingen van de technieken worden besproken op basis van de onderliggende natuurkundige eigenschappen van deze technieken. Om de kwaliteit van de technieken te kunnen vergelijken, is een wiskundig model ontwikkeld om per techniek de verwachte grootteverdeling van een referentie populatie van celblaasjes te berekenen. Het wiskundig model geeft inzicht in de nauwkeurigheid waarmee de technieken de diameter van celblaasjes kunnen meten.

In *Hoofdstuk 4* worden de meest geschikte technieken uit Hoofdstuk 3 geselecteerd en gebruikt om de diameter en concentratie van een referentiepopulatie van celblaasjes te meten. Hoewel elke techniek een andere grootteverdeling en concentratie meet voor dezelfde populatie celblaasjes, meet elke techniek een afname van de concentratie celblaasjes bij toenemende diameter. Door deze relatie tussen de concentratie en diameter van celblaasjes, hangt de gemeten concentratie celblaasjes af van de kleinste celblaasjes die een techniek kan gemeten. De verschillen tussen de kleinst meetbare celblaasjes van technieken verklaren waarom de gemeten concentraties van celblaasjes in menselijk bloedplasma onderling een factor 100.000.000 kunnen verschillen.

Celblaasjes meten met flowcytometrie

Hoofdstuk 5 gaat over het meten van celblaasjes met flowcytometrie. Flowcytometrie is de meest toegepaste techniek om celblaasjes *één voor één* te meten. Door de geringe diameter en de hoge concentratie van celblaasjes worden echter *meerdere* celblaasjes tegelijkertijd belicht door de laserstraal van de flowcytometer, met als gevolg dat deze celblaasjes samen worden geteld als één groter deeltje. Dit fenomeen wordt "zwerm detectie" genoemd. Verder is de relatie tussen lichtverstrooiing en de diameter van celblaasjes beschreven met Mie-theorie. Uit deze relatie blijkt dat een wereldwijd gebruikte standaardisatieprocedure om celblaasjes te meten geen celblaasjes selecteert van 500−900 nm, maar celblaasjes en zelfs cellen met een diameter van 800−2.400 nm. Dat betekent dat in vele studies andere deeltjes zijn bestudeerd dan de veronderstelde celblaasjes.

Brekingsindex van celblaasjes

Een variabele van de Mie-theorie is de brekingsindex van celblaasjes. De brekingsindex bepaalt hoe efficiënt een celblaasje licht verstrooit. Kennis van de brekingsindex van celblaasjes is een voorwaarde voor het afleiden van de diameter van celblaasjes uit het lichtverstrooiingssignaal van bijvoorbeeld een flowcytometer. In *Hoofdstuk 6* is een methode ontwikkeld om de diameter en brekingsindex

van afzonderlijke celblaasjes en andere nanodeeltjes te bepalen. Voor celblaasjes uit menselijk urine is een gemiddelde brekingsindex van 1,37 bij een golflengte van 405 nm gevonden. Deze waarde ligt veel lager dan de tot nu toe veronderstelde waarde tussen de 1,45 en 1,63. Door hun lage brekingsindex verstrooien celblaasjes licht veel minder efficiënt dan synthetische kalibratie bolletjes van dezelfde diameter. Het spreekt dan ook voor zich dat het meten van celblaasjes zeer gevoelige technieken vereist.

Celblaasjes meten met een klein gaatje

Met de techniek "Tunable resistive pulse sensing" worden celblaasjes één voor één door een klein gaatje geleid om de diameter en concentratie van celblaasjes te meten. *Hoofdstuk 7* beschrijft een protocol voor het bepalen en verbeteren van de reproduceerbaarheid van deze techniek.

Zuiveren van celblaasjes

Lichaamsvloeistoffen bevatten naast celblaasjes ook andere deeltjes met een vergelijkbare diameter, zoals eiwitten en lipoproteïnen. Daarom moeten celblaasjes worden gescheiden van deze andere deeltjes voordat ze kunnen worden gemeten. In *Hoofdstuk 8* is een protocol geschreven om celblaasjes uit menselijke lichaamsvloeistoffen te zuiveren. Het protocol is makkelijker te gebruiken dan huidige protocollen om celblaasjes te zuiveren.

De toekomst van diagnostiek op basis van celblaasjes

Als een patiënt het ziekenhuis bezoekt, wordt vaak bloed afgenomen. In dit bloed monster wordt het aantal cellen geteld en het resultaat van deze celtelling wordt vergeleken met referentietabellen van gezonde proefpersonen. Deze informatie helpt een arts om een diagnose te stellen. Omdat de natuurkundige eigenschappen van celblaasjes in lichaamsvloeistoffen verandert tijdens ziekte, zullen celblaasjes in de toekomst deel uit maken van dergelijke referentietabellen. Vereisten voor het gebruik van celblaasjes in de kliniek zijn: (1) kennis van de natuurkundige eigenschappen van celblaasjes, (2) inzicht in de mogelijkheden en beperkingen van technieken voor het meten van celblaasjes, (3) de beschikbaarheid van technieken die de functie en cellulaire herkomst van celblaasjes kunnen meten en die kleinere celblaasjes kunnen meten dan de huidige technieken, en (4) standaardisatie van metingen. Standaardisatie van metingen is van belang om klinische resultaten van verschillende ziekenhuizen onderling te kunnen vergelijken. In *Hoofdstuk 9* wordt de toepasbaarheid van nieuwe technieken voor het meten van celblaasjes besproken.

Hoofdstuk 10 bevat een uiteenzetting over de toekomst van diagnostiek op basis van celblaasjes.

Dit proefschrift biedt diepgaand inzicht in (1) de natuurkundige eigenschappen van celblaasjes, en (2) de mogelijkheden en beperkingen van de huidige technieken voor het meten van celblaasjes. De verworven kennis geeft aanzet tot (3) de ontwikkeling van nieuwe meettechnieken, en (4) standaardisatie van metingen, wat essentiële stappen zijn om diagnostiek op basis van celblaasjes mogelijk te maken.

Gearfetting
Bûtensellige pûdsjes ûnder it fergrutglês

Durk H. Veenstra, Maaike W. Andela, Jantsje Y. Veenstra-Tjalma,
Anne R. Glazema en Edwin van der Pol

Bûtensellige pûdsjes

It minsklik lichem bestiet út sellen. De sellen fan it minsklik lichem skiede withoe folle lytse pûdsjes ôf, dy't yn it Ingelsk "extracellulaire vesicles" hjitte - bûtensellige pûdsjes of selpûdsjes yn it Frysk. Dizze selpûdsjes binne lytser as in tûzenste milimeter. De lytste selpûdsjes binne sels tûzen kear lytser as de dikte fan in minskehier. Om't al ús sellen pûdsjes yn harren omjouwing loslitte, kinne jo harren yn ús bloed, flibe, urine en oare lichemsfloeistoffen fine.

Nei alle gedachten hawwe selpûdsjes klinyske tapassings

Sellen litte pûdsjes los om ôffal fuort te smiten en om fracht te ferfieren nei oare sellen. Om't de grutte, konsintraasje, oarsprong en gearstalling fan de selpûdsjes by sike minsken oars is as by sûne minsken, soenen selpûdsjes klinyske tapassings hawwe kinne. Sa'n tapassing is bygelyks it fêststellen fan sikens en it byhâlden fan it ferrin fan terapy. Klinyske tapassings foar selpûdsjes besteane lykwols noch net, om't de selpûdsjes sa lyts binne dat se net sa bêst te mjitten binne mei de hjoeddeiske techniken.

Doelstelling fan dit proefskrift

It doel fan dit proefskrift is om it mjitten fan selpûdsjes te ferbetterjen. Dit sil barre troch (1) it opdwaan fan nije ynsichten yn de natuerkundige eigenskippen fan selpûdsjes en (2) it krijen fan djiprikkende kunde fan hjoeddeiske en nije techniken foar it mjitten fan selpûdsjes.

Natuerkundige eigenskippen fan selpûdsjes

As jo wat mjitte wolle, dan moatte jo earst witte hokker eigenskippen jo mjitte wolle. De natuerkundige eigenskippen fan selpûdsjes dy't wy mjitte kinne, binne ûnder oare de grutte, konsintraasje, brekkingsyndeks, gearstalling, foarm, tichtens, oerflaktespanning en ferfoarmberhyd (*Haadstik 2*). Yn dit proefskrift rjochtsje we ús foaral op de grutte, konsintraasje en brekkingsyndeks fan selpûdsjes, om't dizze trije eigenskippen it meast wichtich binne foar it mjitten fan selpûdsjes mei optyske techniken.

Begrip krije fan mjittechniken

Yn *Haadstik 3* wurdt in oersicht jaan fan beskikbere en potinsjeel tapasbere metoaden om de grutte en konsintraasje fan selpûdsjes te mjitten. Der wurdt sprutsen oer de wurking, mooglikheden en beheinings fan ferskate metoaden op grûnslach fan de ûnderlizzende natuerkundige eigenskippen fan dy techniken. Om de brûkberens fan de ferskate metoaden te fergelykjen, waard der in rekkenmodel ûntwikkele om per metoade de grutte-ferdieling fan deselde populaasje selpûdsjes te foarspellen. It rekkenmodel jouwt ynsicht yn de sekuerens fan de ferskate metoaden wermei de grutte fan selpûdsjes teoretysk mjitten wurde kin.

De meast geskikte metoaden út Haadstik 3 wurde yn *Haadstik 4* brûkt om de grutte-ferdieling en konsintraasje fan deselde populaasje selpûdsjes te mjitten. Nijsgjirrich genôch mjit eltse technyk in oare grutte-ferdieling en konsintraasje foar deselde populaasje selpûdsjes. Derneist is der ek in oerienkomst: alle techniken litte folle mear lytse as grutte selpûdsjes sjen. As jo selpûdsjes telle wolle, dan moatte jo sadwaande goed yn'e gaten hawwe wat de lytst mjitbere selpûdsjes binne. Yn oare wurden, de gefoeligheid fan in technyk is fan grutte ynfloed op de metten konsintraasje. Dit ynsicht ferklearret it ferskaat yn de konsintraasjes selpûdsjes yn minskebloed, dy't oprinne kin oant ferskillen fan wol 100.000.000 kear!

Selpûdsjes mjitte mei in selteller

Haadstik 5 besjocht it mjitten fan selpûdsjes mei in selteller. Dit is de meast brûkte technyk om selpûdsjes *ien foar ien* te mjitten. Troch harren lytse trochsnee en hege konsintraasje wurde dochs faak *meardere* selpûdsjes op it selde stuit opljochte troch de laserstriel fan de selteller. Al dizze selpûdsjes wurde dan lykwols telt as ien grut selpûdsje. Wy hawwe dit ferskynsel "swaarm deteksje" doopt. Dêrneist is de relaasje tusken ljochtwjerkeatsing en de trochsnee fan selpûdsjes modellearre mei de saneamde Mie-teory. Dêrmei wurdt sjen litten dat de op it stuit breed tapaste standerdisaasjeproseduere selpûdsjes en sellen útsiket mei in trochsnee fan 800 oant 2.400 nm, ynstee fan de trochsnee fan 500 oant 900 nm, dy't hja earst op it each hienen.

Brekkingsyndeks fan selpûdsjes

In fariabele fan de Mie-teory is de brekkingsyndeks fan selpûdsjes, dy bepaalt hoe goed in selpûdsje ljocht ferstruit. Yn *Haadstik 6* is in metoade ûntwikkele om de grutte en de brekkingsyndeks fan nanopartsjes, sa as selpûdsjes, te mjitten. Foar urine-pûdsjes fûnen wy in gemiddelde brekkingsyndeks fan 1,37 by in golflingte fan 405 nm, wat in stik leger is as de faak ûnbedoeld oannaam wearden tusken 1,45 en 1,63. De lege brekkingsyndeks betsjut dat selpûdsjes minder goed ljocht ferstruie as de faak brûkte kalibraasjebaltsjes. Dêrom hat it mjitten fan pûdsjes in gefoelige detektor nedich. De berekkene brekkingsyndeks fan selpûdsjes kin brûkt wurde foar de ferhâlding tusken de ljochtwjerkeatsing en de trochsnee. En dat is dan wer brûkber foar ynterpretaasje fan mjittingen mei de selteller.

Selpûdsjes mjitte mei in lyts gatsje

Mei de metoade "resistive pulse sensing" wurde de selpûdsjes troch in lyts gatsje lutsen om sa de elektryske wjerstân te mjitten. Dizze wjerstân is in maat foar de grutte fan selpûdsjes. Yn *Haadstik 7* is in rjochtline ûntwikkele om de betrouberens en gefoeligens fan dizze metoade te besjen en te ferbetterjen.

Ienfâldige skieding fan selpûdsjes

Om't lichemsfloeistoffen ek in protte oare dieltsjes as selpûdsjes hawwe, moatte selpûdsjes skieden wurde foardat hja metten wurde kinne. It skieden fan selpûdsjes, yn it bysûnder selpûdsjes fan bloedplasma, is tige dreech troch de oanwêzigens fan aaiwiten en fetaaiwiten. Yn *Haadstik 8* is in ienfâldige rjochtline ûntwikkele foar it skieden fan selpûdsjes fan lichemsfloeistoffen, sûnder dat we derby in protte selpûdsjes kwytreitsje.

It paad nei selpûdsje-diagnostyk

As in siik persoan yn it sikehûs bedarret, wurde der faak buiskes mei bloed ôfnommen. Fan dit bloedmûnster wurde de sellen teld en fergelike mei de oantallen fan sûne persoanen. Dit wurdt dien mei saneamde referinsjetabellen. Mei de ôfwikings fan de referinsjetabellen kin de dokter in diagnoase stelle. Yn de takomst sille selpûdsjes ûnderdiel wurde fan sokke referinsjetabellen, om't der sterke oanwizings binne dat harren eigenskippen by sike minsken oars binne as by sûne minsken. Foardat selpûdsjes klinysk brûkt wurde kinne, sille der earst op fjouwer gebieden fjidere stappen setten moatte wurde. (1) Der moat genôch kunde wêze fan de natuerkundige eigenskippen fan selpûdsjes. (2) Wy moatte ynsicht hawwe yn de mooglikheden en de beheinings fan de mjittechniken dy't wy brûke wolle. (3) Der moatte techniken ûntwikkele wurde wermei't it mooglik is om de sellulêre oarsprong en funksje fan de lytste selpûdsjes te mjitten. (4) As lêste sil der in

standaardisaasje fan mjittingen komme moatte. Yn *Haadstik 9* wurde metoaden besjoen foar it mjitten fan selpûdsjes dy't bûten de hjoeddeiske mooglikheden lizze. *Haadstik 10* beljochtet it paad nei selpûdsje-diagnostyk.

Dit proefskrift jout in deeglik ynsicht yn de natuerkundige eigenskippen fan selpûdsjes en de mooglikheden en beheiningen fan de besteande mjittechnyken. Dizze kunde is it begjin fan it ûntwikkeljen fan nije mjitmetoaden en ferbettere standerdisaasjerjochtlinen. En dat is wer in wichtige stap yn de rjochting fan selpûdsje-diagnostyk.

Portfolio

Name:	Edwin van der Pol
PhD period:	July 2009 - January 2015
Supervisors:	Prof. dr. A.G.J.M. van Leeuwen
	Prof. dr. A. Sturk
	Dr. R. Nieuwland

Training

Activity	Year	Workload (ECTS)
Courses		
World of science - Academic Medical Center	2009	0.7
Biophotonics and imaging graduate summer school - National Biophotonics and Imaging Platform Ireland	2009	1.2
Laboratory safety course - Academic Medical Center	2010	0.5
Boot camp - Amsterdam Center for Entrepreneurship	2013	1.2
Oral presentations		
Micro and Nanovesicles in Health and Disease Oxford, United Kingdom (invited)	2010	0.5
International Society on Thrombosis and Haemostasis		
Kyoto, Japan (invited)	2011	1.0
Liverpool, United Kingdom	2012	0.5
Amsterdam, The Netherlands (invited)	2013	1.0
Milwaukee, United States (invited)	2014	0.5
International Society for Extracellular Vesicles		
Gothenburg, Sweden	2012	0.5
Rotterdam, The Netherlands	2014	1.0
Izon Science Nano- and Micro-particle Research Symposium. Oxford, United Kingdom (invited)	2012	0.5
LaserLaB symposium. Amsterdam, The Netherlands (invited)	2012	0.5
"Microparticles: Biomarkers of Disease?" scientific meeting. Leicester, United Kingdom (invited)	2013	0.5
SPIE Photonics West, San Francisco, CA, United States	2013-2014	2.0

Activity	Year	Workload (ECTS)
Conferences and symposia		
APROVE symposia - Academic Medical Center	2010-2014	0.5
Gordon Research Conference - Lasers in medicine and biology. Holderness, NH, United States	2014	1.2
Reviewing		
Journal of Thrombosis and Haemostasis	2010-2014	4.0
Journal of Biomedical Optics	2012	0.5
Journal of Extracellular Vesicles	2012	1.0
Scandinavian Journal of Clinical Laboratory Investigation	2012	0.5
Hearth Research United Kingdom	2012-2013	1.0
Journal of Visualized Experiments	2014	0.5
Cytometry Part A	2014	0.5
Other		
Literature discussion meetings	2012	0.5
Web-master Biomedical Engineering and Physics - Academic Medical Center (amc.nl/bmep)	2012-2015	1.0
Web-master European Metrology Research Programme METVES (`www.metves.eu`)	2013-2015	1.0
Co-founder Exometry B.V. (`www.exometry.com`)	2014-2015	5.0
Open door day Fontys hogeschool Eindhoven	2014	0.3

Teaching

Activity	Year	Workload (ECTS)
Lecturing		
Single elastic scattering of particles equal to or smaller than the wavelength of light. Physics, 3rd year	2011-2015	5.0
Laser safety, journalizing and reporting. Physics, 3rd year	2011	0.4
Scientific writing. Medical informatics, 1st year	2013-2014	1.0
Tutoring		
Computer practicum on coronary circulation. Medicine, 2nd year	2010	0.5
Research practicum. Physics, 2nd year	2010-2015	3.0
Practicum on laser speckle fluctuations. Physics, 2nd year	2010-2014	2.0
Survival guide of scientists. Physics, 4th year	2014	1.0

Activity	Year	Workload (ECTS)
Supervising		
B.Sc. project of Dorus Dekker on "Determination of the size distribution and concentration of microvesicles using dark field microscopy"	2010	1.0
B.Sc. project of Quido Kuiper on "Automated detection of vesicles in transmission electron microscopy images"	2011	1.2
Undergraduate report (profielwerkstuk) of Imie Nieuwland and Sandra Rozeboom on "Woundscabs versus sunscreen"	2012	0.4
B.Sc. project of Randy Meijer on "Refractive index determination of extracellular vesicles using nanoparticle tracking analysis"	2013	1.5
M.Sc. project of Aude Vernet on "Development of a Raman microspectroscopy setup to characterize platelets and extracellular vesicles"	2013	2.0
B.Sc. project of Dayna Every on "Hybrid resistive pulse sensing and Raman spectroscopy setup to determine the size, refractive index and chemical composition of extracellular vesicles"	2014	1.0

Awards and grants

Awards

- Poster prize. Gordon research conference on Lasers in Medicine & Biology. 2014, Holderness, NH, United States.
- Young Investigator Award. International Society on Thrombosis and Haemostasis. 2011, Kyoto, Japan.

Personal grant

- Research Excellence Grant on *Refractive index determination of extracellular vesicles*. European Metrology Research Programme, United Kingdom, 2013

Contributions to collaborative grants

- Joint Research Project on *Metrological characterization of micro-vesicles from body fluids as non-invasive diagnostic biomarkers*. European Metrology Research Programme, United Kingdom, 2011
- Programme on *New technology for monitoring CANCER therapy through extracellular vesicle IDentity (CANCER-ID)*. Technology foundation STW, Utrecht, The Netherlands, 2014

Publications

Publications in this thesis

- E. van der Pol, A.G. Hoekstra, A. Sturk, C. Otto, T.G. van Leeuwen and R. Nieuwland. Optical and non-optical methods for detection and characterization of microparticles and exosomes. *J. Thromb. Haemost.* **8** (12), 2596-607 (2010)
- E. van der Pol, M.J.C. van Gemert, A. Sturk, R. Nieuwland and T.G. van Leeuwen. Single versus swarm detection of microparticles and exosomes by flow cytometry. *J. Thromb. Haemost.* **10** (5), 919-30 (2012)
- E. van der Pol, A.N. Böing, P. Harrison, A. Sturk and R. Nieuwland. Classification, functions, and clinical applications of extracellular vesicles. *Pharmacol. Rev.* **64** (3), 1-33 (2012)
- E. van der Pol*, F.A.W. Coumans*, Z. Varga, M. Krumrey and R. Nieuwland. Innovation in detection of microparticles and exosomes. *J. Thromb. Haemost.* **11** (Suppl. 1), 36-45 (2013)
- E. van der Pol, F.A.W. Coumans, A.E. Grootemaat, C. Gardiner, I.L. Sargent, P. Harrison, A. Sturk, T.G. van Leeuwen and R. Nieuwland. Particle size distribution of exosomes and microvesicles by transmission electron microscopy, flow cytometry, nanoparticle tracking analysis, and resistive pulse sensing. *J. Thromb. Haemost.* **12** 1-11 (2014)
- A.N. Böing, E. van der Pol, A.E. Grootemaat, F.A.W. Coumans, A. Sturk and R. Nieuwland. Single-step isolation of extracellular vesicles from plasma by size-exclusion chromatography. *J. Extracell. Vesicles* **3**: 23430 (2014)
- E. van der Pol, F.A.W. Coumans, A. Sturk, R. Nieuwland and T.G. van Leeuwen. Refractive index determination of nanoparticles in suspension using nanoparticle tracking analysis. *Nano Lett.* **14** (11), 6195-6201 (2014)
- F.A.W. Coumans, E. van der Pol, A.N. Böing, N. Hajji, A. Sturk, T.G. van Leeuwen and R. Nieuwland. Reproducible extracellular vesicle size and concentration determination with resistive pulse sensing. Accepted by *J. Extracell. Vesicles* (2014)

* authors contributed equally

Other publications

- G. Ctistis, A. Hartsuiker, E. van der Pol, J. Claudon, W. L. Vos and J.M. Gérard. Optical characterization and selective addressing of the resonant modes of a micropillar cavity with a white light beam. *Phys. Rev. B* **82**, 195330:1-7 (2010)
- J. van den Akker, A. van Weert, G. Afink, E.N.T.P. Bakker, E. van der Pol, A.N. Böing, R. Nieuwland and E. van Bavel. Transglutaminase 2 is secreted from smooth muscle cells by transamidation-dependent microparticle formation. *Amino Acids* **42** (2-3), 961-73 (2011)
- F.A.W. Coumans, E. van der Pol and L.W.M.M. Terstappen. Flat-top illumination profile in an epi-fluorescence microscope by dual micro lens arrays. *Cytometry Part A* **81** (4), 324-31 (2012)

- D. Nguyen, D.J. Faber, E. van der Pol, T.G. van Leeuwen and J. Kalkman. Dependent and multiple scattering in transmission and backscattering optical coherence tomography. *Opt. Expr.* **21** (24), 29145-56 (2013)
- Z. Varga, Y. Yuana, A.E. Grootemaat, E. van der Pol, C. Gollwitzer, M. Krumrey and R. Nieuwland. Towards traceable size determination of extracellular vesicles. *J. Extracell. Vesicles* **3**, 23298:1-10 (2014)

Book chapters

- E. van der Pol, T.G. van Leeuwen and R. Nieuwland. *An overview of novel and conventional methods to detect extracellular vesicles* In: P. Harrison, C. Gardiner, and I.L. Sargent, ed. Extracellular Vesicles in Health and Disease, 1st edn., Singapore: Pan Stanford Publishing, 2014. ISBN: 978-9814411981
- R. Nieuwland, E. van der Pol and A. Sturk. *Overview of microvesicles and exosomes in health and disease* In: P. Harrison, C. Gardiner, and I.L. Sargent, ed. Extracellular Vesicles in Health and Disease, 1st edn., Singapore: Pan Stanford Publishing, 2014. ISBN: 978-9814411981
- R. Nieuwland, E. van der Pol, C. Gardiner and A. Sturk. *Platelet-derived microparticles* In: A.D. Michelson, ed. Platelets, 3rd edn., San Diego, CA: Academic Press, 2012: 453-67. ISBN: 978-0123878373

Curriculum vitae

Edwin van der Pol was born on February 27th 1984 in Sneek, The Netherlands. After finishing the Athenaeum at the Rijksscholengemeenschap Magister Alvinus in 2002, he attended Twente University to study Applied Physics. In 2006, he graduated for his Bachelor of Science degree in the Optical Techniques group on *Sub picosecond synchronization of two ultrafast lasers*. He continued to study Applied Physics at Twente University and specialized in Optics and Biophysics. He did an internship at Immunicon corporation in Philadelphia, United States, where he improved a fluorescence microscope for detection of circulating tumor cells. In 2009, he graduated for his Master of Science degree in the Complex Photonic Systems group and at the institute for Atomic and Molecular Physics in Amsterdam on *Addressing single optical resonances in micropillar cavities*. In July 2009, he started his PhD research in the department of Biomedical Engineering and Physics and the Laboratory of Experimental Clinical Chemistry at the Academic Medical Center of the University of Amsterdam. His research focuses on the detection of extracellular vesicles and resulted in this thesis. He contributed to research proposals on *Metrological characterization of micro-vesicles from body fluids as non-invasive diagnostic biomarkers (METVES)* and *New technology for monitoring CANCER therapy through extracellular vesicle IDentity (CANCER-ID)*, which were granted

in 2011 and 2014, respectively. For his PhD work, he received the Young Investigator Award from the International Society on Thrombosis and Haemostasis in 2011, a Research Excellence Grant from the European Metrology Research Programme in 2013, and the poster prize of the Gordon research conference on Lasers in Medicine & Biology in 2014.

Stellingen

1. Detectie van extracellulaire vesicles wordt belemmerd door hun kleine grootte.

2. In humane lichaamsvloeistoffen neemt de concentratie van extracellulaire vesicles af bij toename van hun diameter.

3. Een flowcytometer detecteert zowel grote vesicles als zwermen van kleine vesicles, die beide eenzelfde signaal genereren.

4. De gemeten concentraties van extracellulaire vesicles in humaan plasma kunnen onderling tot een factor 10^8 verschillen. Deze verschillen worden veroorzaakt door stellingen $1-3$ en de verschillende detectiegrenzen van de gebruikte meettechnieken.

5. Het rapporteren van een gemeten concentratie van extracellulaire vesicles is alleen zinvol als ook het grootterbereik wordt vermeld.

6. Gegeven het totale membraanoppervlak van extracellulaire vesicles in bloed is het waarschijnlijker dat vesicles een rol spelen bij de bloedstolling dan bij transport van afval.

7. Een voorwaarde om inzicht te verwerven in de functies van extracellulaire vesicles is het bestuderen van modelorganismen, zoals bacteriën [287] en borstelwormen [183].

8. Wondkorsten beschermen de herstellende huid tegen ultraviolette straling.

9. Fouten publiceren is minder fout dan gepubliceerde fouten verzwijgen (bijvoorbeeld E. Boilard et al., *Science* 2010 [41]).

10. De voorspelde zeespiegelstijging in het jaar 2100 door opwarming van de aarde is verwaarloosbaar ten opzichte van de zeespiegeldaling tijdens de volgende ijstijd (op basis van *De menselijke maat* door S. Kroonenberg [173]).

11. Ter behoud van het legendarische karakter van de Elfstedentocht zou het beleid van de *Koninklijke Vereniging De Friesche Elf Steden* zich moeten richten op het maximaliseren van het aantal deelnemers dat de tocht volbrengt.

12. Het feit dat Diederik Stapel een hogere h-index heeft dan Peter Higgs, toont aan dat wetenschappelijke kwaliteit niet kan worden gekwantificeerd.

Dankwoord

Dit avontuur begon in de intercity tussen Amersfoort en Amsterdam. Na een sollicitatiegesprek nam ik toevallig plaats naast Leon Terstappen, die mij adviseerde om een kijkje te nemen bij Ton van Leeuwen in het Academisch Medisch Centrum (AMC).

Op Bevrijdingsdag 2009 fietste ik daarom van de Middenweg naar de Meibergdreef voor een sollicitatiegesprek met Ton. Uit de opmerking "kijk, een 7, dat is niet zo best" bleek al snel dat bij Ton de lat hoog ligt en dat er enige twijfels waren over mijn cijferlijst. Van mijn kant waren er echter ook twijfels over de geheimhouding van de projectomschrijving: "Het projectvoorstel is vertrouwelijk, dus dat kan ik je niet geven. Maar het zou aardig zijn als je nog even met Rienk Nieuwland kunt praten".

Ik zag mijn kans schoon en wist Rienk te charmeren met de Friese samenvatting van mijn Master scriptie, welke wellicht een doorslaggevende rol heeft gespeeld bij de overweging om mij aan te nemen, gezien mijn matige cijferlijst. Een half uur later fietste ik mét een kopie van een projectvoorstel over vesicles naar huis en op 1 juli begon mijn promotietraject.

Het verloop van dit sollicitatiegesprek is kenmerkend voor de samenwerking tussen mij, mijn promotoren en copromotor. Het voortbrengen van nieuwe kennis door het samenbrengen van twee verschillende vakgebieden vereist balans, openheid, humor en misschien ook toeval: vier ingrediënten die volop aanwezig waren. Ton en Rienk, ik ben jullie erg dankbaar voor het vertrouwen dat jullie in mij hebben gesteld. Onze wekelijkse discussies hebben sterk bijgedragen aan de totstandkoming van dit proefschrift. Ton, ik waardeer het dat je naast het leiden van de vakgroep tijd hebt vrijgemaakt voor mijn onderzoek, en ik wil je bedanken voor de vrijheid die je me hebt gegeven. Ik bewonder je creativiteit, brede inzicht in de natuurkunde en openheid. Een mogelijkheid tot samenwerken ga je vrijwel nooit uit de weg. Rienk, ik heb veel lering getrokken uit jouw levenswijsheden ("bluff your way") en je kennis van de biologie en wetenschappelijk schrijven (de 80-20 regel). Jouw experimentele inzichten en ideeën hebben mij een hoop rekenwerk bespaard. Ik heb veel te danken aan jouw staat van dienst in het vesicle onderzoek en jouw besef van ontbrekende kunde. Het is genieten als jij de metrologisten quasi onschuldig vraagt wat de onzekerheid is van de laatste anomalous small angle X-ray scattering resultaten. Guus, ik wil je bedanken voor je scherpe kritiek op onze manuscripten en toekomstplannen. Vanaf de zijlijn hield jij overzicht en stuurde mijn project op cruciale momenten bij, waarvoor ik je erkentelijk ben.

Naast de hulp van mijn promotors en copromotor, is dit proefschrift mede tot stand gekomen door de hulp en ondersteuning van vele collegae, familie en vrienden. Allereerst wil ik alle mensen van het Laboratorium Experimentele Klinische Chemie (LEKC) bedanken voor hun tomeloze inzet. Frank, dit is het tweede dankwoord waarin ik je noem. Sinds onze kennismaking in Philadelphia heb ik veel van je geleerd. Je kritische blik, sterke mening en parate kennis waardeer ik enorm. Ik prijs me dan ook gelukkig met jouw aanstelling in het AMC, wat onmiskenbaar heeft bijgedragen aan de inhoud van dit proefschrift, de planning van mijn promotie en de continuïteit van het onderzoek naar vesicle detectie.

Anita (B.), onder jouw dagelijkse supervisie heeft het LEKC zich ontwikkeld tot het equivalent van een geoliede pipetteermachine met wereldwijde faam. Ik ben erg blij met je expertise in de biochemie en de gesprekken en discussies die we buiten het werk om gehad hebben. Anita (G.), hartelijk dank voor je experimentele ondersteuning. Jouw elektronen microscopie afbeeldingen vormen de fundamenten van dit proefschrift. Het opwerken van 5 L mannelijke urine vlak na je ontbijt is vast een onvergetelijke ervaring die een extra pluim verdient. Chi, zo delicaat als je de pipet hanteert, zo gezwind heb jij een stress poppetje gehalveerd. Mijn dank gaat in het bijzonder uit naar je experimentele ondersteuning buiten het AMC. Onze avonturen in Oxford en Enschede hebben geleid tot een dataset ter dikte van dit proefschrift, waaruit ongetwijfeld een mooi manuscript zal voortvloeien. Marianne, jij hebt mij de fijne kneepjes van de flow cytometer bijgebracht, waarvoor dank. Najat, bedankt voor de energie die je gestoken hebt in het verbeteren van de qNano metingen. De moeilijkheid van deze opgave blijkt uit de term "qNono" die Hajar voor dit instrument bedacht heeft en waar ik tot ongenoegen van sommigen nog steeds veel plezier aan beleef. Yuana, als metrologist van het LEKC heb je een onmetelijke hoeveelheid vesicles geïsoleerd, wat onontbeerlijk is voor het METVES project. René, ik waardeer je sceptische blik en kritiek tijdens de werkbespreking, mede omdat ze mijn focus gericht houden op de klinische toepassing. Tevens gaat mijn waardering uit naar je digitale ondersteuning. Moore, bedankt voor het overbrengen van jouw expertise op het gebied van elektronen microscopie. Anneke, het was mij een waar genoegen om de laatste hoofdstukken van dit proefschrift bij jouw op kantoor te typen. Hartelijk dank voor je secretariële ondersteuning.

Mijn dank gaat eveneens uit naar iedereen van de afdeling Biomedical Engineering & Physics (BMEP), waar een groot deel van dit werk gedaan is. In het bijzonder bedank ik Jelmer en Paul (B.) voor hun bijdrage een de ontwikkeling van de Raman opstelling, Angela en Judith voor hun positieve bijdrage aan de chemie, veiligheid en hygiëne in het lab, Martin (B.) voor de razendsnelle digitale ondersteuning en Jetty voor haar secretariële inzet. Martin (van G.), jouw rekenkunde en ervaring is van onschatbare waarde voor onze groep. Ik wil je bedanken voor jouw bijdrage aan met name hoofdstuk 5. Dirk, jouw kennis van lichtverstrooiing lijkt onuitputtelijk. Onze discussies over de scripts van Mätzler, die ik tussen neus en lippen door ook erkentelijk ben, vormen de basis van 4 hoofdstukken uit dit proefschrift. Henk, met veel plezier heb ik met je samengewerkt tijdens het be-

geleiden van Quido en het onderhouden van de BMEP website. Ed, helaas heeft ons ZonMw project het daglicht nooit gezien. Wellicht kunnen we de pen weer eens oppakken voor een nieuwe projectaanvraag. Cees, bedankt voor je advies over met name de elektrode van de qNano. Nienke, "keeper of the beads", jouw sinterklaas gedicht veranderde mijn eigen perspectief op dit onderzoek voorgoed. Veel succes in Twente! Nicolas, Martijn, Rolf en Roy, jullie humor en kennis van mijn werk heeft geleid tot de titel van dit proefschrift, waarvoor veel dank. Roy en Jeroen (van der A.), ik heb genoten van ons dagelijkse bakje koffie bij Carla, wat goed was voor de ontspanning en zelfs heeft geleid tot een publicatie. Mitra, naast de koffiepauzes op het voetenplein vind ik je ontwikkeling van chemica naar "optica" prachtig. Jeroen (K.), Duc en Paul (C.), met veel plezier heb ik met jullie samengewerkt aan manuscripten op het gebied van optische coherentie tomografie. Maurice, Annemarie, Nienke, Ronald, Oscar en Judith, het optreden met de BEPH-band heeft een fantastische indruk op mij na gelaten. Vanuit de diepste krochten der AMC dank ik mijn (ex-) mede kelder genoten, Gerda, Jasmin, Saskia, Kai, Annemieke en Richelle, maar ook de laatste generatie Tim, Alan, Paul (R.), Dick en Leah voor de goede sfeer en de morele ondersteuning tijdens de koffie.

Tijdens dit onderzoek heb ik de eer gehad om studenten te begeleiden voor hun profielwerkstuk, natuurkunde research practicum, Bachelor onderzoek of Master onderzoek. Imie, Sandra, Bas, Tim, Doris, Quido en Randy, bedankt voor de prettige samenwerking en het leveren van goed werk. Aude, you laid the foundation for the Raman setup, for which I am grateful. Good luck with your new job in Oxford! Dayna, bedankt voor je harde werk aan het afbouwen van de Raman opstelling. Het doet me erg veel deugd dat je een pre-Master gaat doen en dat je parttime aan de opstelling blijft werken.

Andere AMC-ers die ik dankbaar ben zijn Berent Hooibrink voor discussies over flow cytometry en het gebruik van zijn flow cytometer faciliteiten, Jan van Marle en Henk van Veen voor hun ondersteuning van elektronen microscopie, en Mercedes Tuin en Elmar de Pauw bij het opzetten van Exometry B.V..

Binnen de Universiteit van Amsterdam dank ik Sjakie voor brainstorm sessies op bijzondere locaties, welke naar alle verwachting zullen leiden tot een goed vrijdagmiddag experiment. Verder dank ik Alfons Hoekstra voor discussies over lichtverstrooiing en Ivo Mudde voor spectroscopie metingen aan wondkorsten. Van de Universiteit Twente, wil ik Niels Zijlstra bedanken voor fluorescentie correlatie spectroscopie metingen aan vesicles en Cees Otto en Aufried Lenferink voor hun geduld en het beschikbaar stellen van hun Raman opstelling. From the University of Oxford, I would like to acknowledge Chris Gardiner and Ian Sargent for their hospitality, discussions, and measurements with nanoparticle tracking analysis. I enjoyed the visits to your lab. From the University of Birmingham, I would like to thank Paul Harrison for his enthusiasm and excellent editorial about our manuscript on Swarm detection [125]. If a new technology is launched, you bet that Paul has already submitted a manuscript about the feasibility of the technique for vesicle detection.

I greatly acknowledge the entire METVES consortium for their efforts to im-

prove vesicle detection. Our collaboration has been very educational to me. In particular I would like to thank Zoltan for his contributions to Chapter 9 and Michael for his concise but influential comments on the METVES project proposal. A single line from Michael often meant a day of work for Rienk and me.

Since my appointment in the AMC, we have acquired several novel techniques to study vesicles. I would like to thank Oliver Kenyon from Apogee Flow Systems, Andrew Malloy, Patrick Hole, Jonathan Smith, and Claire Hannell from Nanosight, and Hans van der Voorn, Dimitri Aubert, Lloyd Bahlmann, Ben Glossop, Darby Kozak, Rebecca Warr, Anne Bernett, Camille Roesch, and Tini Lawry from Izon Science for discussions and support on their instruments.

Ter afsluiting wil ik enkele vrienden en familieleden in het licht zetten. Durk, Maaike, Jantsje en Anne, tige tank foar jim help mei it oersetten fan de gearfetting. Ik bin o sa wiis mei jim en it resultaat. Iedereen met wie ik tijd heb gedeeld op de Friese wateren ben ik zeer dankbaar voor de onvergetelijke momenten. Luud, hartelijk dank voor 20 ± 1 Mm fietsmobiliteit, koffie en gele pretcilinders. Ik wil alle leden en alumni van A.S.Z.V. SPONS hartelijk danken voor de onmisbare ontspanning in en rond het zwembad. Arnoud alias Freddy en Mariska, ik ben ontzettend blij met jullie als vrienden en paranimfen. Sytse en Marleen, bedankt voor de morele ondersteuning en jullie geduld voor het avondeten. Opa en oma, ik wil jullie als trouwe fans bedanken voor het bieden van een luisterend oor in het weekend. Papa en Ellen, bedankt voor jullie kritiek op de Nederlandstalige samenvatting. Papa, mama, Marleen en Ellen, jullie interesse, ondersteuning en goede zorgen zijn voor mij van onschatbare waarde.

Edwin van der Pol
Amsterdam, 16 december 2014


1 µm